# Three-dimensional shock wave reflection transition in steady flow

**Divek Surujhlal**

A thesis submitted to the Faculty of Engineering and the Built Environment, University of the Witwatersrand, Johannesburg, in fulfilment of the requirements for the degree of Doctor of Philosophy.

Johannesburg, August 2018

# Declaration

I declare that this is my own, unaided work, except where otherwise acknowledged. It is being submitted for the degree of Doctor of Philosophy at the University of the Witwatersrand, Johannesburg. It has not been submitted before for any degree or examination at any other university.

Signed August 10, 2018:

Divek Surujhlal

# Acknowledgements

I would like to thank Professor B.W. Skews for all his important advice and support throughout this work. I have certainly learned a great deal under his supervision which I feel provides me with a solid foundation for research work and for the rest of my career.

I am also very thankful for the constant support of my family which has been a most important factor in my being able to commit myself to the completion of this work.

I gratefully acknowledge the assistance of the technical staff at the Mechanical Engineering Laboratories. In particular, I would like to thank Mr. Shaun Riekert and Mr. Lionel Claassen for facilitating such timeous and high-quality fabrication of the test pieces used for experimental testing. I would also like to thank Mr. Andrew Heydenrych for assistance with troubleshooting certain wind tunnel electrical control faults.

# Abstract

This work details findings of an analytical, numerical and experimental investigation into the physical nature of three-dimensional shock reflection transition. Steady flow shock reflections comprise two types: regular reflection and Mach reflection. Reflection studies have previously been conducted using double-wedge symmetrical test piece configurations. It had been found by previous researchers that the expansion waves resulting from the side edges of the wedges would influence the reflection plane. The three-dimensional nature of real experimental flows gives rise to there generally being a coexistence of regular reflection (at the central portions) and Mach reflection (towards the outer peripheral portions) in between which transition occurs. It is the object of this work to understand three-dimensional transition for flow fields in which edge effects do not influence the reflection plane. Specially modified test piece geometry was developed for this purpose.

Experimental tests were required for validation of the numerical models of the flow field. This was achieved by obtaining oblique shadowgraphs with optical orientation in both yaw and roll to assist in visualising the three-dimensional features of the flow field. These were compared with numerically reconstructed images at the same oblique orientations using a novel reconstruction technique.

The main objective of this work was to identify the degree of correspondence of the three-dimensional transition conditions to those of two-dimensional flows. This was facilitated by means of reducing the three-dimensional analysis to an effective two-dimensional one. It was found that the three-dimensional transition points occur at a higher effective angle than predicted by two-dimensional criteria, and tend towards two-dimensional criteria at reduced free-stream Mach numbers and increased model geometrical spreads.

Another important aspect of this work was the nature of the intersection line in the vicinity of the transition point, i.e., the point of impingement of the incident wave and its Mach surface on the horizontal symmetry plane in between the test pieces. Here it was found that a cusp exists in the sweep profile of the intersection line at the transition point. This was proved from a theoretical standpoint based on a model developed for the analysis of the flow in the vicinity of transition. Evidence of this from the numerical and experimental results is given as well. Higher geometrical spreads and lower free-stream Mach numbers were found to create flatter intersection line profiles at the horizontal symmetry plane on which the transition points were located further forward towards the apex of this line and which gave rise to greater transverse deflections for the streamlines passing through the regular reflection portions.

Further discussion revolves around the nature of the shear and Mach surfaces. The Mach surface heights (representative of the triple line trajectories) are shown to increase monotonically. The shear layer edge trajectory, which originates at the sweep cusp, was found to show considerable transverse divergence but in keeping with the nature and extent of the transition cusp sweep differential, which in some cases was found to be large enough to cause a strong shock solution for the Mach reflection portion. In this case the shear surface edge trajectory diverted from trends seen for other models. The nature of the shear surface as a whole revealed interesting insights into the negative triple configuration of the Mach reflection portions which comprised of convex Mach surfaces. This is in contrast to the geometry obtained for the Mach surface for full Mach reflection numerically studied with a highly-spread geometry. Here, the flat Mach surface was found to increase monotonically towards the periphery in contrast to what was found for flows with edge influences on the Mach surface. It is suggested that this is what precludes complex reflection (central Mach reflection, transitioning to regular reflection further out, with a further transition to Mach reflection at the periphery) from being obtained in such flow fields.

# Scope and contribution

This work presents novel physical findings resulting from the study of three-dimensional shock wave reflection transition. These have contributed to the field in the following ways:

- A novel analytical model has been developed which fully describes the physical conditions of the flow field at the three-dimensional transition point which is free from the influence of edge perturbations. This has led to the discovery of a cusp in the profile on the intersection line of the incident shock surface with the horizontal symmetry plane. Further confirmation of this has been obtained by way of a number of numerical and experimental results. In addition, the developed model is shown to be amenable to resolution of the transition cusp by way of an inverse solution method using measurements from numerical results. The existence of the transition cusp is therefore justified by analytical, numerical and experimental evidence.

- The systematic and controlled study of three-dimensional flow fields and transition has contributed to the understanding of the extent to which three-dimensional transition conditions correspond with that of two-dimensional flows. This has been investigated for a variety of shock and intersection line profiles as well as for free-stream Mach number variations from $M_1 = 2.8$ to $M_1 = 3.4$. Shock geometry variation has been achieved by further modification to the test pieces in terms of altering their transverse spread. These test pieces have successfully facilitated this study by eliminating the influence of edge effects on the three-dimensional transition points.

- The resolution, extraction, and detailed examination of the shear and Mach surfaces for cases exhibiting transition as well as those with full Mach reflection represents the first time this is carried out for flows without edge influences. This aspect has shown interesting results in the way of triple line trajectories, convex orientations of the Mach surfaces (as opposed to concave ones for two-dimensional cases), as well as notable physical conditions and spatial trajectories pertaining to the shear surfaces.

- A novel validation technique has been developed and successfully applied within this work for direct comparison of numerical data with experimental images. The latter was obtained from oblique shadow photography by orientating the optics and optical path in three-dimensional space. The technique that has been developed allows the computational re-construction of shadow and schlieren images from the numerical data for any arbitrary optical path orientation in three-dimensional space (i.e., for roll, yaw, pitch and any combination of these). This represents a useful tool for future experimenters involved with three-dimensional flows.

# Publications arising from this work

Aspects of this work have been accepted or are under review for publication as follows:

1. B.W. Skews, S.S. Lewin and D. Surujhlal, “New approach to the study of three-dimensional shock wave reflection,” presented at the *23rd International Shock Interaction Symposium*, Kruger National Park, South Africa, 2018.
2. D. Surujhlal, B.W. Skews, “Shock wave reflection transition in steady flow,” *J. Fluid Mech.*, Accepted subject to minor modifications.
3. D. Surujhlal, B.W. Skews, “Schlieren image construction for three-dimensional numerical simulation validation,” manuscript submitted for review.

# Contents

# List of Figures

# List of Tables

# Nomenclature

**Acronyms**

| | |
|---|---|
| CAD | Computer-Aided Design |
| CNC | Computer Numerical Control |
| DMR | Direct Mach Reflection |
| FDS | Flux-difference splitting |
| FRU | Flow Research Unit |
| IMU | Inertial Measurement Unit |
| MEMS | Microelectromechanical systems |
| RAM | Random Access Memory |
| TC-1 | Triple Configuration of the first type |

**Greek Symbols**

| | | |
|---|---|---|
| $\beta$ | Sweep angle defined relative to oncoming flow vector | $^\circ$ |
| $\gamma$ | Angle between post-reflection velocity vector and intersection line (as viewed on horizontal symmetry plane) | $^\circ$ |
| $\Delta t$ | Sampling rate of sensor | s |
| $\delta$ | Flow deflection angle | $^\circ$ |
| $\Theta$ | Filtered absolute angle | $^\circ$ |
| $\theta$ | Shock angle | $^\circ$ |
| $\Lambda$ | Raw accelerometer reading from IMU sensor | $^\circ$ |
| $\lambda$ | Optical angular orientation in yaw | $^\circ$ |
| $\rho$ | Fluid density | $\mathrm{kg/m^3}$ |
| $\sigma$ | Time constant for complementary filter | s |
| $\tau$ | Constant for complementary filter formulation | |
| $\tau$ | Net deflection angle of post-reflection flow relative to free-stream vector (as viewed on horizontal symmetry plane) | $^\circ$ |

|  |  |  |
|---|---|---|
| $\phi$ | Optical angular orientation in roll | ° |
| $\chi$ | Ratio of specific heats |  |
| $\Psi$ | Raw gyroscope reading from IMU sensor | ° |
| $\Omega$ | Shock angle relative to reflecting surface | ° |

**Roman Symbols**

|  |  |  |
|---|---|---|
| $b$ | Half-span of wedge or test piece | mm |
| $h$ | Distance from leading edge to horizontal symmetry plane | mm |
| $h$ | Fluid static specific enthalpy | J/kg |
| $h$ | Full CFD domain height | mm |
| $h_1$ | Distance of back face inner control vertex from side of model | mm |
| $h_3$ | Distance of back face outer control vertex from side of model | mm |
| $h_{CV}$ | Distance of lower face apex control vertex from back face of test piece | mm |
| $I$ | Integrated pixel intensity of numerically constructed schlieren image | $\mathrm{kg/m^3}$ |
| $l$ | Full CFD domain length in the streamwise direction | mm |
| $M$ | Mach number |  |
| $MS$ | Mach surface |  |
| $p$ | Fluid static pressure | Pa |
| $\vec{p}$ | Vector of control points (or knot vector) |  |
| $P_b$ | CFD domain boundary pressure | Pa |
| $R$ | Ratio of pre- and post-shock reflection velocities |  |
| $S$ | Slipstream surface |  |
| $s$ | Mach stem height | mm |
| $T$ | Three-dimensional transition point |  |
| $t$ | Parameter for Beziér curve formulation |  |
| $T_b$ | CFD domain boundary temperature | K |
| $u$ | Fluid velocity in the streamwise direction | m/s |
| $V$ | Flow velocity magnitude | m/s |
| $w$ | Full CFD domain width in the transverse direction | mm |
| $w_T$ | Velocity component tangential to shock wave | m/s |
| $x_L$ | Chord length of test piece | mm |

|  |  |  |
|---|---|---|
| $x_l$ | Additional length for initial slice required for reconstruction with optical yaw | mm |
| $z_H$ | Back face height of test piece | mm |
| $z_l$ | Additional height for initial slice required for reconstruction with optical roll | mm |

### Superscripts

|  |  |
|---|---|
| $'$ | Denotes effective quantity |

### Subscripts

|  |  |
|---|---|
| 1 | Point on near-side of field of view of the flow domain; or free-stream quantity |
| 2 | Point on far-side of field of view of the flow domain; or quantity behind incident shock |
| 3 | Quantity behind reflected shock wave |
| 4 | Quantity behind Mach stem |
| $D$ | Quantity at the detachment condition |
| $f$ | Denotes normalised distances/coordinates |
| $i$ | Incident wave |
| $MR$ | Mach reflection portion |
| $r$ | Reflected wave |
| $RR$ | Regular reflection portion |
| $Schx$, $Schz$ | Denotes integrated density gradients computed for schlieren reconstruction in the $x$- or $z$- directions |
| $vN$ | Quantity at the von-Neumann condition |

# Chapter 1

# Introduction

## 1.1 The formation of shock waves in steady flow

Steady fluid flow about an arbitrarily-shaped body placed in its path exhibits considerably different characteristics depending on whether the free-stream flow speed is subsonic (lower than the local sound speed) or supersonic (above local sound speed). The distinction between the two regimes relies on the fact that the obstructing body transmits pressure signals to the fluid upstream of it, this transmission occurring at the local sound speed. In the former case of a subsonic flow regime, the pressure signals reach the oncoming flow streams well before the body is encountered by the fluid. This causes the flow to undergo a gentle local directional change and adjust its path to follow that of the body - in as far as other effects such as boundary-layer growth do not further alter the approaching flow. The directional adjustment is made some distance upstream of the body. A schematic of this is shown in Figure 1.1a.

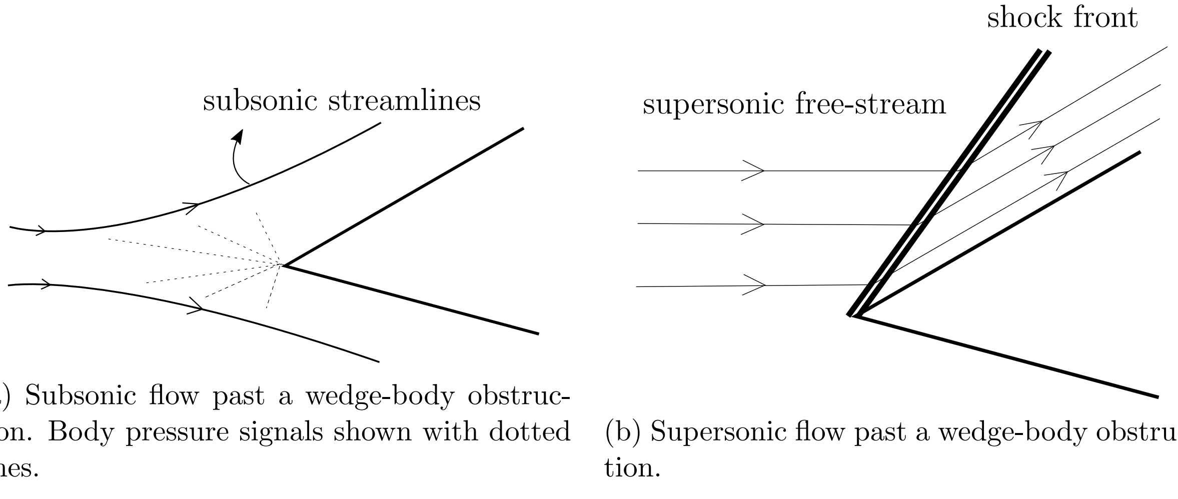

(a) Subsonic flow past a wedge-body obstruction. Body pressure signals shown with dotted lines.

(b) Supersonic flow past a wedge-body obstruction.

Figure 1.1: Comparisons between free-stream steady flow speed regimes.

In the latter case concerning a supersonic steady flow free-stream, the pressure signals emitted by the body are transmitted at a speed slower than that with which the oncoming flow approaches. By virtue of the flow being compressible, the natural phenomenon is for there to be a coalescence of the fluid at some finite distance from the body, and not necessarily at the same distance from all body surfaces. The locus of this coalescence forms a shock wave, and allows for an abrupt change of direction after which the flow is locally parallel to the body. This situation is shown schematically in Figure 1.1b. Steady flow shock waves, in general, also give rise to sudden property changes through them, always resulting in a decrease in velocity and an increase in static pressure.

The schematics of Figure 1.1 show a two-dimensional flow field, wherein the analysis is constrained to within the plane of the page. In reality, however, shock waves are actually shock surfaces, as shown in Figure 1.2b. But this is again somewhat of an idealisation, as planar shock surfaces would theoretically only be realisable if the body about which they form is infinitely long in the transverse direction. For finite aspect-ratio bodies the shock surfaces are swept backwards and downstream as shown in Figure 1.2c. Furthermore, due to the three-dimensional nature of the shock wave, the post-shock flow velocity vectors are also comprised of three components. The additional dimension can be thought of as an additional degree-of-freedom by which an arbitrary streamline may have its local properties altered thus leading to vastly different flow conditions than those realisable in two-dimensional flows, as will be shown in this work.

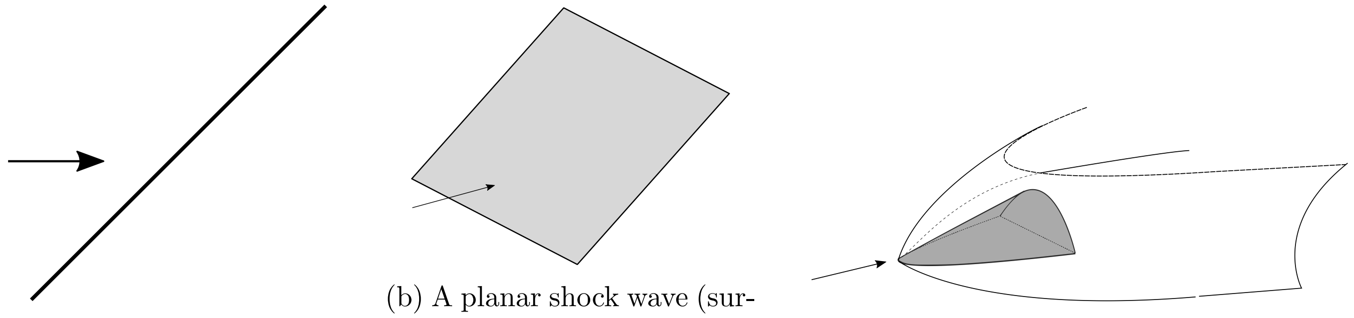

(a) A shock wave in a two-dimensional flow.

(b) A planar shock wave (surface) in a three-dimensional flow.

(c) Swept shock surface about a finite aspect-ratio body.

Figure 1.2: Representations of two- and three-dimensional shock waves - the arrow shows the flow direction for the free-stream.

## 1.2 Background

Numerous works have been undertaken to investigate the physics of two-dimensional supersonic flow fields. Of particular interest is the phenomenon of reflection and interaction of shock waves, and these phenomena are relevant to, amongst other things, aircraft engine intakes. A brief overview of shock reflection is required to put the current research into context. First, reflection phenomena are introduced for two-dimensional flows which enables the extension of those concepts to three-dimensional cases.

Consider a two-dimensional wedge-body placed in the vicinity of a wall surface, as shown in Figure 1.3a. This wall is idealised to be rigid, smooth and adiabatic, to preclude boundary layer and thermal effects. The idealised wall surface is equivalent to a symmetry plane present in experimental setups in which wedge bodies are located symmetrically about a horizontal image plane in a wind tunnel test section. Upon encountering the wedge and wall the free-stream is required to deflect through a shock wave and move towards the wall. The flow here is also supersonic, and upon nearing the wall a second shock wave naturally occurs thereby returning the flow to be parallel to the wall in the same way that the free-stream was turned to be parallel with the wedge. The second shock is called the reflected shock and there are two main configurations for shock reflections in steady flows. Regular reflection produces shock configurations of the type shown in Figure 1.3a, whilst Mach reflection is shown in Figure 1.3b. Further details regarding these reflection types, and the physics of transition between them, can be found in Chapter 2.

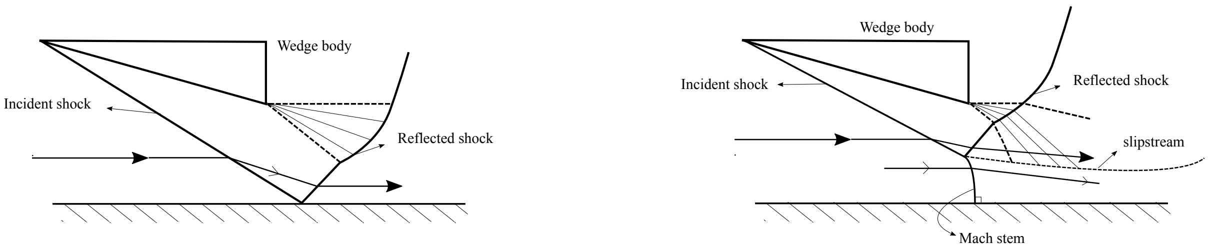

(a) Regular reflection shock configuration. (b) Mach reflection shock configuration.

Figure 1.3: Schematics of regular and Mach reflection configurations in steady flow.

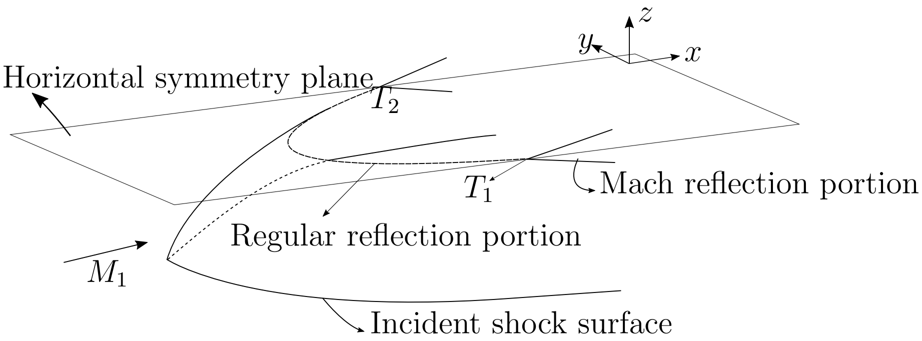

Figure 1.4: Dual existence of reflection types in a three-dimensional flow field with transition points indicated as $T_1$ and $T_2$.

For most three-dimensional flows investigated at the time of writing, both regular reflection and Mach reflection types occur in the same flow field, as shown in Figure 1.4. There is a physical transition mechanism occurring between one reflection type and the other as one considers spanwise stations moving progressively outwards in a transverse direction. It is important to note that this is in addition to the transition conditions relevant to the reflection in the vertical mid-plane of the flow domain, as would be envisioned in a two-dimensional study. The study of the physical processes and fluid dynamics of the transition mechanisms in a three-dimensional flow is an important step towards elucidating further information on real flow fields, in which such a transition is usually present. This is the main concern of this work.

## 1.3 Motivation

Interest in three-dimensional supersonic flows, in which there is a dual-existence of the different reflection types, arose from earlier studies of the three-dimensional fields produced by wedge models. It was first found by Skews [7] that the transition of the reflection pattern at the vertical mid-plane was influenced by edge Mach cones. These comprise edge signals transmitted to the flow field in the vicinity of the Mach cone, as shown in Figure 1.5a. The effect of these signals on the wedge surface flow is to divert the streamlines towards to the wedge edge, which occurs at the locus of the intersection of the Mach cone with the wedge surface and the streamlines. This results in the formation of edge vortices shown in blue in Figure 1.5a. Additionally, the edge Mach cones were found to envelop the transition point $T$ separating the regular and Mach reflection portions of the three-dimensional interaction (Figure 1.5b). The effect of these transmitted signals on the transition point $T$ is to communicate body aspect ratio information to this point, as well as to exact an expansion effect on the flow in and around this region. A study of three-dimensional transition under the influence of such edge-effects would be unrepresentative of the true physical nature of transition. The current research is thus motivated by the requirement to eliminate edge effects from influencing the transition point $T$ in order for a proper study of the associated physical conditions at transition to be made. Also, it is necessary to reduce any further effects due to model geometry which could be communicated to this transition point by way of information paths opening up, if for example, there are subsonic pockets in the flow field.

Three-dimensional fields exhibiting transition of the nature dealt with in this work are readily realised regarding aircraft stores attached to the underside of a wing of a supersonic aircraft [1, 2, 3].

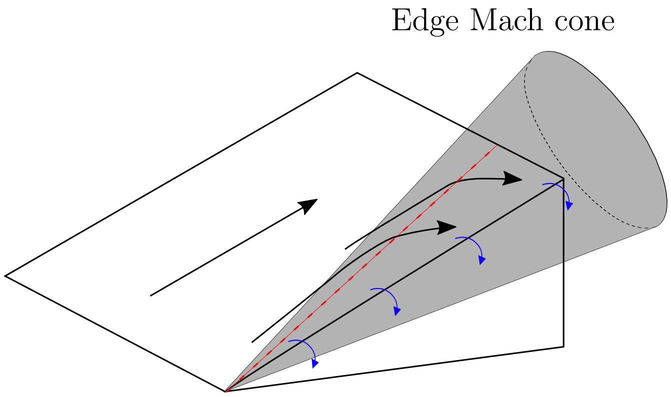

(a) Mach cone and its effect on the flow in its vicinity. Intersection of the Mach cone with the wedge surface shown with a red dotted line along the wedge surface. Edge vortices shown in blue.

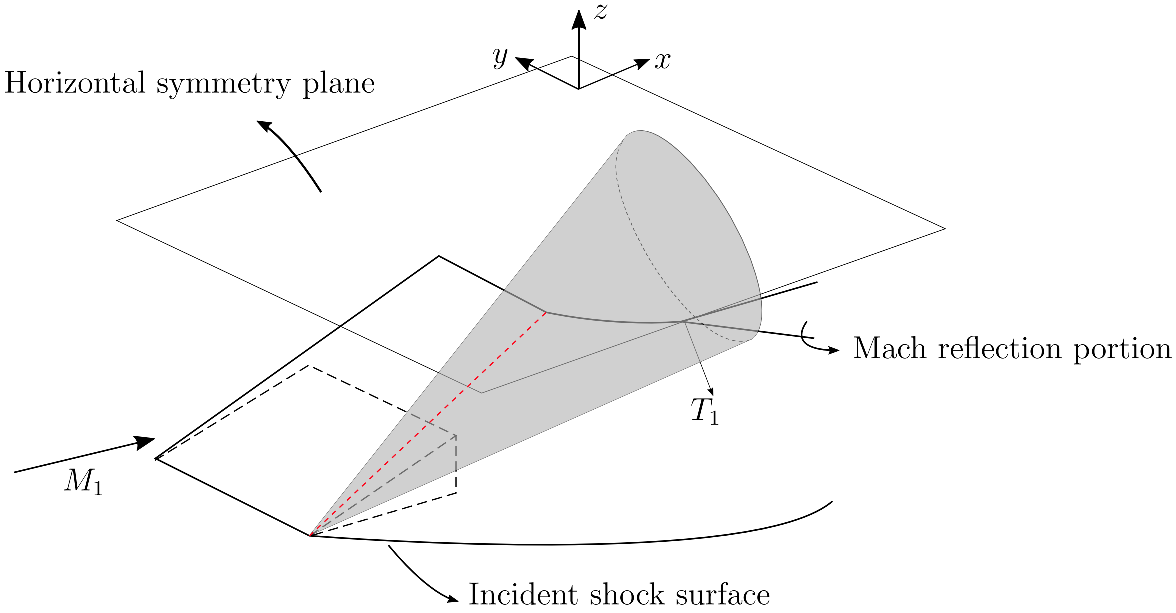

(b) Edge effects influencing three-dimensional transition points (single wedge half-span shown here). Intersection of the Mach cone with the incident shock surface shown with a red dotted line after which the regular reflection portion starts to sweep back.

Figure 1.5: Formation and effects of the edge Mach cone.

# Chapter 2

# Literature review

## 2.1 Introduction

This Chapter first presents introductory details related to two-dimensional shock reflections, for which regular and Mach reflection types exist in a steady flow. These flows are generally experimentally studied using double-wedge configurations, in which wedges are placed symmetrically opposite each other in a wind tunnel test section. The symmetry plane between them is thus an idealised rigid, adiabatic, perfectly smooth wall surface.

Various transition criteria are explored for the physical conditions permitting a certain reflection type to exist in a two-dimensional flow. The reflection hysteresis phenomenon is also briefly considered, which makes applicable different transition criteria depending on whether the domain for shock reflection transition is being entered with an initial configuration of Mach reflection, or regular reflection. These topics are all for two-dimensional flows, but are very relevant for the three-dimensional ones. Three-dimensional edge effects are next considered, which result from the finite aspect ratio wedges used in experiments. The edge signals are crucial to understanding the reasons for certain experiments not producing the hysteresis phenomenon, whilst two-dimensional numerical simulations do. Lastly, the details regarding three-dimensional regular intersection of planar shock surfaces is examined, which elucidates certain relevant flow physics.

## 2.2 Two-dimensional shock interaction

In order to understand the transition between different shock interaction configurations, a physical interpretation needs to be made of the different types of shock interactions in steady flow. As such, only regular and Mach interactions will be considered. The theoretical foundation for the gas flows about these shock configurations is developed from two- and three-shock theories. These will be presented for the two-dimensional case, together with their governing equations, for which flow is constrained to exist in a single plane (i.e that of the paper). The reflection transition criteria will also be presented. These provide the physical basis for the existence of the different reflection configurations given certain free-stream states, and discriminate between which type(s) are physically able to exist at the reflection line. This section forms the basis for the application of the principles explained here to the interaction of shock waves in three-dimensional space.

### 2.2.1 Regular reflection

Consider a supersonic free-stream, at a Mach number of $M_1$, as shown in Figure 2.1. The flow is made to turn in on itself by means of a wedge body and an idealised wall surface which we

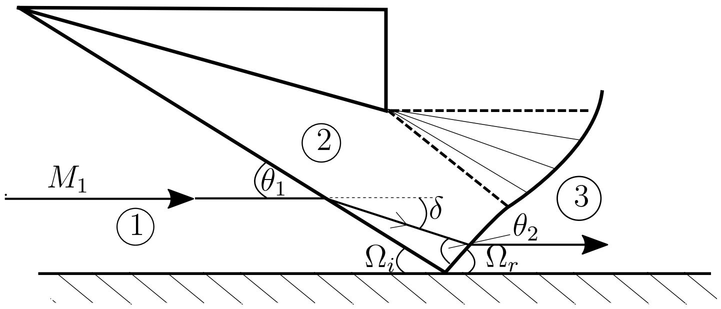

Figure 2.1: Regular reflection configuration.

will assume to be perfectly rigid, smooth, and adiabatic. Due to the condition that disturbances from the wedge cannot propagate upstream in a supersonic flow, a shock wave is formed from the leading edge of the wedge. As a result of the wedge in the flow field, the gas must change its direction and turn to follow the wedge contour, which happens to be straight in this case. It does so once it passes through the shock attached to the leading edge, termed the incident shock hereafter. Through the incident shock, flow properties are altered discontinuously in space, and the flow direction abruptly changes. The Mach number of the fluid is now $M_2$. The gas has been turned by an angle equivalent to that of the wedge angle, $\delta$. Note that the shock wave is formed at an angle $\theta_1$ with respect to the free-stream.

Upon passing through the incident shock, and becoming inclined to the horizontal, the gas starts to approach the wall surface in the same way as it approached the wedge surface in region 1. Therefore, since the flow is supersonic, again the same idea applies here and the flow must be turned parallel to the wall through another shock wave. The shock here is termed the reflected wave hereafter, and is not at the same angle to the wall as the incident shock is relative to the free-stream. That is to say, reflection is generally not specular, as $\theta_i \neq \Omega_r$, because $M_2 < M_1$ and the reflected shock is weaker than the incident shock [18].

In experimental flows where the incident shock wave is formed by a wedge-body, the trailing edge of the wedge serves as a means of expanding the flow. In certain instances this is not desired, especially in studies involving investigation of the reflected wave, although this is difficult to avoid. The reason that the reflected wave is affected by the trailing edge expansion is that the expansion fan characteristics springing from the trailing edge serve to weaken the reflected wave along the segment subtended by the characteristics. This is due to the pressure drop it induces along the wave, and as a result it develops a curved shape. In figure 2.1, the leading and trailing expansion characteristics are shown by the bold dotted lines, and those in the region between these two characteristics are shown as solid lines. It should be noted that the flow in region 3, behind the reflected shock, is somewhat distorted due to the presence of the curvature of the reflected wave. This region also experiences an expansion effect to some extent because of the refraction of the expansion characteristics though the reflected wave. The region is consequently not uniform far away from the interaction point, as is often assumed by most theories on reflection [21, 27, 31].

### Governing equations of regular reflection

In order to describe the states in front and behind each of the shock waves in regular reflection, the two-dimensional gas dynamic relations for oblique shocks must be invoked. Since the governing equations relate the gas properties on either side of a shock wave, the same relations apply irrespective of whether one is considering the incident or the reflected shock. In their most general form, these equations are

$$\rho_i u_i sin(\theta_i) = \rho_{i+1} u_{i+1} sin(\theta_i - \delta) \tag{2.1}$$

$$p_i + \rho_i u_i^2 sin^2(\theta_i) = p_{i+1} + \rho_{i+1} u_{i+1}^2 sin^2(\theta_i - \delta) \tag{2.2}$$

$$\rho_i tan(\theta_i) = \rho_{i+1} tan(\theta_i - \delta) \tag{2.3}$$

$$h_i + \frac{1}{2} u_i^2 sin^2(\theta_i) = h_{i+1} + \frac{1}{2} u_{i+1}^2 sin^2(\theta_i - \delta) \tag{2.4}$$

where $i = 1, 2$ for initial states before and after the incident wave respectively [27]. In addition, there is a compatibility relation that constrains the above governing equations to return permissible states characteristic of regular reflection, namely

$$\delta = tan^{-1}\left[2cot(\theta_1)\left(\frac{M_1^2 sin^2\theta_1 - 1}{M_1^2(\gamma + cos(2\theta_1)) + 2}\right)\right] \tag{2.5}$$

for which $\delta$ is constant for regular reflection, since the flow turned by the wedge must be turned back through the same angle to be parallel with the wall [27]. Flow deflection angle $\delta$ in Equation 2.5 is a function of free-stream Mach number $M_1$ and the shock angle required for the given deflection, $\theta_1$. However, not all combinations of $M_1$ and $\theta_1$ permit physically realisable solutions for regular reflection. Transition criteria are given further attention in a later section, however it is enough to state here that in these instances the shock configuration is altered. This new configuration is termed Mach reflection.

### 2.2.2 Mach reflection

Certain constraints on the inclination of the shock waves and conditions of the free-stream exist such that regular reflection is not always realisable for an inviscid supersonic flow bounded by a wedge and a wall. Such constraints will be dealt with in the next sections, but for now suffice it to state that the system of shock waves will change its configuration to that shown in Figure 2.2. Certain angles shown in Figure 2.1 are omitted here for clarity, but still apply.

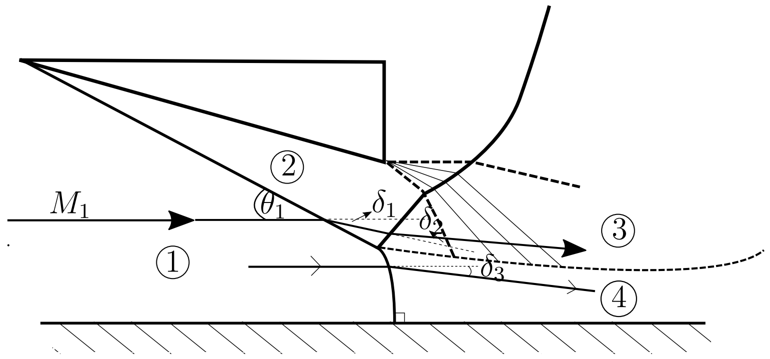

Figure 2.2: Mach reflection configuration.

Once again, there is an incident shock wave formed by the presence of the wedge. There is also a reflected wave, along which expansion characteristics impinge, which attenuate this wave to a certain extent. However, unlike in regular reflection, the reflected wave does not cause a flow deflection fully opposing that induced by the incident wave. Instead, it is only able to turn the flow back by an angle $\delta_2$ where $\delta_1 - \delta_2 = \delta_3 > 0$ [27]. An important feature of Mach reflection is that the incident and reflected wave meet at a point away from the wall surface. The distance between this point and the wall is bridged by a Mach stem. All three shocks meet at a point termed the triple point. The Mach stem shock separates the free-stream from the region behind it, with the effect that the free-stream flow processed by this shock, and that processed by the combined system of incident and reflected waves are at different states. These regions are separated by a slipline, shown in the figure as a dotted line emanating from the triple point. For the local flow close to the triple point, the pressures in regions 3 and 4 are required to be identical, as are the flow directions. These boundary conditions are to be satisfied in order to permit the solution of the flows in the various regions to be physically realisable. However, various theoretical solutions, such as those relating to the prediction of Mach stem height, relax these conditions somewhat in the interests of practical computation of the required solution [31, 27].

### Governing equations of Mach reflection

As with regular reflection, two-dimensional gas dynamic relations across oblique shock waves are invoked as follows,

$$\rho_i u_i sin(\theta_i) = \rho_{i+1} u_{i+1} sin(\theta_i - \delta_i) \tag{2.6}$$

$$p_i + \rho_i u_i^2 sin^2(\theta_i) = p_{i+1} + \rho_{i+1} u_{i+1}^2 sin^2(\theta_i - \delta_i) \tag{2.7}$$

$$\rho_i tan(\theta_i) = \rho_{1+1} tan(\theta_i - \delta_i) \tag{2.8}$$

$$h_i + \frac{1}{2} u_i^2 sin^2(\theta_i) = h_{i+1} + \frac{1}{2} u_{i+1}^2 sin^2(\theta_i - \delta_i) \tag{2.9}$$

for $i = 1, 2$ i.e across the incident and reflected shock waves [27]. Across the Mach stem in the region close to the triple point the oblique relations also hold [27].

$$\rho_1 u_1 sin(\theta_3) = \rho_4 u_4 sin(\theta_3 - \delta_3) \tag{2.10}$$

$$p_1 + \rho_1 u_1^2 sin^2(\theta_3) = p_4 + \rho_4 u_4^2 sin^2(\theta_3 - \delta_3) \tag{2.11}$$

$$\rho_1 tan(\theta_3) = \rho_4 tan(\theta_3 - \delta_3) \tag{2.12}$$

$$h_1 + \frac{1}{2} u_1^2 sin^2(\theta_3) = h_4 + \frac{1}{2} u_4^2 sin^2(\theta_3 - \delta_3) \tag{2.13}$$

It should be noted that the Mach stem is not a straight oblique or normal shock. Its local curvature varies along it, and it is generally accepted that it is perpendicular to the wall at the foot of the stem, as shown in Figure 2.2. It is due to this curvature that the flow in region 4 is not uniform, in the same way that the flow is not uniform in region 3 due to the effect of the expansion characteristics in this region. Therefore, the compatibility conditions

$$\delta_2 = \delta_3 \tag{2.14}$$

$$p_3 = p_4 \tag{2.15}$$

apply only in the vicinity of the triple point. Certain analytical solutions have simplified the situation somewhat by taking the Mach stem to be a normal shock wave, but still preserving the direction condition of Equation 2.14 [21]. Others [31] have taken the Mach stem to be a normal wave, but with a post-shock pressure computed as the average pressure of that for a normal shock and that at the sonic throat behind the Mach stem (see below). Both approaches lead to inconsistency in the solution, foregone in the interest of a practically computable solution which approaches that of a real Mach reflection situation. Nevertheless, the Mach stem is everywhere a strong shock, even in the immediate vicinity of the triple point. Immediately behind the stem the flow is therefore subsonic in a two-dimensional planar flow field. Hence, we see that the approximation of the Mach stem shock as a normal shock is not unreasonable.

Additionally, the expansion characteristics also have the effect of interacting with the slipstream. As stated in [5], this interaction serves to accelerate the flow in the subsonic patch behind the Mach stem due to the induced pressure-drop in this region. In addition, the slipline starts to curve upwards at the sites of impingement of the expansion characteristics. The overall effect is that the slipline is shaped into a nozzle, in which the flow behind the Mach stem is accelerated, becomes sonic, and is expanded to supersonic speeds once more. However, of importance is the subsonic pocket which exists behind the Mach stem and before the throat. This is susceptible to downstream influences affecting the triple point, and has been a region of interest for studies looking at the transition from one type of reflection to another. It should be noted, as stated in [21], that the subsonic patch is only susceptible to influences that directly affect the gas flow in this patch. Downstream influences that ostensibly affect the supersonic region behind it would clearly not have an influence on the subsonic patch. It is clear then, that another source of disturbance to the subsonic region behind a Mach stem could readily be propagated through transverse information paths in a three-dimensional situation where Mach reflection exists in the core, central region, especially in experimental configurations in a wind tunnel test section. This has been an area of interest due to its relevance in understanding the stability (or lack thereof) of one reflection type versus another, and will be discussed in detail in later sections.

## 2.3 Two-dimensional reflection transition

Reflection transition has been a topic of great interest and importance for the last four decades. A great number of works have been produced regarding the physical mechanism of transition. This was spurred on by the apparent disagreement between numerical models and experimental data regarding the conditions of the flow at which transition occurs, as well as the associated hysteresis phenomenon, which was realisable in numerical two-dimensional models but not to the same extent in experimental investigations. It is not the aim of this section to review each contribution to the understanding of two-dimensional transition phenomena, but rather to explain the underlying physical principles which are necessarily taken forward in this study in an effort to understand three-dimensional transition.

The two criteria governing the transition from regular to Mach reflection (and vice versa) originally proposed by von Neumann in 1943 are the detachment and von Neumann criteria.

### 2.3.1 Detachment Criterion

The detachment criterion for the transition in oblique shock reflection is based on the mode of detachment of an oblique shock from the leading edge of a wedge. In this basic case, either the free-stream Mach number or wedge deflection angle do not permit an attached shock solution (see Figure 2.3). In the same way, if the Mach number $M_1$ or flow deflection angle $\delta$ after the incident shock would not permit an attached shock solution required for the flow to turn itself parallel with the wall by an angle $\delta$, then Mach reflection would ensue. This can be better illustrated with the use of a shock polar as in Figure 2.4, in which the red polar (labelled D) indicates the detachment condition. The fact that the reflected polar becomes tangent to the pressure-ratio axis is indicative of this polar curve being the limiting case in which there can be regular reflection at the condition indicated RR on Figure 2.4. Any further flow deflection through the incident shock produces a polar that does not cross or become tangent to the pressure ratio axis. In this latter case, we would obtain Mach reflection as there would be a non-zero deflection after the reflected wave, indicating a finite deflection angle near the triple point. At detachment, if an infinitesimal

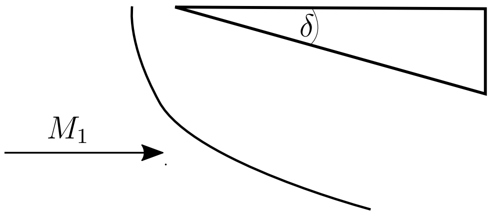

Figure 2.3: Shock detachment from a wedge.

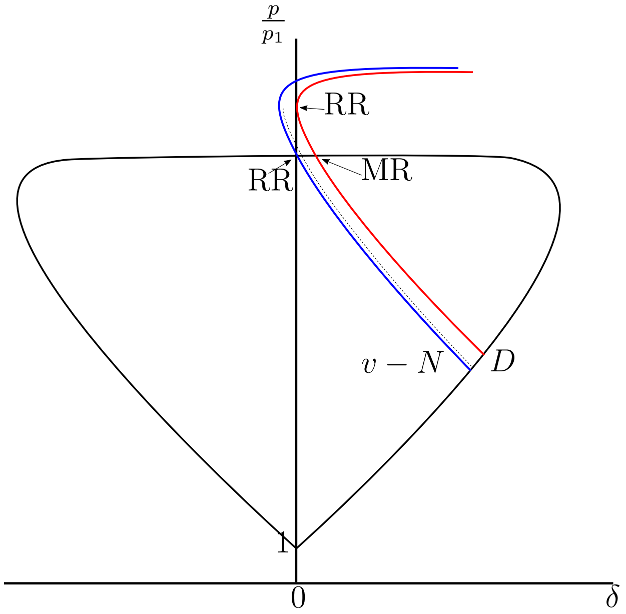

Figure 2.4: Shock polars for transition conditions.

increase in flow deflection after the incident wave is considered, there would occur Mach reflection (MR) as indicated in Figure 2.4 at the intersection of the incident and reflected polars to the right of the pressure-ratio axis. This would be accompanied by a distinct drop in the pressure ratio for the MR solution as the reflection transitions from RR.

It is also worth mentioning here that if one were to increase the flow deflection angle behind the incident shock in an effort to realise Mach reflection, there would come a point where the flow behind the reflected wave is first sonic before detachment occurred. This is known as the sonic condition [27] which is very close to the detachment condition in terms of free-stream Mach number and flow deflection angles that define it. Hence, this condition is omitted from Figure 2.4 for the sake of clarity.

### 2.3.2 von Neumann condition

The blue polar curve (labelled $v - N$) drawn in Figure 2.4 shows the point at which the reflected polar coincides with the highest pressure-ratio obtainable across an incident shock with the same free-stream conditions. This corresponds to a normal shock solution as the post-reflected shock net deflection is zero and gives rise to the suggestion that Mach reflection can also occur at this intersection point. This can be realised if one imagines a polar just to the right of the von-Neumann condition polar, shown as a dotted line in Figure 2.4, where there is an intersection with the upper part of the incident polar. In the limit of an infinitesimal increase of the flow deflection behind the incident wave beyond that of the von-Neumann condition, it is seen that there is a smooth pressure transition between regular and Mach reflection. The state behind the reflected wave is now located on the reflected polar intersection with the incident polar, off the pressure ratio axis for Mach reflection to occur. In light of the smooth pressure transition, this condition has also been termed the mechanical equilibrium condition. This fact is one of the main arguments for this condition being readily obtainable in experimental flows, as the detachment condition does not allow this smooth pressure transition - there is a rather large pressure jump between states on the detachment polar permitting regular and Mach reflection, and transition at the detachment condition would require this to happen. It is mentioned here that the von Neumann criterion does not apply for $M_1 < 2.2$ for $\chi = 1.4$ (ratio of specific heats) as this is at the upper free-stream Mach number limit at which a normal shock would have a downstream pressure equivalent to that downstream of a regularly reflected shock at the same free-stream conditions [27].

### 2.3.3 Dual-solution domain

As has been shown in [27], in the region between the von-Neumann and detachment polars there exist states along every intermediate polar on which both regular and Mach reflection would be possible. On each such polar, states which lie on the pressure-ratio axis correspond to regular reflection, whilst those at the intersection of reflected and incident polars correspond to Mach reflection. In this dual-solution domain both reflection types are theoretically possible. As mentioned, the von-Neumann condition has been favoured in certain experimental studies, but both types have been observed in later numerical and even experimental works such as [20].

In terms of flow deflection, shock angles and free-stream Mach numbers, the dual solution domain can be seen in Figures 2.5 and 2.6. These show the flow deflection $\delta$ and shock angles $\theta$ at a given Mach number for which the von-Neumann and detachment conditions apply. Above the detachment condition, only Mach reflection is possible, and below the von-Neumann line only regular reflection is possible. Between the two curves lies the dual-solution domain for which $\delta_{vN} < \delta < \delta_D$ for the flow deflection angle, and $\theta_{vN} < \theta < \theta_D$ for the shock angle.
The fact that there are limiting conditions that permit either one or the other reflection type to occur leads to a concept of hysteresis regarding the reflection types. This depends on whether the Mach number or flow deflection angle is increased or decreased from a point in either of the regions in Figures 2.5 or 2.6 at which only one reflection type is possible. The physical principle behind this was originally proposed by Hornung et al. (1979) [4], and re-iterated in a later related work [5] in which an experimental investigation of this hypothesis was done. It relies on the fact that in an already-established Mach reflection, independent of the process by which it is established, an information path is opened up between the wedge and the subsonic patch downstream of the Mach stem. This means that a length scale (i.e the wedge surface length) is communicated to the reflection point by means of the expansion signals at the trailing edge. These signals have been shown in Figure 2.2. Therefore, for a deflection angle which is decreased from above the detachment line to within the dual-solution domain, $\delta_{vN} \leq \delta \leq \delta_D$, Mach reflection is expected to persist up until $\delta = \delta_{vN}$, after which any further decrease in $\delta$ would give RR. The reverse is true when considering an increase in deflection angle from below the von-Neumann transition line. Here, no such information path is established as $\delta$ is increased to within the dual-solution domain, since the flow is everywhere supersonic and there is no physical basis for which an information path between the wedge and the reflection point can exist. This gives rise to the persistence of RR up until $\delta = \delta_D$. This difference in transition states depending on the initial reflection type gives rise to the hysteresis phenomenon discussed in the next section.

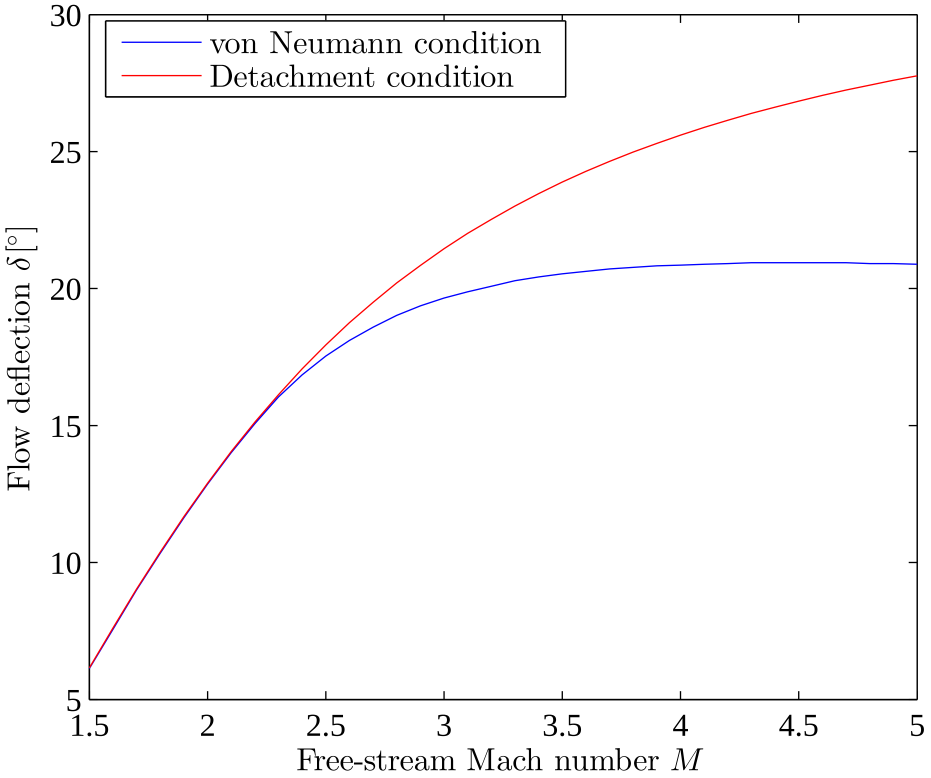

Figure 2.5: 2D transition criteria based on flow deflection angle.

## 2.4 Introducing three-dimensional flows and edge effects

This section is mainly informed by the conceptions of Skews in [7, 8] who contributed significantly to discussions around the differences between experimental and numerical results for the reflection transition of what were ostensibly two-dimensional studies of shock reflection. First, a brief overview of the progress made to understand the true nature of double wedge experimental flows is given.

### 2.4.1 Hysteresis discrepancy

The hysteresis phenomenon mentioned in Section 2.3 underwent significant experimental and numerical investigation since its conception by Hornung *et al.* [4], and certain contributions are mentioned here. The experiments carried out by Hornung and Robinson [5] were specifically in an attempt to demonstrate the existence of Mach reflection up until the von-Neumann condition with decreasing wedge angle, and the persistence of regular reflection up until the detachment criterion with increasing wedge angle. Interestingly, despite numerous tests, transition was consistently obtained at the von-Neumann criterion regardless of whether the wedge angle was increased or decreased from above or below the detachment and von-Neumann conditions. Other studies were in agreement with these findings, and it remained to find out the physical reasons for hysteresis not being obtained in the experimental setups.

A most thorough work by Fomin *et al.* (1996) [10], postulated that, of the numerous factors investigated for being the cause of the aforementioned discrepancy, hysteretic behaviour was most dependent on wind tunnel noise and wedge aspect ratio, as explained in [7]. That wind tunnel

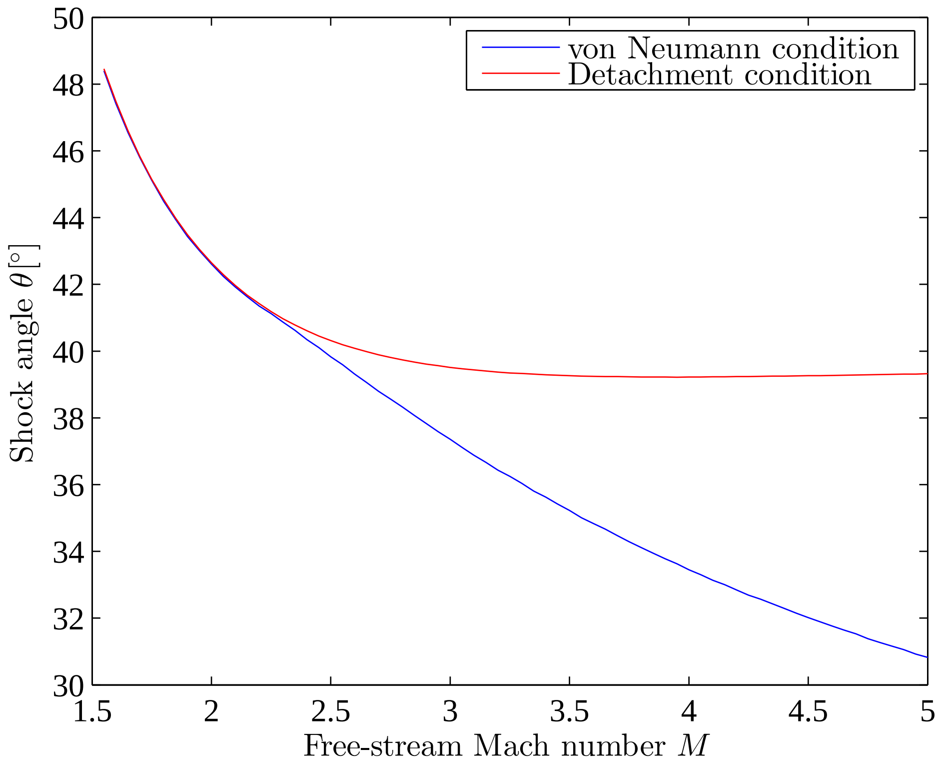

Figure 2.6: 2D transition criteria based on shock angle.

noise was the main cause for the discrepancy was favoured, this being well-founded on numerical simulations done at the time wherein reflection conditions were intentionally tripped by introducing disturbances into the flow field. This is in the same vein as those carried out relatively recently by Mouton [20] who investigated reflection transition by way of laser energy deposition onto the surfaces of wedge models. The effect of noise reduction also underwent significant investigation, and tunnel start-up-induced noise was eliminated by varying wedge angles during a test rather than shutting the tunnel down before changing the wedge angle. Interestingly, hysteresis was not obtained in such experiments done by Hornung and Robinson [5], but were present to a limited extent as found by Chpoun *et al.* [22] in an open jet continuous facility. However, the experiments by Ivanov *et al.* [11] carried out in a low-noise wind tunnel demonstrated hysteresis to the extent that transition from regular reflection to Mach reflection was obtained at the detachment condition. This marked the first set of results which demonstrated persistence of regular reflection to such an extent, and credited reduced free-stream perturbations as one of the governing factors for the realisation of such results. Ivanov *et al.* [11] also showed the persistence of Mach reflection as the wedge angle was reduced from above the detachment criterion, through the dual-solution domain until slightly below the von-Neumann condition, thus successfully demonstrating hysteresis. It is emphasised that the wedge geometries were made to adhere to inlet aspect ratio constraints (discussed below) which precluded interference from three-dimensional edge effects, these playing a key role in tripping transition to Mach reflection prematurely at the von-Neumann condition. Much later, tests conducted by Mouton [20] obtained hyteresis to a certain extent within the dual-solution domain as a means for demonstrating the extent of flow quietness in the free-stream.

The experimental works carried out were informed by two-dimensional numerical results which indicated that hysteresis is indeed possible [13, 23]. These studies were performed in an idealised two-dimensional domain in which the flow field was constrained to within a single plane. This is not the case for experiments, the discriminating factor being that the wedges used are always of finite aspect ratio. This gave rise to questions concerning the effect of the finite aspect ratio on the flow field and whether this has any effect on the hysteresis discrepancy. This idea was borne out of results obtained in double wedge studies [9] which showed flow features that were unexpected for a purely two-dimensional symmetric flow.

### 2.4.2 Finite aspect ratio edge effects

A schematic of the three-dimensional flow field is given in Figure 2.7, which is drawn for a quarter-model i.e the half-span of a single wedge is shown, with the far side being terminated at the vertical symmetry plane. The incident wave surface I is shown in orange, and is seen to diffract around the side edge of the wedge, as well as to sweep backwards. These changes occurring on the incident wave are shown in yellow and start from the locus of the intersection of the edge Mach cone with the incident shock surface. The central core of undisturbed flow is shown in orange and this region thus narrows towards the horizontal symmetry plane. The reflected wave R is shown uncoloured. The line of reflection (termed the intersection line from here onwards and shown in green) changes from regular reflection near the central portion to a Mach reflection at the periphery which is characterised by the Mach surface $M$ shown in blue. The slipstream surface $S$, previously drawn as a line for the two-dimensional case, is coloured red. The wedge finite aspect ratio gives rise to a centred Mach cone along the side edge of the wedge, as shown in Figure 2.8. Within the Mach cone, signals are propagated in the same way as with a centred expansion fan at the trailing edge of a wedge. This causes a decrease in pressure, and an associated diffraction of the incident shock around the wedge edge, which is shown as the yellow translucent surface in Figure 2.8. Here, the incident shock surface is drawn up until it lines up with the reflection line of the planar orange shock surface over the wedge. The incident shock surface is drawn up until it intersects with the symmetry plane a distance $h$ above the wedge leading edge. Importantly, the dimensions of the wedge and its proximity to the reflection (symmetry) plane dictate the degree to which the Mach cone influences certain regions of the flow field, as given in [7].

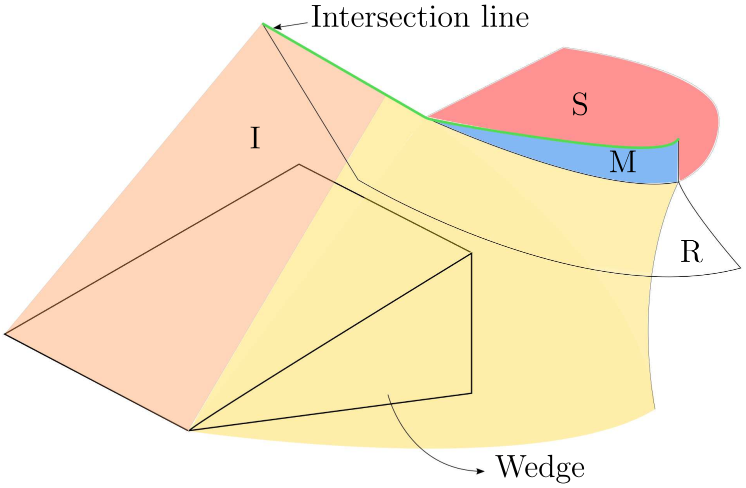

Figure 2.7: Schematic of the three-dimensional flow field existing for a quarter-model of the double wedge configuration, adapted from [7]. Line of intersection of shock surfaces with the horizontal symmetry plane shown in green.

In particular, the intersection point $P$ of the Mach cone with the incident shock surface is a distance $p$ from the leading edge along the wedge surface, which is formulated by

$$p = \frac{b}{\sqrt{\tan^2\mu - \tan^2(\theta - \delta)}}$$

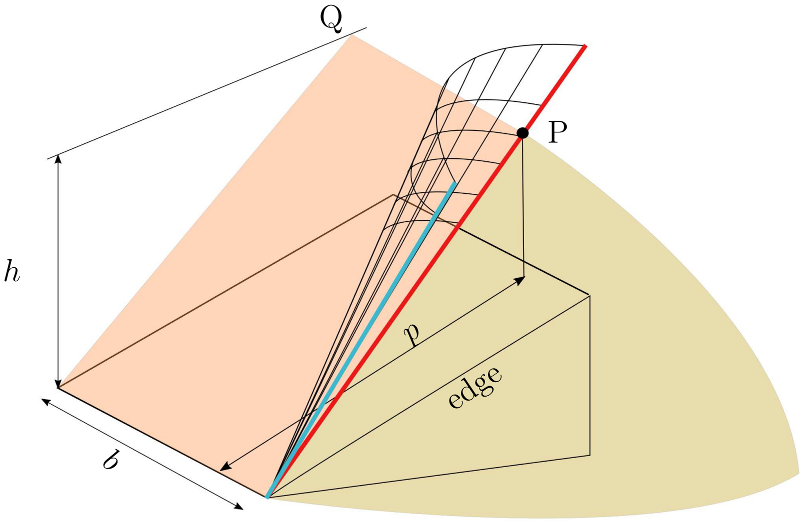

Figure 2.8: Influence of the Mach cone on the incident wave surface shown for a quarter-model. Shock surfaces drawn up until intersection with the horizontal symmetry plane. Intersection of the Mach cone with the shock surface is shown with the thick red line. Intersection with the wedge surface shown with the thick blue line.

where $b$ is half of the wedge span, $\theta$ is the shock angle, $\delta$ the wedge angle and $\mu$ the Mach angle for the flow between the shock surface and wedge. This leads to the definition of a minimum inlet aspect ratio, of wedge half-span to leading edge distance from the reflection plane, which precludes edge influences on the vertical mid-plane reflection point. A higher inlet aspect ratio would allow a two-dimensional core flow to exist all the way up until the shock intersection point at the mid-plane, free of edge influences and three-dimensional effects. The limiting minimum inlet aspect ratio is given by

$$\left(\frac{b}{h}\right)_{min} = \frac{b}{p}\frac{cos(\theta - \delta)}{sin\theta}$$

Therefore, it is seen that the classification of a flow as being two-dimensional is not exclusively dependent on wedge span, but is also a function of wedge spacing because large-span wedges may still permit the mid-plane reflection point, Q in Figure 2.8, to be enveloped by the edge Mach cones thereby creating a three-dimensional flow situation in the central regions.

The above discussions have assumed a reflection configuration that locates regular reflection in the central portion, with Mach reflection outwards at the periphery. Further consideration is given to cases in which there is Mach reflection all along the intersection line.

### 2.4.3 Three-dimensional Mach reflection regions

A different set of flow conditions exist when there is Mach reflection at the central portion of a three-dimensional flow field. In terms of the shock configurations, the case in which there is a full Mach surface covering the entire intersection line is considered.

Firstly, it is well-known that in two-dimensional flows with Mach reflection, there is subsonic flow immediately downstream of the Mach stem. Although a number of works have shown the stem to be curved [28, 29, 30] such that it has an oblique portion nearest to the shear layer (or slipstream), the strong shock solution is generally applicable to all portions along the stem [21, 32]. It was pointed out by Hornung and Robinson [5] that expansion characteristics impinging on the shear layer, after being refracted through the reflected wave, cause a streamiwse pressure-drop in region between the shear layers (Figure 2.9). This happens to the extent that the flow behind the Mach stem is re-accelerated, and by virtue of the formation of a throat between the shear layer and the symmetry line, to sonic conditions after which the flow becomes supersonic once more. It is in the subsonic region between the Mach stem and the throat that any influences, by way of pressure signals, could directly affect the Mach stem. Conversely, there can be no propagation of information upstream to the subsonic region should the signal originate downstream of the throat.

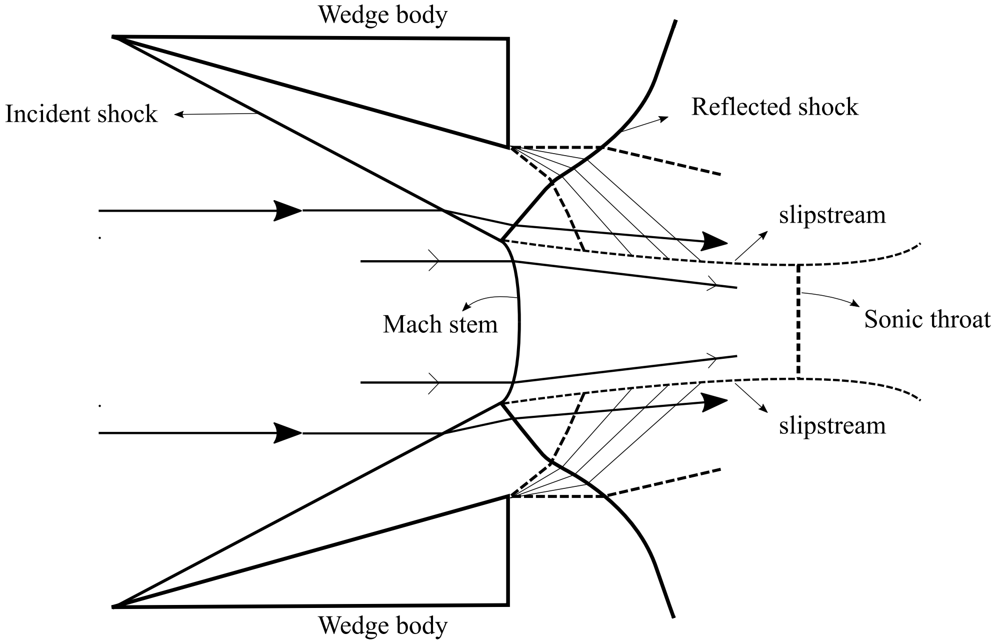

Figure 2.9: Two-dimensional Mach reflection schematic with sonic throat as shown.

Considering a three-dimensional situation, a top view of the Mach reflection is given in Figure 2.10. In this case, there is the addition of the edge Mach cones, within which corner signals from the wedges are present. It can be seen that such edge signals, unlike those of a two-dimensional expansion fan, may penetrate into the central core flow, thus affecting the subsonic region behind the central Mach surface portion. Consequently, such signals are able to influence the Mach surface height and it is because of this that Ivanov *et al.* [11] proposed that the Mach stem height at the central vertical plane for a flow with three-dimensional influences differ from that of an essentially undisturbed core in a three-dimensional flow. In other words, should the Mach stem height at the central plane be similar to that for a two-dimensional numerical simulation, then the core region of the experimental flow can be taken to be free of edge influences.

An initial concept of a shock configuration with a complete Mach reflection was given by Skews in [7], and was further refined following the experimental and numerical work by Ivanov in [12]. Interestingly, it was found that the Mach stem height varied non-monotonically, with undulations in the transverse direction along the sweep of the intersection line (Figure 2.11a). The Mach stem was found to be largest at the central plane, decreasing further outwards, before increasing in height at the periphery. An even more complex reflection was obtained by Ivanov [12, 13], where the Mach stem in the vertical symmetry plane was lowered such that the transverse height decrease noted earlier for full Mach reflection transitioned to a regular reflection portion, before once again transitioning to a Mach stem surface at the periphery as shown in Figure 2.11b. These studies were carried out with test piece dimensions to intentionally have edge effects influence the reflection plane. It still remains to study such flow fields in the complete absence of such effects at the horizontal symmetry plane.

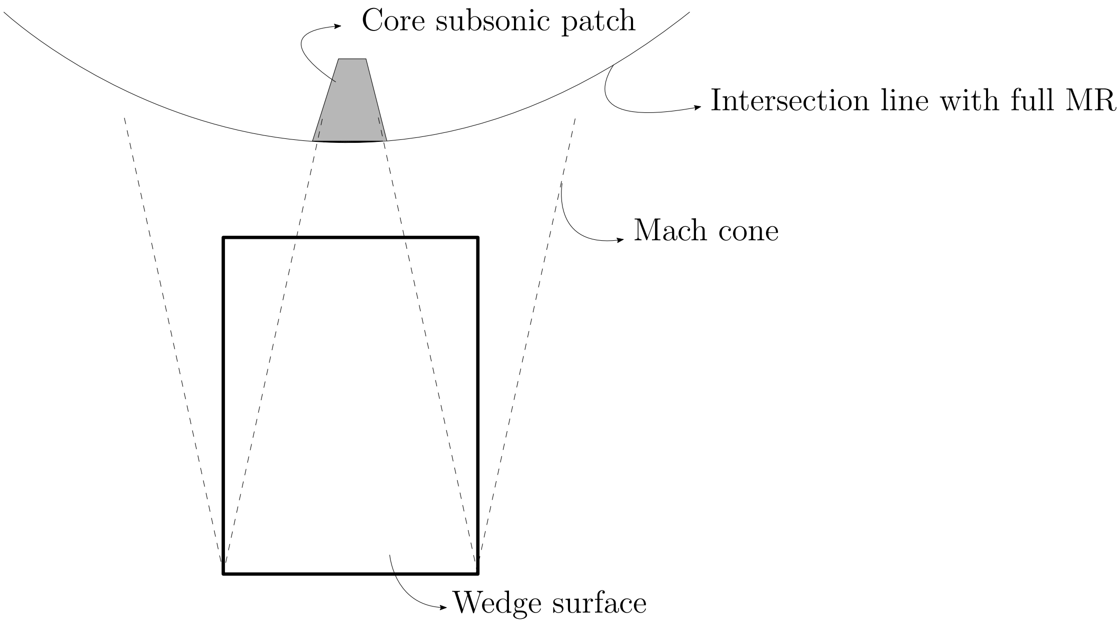

Figure 2.10: Top view of fully three-dimensional Mach reflection with subsonic patch affected by edge signals.

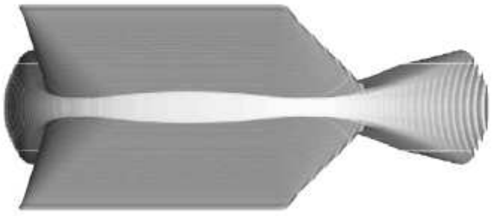

(a) Front view of three-dimensional full Mach reflection from Ivanov's numerical calculations showing undulating Mach surface [12].

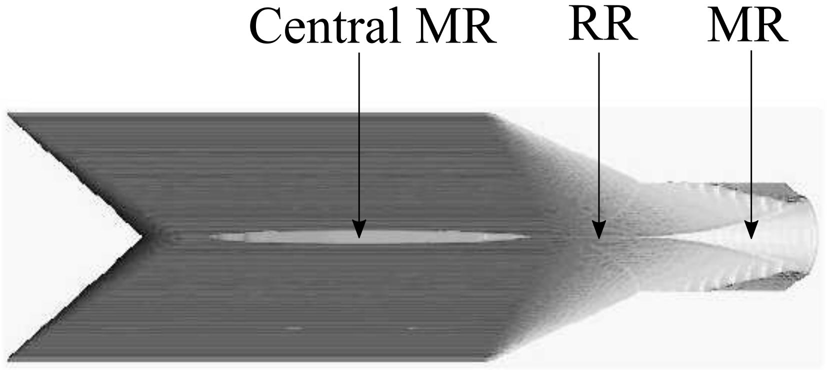

(b) Front view of three-dimensional complex reflection from Ivanov's numerical calculations [12].

Figure 2.11: Three-dimensional numerical results obtained with finite aspect-ratio wedges showing full Mach reflection and complex reflection configurations [12].

## 2.5 Fully three-dimensional flows

An overview of the details concerning the governing principles of three-dimensional edge effects has been covered. Attention is now given to situations in which there is fully three-dimensional flow throughout the flow field with a regular reflection central portion transitioning to Mach reflection further outwards. In such situations, the edge Mach cones envelope the intersection line and the three-dimensional transition points. Some of the points discussed here are directly applicable to further analyses of general three-dimensional flows, regardless of whether they occur due to double wedge configurations or some other body shapes for which the flow field contains a symmetry plane existing as an idealised reflecting surface.

The general three-dimensional flow field is as shown in Figure 2.7. The situation in which Mach reflection exists at the central vertical plane has been previously considered in subsection 2.4.3. Here, the situation is that of a central portion of regular reflection which transits to Mach reflection along the intersection line. The intersection line is the locus of shock interaction points on the horizontal symmetry plane, with a certain portion being that of regular reflection and others being formed by intersection of Mach surfaces.

Early numerical evidence of a flow field of this nature was given by Marconi [6], but in the absence of an edge for the axisymmetric bodies considered in that work. Axisymmetric bodies were numerically studied as being located in close proximity to each other, thus creating a idealised plane of symmetry in between them, or equivalently, an idealised flat plate surface as in Marconi's study. It was shown that the shock interaction indeed changed from regular to Mach reflection along a swept intersection line, as shown in Figure 2.12. It was suggested that the increasing angle of the incident shock at stations further outwards in a transverse direction caused the transition to Mach reflection. This work postulated the use of an analysis plane to reduce the flow conditions to the familiar two-dimensional effective situation. This reduction as applied to the analysis of three-dimensional regular reflection is discussed in a separate section (Section 6.2). Consideration was also given to the trajectory of the triple point after transition. It was found that the initial slope never exceeded 4° relative to the symmetry plane as shown in Figure 2.13 of Marconi's results, thus leading him to suggest difficulty in experimental validation of the transition points. This was not to be, however, as oblique shadow photography [7, 8, 24], such as the examples given in Figure 2.15, and laser vapour screening visualisation [13, 14, 15] (see examples in Figure 2.14) enabled well-resolved location of these three-dimensional transition points for double wedge configurations. This is despite the difficulties associated with three-dimensional re-construction of images obtained from oblique shadow photography experiments.

Oblique shadowgraphs are shown in Figure 2.15 for a general case of fully three-dimensional reflection obtained with a double wedge configuration. Further image results of this type are studied in more detail in [8]. From Figure 2.15a, the incident and reflected waves are clear to see. Although the images of these mask the fact that they are swept surfaces, higher yaw and roll angles of the optics show these waves as being curved, as can be seen for the reflected waves. This is because the image of these waves show as that portion to which the oblique line-of-sight is tangent along the wave surfaces. The interaction of the shock surfaces is at the symmetry plane of these images, which displays a number of interesting features. The first is the Mach surface, which starts off at the wall (labelled as "Wall MS" in Figure 2.15a) and is seen by the irregular vertical structure running along the height of the image. This sweeps round to the forward portions of the interaction i.e. to the left of the image. The foreshortening of the image shows the Mach surface continuing

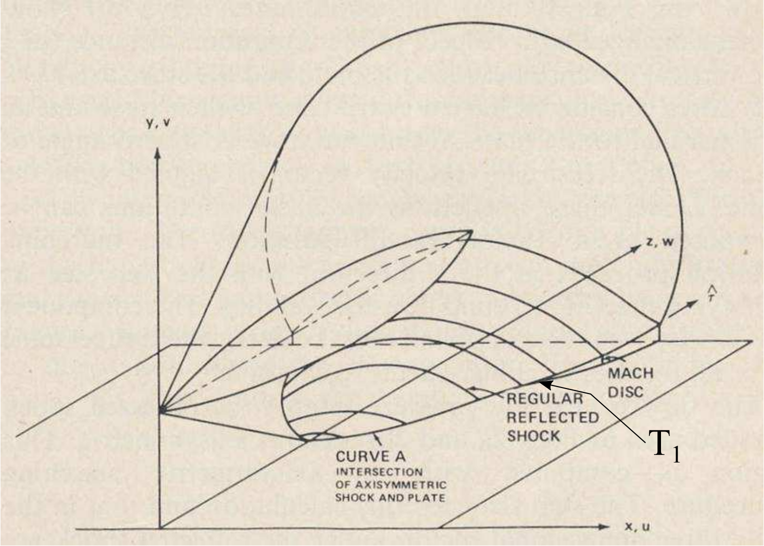

Figure 2.12: Schematic of flow field obtained with Sears-Haack body in proximity with symmetry plane [6] with transition point labelled as $T_1$.

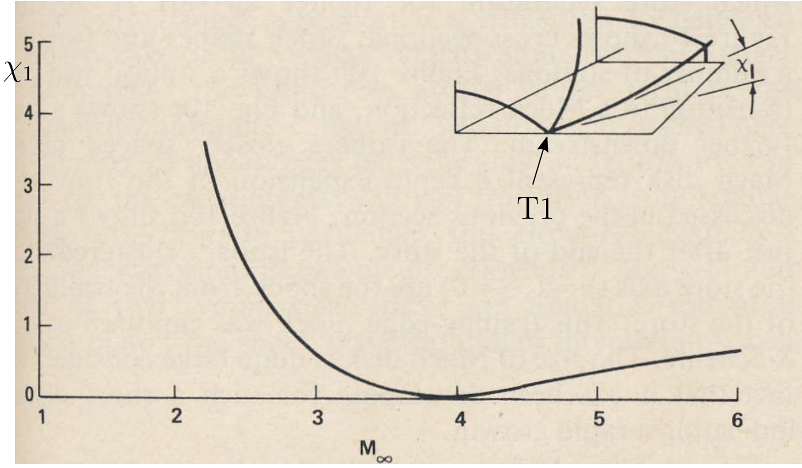

Figure 2.13: Initial slope angle ($\chi_1$) of triple line at transition as per the results of Marconi [6]. The transition point is as shown in Figure 2.12

.

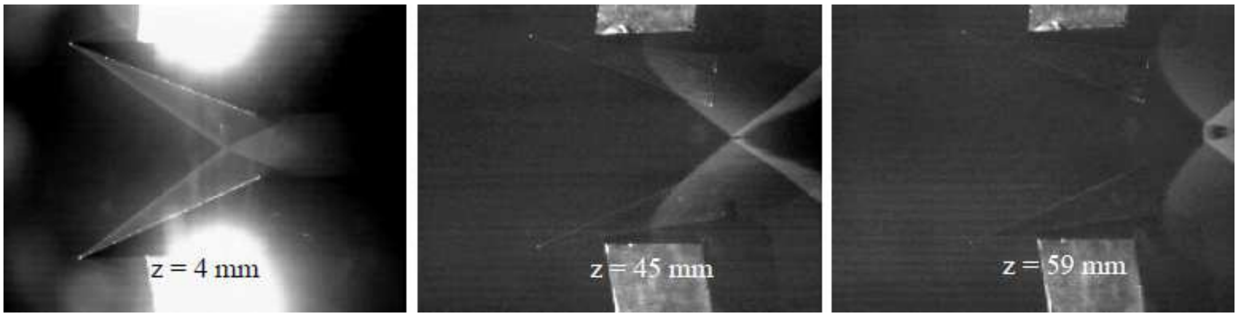

Figure 2.14: Laser vapour screening results of Ivanov [12] for which vapour sheet was generated parallel with the free-stream flow. Locations on $z$-coordinates gives the transverse distance of the vapour sheet from the central vertical symmetry plane.

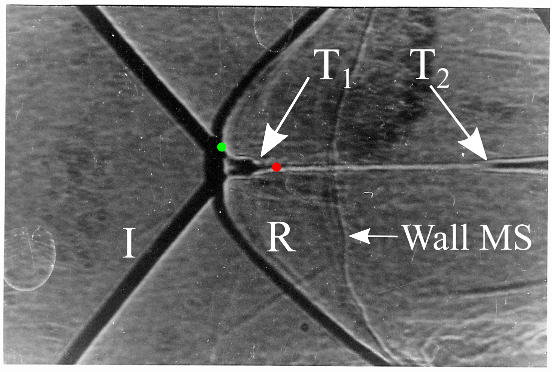

(a) Oblique shadowgraph showing transition points (indicated with arrows) and incident (I) and reflected (R) waves.

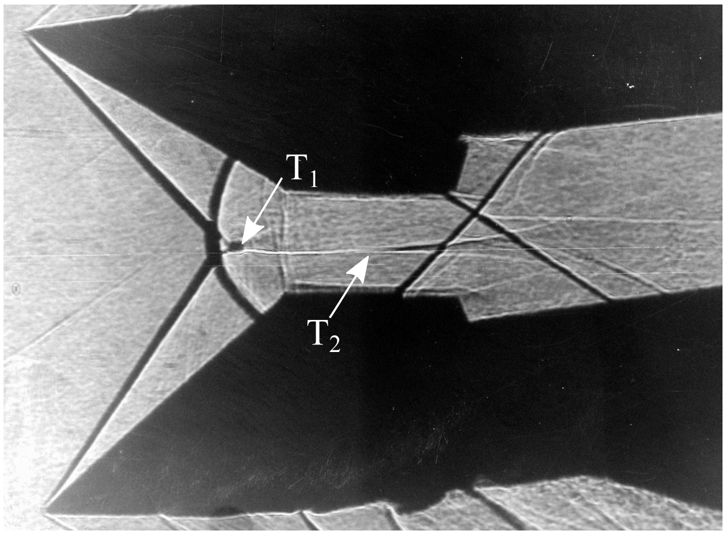

(b) Full reflection pattern seen in the context of wedges as photographed at an oblique angle.

Figure 2.15: Oblique shadowgraphs of the kind used in the current work [16].

to sweep forwards, this time towards the right of the image, and it appears behind the interaction of the tangent incident and reflected waves as a bubble-like structure. The Mach surface terminates at the left-most arrow ($T_1$) in an interesting manner. If the Mach surface is tracked from the leftmost green dot to the red dot to the right of it, the Mach surface seems to decrease in height and subsequently plateau for a short distance after which there is an abrupt drop in height until the transition point $T_1$ is reached at the left-hand arrow. Next, regular reflection ensues until the second transition point $T_2$ is reached at the right-hand arrow. The regular reflection line is clearly shown as the white horizontal line bridging the two transition points. Figure 2.15b shows the reflection with optical yaw and roll and it is seen that the three-dimensional transition points exhibit some kind of instability as noted in [8]. The presence (or absence) of these features at transition would be of interest in the current work for which the three-dimensional transition points are free of edge influences. These are the types of images and features to be interpreted in the current work and which clearly resolve the transition points.

The work by Marconi examined the pressure conditions on either side of the three-dimensional transition points, with it being revealed that there is no pressure jump across the three-dimensional transition points for interactions without the double Mach reflection seen in that work. This is in contradiction to what is expected for purely two-dimensional flows at the detachment condition, where there is a considerable and abrupt pressure adjustment between regular and Mach reflection. The two-dimensional von-Neumann condition permits a smooth pressure change for two-dimensional transition, a defining factor causing it to be considered the favourable criteria from a physical standpoint, especially in light of numerous experimental works showing transition to occur at this point.

The full influence of wedge edge effects was examined in [7, 8] which gave insight into the importance of such three-dimensional effects in hastening transition at the von-Neumann criterion. Consider Figure 2.16, which shows the shock intersection line for a three-dimensional interaction created by a double wedge configuration. As before, there is a central regular reflection region incorporating the intersection line apex which is defined as the forward-most portion $EE$ of the intersection line. It should be noted that the intersection line apex is straight due to the presence of the wedge and that swept bodies would create a fully swept intersection line profile with an apex at a single point. Also indicated are peripheral Mach reflection portions, with transition points labelled as $T_1$ and $T_2$ in between the peripheral Mach reflection and central regular reflection portions. The points at which the primary Mach cones (shown as fine dotted lines) intersect the shock intersection line are labelled as $E$, and points $T$ are enveloped by the Mach cones, as shown. It should be noted that the regular reflection portion (shown with the thick dotted lines) can persist even whilst under the influence of the edge Mach cones.

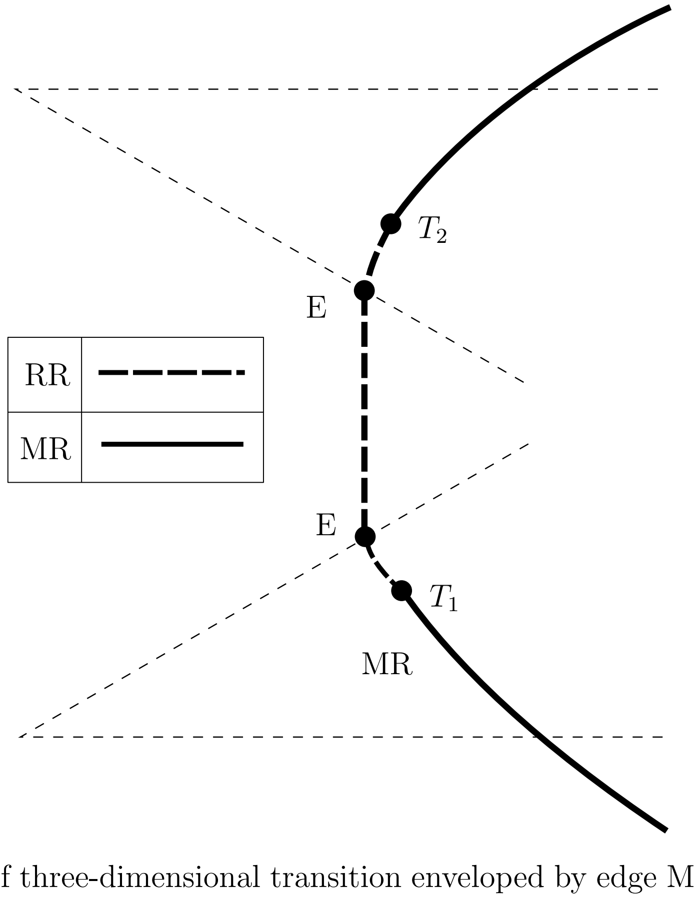

Figure 2.16: Top view of three-dimensional transition enveloped by edge Mach cones for a general double wedge setup.

There are various mechanisms which may be implemented to shift points $T_1$ and $T_2$ inwards along the intersection line towards the central portion of the flow. It should be noted that since this work focuses on steady flow, this so-called inward trajectory of the transition points is in reference to the differences in their spatial location for correspondingly different boundary conditions. Consider one such mechanism to be in the form of an increasing wedge angle, as used in previous transition experiments. For a two-dimensional case, it would be expected from the theory that transition would occur at the detachment criteria. It is suggested in [7, 8] that propagation of points $T$ inwards is physically feasible up until they reach points $E$. During this inward trajectory, the pressure downstream of the shock interaction in the central two-dimensional portion of the flow is continually increasing due to the increasing wedge angle. This is seen by considering a shock polar's intersection with the pressure axis being moved upwards along the axis as the wedge angle is increased, the intersection point moving closer to that of the von-Neumann polar and the highest point of the incident polar (see Figure 2.4 if needed). This pressure increase is of course being matched on the Mach reflection side in order for there to be pressure compatibility on both sides of the transition points along the intersection line. As the wedge angle is increased further still, there comes comes a point when the pressure compatibility can no longer be preserved across the transition point $T$, this situation being reached just as the core flow reaches the von-Neumann condition. The converse of this example is given in [8] where a flow in the dual solution domain in considered, and which has a regular reflection in its core flow (i.e. the flow region not influenced by edge Mach cones) hypothetically obtained after a wedge angle increase. It is concluded there that no physical mechanism exists for which the pressure jump from the Mach reflection side to the regular reflection side can be sustained. Therefore, core flow transition (i.e. the shock reflection transition within the core flow region) must occur at the von-Neumann condition and the spatial limit of the inward three-dimensional transition point trajectory is the point at which the edge Mach cone meets the incident shock surface at $E$. It thus remains to be seen the spatial behaviour and changes of the transition points in the absence of edge effects - one of the aims of the current work.

In order to understand three-dimensional shock interactions, further analytical developments will be described in Section 6.2. This will additionally describe an analytical model of three-dimensional transition points in the absence of edge effects.

## 2.6 Conclusions

A variety of aspects surrounding the nature of shock wave reflection and transition are examined in this Chapter, for both two-dimensional and three-dimensional flow fields. In addition, an overview of the various works done gives an idea of the current state of research regarding three-dimensional transition. It can be seen that three-dimensional flows have undergone extensive conceptual, numerical and experimental investigation, but all in the presence of edge influences from finite aspect-ratio wedge bodies. The current work aims to eliminate such effects from influencing the reflection plane at all and to subsequently understand certain physical aspects of three-dimensional transition.

# Chapter 3

# Research objectives

The primary objective for this work is to examine three-dimensional reflection transition in the absence of the influence of edge effects and to ascertain the extent to which three-dimensional transition corresponds to that for two-dimensional flows.

Further work required for the study of three-dimensional shock reflection is to involve:

1. Numerical computations of the flow field for various geometrical configurations of models (located symmetrically) which preclude edge effects from influencing three-dimensional transition points, in order to obtain different types of shock reflection configurations. Specifically, it is required to investigate:
    - The orientation of the streamlines, particularly in the vicinity of the transition points.
    - The proportion of reflection types along the intersection line and the orientation of the streamlines aft of the Mach surface.
    - The possibility of obtaining a Mach surface region in the central portion of the flow field, transitioning to regular reflection further outwards and again to Mach reflection at the periphery. This will be termed a complex reflection pattern.
2. Experimental tests for the validation of the numerical data, and visualisation of the shear surfaces using oblique shadow photography.

# Chapter 4

# Experimental facilities

## 4.1 Introduction

All experimental tests were run in the supersonic wind tunnel at the Flow Research Unit (FRU) at the University of the Witwatersrand. The wind tunnel is equipped with a variable-contour sliding block nozzle, which allows a continuous variation of the test section Mach number in the range $M_1 = 1.1$ to $M_1 = 3.4$. The details of this facility and the associated devices and apparatus used will be discussed in this section. Further details regarding technical specifications of the various devices used during wind-tunnel operation can be found in the Appendix.

## 4.2 Supersonic wind tunnel layout and operation

### 4.2.1 Air supply and storage vessel refill

The supersonic wind tunnel (SSWT) used was a blow-down type. Operating specifications of the wind tunnel are given in Table 4.1.

Table 4.1: SSWT specifications.

| | |
|---|---|
| Type | Blow-down |
| Calibrated Mach range | $1.1 - 3.4$ |
| Test section dimensions | 101.6 mm ×118 mm |
| Operational stagnation pressure | 250 kPa |

The wind tunnel is directly coupled to a supply pressure vessel, which stores the supply air for a number of blow downs. The vessel is filled with air that is drawn into a compressor from atmosphere. Air is made to flow from the compressor outlet into a drier chamber containing silica sand pellets. This acts to extract moisture from the air, prior to it being stored within the air supply pressure vessel. A schematic of the compressor and drier is shown in Figure 4.1.

Ball valves 1 and 2 are closed during operation of the compressor when the supply tank is being filled. Air lines from the compressor outlet direct the supply air to oil and water filters, which remove unwanted dust or entrained species in the air. The air is then directed to the silica sand drier chamber, which itself becomes pressurised during the time in which the compressor is operating. This further extracts moisture in the air, and is necessary in order reduce the possibility of there being condensation during expansion of the air at the wind tunnel nozzle section. After

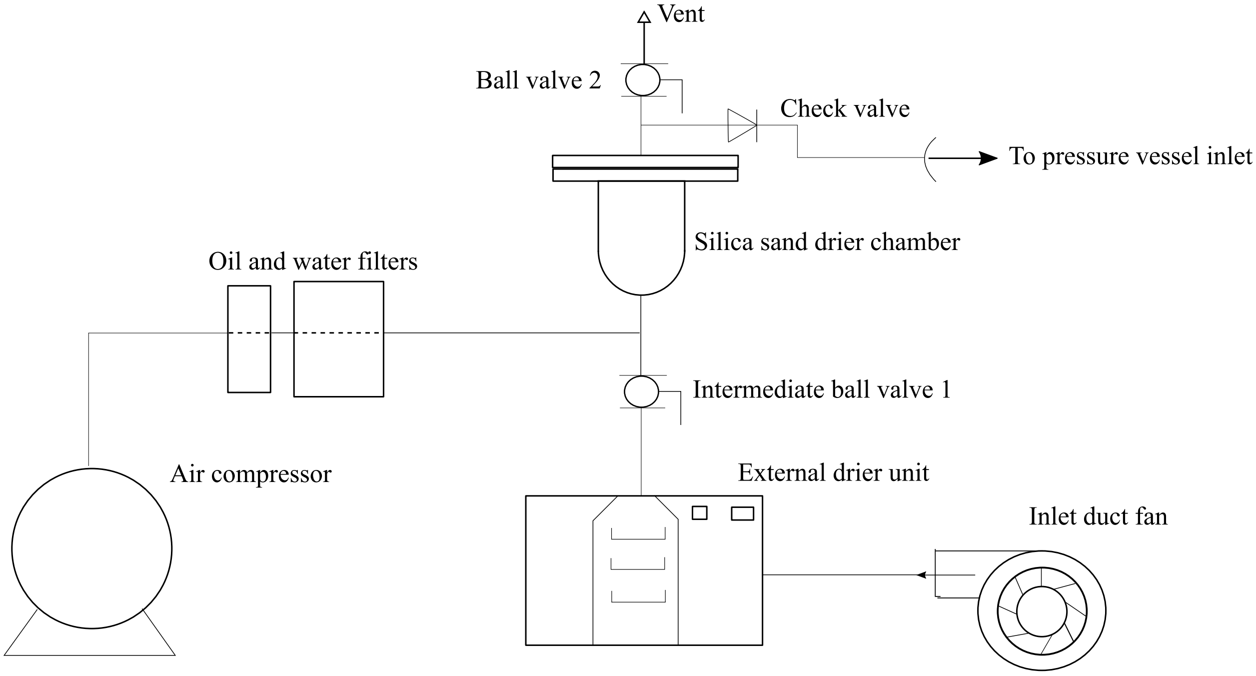

Figure 4.1: Air supply valve diagram.

this, the air is directed to the inlet of the pressure vessel, which is fitted with a check-valve. This ensures that pressurised air in the vessel does not reverse and hinder the compression process during vessel refill periods. The compressor is automatically shut down once supply tank pressure is at approximately 14.2 bar. This is a safety feature used to prevent the vessel pressure from reaching or exceeding its rated pressure of 17 bar.

Once the compressor is shut down, valve 2 is opened prior to opening valve 1. Opening valve 2 vents the pressurised air in the silica sand drier chamber to atmosphere. Having performed its function of moisture extraction from the supply air, the silica sand pellets need to be dried. This occurred at the conclusion of each day of testing by switching on the drier unit. For this process, air is drawn in via the inlet duct fan, heated and directed into the silica sand drier chamber.

### 4.2.2 Supersonic wind tunnel facility

The supersonic wind tunnel main facility comprises of the components shown in Figure 4.2.

As discussed in the previous subsection, the pressure vessel is supplied with air from the compressor and a few associated devices. Once pressurised, the supply air is kept within the tank by means of a check-valve between the vessel inlet and the silica sand chamber, as well as by means of a pressure-relief valve (PRV) connected at the outlet of the vessel. The PRV is normally closed, thus no air is able to vent from the vessel.

When the tunnel is in operation during a test, the PRV serves the purpose of providing a constant pressure supply to the settling chamber. The way in which this is accomplished is by means of a pneumatic control system, the details of which are discussed later. Air is discharged from the pressure vessel at a pressure sufficiently reduced to that required in the settling chamber. This is taken to be the stagnation conditions for the flow upstream of the wind tunnel nozzle. Upon reaching the settling chamber, the flow is made to encounter baffles, which are screens used to smooth out large-scale eddies in the flow field. Next, the air is accelerated through the convergent

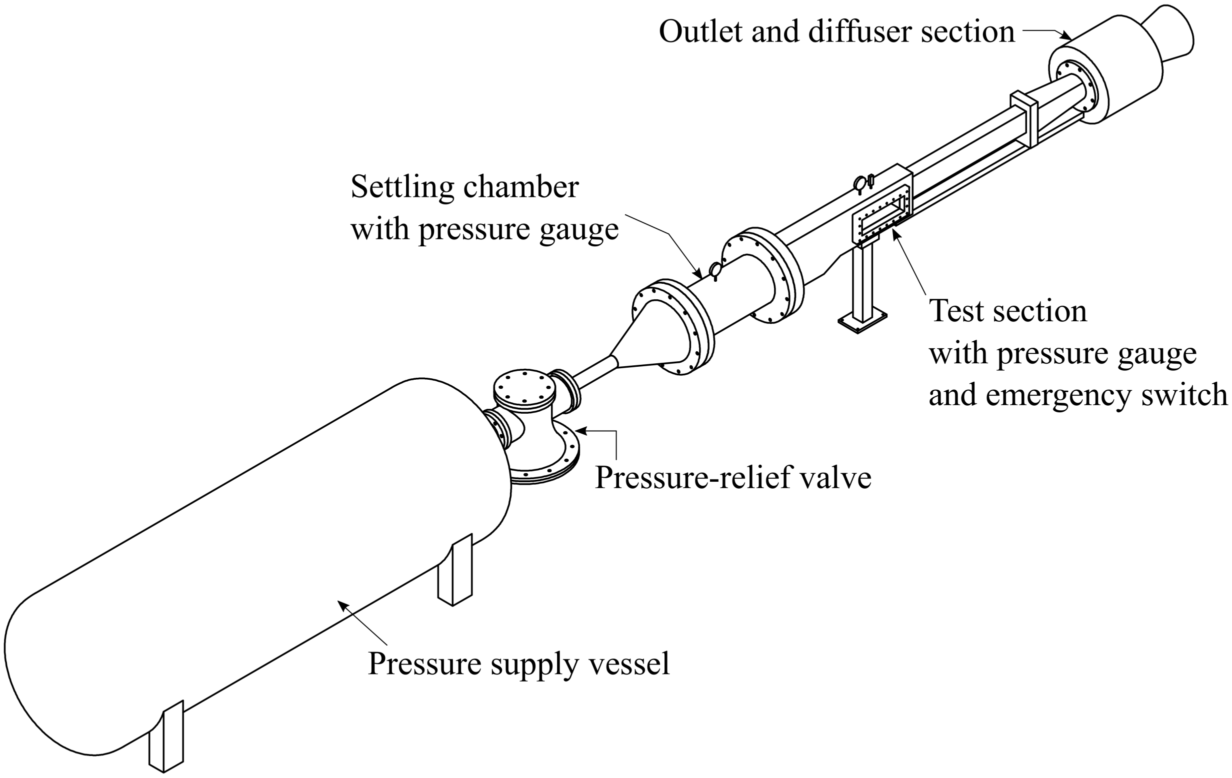

Figure 4.2: Overview of supersonic wind tunnel facility layout.

part of the nozzle section, and upon becoming sonic at the region of minimum area, is expanded to supersonic speeds through the divergent part of the nozzle.

The nozzle throat area can be steplessly adjusted to provide the desired Mach number in the test section. This is done by means of a Veeder counter, which is a chain-driven mechanism attached to the floor beam of the test section (see Figure 4.3). As the Veeder wheel is rotated, the floor beam is horizontally moved. This in turn causes the bottom block of the nozzle section to translate either towards or away from the top nozzle block, thus decreasing or increasing the nozzle throat area, respectively. The expansion of the nozzle is necessary in order to allow a conversion of the energy of the air, built-up during the convergent nozzle section, into kinetic energy for further acceleration beyond Mach 1. Such an energy conversion is that of the thermal energy of the air into kinetic energy - in fact this could be felt when the tunnel test section was opened.

Upon reaching the test section at the desired Mach number, the flow area of the air is reduced due to the presence of the test model in the test section. This area reduction should never be too great, as this would cause the tunnel to become blocked, and a promote a disgorge of supersonic test section flow such that a normal shock would form upstream of the test section causing subsonic test section flow. It is generally accepted that an area reduction of not more than 9% of the nominal test section cross-sectional area is acceptable for this wind tunnel.

After flowing past the test models, air flows through the diffuser section where it is made to converge to sonic speeds, and then made to diverge to subsonic speeds. The subsonic air flows through an exhaust duct and vents out on the roof of the laboratory building.

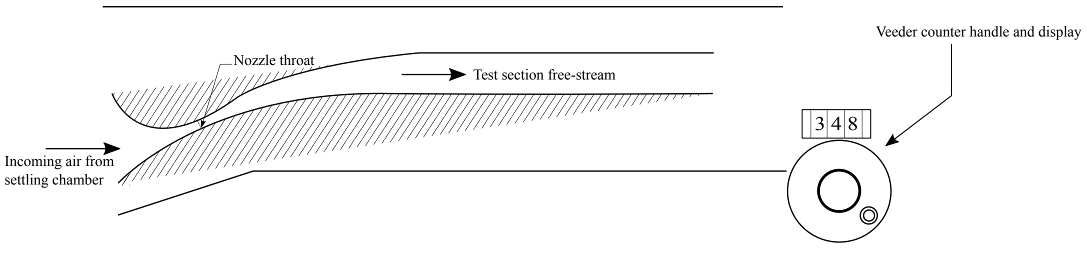

(a) Veeder counter mechanism and air flow through nozzle throat.

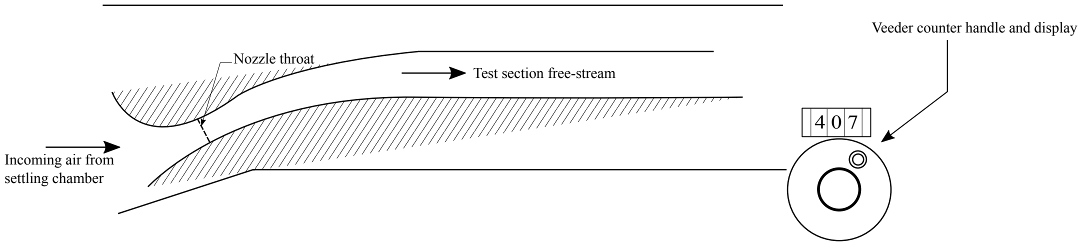

(b) Veeder counter mechanism and air flow through nozzle throat at a lower Mach number than in (a).

Figure 4.3: Operation of Veeder counter mechanism and nozzle throat area variation.

### 4.2.3 Wind tunnel pneumatic control system

A pneumatic control system is installed in the supersonic wind tunnel control room to allow for safe and reliable operation of the wind tunnel. A schematic of this is shown in Figure 4.4, with associated components and their respective functions listed in Table 4.2.

The main auxiliary components of the wind tunnel (see Figure 4.4) are the pressure supply tank and the compressor (not shown in Figure 4.4). The compressor supplies the tank with pressurised air and shuts down once the tank reaches the operating pressure of 14.2 bar. Once pressurised, the air in the tank is contained because the main pressure relief valve is normally closed. However, some of the pressurised air is tapped off from this valve through Line A.

This air passes through a strainer on (A) after which some of it is fed through to the pilot valve, and some is fed through to the control board pressure regulator on Line 1. During the start of a test, the standard procedure is to adjust the regulating dial on the control board to pass the air on Line 2 to the pilot valve diaphragm. Once the pressure on the diaphragm is high enough, the pilot valve opens. This causes the air that has already passed through Line A into the pilot valve to pass out into Line 3. Air is contained in this line until the actuating solenoid valve (SV 1) is activated. This is made possible by pressing a button on the interface of the computer control program. This sends an electrical signal to the data acquisition system (DAQ), which in turn is transmitted to a solid state relay (SSR) switch, which, upon closure, activates SV 1. Thus, Line 4 is opened for air to pass through it and into the diaphragm chamber at the bottom of the main valve (Line B). The air in Lines 3 and 4 is termed the control air. The main valve opens under a sufficiently high pressure threshold, and the internal mechanisms of the main valve allow air at a pressure reduced compared to the supply tank to exit at the main valve outflow port and into the settling chamber.

This air is monitored a feedback mechanism. First, some of the pressurised air is fed back to the underside of the pilot valve diaphragm. When the pressure in this line (and thus the pressure in the settling chamber) is equal to the pressure on the pilot valve diaphragm, the pilot valve throttles, and sustains its extent of opening. This means that the pressure set at the control board is what is realised in the settling chamber and is the stagnation pressure for the test section flow. The feedback mechanism is what allows for a constant pressure supply to the settling chamber. If, for example, the settling chamber experiences an increase in pressure, the pilot diaphragm will close, meaning air at a lower pressure will pass through Lines 3, 4 and B; this will have the effect of slightly closing the main valve and lowering the pressure at the settling chamber thus offsetting the initial increase. The opposite happens when the settling chamber experiences a decrease in pressure to that lower than the set stagnation pressure condition.

An emergency shutdown mechanism was introduced into the wind tunnel control system. This is realised by a pressure switch attached to the test section. Should the test section pressure increase abnormally, the switch causes SV 1 to close, whilst SV 2 is opened to atmosphere. Thus, no air is passed from Line 3 to Line 4 across SV 1, and the air in Lines 4 and B is vented to atmosphere due to SV 2 being open.

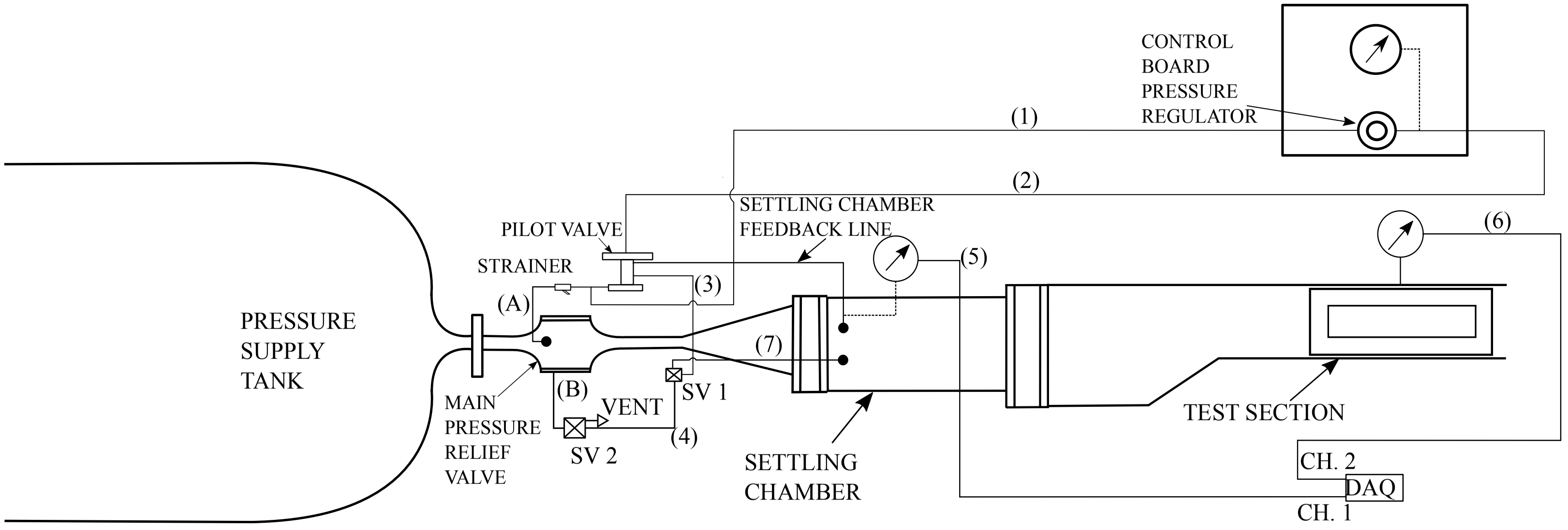

Figure 4.4: SSWT valve diagram.

Table 4.2: Pneumatic line functions.

| Line no. | Function |
|---|---|
| A | Tapped off main supply to pilot valve |
| B | Control air for opening main valve diaphragm |
| 1 | Tapped off main supply to control board regulator |
| 2 | Initial pilot diaphragm pressure |
| 3 | Control air line for main valve |
| 4 | Control air line through SV 2 |
| 5 | Settling chamber transducer connection to data acquisition system (DAQ) |
| 6 | Test section transducer connection to DAQ |
| 7 | Settling chamber emergency shut down line to SV 1 |

## 4.3 Flow visualisation and optical system

Visualisation of the flow field in a manner such that three-dimensional features are observed required the use of oblique shadowgraphy and schlieren photography. Each of these methods employed in this investigation are briefly described in this section, as well as the equipment required to reliably orientate the optics to observe three-dimensional flow features with a quality that allows insight into the nature of the flow fields to be discussed later.

### 4.3.1 Flow visualisation through a compressible gas medium

Air-generated shock waves are not visible to the naked eye under the conditions present in the wind tunnel test section. Therefore, optical techniques are used to render such flow features observable under a specific set of camera and lighting conditions. In general, when light is passed from one medium to another that have different refractive indices, the light rays are refracted. Regarding the visualisation of compressible gas flows, light is passed from the air outside of the test section, into the test section and out the other side. The test section contains compressible flow features, and as such, contains regions of variable density. This causes a change in the refractive index of the medium through which the light passes, hence causing the light rays to be deflected depending on where such changes occur in the flow field. Therefore, a camera placed opposite the light source on the side of the test section out of which the light emerges would construct a final image in which shock waves (and other compressible flow features) appear as dark (or lighter) regions, depending on how light rays are deflected through the test section.

This is the basic principle which underpins schlieren and shadowgraph photography, each having their own merits based on the type of flow features to be visualised. Thus, a brief outline of each is given next.

#### Schlieren photography

The final result of schlieren photography is the visual representation of density gradients in a specific direction i.e $\frac{\partial\rho}{\partial x}$, or $\frac{\partial\rho}{\partial y}$ etc. Use of the knife-edge and the way in which the final schlieren image is generally formed is shown in Figure 4.5. As rays are deflected through the test section due to the flow compressibility, some are prevented from reaching the camera lens due to the presence of the cutoff. These are rays that are deflected in a sense normal to the knife-edge, and the ray deflection is a function of the density gradient in the test section. Therefore, the final image shows

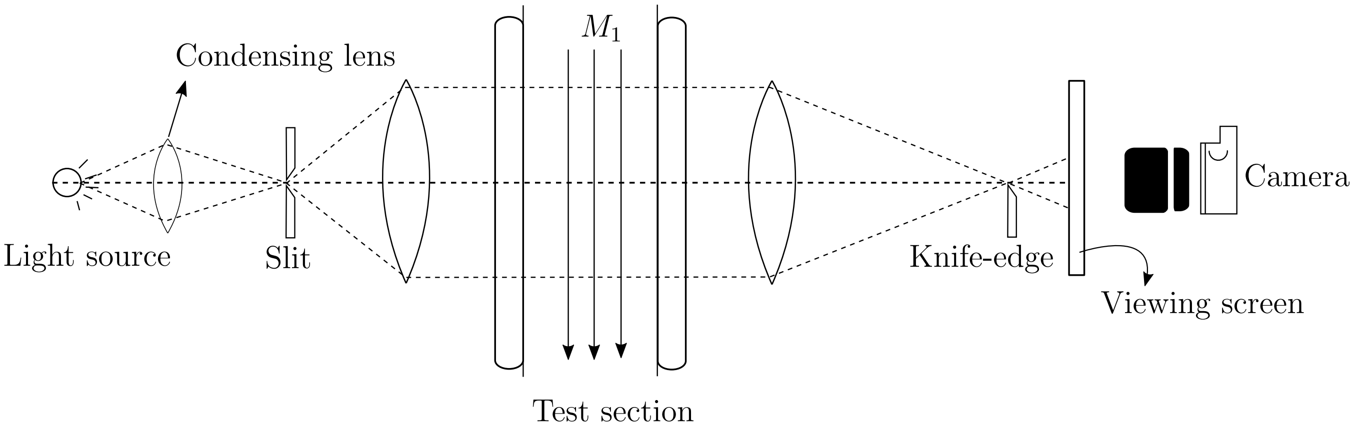

Figure 4.5: Schematic of a typical schlieren setup.

density gradients normal to the knife-edge. Should the knife-edge be placed horizontally, then one would obtain a final image depicting $\frac{\partial \rho}{\partial y}$, and $\frac{\partial \rho}{\partial x}$ if the knife edge were placed vertically. The result is that a schlieren image may not allow one to clearly observe all flow features because the image appears with large dark portions due to the sensitivity of schlieren imaging to resolve first order density gradients. An example of what is meant by this is shown in Figure 4.6.

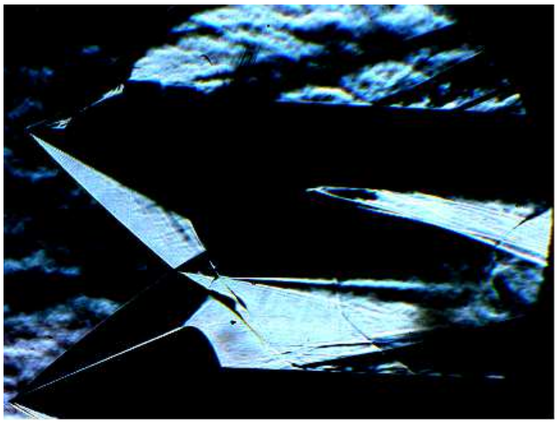

Figure 4.6: Example of a schlieren image taken with optical yaw with a free-stream Mach number of $M_1 = 3.0$.

**Shadowgraph photography**

This photography method is very similar to schlieren outlined above. However, shadowgraph images depict the second derivative of density in the final image. This is because, unlike schlieren, the knife-edge cutoff is omitted from the arrangement of optics equipment. Therefore, the shadowgraph is sensitive to flow density changes in all directions. The result is that flow features with a small spatial variation of density gradients are not vividly depicted in the shadowgraph. This is especially true for features such as expansion fans and downstream portions of shear layers arising during Mach reflection of shock waves. However, an important advantage of shadowgraph imaging is the clarity with which the flow field is depicted in the final image. An example is shown in Figure 4.7, with the same optical orientations for comparison with the schlieren equivalent of Figure 4.6. Clearly, a lot more of the details of the flow field are made visible in the shadowgraph than in the schlieren image. Further details become clearer with image cropping and zooming, together with contrast and light adjustments as will be seen later. This is an especially important attribute of shadowgraphs which meant it was used almost exclusively throughout this study in order to properly visualise the three-dimensional nature of shock reflection and transition, in preference to schlieren photography. It was also important to maintain image clarity when obtaining images with the optical equipment having been yawed and rolled with respect to the tunnel axis. This was important to allow proper interpretation of the flow field in three-dimensions. This was also made possible through the use of a moveable optical gantry system, discussed next.

### 4.3.2 Optical system with moveable gantry

The optical system used was specifically modified from the typical configuration in Figure 4.5 to make use of mirrors rather than lenses, the resolution loss of the former being of less concern than that of the latter. The resulting implementation is a U-type configuration shown in Figure 4.8, and has been used very reliably for numerous flow visualisations for supersonic steady flow studies in the Flow Research Unit in the past. Each change of direction of the primary optical

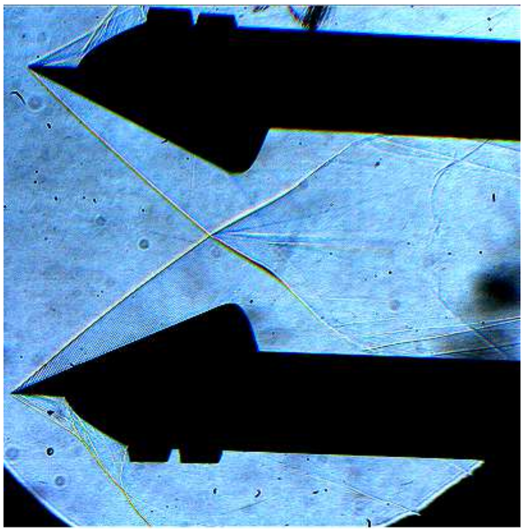

Figure 4.7: Example of a shadowgraph image taken with optical yaw with a free-stream Mach number of $M_1 = 3.0$.

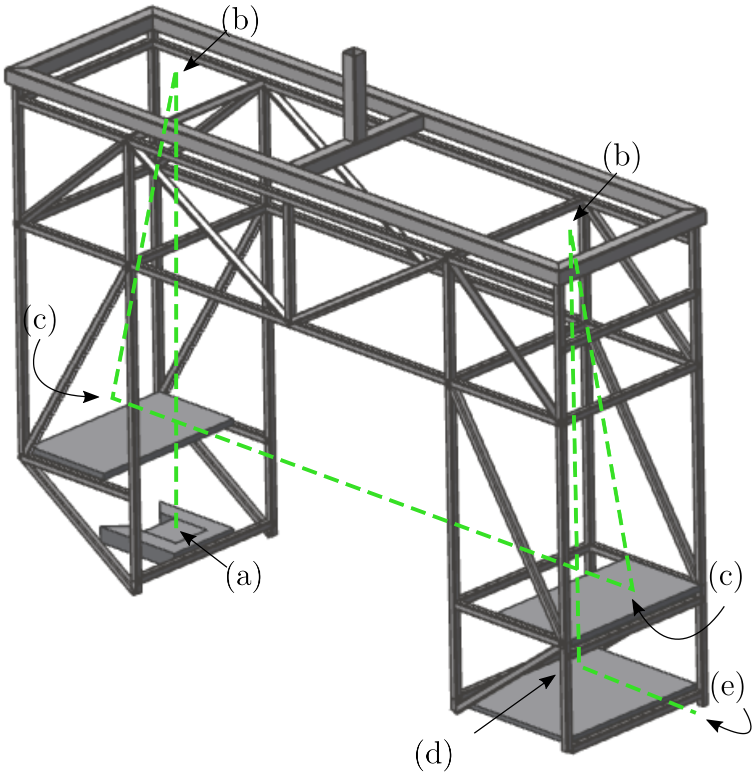

Figure 4.8: Optics gantry showing primary light ray trace.

path (shown in green in Figure 4.8) denotes the location of a component of the optics system. The light source used was a Xenon flash lamp, positioned at (a). The light from here was focused through a condensing lens onto a slit (in the same way as shown in Figure 4.5). Thereafter, it is made to fall on a first parabolic mirror at (b), which is placed at its focal length away from the slit. This allows the light reflecting off the parabolic mirror to be collimated upon reaching a planar mirror located at (c). Thus, this same collimated light is passed through the test section perpendicularly to the free-stream flow with the gantry in its datum configuration (i.e, no yaw or roll). The test section is located in the middle of the gantry. Having passed through the test section windows and exiting the test section, the light reaches a second planar mirror (c), and is reflected onto a second parabolic mirror (b). This focuses light onto another smaller planar mirror at (d), which re-directs the light into a focusing lens positioned between (d) and (e). This focusing lens is used to aid image capture by the digital camera at (e). Single shot photography was used for all experiments in order to obtain high-resolution images. Use of a high-speed camera may have allowed a significantly higher frame rate, however, this would have been at the cost of low-resolution as shown in [7].

As mentioned, in order to visualise three-dimensional features of the flow-field, the optics gantry was rolled and yawed with respect to the tunnel axis. Roll ($\phi$) and yaw ($\lambda$) motions of the gantry are depicted in Figure 4.9.

For highly three-dimensional flows, the orientation of the optics is clearly integral to the final image captured by the camera. Images obtained with yaw and roll look considerably different due to the different portions of the shock surfaces through which the light rays pass at different gantry orientations. This is an important consideration for three-dimensional reconstruction and validation of the computational models. It was therefore a priority to implement a sensing system that could work with the optics gantry in order to give a clear indication of the true orientation of the optics. The details of the implementation of the gyroscope and accelerometer chip used for this is discussed next.

### 4.3.3 Inertial measurement unit (IMU)

The MPU-6050 IMU is a chip containing a combination of a three-axis MEMS gyroscope and accelerometer. This model specifically had been frequently used in robotic self-righting and home-made drone applications and so it was decided that it would be well-suited for indicating the orientation of the optics gantry in both yaw and roll. The IMU chip was interfaced with an Arduino UNO as shown in Figure 4.10. This was in turn connected to a laptop in order to retrieve and display the IMU data. The sensor follows the convention of having its $x-$ and $y-$axes in the plane of its board, with the $z-$axis being out-of-plane. The MPU-6050 unit outputs data from the gyroscopes and the accelerometers for each of the three axes ($x$, $y$ and $z$). The gyroscope senses angular velocity (or change in angle in the time interval from one reading to the next). For a sample rate of approximately 25 Hz, the gyroscope outputs would not have been of any use when adjusting the optics gantry to the desired orientation. Therefore, the gyroscope readings are effectively integrated step-wise over the time interval for which the sensor is operational. Numerically, this translated to the addition of each change in angular position multiplied by the sampling rate. However, it is well-known that this method of numerical integration results in systematic errors that increase with time. This issue was addressed when the outputs from the accelerometers together with the gyroscopes were combined.

The accelerometers are thus also required in order to compute the angular orientation of the IMU chip, and thus the optics gantry. The IMU chip outputs three acceleration readings which are the axis-components of acceleration. These are combined to give the yaw and roll of the sensor. Based on the way in which the sensor was mounted on the optics gantry, the gantry yaw angle was calculated from accelerometer data as

$$\lambda = tan^{-1}\left(\frac{A_X}{\sqrt{A_Y^2 + A_Z^2}}\right) \tag{4.1}$$

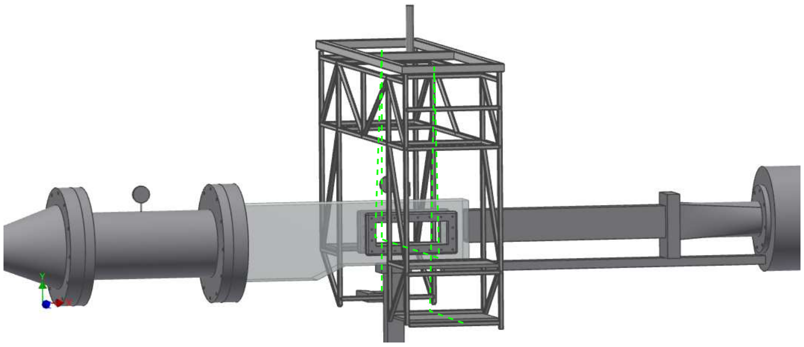

(a) Optics gantry at yaw $\lambda = 0°$ yaw and roll $\phi = 0°$.

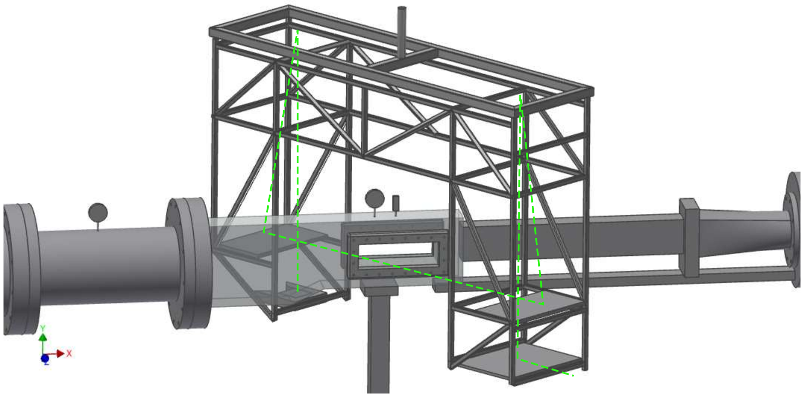

(b) Optics gantry yawed ($\lambda > 0°$) with roll $\phi = 0°$.

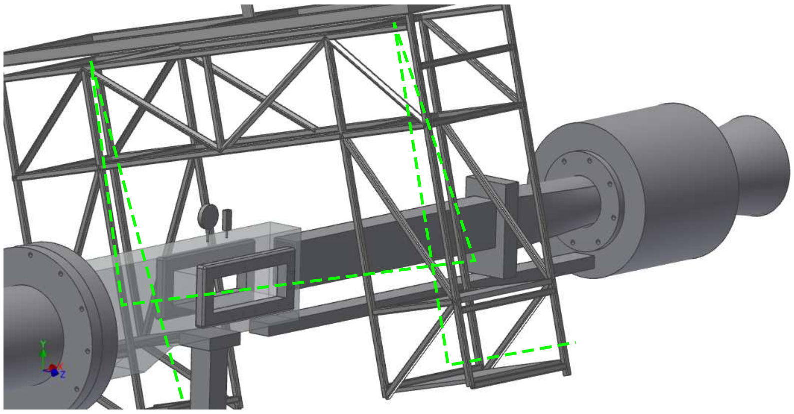

(c) Optics gantry rolled ($\phi > 0°$) with yaw $\lambda = 0°$.

Figure 4.9: Roll ($\phi$) and yaw ($\lambda$) of optics gantry for visualisation of three-dimensional flow fields. Primary light ray trace shown as the green dotted line.

and the pitch angle as

$$\phi = tan^{-1}\left(\frac{\sqrt{A_X^2 + A_Y^2}}{A_Z}\right) \tag{4.2}$$

with $A_X$, $A_Y$ and $A_Z$ being the component accelerations along the three axes of the sensor. It is important to note that this formulation of angular orientation relies on the assumption that the net force experienced by the sensor is created by a net acceleration of $1g$ downwards (i.e equivalent to its weight). Therefore, perturbations to this caused by moving the gantry would in turn cause

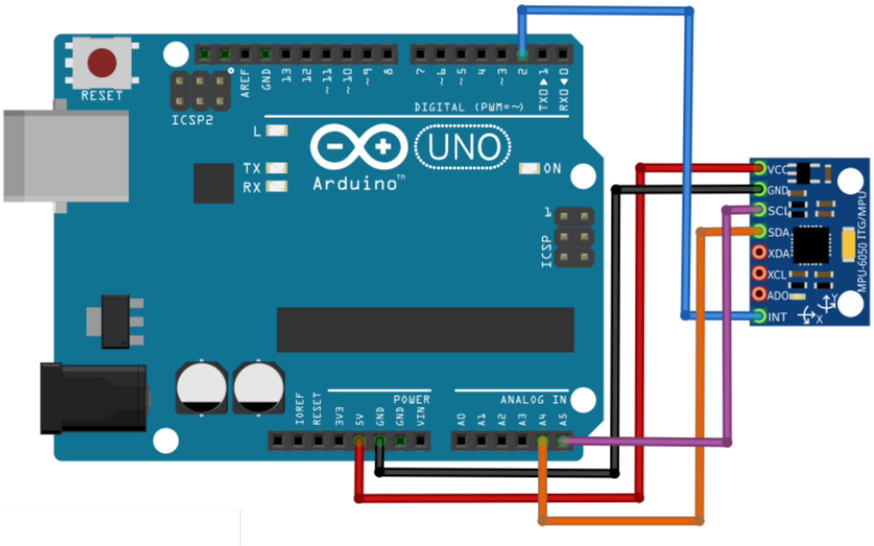

Figure 4.10: Connection diagram for the IMU sensor and Arduino UNO micro-controller.

fluctuations in the sensor output. However, these fluctuations would last for a relatively short time-scale compared with the gyroscope integration errors.

Thus, it is seen that there are two calculations performed on the sensor outputs to obtain the gantry angular orientation. One result exhibits drift over time (gyroscope data) and the other is highly sensitive to short-term perturbations (accelerometer data). Filtering and combining the two results yields a generally acceptable reading of absolute angular position relative to the position at which the sensor was when it was first switched on. This combination was achieved with the use of a complementary filter, the general form of which is given by

$$\Theta_i = \alpha\Psi_i + (1-\alpha)\Lambda_i \tag{4.3}$$

where $i = x, y, z$ for each axis, and $\Theta_i$ is the filtered absolute angle about the $i^{th}$ axis, $\Psi_i$ and $\Lambda_i$ are the gyroscope and accelerometer data for the $i^{th}$ axis. The constant $\alpha$ is given by

$$\alpha = \frac{\sigma}{\sigma + \Delta t}$$

in which $\sigma$ is some time constant greater than the period of accelerometer noise (approximately 0.96 s) and $\Delta t$ is the sampling rate (0.04 s) of the sensor.

The implementation of the IMU sensor for optics orientation measurement was highly successful. The sensor is able to read to 0.01 of a degree, although some output drift was not entirely unavoidable and the final angular orientations of the optics is estimated to be within $\pm 0.1^\circ$ of the nominal quantity used for image processing and validation. This small uncertainty margin is what distinguishes use of the current IMU sensor over manual measurement techniques used in past work at the FRU supersonic wind tunnel facility with oblique flow field imaging.

## 4.4 Test model geometry development

This section describes the development of the the test model geometry. An important aspect of model development was the need to be able to computationally generate the G-code toolpaths for the CNC machine used to fabricate the test pieces. This was in addition to ensuring that the models would eliminate edge perturbations from influencing the reflection plane and transition points.

### 4.4.1 Main geometrical properties

The test model geometry was based on two main requirements:

1. Edge effects, involving expansion signals influencing the plane of reflection, were required to be necessarily reduced.
2. The presence of a known geometrical boundary condition for the purposes of generating flow fields with varying intersection line profiles along which the various reflection configurations should occur.

The test model geometry developed addressed each of the above two requirements by being curved along the length of the model, and by having a sweepback along the lower surface of the model, respectively. This sweepback had a known profile, and thus the streamline direction along this profile was based on the geometry of the model, thus creating a known boundary condition. The sweep also directly influenced the shape of the incident bow wave, as will be seen later. The main geometrical features of a typical model are shown in Figure 4.11. It should be noted that all model geometries bear resemblance to the front portion of an aircraft fuselage.

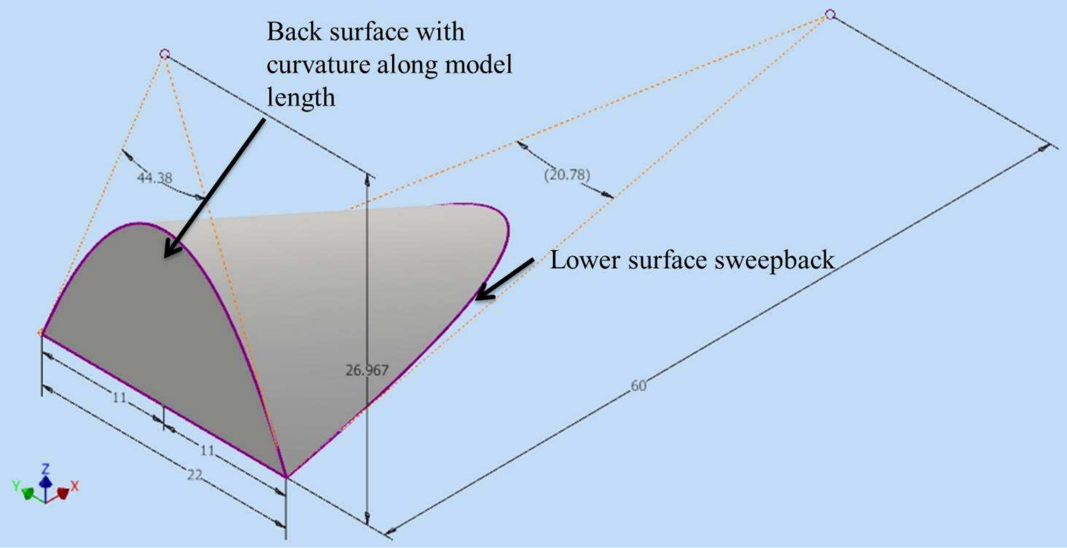

Figure 4.11: Typical model with construction surfaces labelled. Dimensions in mm for lengths and degrees for angles.

### 4.4.2 Surface construction

As a result of the required characteristics of a typical test model, the model geometry was inherently complex. It was therefore necessary to develop a basic geometry template of these models in such a way that this could be conveniently manipulated and altered for subsequent models. In addition, the entire geometry was required to have an algebraic definition, in order for the points along the relevant surfaces to be extracted using a scripting language. This was so that a variety of models could be generated with desired geometrical properties, and so that the coordinates of each point on the model surfaces could be extracted using a self-developed script for Computer

Numerical Control (CNC) machining.

The two main surfaces of the models were the back surface (viewed in the $y - z$ plane) and the lower surface (viewed in the $x - y$ plane). These are shown in Figures 4.12a and 4.12b respectively. These were created using non-uniform rational B-splines, which will be explained below. A loft feature was created between these two surfaces in the Computer Aided Design (CAD) package used. This means that the shape of the back surface was blended into that of the lower surface to create a model such as that in Figure 4.11. It is thought that this is made possible by surface interpolation algorithms used in the CAD software package used. These software-specific algorithms are not publicly available.

An important feature of the types of models developed is that at each transverse section plane, there is a planar wedge body formed by the section edges (for example, see Figure 4.13).
This wedge body formed on the section plane varies in apex angle for each transverse sectioning station. However, an important general observation, also noted in the work done in reference [17], was that the resulting shock configuration did not conform to the two-dimensional configuration generated from a planar wedge with the same apex angle as the wedge in the section-planes of the models developed here. This is to be discussed in later sections of this work.

The model and relevant surfaces shown in Figures 4.11 and 4.12 were further developed and modified. Such modifications included the increase of the spread of the back face of the models to investigate the effect of this on reflection transition phenomena. As a result of this, the back surfaces were modified to be of the form shown in Figure 4.14, where there are six control vertices (indicated by small circles) which control the geometry of the curve forming the back surface. The lower surface remained unchanged in formulation, and was formulated with three control vertices. A larger number of control vertices allows local control of the curve to a greater extent [33]. The control points form a polygon, the outline of which can be seen in Figures 4.12a and 4.12b in dotted lines for each of the respective surfaces.

### 4.4.3 Surface algebraic formulation

The formation of the model geometry was required to be easily given to a generalised algebraic definition. This was so that generation of the machining codes could be automated. Within the context of this definition, any number of model shapes could be generated, the CNC codes for which could be automatically formulated by way of functions written in MATLAB.

Non-uniform rational B-splines (NURBS) were used to create the shapes of the back and lower surfaces. However, the lower surface formulation required a bounding curve that could be defined by three control vertices. The simplicity of using three control vertices on the lower surface allowed for the tool paths to be analytically determined using the algebraic Beziér formulations. For the lower surface, the order of the B-spline formulation matched the number of control points, and the NURBs creation of the lower surface therefore degenerated into a Beziér curve. The CNC jig used required the mounting of the models in such a way that the tool would traverse the shape of the lower surface, in successively smaller arcs until it reached the apex of the back face. The tool-path used is schematically shown in Figure 4.15. Every alternate curve was traversed by the tool in the opposite $y-$ direction to the previous curve. This means that the tool moved in a weaving motion across the face of the part, successively traversing the Beziér curves formed at each station. It can be seen that there is a collection of points below each tool path curve. These were additional points to which the tool would be fed, in order to complete the profile and which

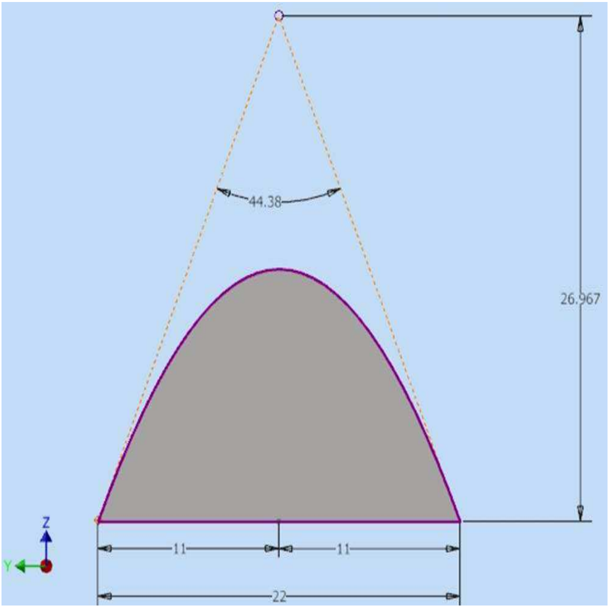

(a) Back surface.

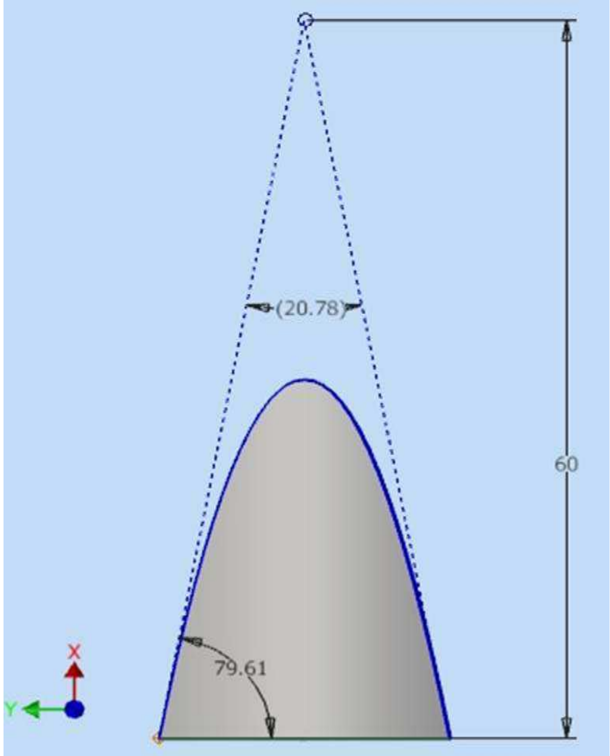

(b) Lower surface.

Figure 4.12: Main surfaces used in model geometrical construction. Dimensions in mm for lengths and degrees for angles.

ensured that the lower surface edge would be correctly formed and separated from the material block during the machining process.

Firstly, a coordinate system was required to be defined. The CAD coordinates were chosen in order to conveniently create the models in the software package used. The CNC coordinates were based on the way in which each model would be orientated during machining. The two coordinate

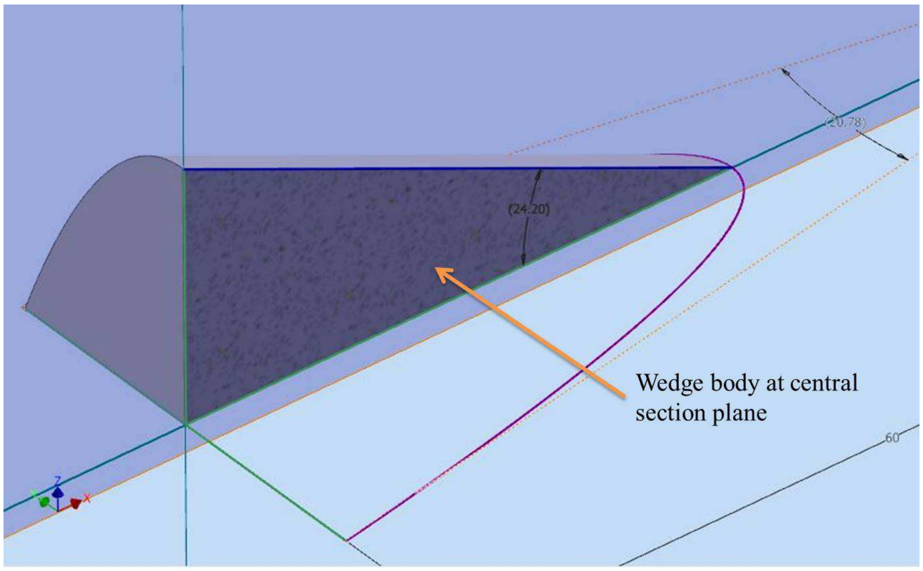

Wedge body at central section plane

Figure 4.13: Central section plane showing planar wedge body.

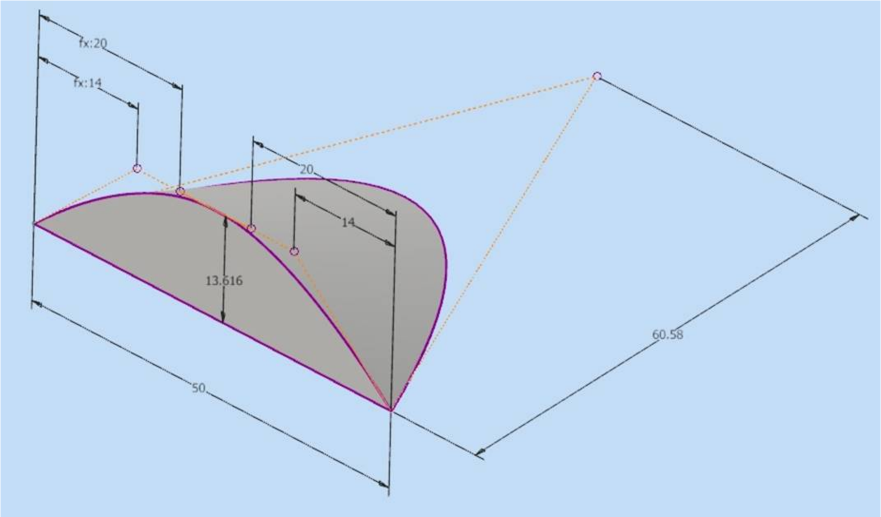

Figure 4.14: Geometry after further development - six back-face control vertices. Dimensions in mm for lengths and degrees for angles.

systems (CAD and CNC) are shown in Figure 4.16. The transformation equations used to adjust the frame of reference to that of the CNC coordinate system were derived as

$$x_{CNC} = z_{CAD} \tag{4.4}$$

$$y_{CNC} = y_{CAD} \tag{4.5}$$

$$z_{CNC} = x_{CAD} - x_L \tag{4.6}$$

where $x_L$ is the distance from the back surface to the apex of the lower surface (i.e the origin of the CNC coordinate system). $x_L$ is obtained because the distance from the back surface to the lower surface apex control vertex ($h_{CV}$) is known and is specified as an input for calculating $x_L$. It should be mentioned here that $h_{CV}$ was chosen based on the requirement for the mid-section wedge of the model to have an apex angle for which only Mach reflection was theoretically possible in the two-dimensional double wedge setup for the same flow deflection angle. The mid-plane wedge angle was 24.20° for all models.

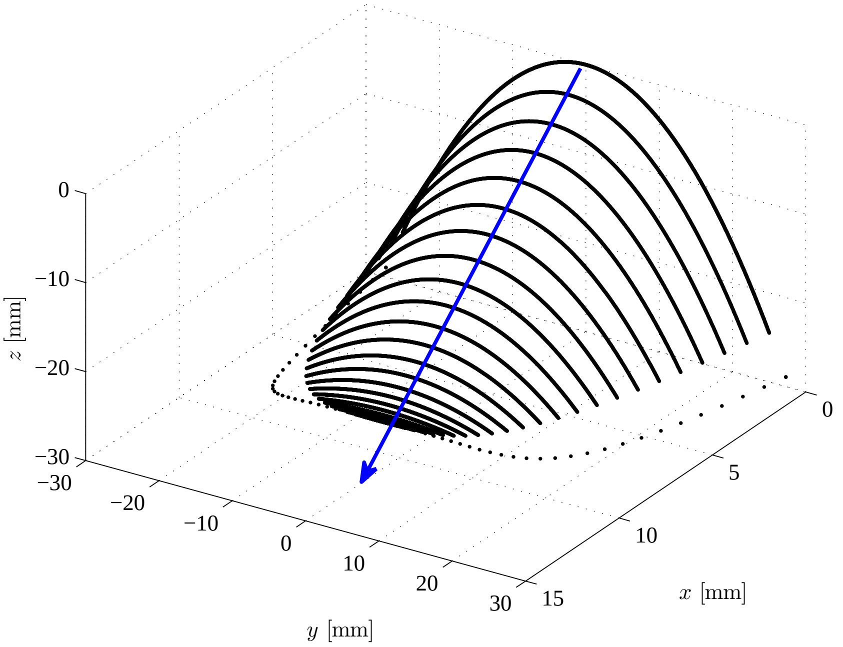

Figure 4.15: Representation of CNC tool path (some path curves excluded for clarity). General machining direction indicated with blue arrow.

In order to create the surface of the models, the lower face was blended into the back face. This was done by starting with the Beziér formulation of the lower face. Next, each successive control vertex polygon was formed, each being geometrically similar to the previous one. The base control points (points 2 and 3 in Figure 4.16) were moved along the curve of the back face. The apex control point (point 1) was located in space by constraining it to have the same $x-$coordinate as the base control points. Its $y-$coordinate was constrained to be at the mid-point between the base points. The z-coordinate was calculated by using a linear trajectory of the apex point 1 to the back surface apex as shown. It is important to note here that the formulating polygons were not interpolated nor blended into each other. This algorithm relies heavily on the location of the base points of each formulating polygon, from which the apex control point is obtained. A CAD-based macro was used to extract numerous points along the bounding curve of the back face with a spacing interval of at most 0.01 mm in order to satisfactorily resolve the curvature of this face.

### Formulation of each successive Beziér curve

A Beziér curve defined each succesive tool path as the tool moved in the $x-$direction relative to the CNC reference frame. Each Beziér curve was progressively smaller in shape, until the tool reached the apex of the back face of the model. The formulation of each curve (i.e tool path) primarily required that the location of the three control vertices were specified. The location of the two base control vertices were obtained from the points extracted from the back face. The apex control vertex was initially located as per the construction of the lower face. Its subsequent trajectory was defined (as above) as a linear interpolation from its initial location to the apex of the back face (see Figure 4.16). Here, the algebraic formulation of these Beziér curves is shown.

Of primary importance is that Beziér curves are parametric (parametrised by a variable $t$ here), and they have their start and end points at the base control vertices. If we consider the general case of a curve to be formulated from $n+1$ control points, each of which is located at $\vec{p_i}$ in space,

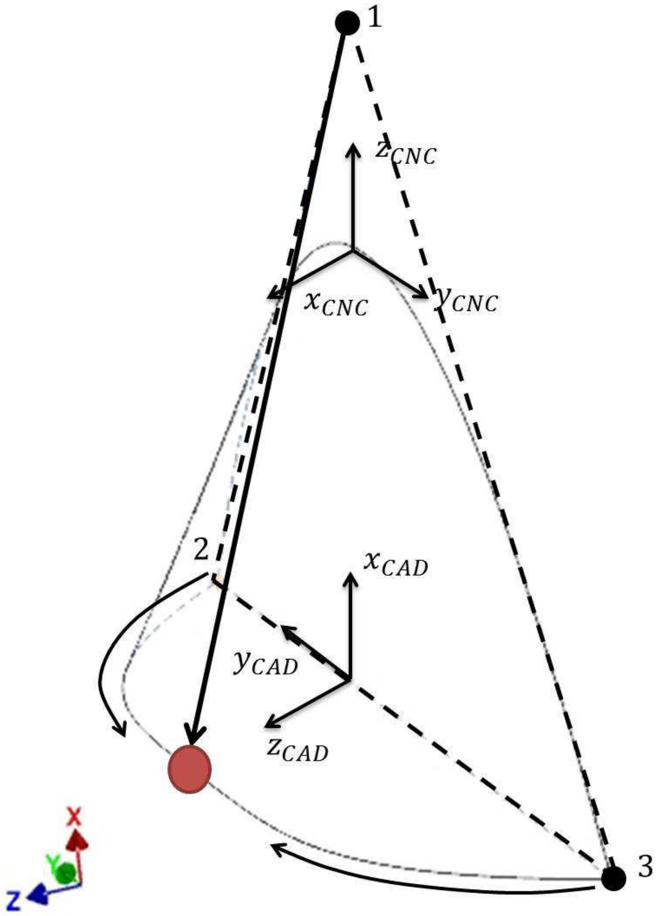

Figure 4.16: Model coordinate systems and Beziér polygons.

then we define a blending function as

$$\vec{p}(t) = \sum_{i=0}^{n} \vec{p_i} J_{n,i}(t) \tag{4.7}$$

$$J_{n,i} = C_{n,i} t^i (1-t)^{n-i} \tag{4.8}$$

$$C_{n,i} = \binom{N}{i} = \frac{N!}{i!(N-i)!} \tag{4.9}$$

with $t \in [0,1]$.
This equation set gives the formulation of a single Beziér curve for a set of control points. The geometric interpretation of this is explained from Figures 4.17a and 4.17b.

Here, it can be seen that the control vertices are located at points 1, 2 and 3 (as before) and connecting lines join each pair of adjacent points. A line $AB$ is drawn with endpoints on each adjoining line (lines $1-2$ and $1-3$). Now, we imagine line $AB$ to have started as line 12, and then move itself such that point $A$ moves from point 2 to point 1, and likewise point $B$ moves from point 1 to point 3. Along line $AB$, there is another point $C$. As $AB$ rotates itself, point $C$ traverses the length of line $AB$, such that it starts off at point $A$, and ends up at point $B$. Point $C$ locates itself along line $AB$ such that it is $t \times 100$ percent of the way along line $AB$. This means that as parameter $t$ is varied, so does the location of point $C$. The path along which point $C$

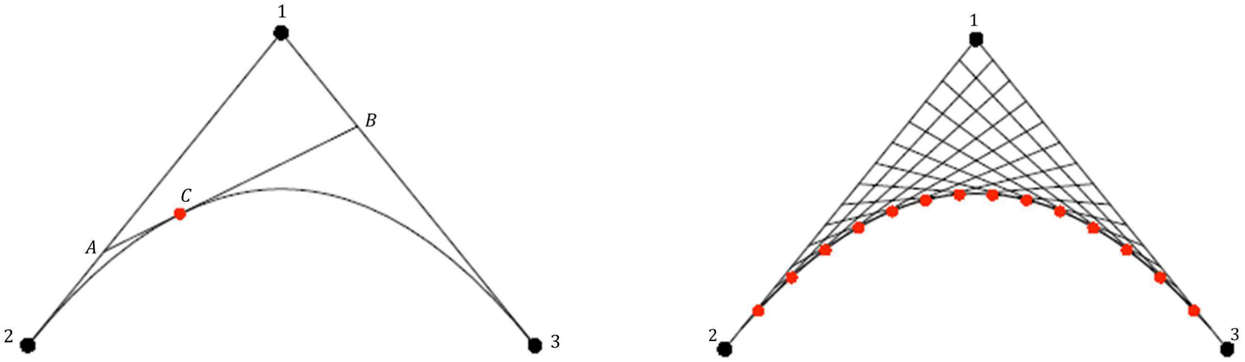

(a) Single point formulation.
(b) Completed Beziér curve.

Figure 4.17: Construction of a Beziér curve as from [33].

traverses forms the Beziér curve, as shown in Figure 4.17b.

This process of generating Beziér curves is repeated for each successive set of control vertices until the entire model surface is complete.

### 4.4.4 Geometry of test models

As mentioned in subsection 4.4.2, various models were developed, each with a successively greater back-face spread. This was achieved by moving the back-face NURBS control vertices further apart. Larger back-face spreads were found to create increasingly flatter central portions on the model, meaning that the larger central regions of the flow would be exposed to test piece geometry approaching that of a flat wedge but without edge effects influencing the reflection plane. Initially, an initial model geometry concept was developed in [17] based on three control vertices for both the back- and lower-faces of the model, resulting in a very low spread surface geometry. To illustrate the increasing spread used for subsequent models developed, Figure 4.18 shows two models each with six control vertices, the latter of which has the lowest back-face spread of the models used in this work. The pieces developed here were chosen to be symmetrical about the vertical symmetry plane such that $h_1 = h_2$ and $h_3 = h_4$.

Five test pieces were originally intended to be tested in the wind tunnel. The geometrical specifications for each are shown in Table 4.3. $x_L$ refers to the chord length of each model. The model numbers denote the design iteration as further modifications were introduced starting from the original concept model. Increasing model numbers also refer to an increased geometrical spread.
The measure of model surface spread was not exclusively determined by the span of the model, as seen by the fact that Model 8 had a larger span than the rest of the models but also had a

Table 4.3: Test model geometric parameters. All lengths in mm, angles in degrees.

| Model no. | $z_H$ | $x_L$ | $h_1$ | $h_3$ | Span | Vertical symmetry angle | LE spacing |
|---|---|---|---|---|---|---|---|
| 8 | 13.6 | 30.3 | 30 | 24 | 60.0 | 24.20 | 38 |
| 10 | 13.6 | 30.3 | 20 | 14 | 50.0 | 24.20 | 38 |
| 11 | 11.0 | 24.5 | 20 | 8 | 50.0 | 24.20 | 38 |
| 12 | 11.0 | 24.5 | 15 | 4 | 50.0 | 24.20 | 38 |
| 13 | 11.0 | 24.5 | 10 | 4 | 50.0 | 24.20 | 38 |

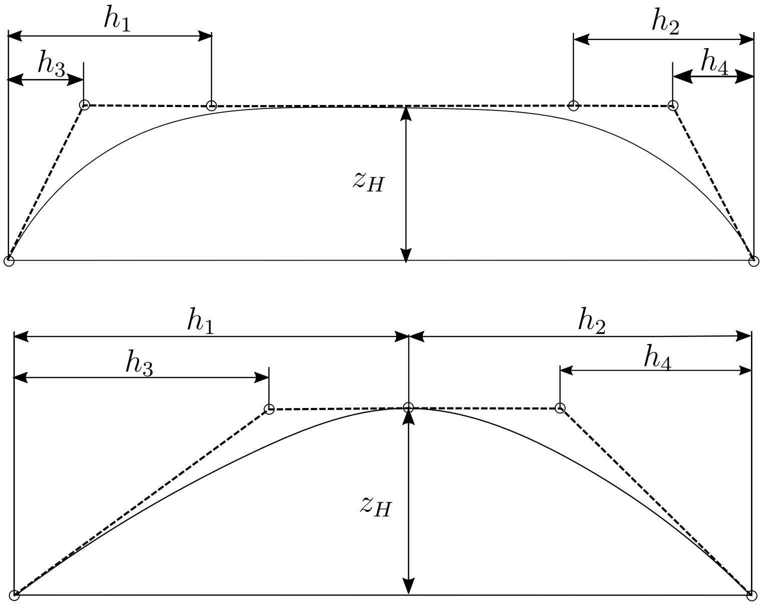

Figure 4.18: Comparison of back-face spread variation of test models.

high back-face apex curvature whereas the other models had back-faces with greater degrees of flatness at their tops and larger back-face areas. The geometrical differences between the test pieces can be seen in Figure 4.19, which contains photographs of the models after manufacture. The original model was an initial concept [17] from which further modifications for Model 8 and onwards were developed. As shown in Figure 4.19 for Model 11, the test pieces were mounted on a sting assembly which was secured in place within the tunnel test section. This assembly is demonstrated next.

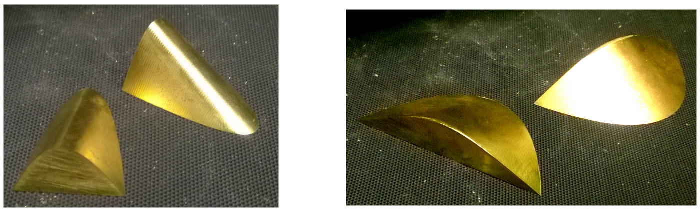

Original model Model 8

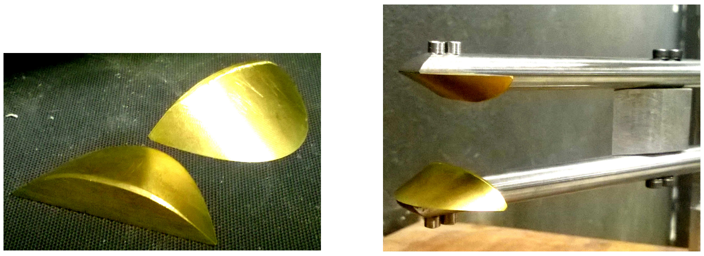

Model 10 Model 11 (as mounted)

Figure 4.19: Photographs taken of test pieces after manufacture. Model 11 is shown as mounted on the sting assembly for placement in the wind tunnel test section.

## 4.5 Test model sting assembly

The full sting assembly is shown in Figure 4.20. The test pieces (brass) are shown at the foremost part of the assembly. They are attached to support rods which have an extended length in order to facilitate a highly yawed line-of-sight for oblique photography. The consequence of a short pair of support rods is that the line-of-sight of the camera would be obscured by the test section window frames. Due to the extended length of the support rods, the stiffener was necessary to reduce the bending and flexing of the rods which had been observed to occur on such types of assemblies in previous tests run in the supersonic wind tunnel facility at the FRU. The assembly was attached to the test section using the mounting slots as shown in Figure 4.20. In order to mount the assembly in the test section, the sliding section on the wind tunnel had to be opened, the assembly bolted into the test section and finally the sliding section had to be bolted closed onto the rear of the assembly. This ensured that the assembly would remain firmly in place for the duration of each test.

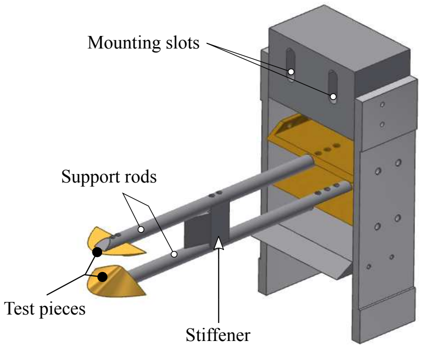

Figure 4.20: Test model sting assembly.

## 4.6 Conclusions

An overview of the experimental facilities used for this work has been given. The use of the supersonic wind tunnel at the FRU has evolved to an established practice, with standard operating procedures, precautionary checks and test log documentation to be followed and completed. The configuration of the optical instrumentation was vital to this work as this was the single method available for collecting oblique photographs to image the three-dimensional nature of the flow field. Also of importance was the IMU instrumentation in order to obtain accurate and precise measurement of optical orientation for further image processing techniques over a large quantity of experimental tests. Finally, a number of test model geometries were developed, together with an automated system for obtaining the CNC G-code for the complex NURBS-based lofted surface geometries used for the test pieces.

# Chapter 5

# Numerical modelling of experimental conditions

## 5.1 Introduction

Numerical modelling and solution of the flow field realised in experiments proves invaluable for the investigation of flow features and flow physics. Sufficient comparison between numerical results and experimental images must be made in order to validate the numerical model procedures and solutions. This having been completed to an extent that allows one to utilise the numerical models with confidence that it represents the experimental flow field conditions, further investigations can be carried out using both the numerical and experimental data.

The process of validating the numerical models of the flow field will be examined in Section 6.1. For now, attention is given to the procedures followed to configure the computational flow field domain geometry, its discretisation, and thereafter, its solution. A commercial computational fluid dynamics (CFD) package, ANSYS Fluent 17.2, was used to model the flow field.

## 5.2 Domain geometry

The layout of the computational domain was based on considerations of the two-plane symmetry of the test model configuration. In addition, it was decided to model the full-scale width of the test section in order to capture as much of the flow field and as many of its features, as well as to aid in numerical shadowgraph reconstruction. Both aspects rely on a domain geometry that is representative of the experimental flow domain to as great an extent as is computationally feasible. However, due to the above-mentioned symmetry of the domain, half of the wind tunnel test section span was used for the CFD domain which was 50.8 mm (2 in.) in width. Approximately one characteristic length, taken to be the chord of the test piece, was added upstream of the leading edges of the test pieces, and three characteristic lengths added downstream behind the test pieces. The length of the final domain slightly exceeded that which could be viewed in the wind tunnel test section. The domain was thus 110 mm in length along the streamwise direction. The domain height was taken to be half of that used as the leading edge spacing between the test pieces. This was fixed at 38 mm, and due to horizontal symmetry the CFD domain was given a height of 19 mm.

The domain geometry used for numerical simulation is shown in Figure 5.1. This Figure also shows the coordinate system (placed at the leading edge where $z = +19$ mm) used for all post-processing operations. The domains were generated in Autodesk Inventor Professional 2016 and exported in STEP format to the ANSYS geometry package. The half-span of the upper test piece was included in the domain as a wall-type boundary (i.e., with no inflow/outflow). The shape of this boundary was altered corresponding to the particular test piece under investigation. The same boundary-type was selected for the planar surface on which the test piece sits, as well as for the vertical plane (in the $x - z$ plane) parallel to the free-stream flow adjacent to the two green-coloured surfaces. These green-coloured surfaces were designated pressure far-field boundaries, for which the absolute pressure was set at 101325 Pa, the temperature at 300 K, and the free-stream flow speed set to $M_1$ to match experimental free-stream conditions. The pressure far-field boundaries were used to initialise the flow field. It was ensured that at the back face of the domain the flow was supersonic, so as to preclude any influence of the placement of the back face on the flow field ahead of it, by virtue of signal propagations upstream. The lower horizontal and far-side vertical surfaces were set to be symmetry planes. This allowed a dramatic reduction in computation time.

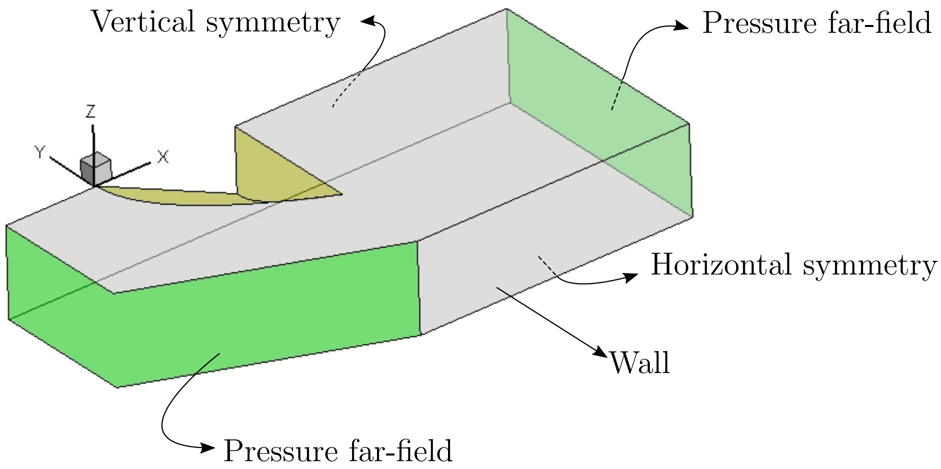

Figure 5.1: Quarter-model domain geometry with coordinate system at $z = +19$ mm.

For clarity on visualising the domain geometry, Figure 5.2 is included, after the quarter-model of Figure 5.1 has been reflected once about one of the symmetry planes (resulting in a half-model) and this half-model reflected about the other symmetry plane.

## 5.3 Domain discretisation and adaptive refinement

Given the complex and three-dimensional nature of the flow field, the discretisation (meshing) of the domain required as uniform a mesh as could be practically generated for each model. This was to avoid highly skewed cells being located in regions of interest in the flow field. A hex-dominant mesh was selected, whilst ensuring that severely skewed cell faces resulting from conversion from tetrahedrons to hexahedrons were located a considerable distance away from the main regions of interests in the domain. Meshing was carried out in ANSYS Mechanical. Settings used for the meshing process are given in Table 5.1. Further explanations are given in the subsections thereafter.

### 5.3.1 Adaptive mesh refinement and coarsening

Adaptive refinement of the starting grid of the domain involves dividing up the cells in which the gradients of certain flow properties are are greater than a certain threshold. This is the refine-

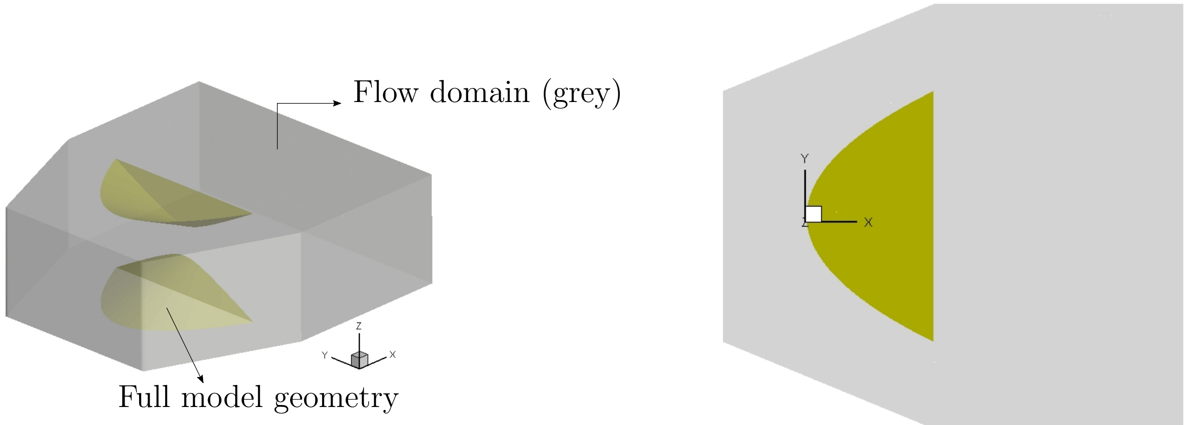

(a) Full computational domain with full model geometry coloured.

(b) Top view of domain.

Figure 5.2: Additional views of the full computational domain after reflection about symmetry planes.

Table 5.1: Settings for meshing process in ANSYS Mechanical.

| Setting | Configuration |
|---|---|
| Advanced sizing functions | Off |
| Cell control | Hex-dominant |
| Cell size (starting grid) | $[1.0, 1.2, 1.5]$ mm |
| Variables for adaption | $p, T, \rho, V$ |
| Adaption thresholds (refine, coarsen) | $1.0\%, 0.75\%$ |
| Adaption interval | 1000 iterations |
| Max. no. cells | Unlimited |

ment threshold. The same principle is used for coarsening, but cells are then combined together when property gradients are lower than the coarsening threshold. The flow properties used here were static pressure, static temperature, local density, and local velocity. Cells in which property gradients were greater than 1.0% of the maximum were allocated to be refined, whilst those less than 0.75% were allocated for coarsening.

Coarsening and refinement was automatically carried out by the software package until property gradients in each cell did not warrant the need for further refinement/coarsening based on the respective thresholds. However, in the interests of achieving practical compute times, the maximum refinement level was capped at that for which the smallest resulting cell size would be of the order of $10^{-4}m$ in order to capture the shock waves properly. Final adapted mesh configurations are shown in Figure 5.3 for an external view of the entire domain, as well as for a sample of $x-$, $y-$ and $z-$ slices extracted from the domain. As can be seen in Figure 5.3, it is important to note that not only was the mesh around the shock waves refined, but so were cells within expansion waves, the wake of the test pieces, as well as shear layers. This resulted in the necessary resolution of these features.

### 5.3.2 Mesh independence

The process of ensuring that the computed results of the numerical model can be confidently used for further investigation is largely determined by grid convergence or mesh independence studies.

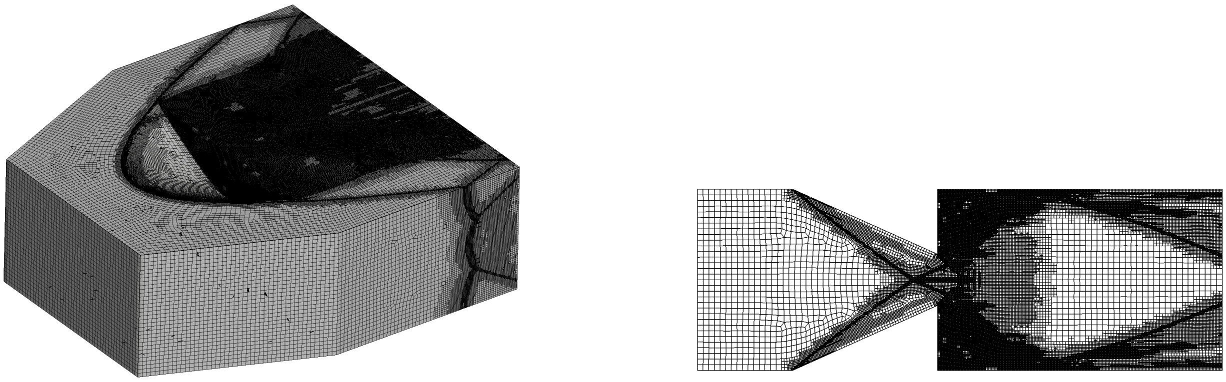

(a) External view of domain with adapted mesh.

(b) Vertical slice at $y = 0$ mm.

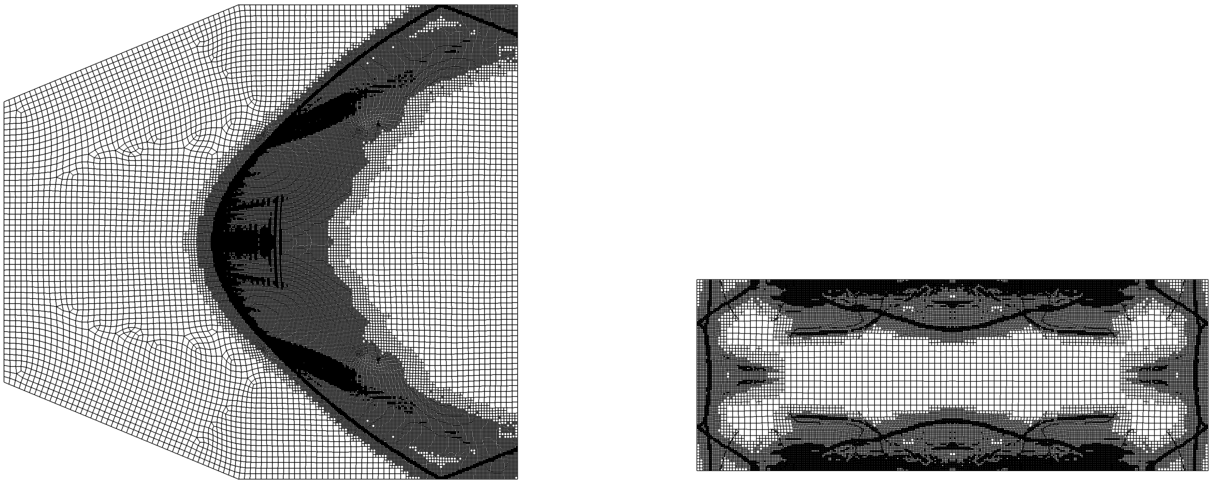

(c) Horizontal slice at $z = 0$ mm.

(d) Vertical slice at $x = 80$ mm.

Figure 5.3: Final mesh configurations after adaption.

This process was largely based on the considerations outlined in [25, 26]. It should be made clear here that this process in no way ensures correlation/correspondence to any degree of the computational results to experimental ones. It only permits one to minimise the uncertainty associated with the computational models.

An initial grid is generated with a cell size that is an initial guess. The grid is solved and the results of convergence monitors stored. The monitors used were the volume-weighted average of static pressure and velocity for the entire domain. These values were compared with the next grid, obtained from a starting grid that was coarser/more refined. The desired outcome of such a process is to reach a point at which any further refinement of the starting grid would be superfluous, and that the coarsest starting grid that returns an acceptable solution should be used for all further CFD cases. Clearly, one requires the definition of exactly what an "acceptable" computed solution is, especially during cases when preliminary computational runs were carried out in order to develop test model geometry (as was done during this work), with no experimental data available for comparison and validation.

It was decided to refine the starting grids and continue generating solutions for each until the convergence monitors for the previous grid were within 1% of the following grid. Three starting grid cell sizes were chosen (1.50 mm, 1.20 mm and 1.00 mm). The results for the grid convergence study undertaken are given in Table 5.2. The fact that Mesh 0 diverged shortly after the first

Table 5.2: Results of grid convergence study.

| Mesh no. | 0 | 1 | 4 |
|---|---|---|---|
| Cell size [mm] | 1.50 | 1.20 | 1.00 |
| Pressure (vol. avg.) [Pa] | Diverged | 139447.31 | 140242.64 |
| Velocity (vol. avg.) [m/s] | Diverged | 971.66 | 971.08 |

mesh adaption illustrated that the starting grid could not be allowed to be too coarse, as the adaptive refinement resulted in severely skewed cell faces. This same effect was noticed for the intermediate meshes not shown in Table 5.2 (i.e Meshes 2 and 3). These were unstructured grids, the cells of which were free to conform to the body shapes of the domain. In doing so, these cells became heavily skewed with the result that upon adaption the solution diverged. The two finer, structured starting grids reduced this skewness effect (i.e Meshes 1 and 4).

The percentage difference between monitors of Mesh 1 and 4 were 0.57% and 0.06% for pressure and velocity monitors respectively. The finer Mesh (Mesh 4) was used because during its solution the refinement levels could be lowered (as it was a finer starting grid) in order to resolve the flow features, and thus refinement was expected to occupy less time during solution.

## 5.4 Solver settings

A three-dimensional density-based steady state solver was selected for all CFD cases for this research. A summary of the solver settings is shown in Table 5.3. The pressure far-field boundary Mach numbers were set to be those particular to the case to be run. In this research, Mach numbers in the range $M_1 = 2.8 - 3.4$ were used, in Mach 0.2 increments. An inviscid (Euler) model was selected because inertial effects were dominant over viscous effects in this high-speed flow setup. Also, boundary layer effects and wall interactions were not of concern in these investigations. However, it became evident later that the discovery of novel phenomena at the transition points warranted further numerical investigation in order to check their existence in viscous, real flows. A $\kappa-\omega$ model was set up and solver independence was checked in a similar way to grid independence by comparing convergence monitor values between the standard formulation and the shear-stress transport (SST) model. Of particular interest was the resolution of the transition point in the horizontal symmetry plane and the shock geometry and streamline trajectories in the vicinity

Table 5.3: Solver settings used in Fluent.

| | | |
|---|---|---|
| General | Type | Density-based |
| | Time | Steady |
| Models | Energy equation | Enabled |
| | Viscous model | Inviscid/$\kappa-\omega$ (SST) |
| Boundary conditions | Pressure Far Field | $P_b = 101325$Pa; $T_b = 300$K |
| Solution Methods | Formulation | Explicit |
| | Flux type | Roe-FDS |
| | Gradient | Least squares cell-based |
| | Flow | Second order upwind |
| Solution controls | Courant number | 0.5 |
| Volume monitors | Pressure volume-weighted average | Full domain |
| | Velocity volume-weighted average | Full domain |

of this point. Convergence criteria were set to ensure monitors were converged to within $10^{-5}$ tolerance after a single mesh adaption at 1000 iterations for inviscid models and 4000 iterations for viscous models. Models were solved using the Fluent parallel solver across 7 cores, with approximately $1.8 \times 10^6$ cells per core. This resulted in significantly faster compute times of 36 to 72 hours compared to using the serial solver for which simulations would run for up to 170 hours and more.

## 5.5 Conclusions

This Chapter has elaborated on the procedures used for configuring the numerical models in the commercial CFD package ANSYS Fluent 17.2. The establishment of grid independence and applicable refinement levels and thresholds were important precursors to facilitating numerous further CFD simulations to be run once the procedures detailed in this Chapter were sufficiently validated by experimental data. The CFD results proved extremely useful in elucidating physical aspects of the flow field which would not have otherwise been possible.

# Chapter 6

# Results and Discussion

## 6.1 Numerical schlieren/shadowgraph reconstruction and validation

The validation of three-dimensional flow fields by way of comparison between experimental images and CFD data requires techniques that are considerably different than those applicable to two-dimensional studies. The main consideration of three-dimensional flow fields is the difference in shock configuration at each transverse slice of the flow field, which means that there is no single plane that accurately compares the CFD solution with the images obtained from experiments. This requires the use of techniques to visualise the entire integrated CFD domain.

### 6.1.1 Introduction

Implementation of shadowgraph/schlieren photography in an experimental study of a three-dimensional flow results in a two-dimensional image formed by light traversing the transverse dimension of the test section. Furthermore, for optics that are yawed/rolled, so is the trajectory of the light path through the test section (as described in subsection 4.3.2) resulting in a marked variation in visible flow features for various optical orientations. However, regardless of optical orientation, the final image is the result of an integration of density gradients and second derivatives in space along the optical path through the tunnel test section.

Current bundled CFD post-processing tools permit shadowgraph and schlieren visualisation in a single plane within a domain. In a lot of cases, the mid-plane of the computed flow field is compared with that obtained from experiment, even though the computational domain is three-dimensional. Single plane visualisation has merit for axisymmetric and two-dimensional flows, as shown in [41, 42]. However, this is clearly unrepresentative of the experimental image obtained when there are significantly different flow features and topologies along the light path and a single plane would not be able to account for these. In specific relation to the visualisation methods used in this research, the problem remains to arrive at a suitable visualisation of the three-dimensional CFD data so as to validate it with yawed/rolled points-of-view corresponding to those used in the experiments. A method of doing this is developed in this section, with the aim of direct comparison with experimental images for validation of the numerical models.

Various methodologies have undergone staggered development regarding image construction from CFD solution data and comparison with images obtained from experiments. Attention to these have arisen in conjunction with CFD software development [38, 39], particularly that regarding post-processors, or else with relevance to modelling of an optical setup by way of simulating each of the components [40]. In the latter work ray-tracing is used to model light ray paths thoughout an optical system and through a test section, even though the test data is two-dimensional and is taken to be an infinitesimal thickness in the transverse direction. Emphasis was placed on modelling other aspects of a shadowgraph optical system in order to assess the effects of type and placement of equipment in the surrounds of the test section for setup optimisation.

In earlier works regarding numerical image construction, emphasis is placed on numerical integration of various properties across the domain of a CFD solution for both two-dimensional and three-dimensional flow domains. This was necessitated by the need for more effective post-processors at the time. From the publicly available literature on this aspect, the early attempts to construct shadowgraph and schlieren images from CFD data consisted of numerical integration of density gradients and second derivatives across terahedra inserted within the domain [38]. Rays of light are traced through these tetrahedra and density gradients are integrated along a straight-line light path. However, dependencies of the final image quality on the size and spatial density of the tetrahedra is unclear. The technique was advanced by Yates [39] which involved a simplified straight line ray-tracing method combined with more complex line integration of functions of the flow refractive index. The straight line approximation considerably reduced computational resources required, whilst allowing good comparisons with experimental data. However, to the author's knowledge, no work has been undertaken concerning the combination of shadowgraph/schlieren visualisation of three-dimensional CFD data for validation purposes with an oblique line-of-sight (i.e with a yawed/rolled optical axis). Hence the need to take the above-mentioned solutions a step further in order to validate the current numerical models used in this research.

The current approach draws from previous attempts to re-create the visualisation used in the experimental setup. It is also based on numerical line integration used in ray-tracing, but with the simplification of approximating the integration paths as straight and collimated through the test section along the optical path. It also involves integration of density derivatives, and not functions of local refractive indices. The result is a much more simplified approach to shadowgraph and schlieren image reconstruction, which is applicable to any optical orientation in yaw and roll. It would be a simple matter to extend the applicability of this approach to images formed with pitched optical configurations. In addition, the variety with which the resulting integrated density derivatives may be combined allows a large variation of images to be generated for a single test case to selectively emphasise certain regions or flow features. This ensures sound interpretation of the flow field and when used with other aspects of CFD post-processing tools (such as volume-rendering) allows features to be easily identified in the experimental images.

It should be noted that the solution described here can be thought of as the inverse of those dealing with tomographic reconstruction [43], which is primarily concerned with obtaining the density field from images of the flow. The approach taken here is to generate integrated images based on a known density gradient field.

### 6.1.2 Problem setup

Consider the full CFD domain shown in Figure 6.1, with length in the streamwise direction as $l$, width $w$ and height $h$. The domain is discretised into slices as shown, and the first derivatives of the density in each planar direction at each point of the grid are extracted. The locations of the density derivatives correspond to the grid nodes, and are unevenly spaced due to mesh adaption used during numerical simulation. In addition, these slices of the flow field vary in dimensions based on their transverse location in the domain - for example, a slice in the mid-plane is very differently sized to one taken from the extremities of the domain width.

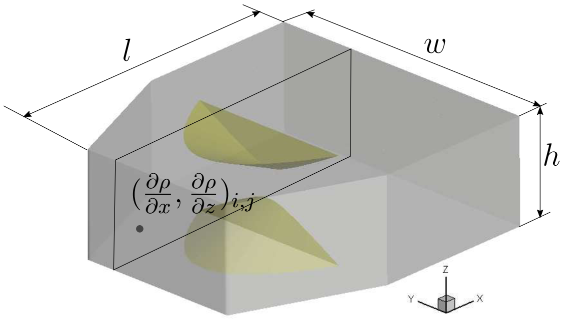

Figure 6.1: CFD domain with slice discretisation.

### 6.1.3 Numerical integration along an arbitrary three-dimensional optical path

Given the non-uniform spatial locations of the extracted density derivatives and differences in slice dimensions, the task of integration along an arbitrary path in three-dimensional space in order to form an accurate image requires interpolation of the slice data onto a secondary grid. The secondary grid was chosen to have elements of the same size as the smallest cell from the final adapted mesh of the CFD solution. This ensured that interpolation of refined features (which are features of interest) onto the secondary grid occurred with minimal loss of visual information so that these features would be properly visible on the final image.

The first slice of the domain is thus interpolated onto a larger slice, of the same length $l$ and height $h$ of the domain. A top view of the domain with this initial slice is shown as the black line at the top of Figure 6.2 for the case of an optical axis yawed by $\lambda$ and no roll. Furthermore, there is an additional portion that is appended to the left of the initial slice, shown in red in Figure 6.2. This extra portion accounts for optical yaw and allows each subsequent slice to be of the same dimensions, thus simplifying the method of integration whilst covering the entire domain. Its length is given by

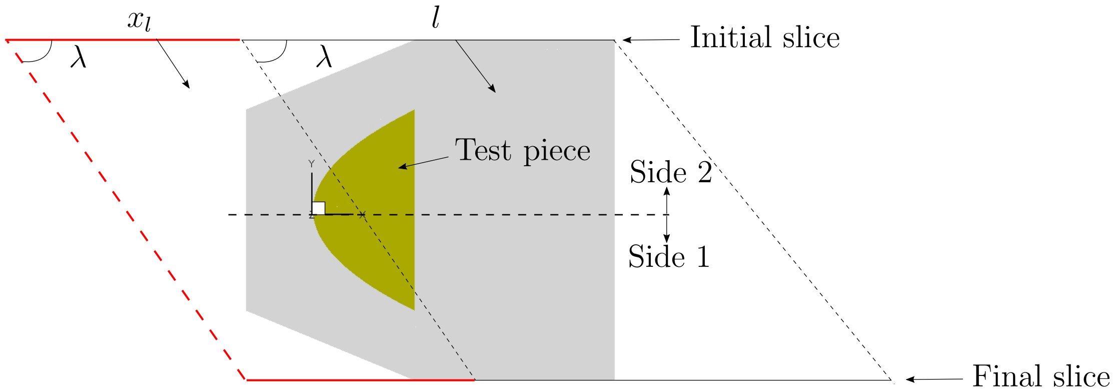

Figure 6.2: Top view of domain showing integration scheme. Side 1 refers to the region on the side of the vertical symmetry plane (horizontal dotted line) closest to the camera, Side 2 refers to that region closest to the light source.

$$x_l = w \tan\lambda$$

and for the case of having optical roll

$$z_l = h \tan \phi$$

where $\phi$ is the angle of roll (see Figure 4.9 for roll orientation of the optics).

Each subsequent slice is interpolated onto a secondary grid of the same dimensions as the initial slice and its appended length $x_l$ or $z_l$. Its streamwise location is shifted to maintain the yaw and/or roll angles used. This is shown with the dotted lines in Figure 6.2. The integration assumes a linear variation of density gradients between slices [38] along the line-of-sight, and the sum of these integrals gives the schlieren intensity:

$$I_{Schx} = \sum_{k=1}^{n-1} \int_{y_k}^{y_{k+1}} \frac{\partial \rho}{\partial x} ds \approx \sum_{k=1}^{n-1} \frac{1}{2} \left( \left( \frac{\partial \rho}{\partial x} \right)_k + \left( \frac{\partial \rho}{\partial x} \right)_{k+1} \right) \frac{\Delta y}{\cos \lambda} \tag{6.1}$$

where $\Delta y$ is the inter-slice spacing between the $k^{th}$ and $(k+1)^{th}$ slice, and $s$ is the integration path in space across $n$ slices. Integration of $\frac{\partial \rho}{\partial x}$ corresponds to having a vertical knife-edge in the experimental setup. A similar formulation applies for the integration of the density gradients in the $z$-direction for schlieren intensity $I_{Schz}$, corresponding to a horizontal knife-edge. For integrated shadowgraph images, the Laplacian of the density field is calculated for each slice, and interpolated onto the secondary grid. Integration is carried out in the same way as above to arrive at the integrated shadowgraph image.

Integration is carried out for each node on the secondary grid, across all slices, resulting in a matrix of intensity values with dimensions that match the secondary grid of each slice. Therefore, the more refined the secondary grid, the higher the resolution of the constructed image. A number of secondary grid sizes were sampled to explore their capability to resolve features of interest, before arriving at the final resolution used in this study. This also allowed a good compromise between CPU time and the final resolution, with run times of approximately 90 minutes on an $i3$ processor with 8 GB RAM.

### 6.1.4 Technique evaluation in conjunction with volume-rendering

**Image formation and discretisation study**

Once schlieren and/or shadowgraph intensity values are obtained, they may be further combined in various functions in order to visualise different aspects and features of the flow field. Of particular relevance to the images generated here, this included "bright-field schlieren", as used in [44, 45], given by

$$\sqrt{\left( \frac{\partial \rho}{\partial x} \right)^2 + \left( \frac{\partial \rho}{\partial z} \right)^2} \tag{6.2}$$

Shadowgraph formulation resulted in images for which strong features, such as shock waves, were readily displayed. Weak features, such as expansion fans and shear layers, were more readily displayed on schlieren-type images.

The effect of slice discretisation and secondary grid sizing was also investigated to assess such effects on feature visibility of the constructed images. Nominal resolution settings for the formulation of constructed images from the CFD data comprised approximately one slice per 1 mm along the transverse direction of the flow domain, and a secondary grid cell size of 0.1 mm. Further cases were generated using higher resolutions of both slice discretisations and secondary grids increased by a factor of 1.5 for each subsequent case. The resolution improvements were negligible for the validation purposes for which the technique is used in this study as improved clarity of flow features was not readily discernible. However, the global Structural Similarity image (SSIM) quality assessment measure (detailed in [46]) was monitored during the comparison of the various resultant images at different slice discretisation settings. Finer slice discretisations resulted in SSIM values of approximately 0.75 for a range of optical angles in yaw and roll combinations with slice discretisations set at 150, 240, and 360 slices across the domain. This indicated good overall correlation with the initial discretisation setting of approximately one slice per 1 mm. Secondary grid refinements were found to have a greater impact on images (observable at a glance at the resultant images), with best results seen for grid cells of the same size as the smallest of the CFD cells obtained after grid adaption.

Furthermore, volume rendering of shock surfaces in CFD post-processing provided another useful tool with which to interpret both the integrated numerically-constructed images, as well as those obtained from experiment. It was with the aid of volume rendering that features seen in the constructed and experimental images could be correlated with the corresponding three-dimensional surfaces as observed in space.

The general flow field that was visualised is shown schematically in figure 6.3. The oncoming free-stream deflects about the specially-designed test pieces (see Section 4.4) to produce central regular reflection and peripheral Mach reflection, which are the shock structures indicated in figure 6.3a. In between the two reflection patterns is the transition point T. Shear layers emanate from the upper and lower edges of the Mach surface (called triple lines) as indicated in figure 6.3b. The shock surfaces and shear layers are the main features in this study, and hence their visualisation is of interest.

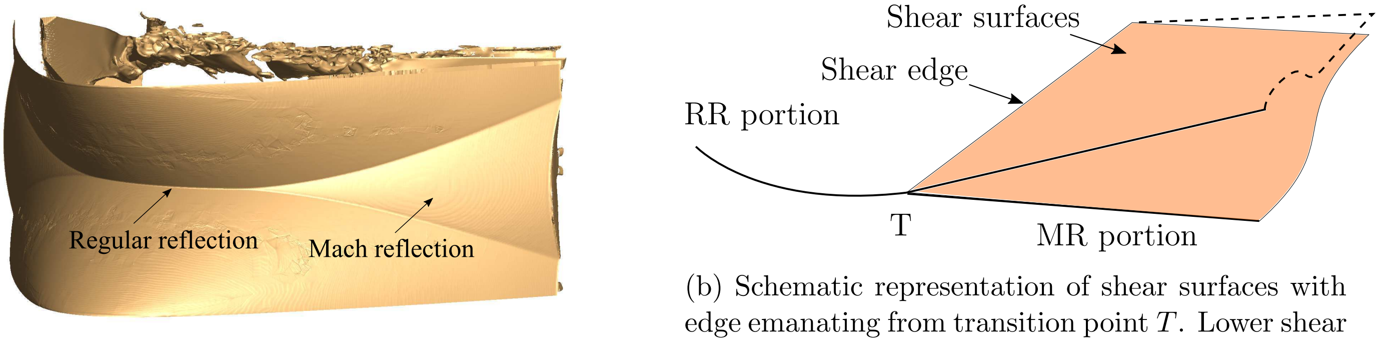

(a) Overview of shock surface with regular and Mach reflection portions shown.

(b) Schematic representation of shear surfaces with edge emanating from transition point $T$. Lower shear surface is coloured orange and the edges of the upper surface are dotted as shown.

Figure 6.3: Overview of flow field.

### Feature visibility in constructed images

An instance in which image construction and volume-rendering techniques were used is now examined for the case in which the optics were yawed by $\lambda = 40°$, and rolled at $\phi = 0°$. From here on, feature labels on images will have subscripts 1 for features on the side of the vertical symmetry plane closest to the camera, and 2 for features on the other side of the vertical symmetry plane. Figure 6.4a shows the image obtained from the experiment. The validation process (discussed later on) demonstrates good correspondence of the computational data with the image from the

experiment. It can be seen that the line of sight is such that the shock wave configuration is viewed through a portion of the Mach surface. This is the reason for the narrowing triangular feature at the middle of the vertical distance between the test pieces. There is the narrowing portion of the Mach surface nearest to the camera, narrowest at the transition point $T_1$, after which the regular reflection line extends to the right. This extends as far as the second transition point $T_2$, which is more clearly shown in Figure 6.4b and in the accompanying sketch of Figure 6.4c. Attached to both transition points are shear layers, identified by the blurry structures emanating from the transition points. Figure 6.5a shows the volume-rendering of the density iso-surfaces which puts certain features in context with the entire numerically-solved flow field including the test pieces by making the iso-surfaces translucent. This is also done for the same orientation as the experimental image at $\lambda = 40°$, $\phi = 0°$ in Figure 6.5b. Figure 6.6 shows the numerically-constructed schlieren and shadow images, resulting from implementation of the methods previously discussed.
The main point here is that certain structures are afforded more clarity depending on how the integrated density gradients and shadowgraph variables are combined. The integrated shadowgraph (figure 6.6a) shows the strong features of the flow field, these being the incident and reflected waves. Transition points are observed by virtue of the inception of shear layers from each transition point, however their exact location is not readily seen especially regarding the far-side transition point. Shear layers are observed as the slightly darker patches near the symmetry line of the image. The slanted lines between the incident and reflected waves as well as those representing multiple Mach stems of a lighter shade straddling the symmetry line result from the integration (effectively superposition) of each shadowgraph slice of discrete transverse locations to form the final image. However, the near side Mach surface appearing as the central narrowing triangle due to foreshortening in figure 6.4b is not seen in the shadowgraph. Rather, it is visible in the image computed from integrated density gradients in the streamwise direction ($x$) i.e, a vertical knife-edge numerical schlieren (figure 6.6b). This is an important feature to be able to visualise, as it correlates the view orientation of both the camera used in the experiment and the line-of-sight used for computationally constructing this image, which were nominally set to the same orientation. This credits the IMU system implemented during experiments with being able to properly measure optical system orientation. Visualisation of the shear layer is an important visual cue to the location of transition points in the flow field. This is made possible by the use of horizontal knife-edge schlieren images, formed with integrated density gradients in the $z$-direction (figure 6.6c). Here, the nature of the shear layers (appearing as the blurry structures) is accentuated by invoking a smaller range of intensity values (see figure 6.6d). Pixels with intensities exceeding the scale are saturated and become either fully black or white. The scale used to observe the shear layers was an order of magnitude lower than that used in figure 6.6c, and therefore resulted in large portions of the rest of the image being saturated. Here, however, the inception of the shear layers and transition points are visible and are as indicated. The correlation of experimental and constructed images are good but the blurred nature of the shear surfaces obscures visualisation of the transition points necessitating further image processing on both image sets.

Thus it is seen that the numerically-constructed images from the CFD data provide good insight into the flow field due to their selective enhancement of certain flow features. It now remains to demonstrate validation of the numerical models by using the constructed images and comparing them with those obtained from experiment.

### 6.1.5 Validation results and observation of flow features

Validation of numerical CFD solutions required direct comparison of the constructed images with those obtained from experiment. For each case of optical orientation used in the experiment,

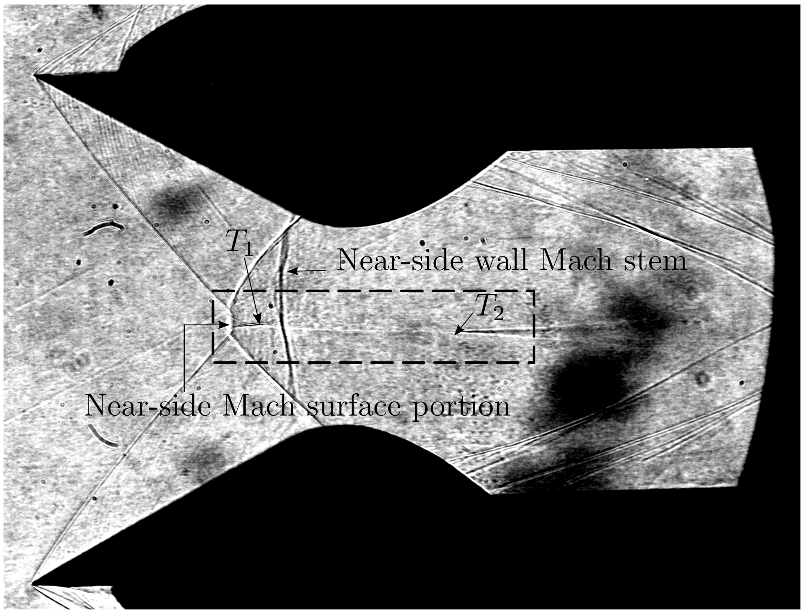

(a) Image obtained from experiment for Model 8 at $M_1 = 3.0$, $\lambda = 40°$, $\phi = 0°$. $T_1$ and $T_2$ refer near- and far-side transition points respectively.

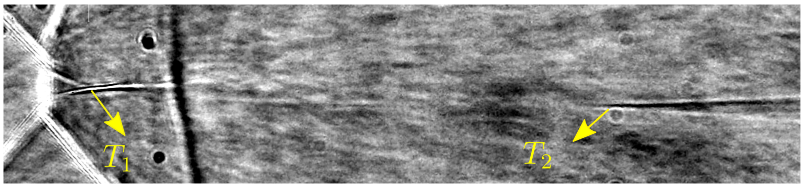

(b) Detail-view of (a) zoomed in on boxed region to show transition points. Shear surface from $T_1$ and the regular reflection (intersection) line lies horizontally between $T_1$ and $T_2$.

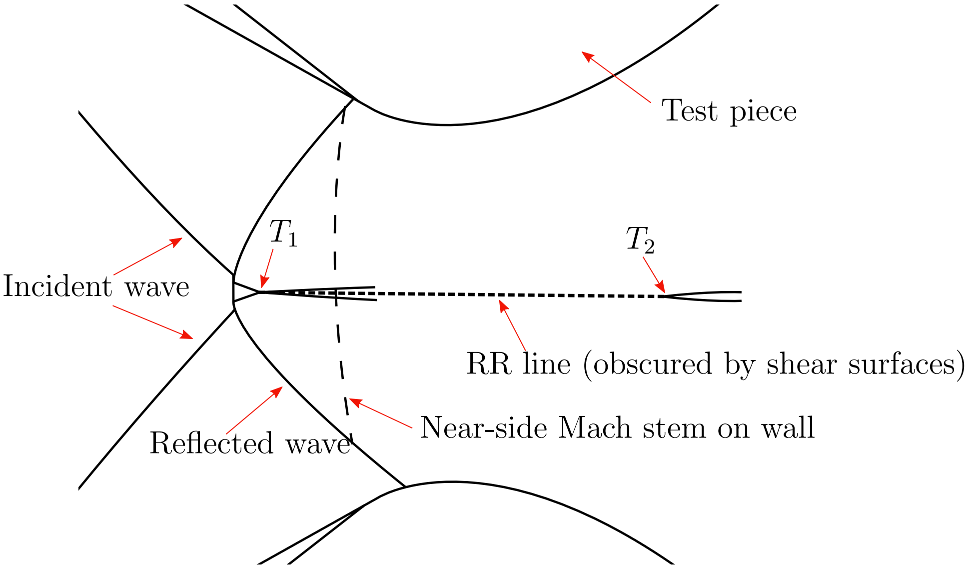

(c) Sketch of features.

Figure 6.4: Depiction of relevant flow features for $M_1 = 3.0$, $\lambda = 40°$, $\phi = 0°$.

corresponding images were constructed using the techniques described above for the same camera orientations. Scaling of integrated intensity values of the images was done in order clarify features and to aid in the comparison process, however, the final images shown here are a result of a compromise between image clarity and visibility of all flow features. For example, visibility of the

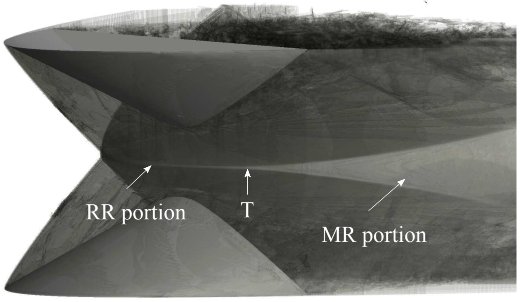

(a) Isometric view of volume-rendering.

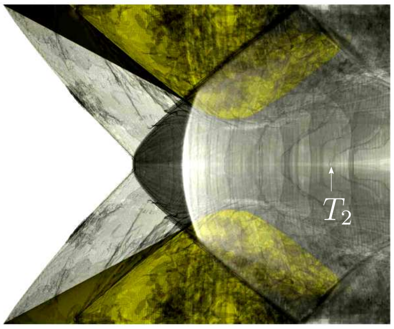

(b) Volume-rendering with line-of-sight corresponding to $\lambda = 40°$, $\phi = 0°$. $T_2$ corresponds to far-side transition point.

Figure 6.5: Volume-rendered images of CFD with density iso-surfaces.

shear layers diminished rapidly with increased scaling thresholds. However, it was necessary to have a scale as broad as possible in the interest of smaller and fewer regions of saturation which appeared as blotchy black or white regions obscuring other flow features such as peripheral Mach surfaces.

It was also found that schlieren images computationally constructed with a parallel knife-edge were associated with greater contrasting of the various flow features and enhanced clarity. These were overlaid onto the images from the experiments, and their opacity progressively adjusted in order to compare the spatial locations of corresponding flow features in each image. Results are shown here for Model 8 in a free-stream flow of $M_1 = 3.0$. Here, the images from experiment and those computationally constructed are shown above one another vertically, as the overlaid comparison would make it difficult to distinguish between each image individually. The image from the experimental test is shown on top of the constructed image at the bottom. Furthermore, the white dotted line in each Figure shows the spatial correspondence of the interaction point of the shock waves. The opportunity is taken here to explain the interpretation of the images based on identification of the flow features with yawed and rolled optics. This demonstrates the ability of the image construction technique to display features in an integrated density field.

The first image to be considered is shown in Figure 6.7, taken with zero optical yaw and roll. It is clear to see that there is a difference between the images behind the interaction point. The image from the experiment shows two similar flow structures on top of each other, whilst that constructed from the CFD solution shows the same structures singularly in the middle of the image. The reason for this is that there was a slight optical roll for the experiment, obtained from the fact that the datum orientation of $\lambda = 0°$, $\phi = 0°$ was set by sight and the IMU sensor was to provide the change in angle from this point for subsequent orientations. However, regardless of this slight roll, which was estimated to be approximately 0.02° based on the geometry of the optics, spatial correlation of the various features are excellent, and the slight roll offset is taken to be negligible in determining the orientations of the camera for further tests.

Just after the interaction point, there is a line that extends to the right, prior to it diverging. Its horizontal extension corresponds to the line of regular reflection on the symmetry plane. Its divergence indicates the growth of the Mach surface on either side of the vertical symmetry plane. Given that there is a slight roll in the image from the experiment, the features on both sides 1 and 2 are visible. Transition points $T_1$ and $T_2$ are also visible and are indicated at the points at

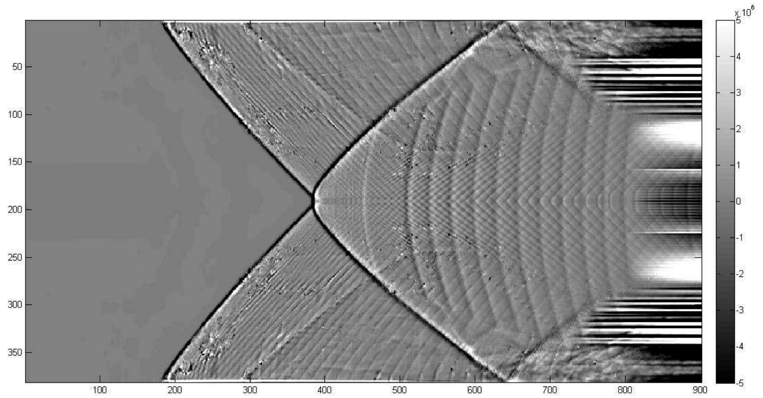

(a) Computationally constructed shadowgraph.

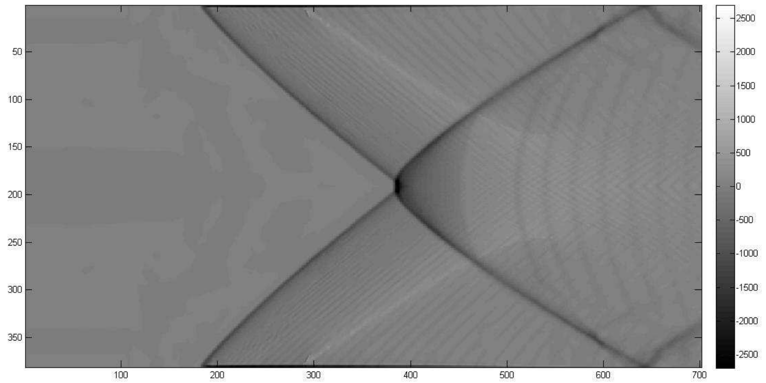

(b) Vertical knife-edge schlieren (computationally constructed).

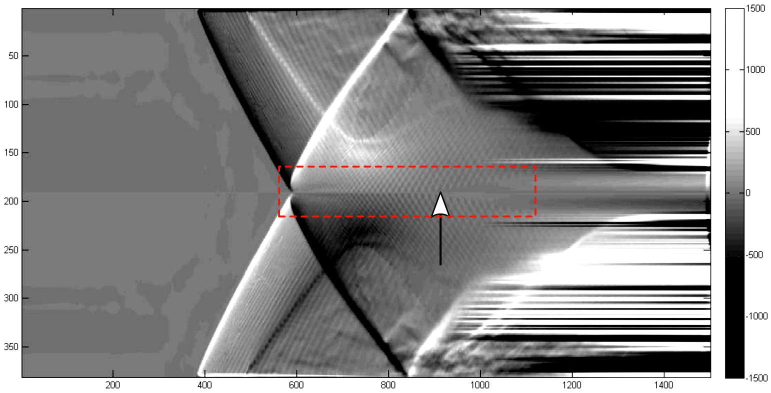

(c) Parallel knife-edge schlieren (computationally constructed) with arrow showing shear layer inception on far-side.

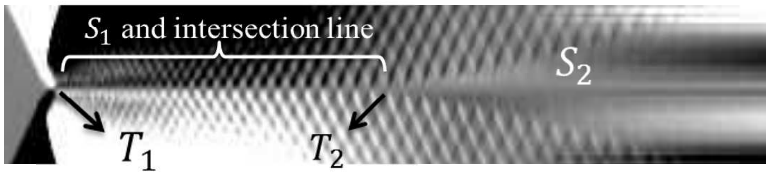

(d) Detail view of (c) at narrow scale range zoomed in on red boxed region showing transition points and shear surfaces.

Figure 6.6: Images numerically constructed for Model 8 at $M_1 = 3.0$, $\lambda = 40°$, $\phi = 0°$ using different methods for flow field interpretation and validation.

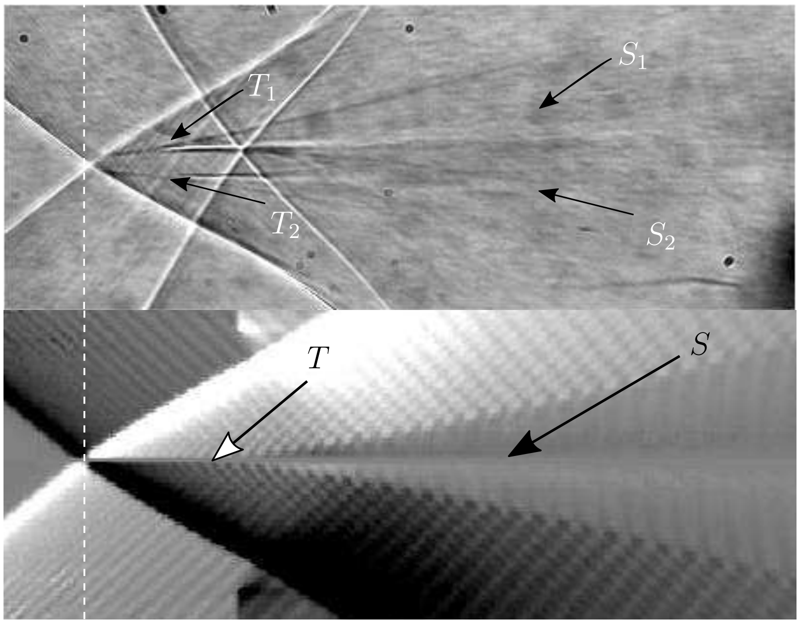

Figure 6.7: Images obtained from experiment and computationally constructed for Model 8 at $M_1 = 3.0$, $\lambda = 0°$, $\phi = 0°$.

which the regular reflection line starts to diverge and transition to Mach reflection. This is seen in the constructed image for a single transition point. The blurred structure emanating from the transition point(s) in both the experiment and constructed images is the shear surface $S$ formed due to the existence of the Mach reflection portion at the peripheral stations of the flow field. Both regions 1 and 2 have separate shear surfaces corresponding to the respective Mach reflection portions. There is a more gradual density gradient across a free shear flow than with a shock wave, which is reflected in the way that the constructed schlieren imparts a blurred effect to the shear layers. These are not as easy to visualise in the shadowgraphs from the experiment. Their observed widening is due to their inclination to the optical axis as well as mixing. There are additional waves downstream of the transition points with a steeper angle than the incident waves. These are expansion waves resulting from the trailing edge of the test pieces and do not further impede visualisation of the flow field for the oblique images discussed further. For now, attention is given to those images produced with oblique camera orientations.

Figures 6.8 to 6.9 shows images from experiments and corresponding constructed ones at two particular angles of yaw ($\lambda = 10°, 20°$) with $\phi = 0°$, notwithstanding the small roll offset. Although these images are obtained with small variations in optical yaw, they provide an understanding as to how the various flow features are transformed in spatial location and appearance from one orientation to the next.

Figure 6.8 shows very similar flow features and locations to Figure 6.7, save for the extended regular reflection line on side 2 extending downstream from the interaction point (indicated by the blue braces in the image). This is seen in both the experiment and constructed images and is expected due to the increased optical yaw. Conversely, the regular reflection line on side 1 of the domain (indicated by the red braces in the image) appears to have shortened in length and the transition point $T_1$ is located closer towards the interaction point. It should be emphasised here that the "interaction point" is actually that portion of the intersection bow wave whose tangent is collinear with the optical path through the test section. This appears to be a so-called point at which the incident and reflected waves meet. However, the portion of these waves that are observed in the images are also those portions along the wave surfaces whose tangents are collinear with

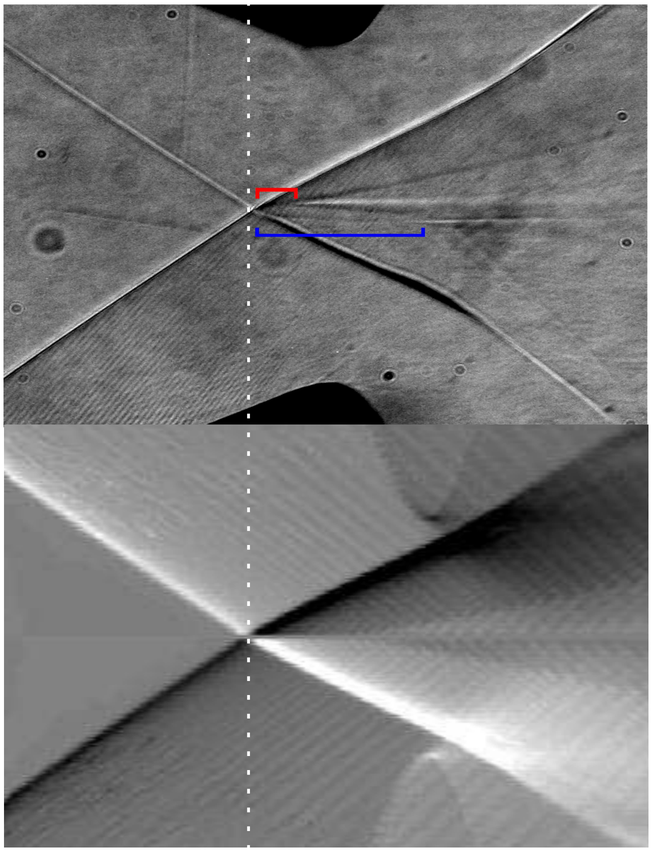

Figure 6.8: Images obtained from experiment and computationally constructed for Model 8 at $M_1 = 3.0$, $\lambda = 10°$, $\phi = 0°$. Red and blue braces bound the regions along which the regular reflection lines exist for sides 1 and 2 respectively.

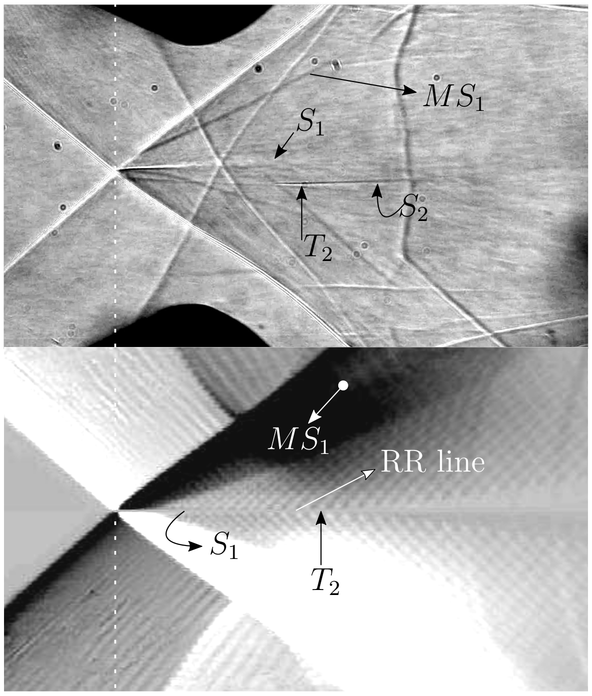

Figure 6.9: Images obtained from experiment and computationally constructed for Model 8 at $M_1 = 3.0$, $\lambda = 20°$, $\phi = 0°$.

the optical path. In all figures showing comparison of experimental and numerically-constructed images, the vertical white dotted line on each image pair is included to show alignment of the interaction points on each image.

This explains the gradually increasing curvature of the incident waves as optical yaw is increased. This is seen for as small an optical yaw as $\lambda = 20°$ (Figure 6.9). Images obtained here show features in a more exaggerated way than Figure 6.8. The image obtained from experiment clearly shows a considerable difference in the horizontal location of the transition points, but this is aided by virtue of the roll offset which clarifies the transition points. For the constructed image below it with no such offset, this difference in transition point location is seen because of the way in which the shear surfaces show up on the final image. Close behind the interaction point, there is a blurry structure which is the shear layer resulting from $T_1$. This is also seen for the image from the experiment (labelled). Looking back at the constructed image, this shear layer appears to dissipate, which is why its visibility attenuates downstream of the interaction point in the final image and it is overridden by the visibility of the regular reflection line on side 2 of the vertical symmetry plane. Once again, this line extends to the right of the image and diverges at $T_2$ to form the far-side Mach surface and also gives rise to the far-side shear surface, which is seen as the secondary blurry structure widening from the middle of the image. This diffusion and widening of the shear surface is also seen in the images from the experiment. In addition, the Mach surface edge (i.e triple line) on the near side is seen clearly in the experimental images, labelled as $MS_1$, however the same cannot be said of that on side 2 of the flow field as its visibility is impeded by the features in front of it along the optical path. $MS_1$ is visible on the constructed image, but barely so due to the dark patches obstructing it from the test piece expansion features. $MS_2$ is seen in the constructed images as the central diverging portion starting at the termination of the regular reflection line (at $T_2$), but this is due to the contrast provided by the parallel knife-edge schlieren setting with which the images were constructed. Having compared the computational and experiment images by overlaying them on one another, it can be said that the Mach surface growth rate seen in the experiment is also present to the same extent in the CFD data.

The features discussed above are made clearer by obtaining images with optical roll, for which two orientations were used: $\phi = 5°$ and $\phi = 9°$ for various yaw angles. The images obtained from experiment and the numerical construction method are shown in Figures 6.10 to 6.14. The use of optical roll allows for better distinction between features on either side of the vertical symmetry plane. Higher roll angles also allow for observation of features at or close to the intersection line on the horizontal symmetry plane. This is clear to see from Figure 6.10, which gives a much clearer impression of the features of the flow field behind the interaction point. The widening of the Mach surface labelled $MS_1$, transition point $T_1$ and shear surface $S_1$ are all made clearly visible in the image obtained from the experiment. The corresponding features are also seen in the computationally constructed image below it, these agreeing very well with those from the experiment in terms of spatial location. The same features on the opposite side of the vertical symmetry plane are less clear to see in the experiment image as well as in the constructed one. The experiment image, being a shadowgraph, attenuates the visibility of these features rapidly with distance from when they first occur. For example, the spatial trajectory of shear surface $S_2$ was unable to be tracked very much further from the transition point $T_2$, which may also be due to mixing occurring along it. The same can be said of the Mach surface $MS_2$ in terms of reduced visibility along its path. The constructed schlieren image does not attenuate such features to as great an extent as the experimental shadowgraph as seen by the features visible on side 1 of the constructed image. This credits the proposed technique as a useful means of providing further insight into the trajectory and tracking of such features over and above available experimental

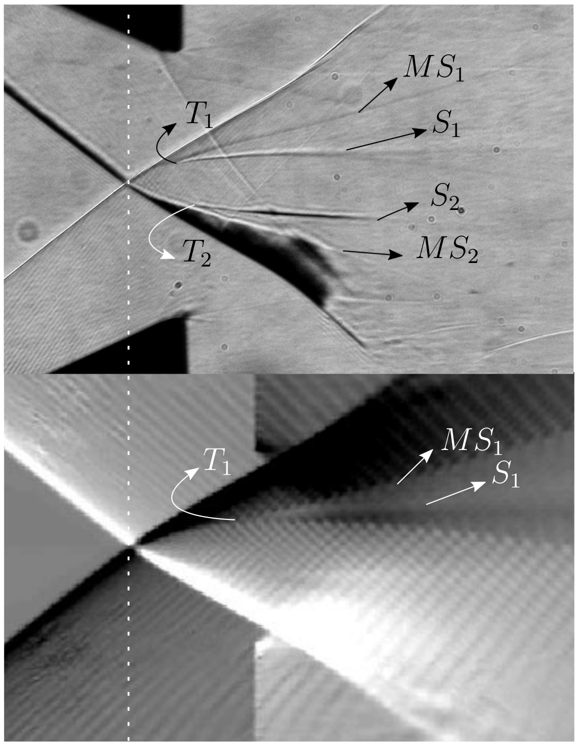

Figure 6.10: Images obtained from experiment and computationally constructed for Model 8 at $M_1 = 3.0$, $\lambda = 0°$, $\phi = 5°$. Triple lines of Mach stem surfaces denoted by $MS_1$ and $MS_2$, shear surfaces labelled as $S_1$ and $S_2$ for near-and far-side features respectively.

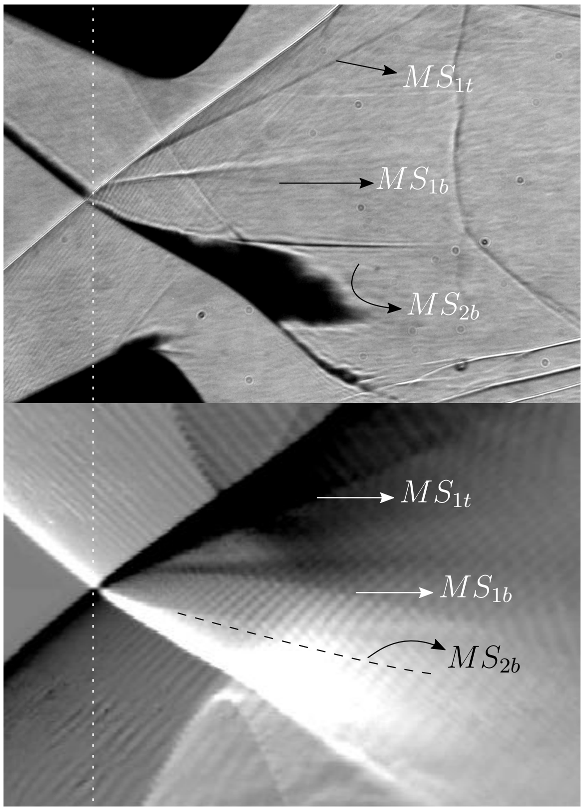

Figure 6.11: Images obtained from experiment and computationally constructed for Model 8 at $M_1 = 3.0$, $\lambda = 15°$, $\phi = 5°$. Near- and far-side triple lines of Mach stem surfaces denoted by $MS_1$ and $MS_2$ respectively, with subscripts $t$ and $b$ for bottom and top triple lines respectively.

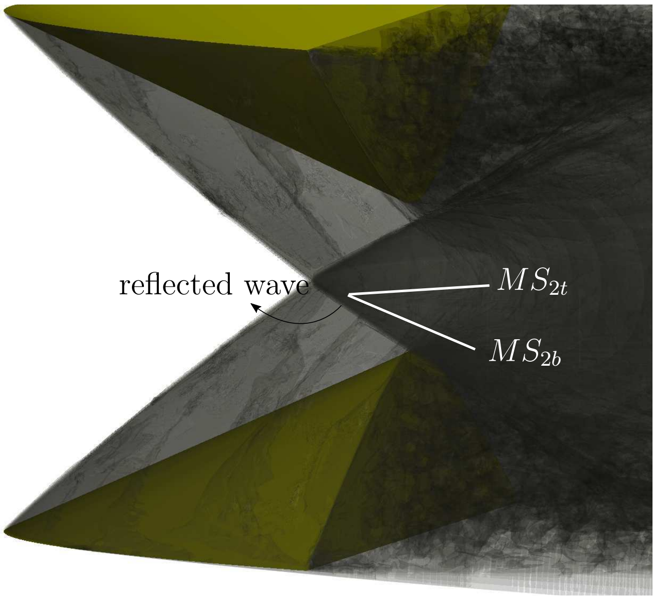

Figure 6.12: Volume-rendering at orientation $\lambda = 15°$, $\phi = 5°$. Far-side triple lines of Mach stem surfaces denoted by $MS_2$, with subscripts $t$ and $b$ for bottom and top triple lines respectively.

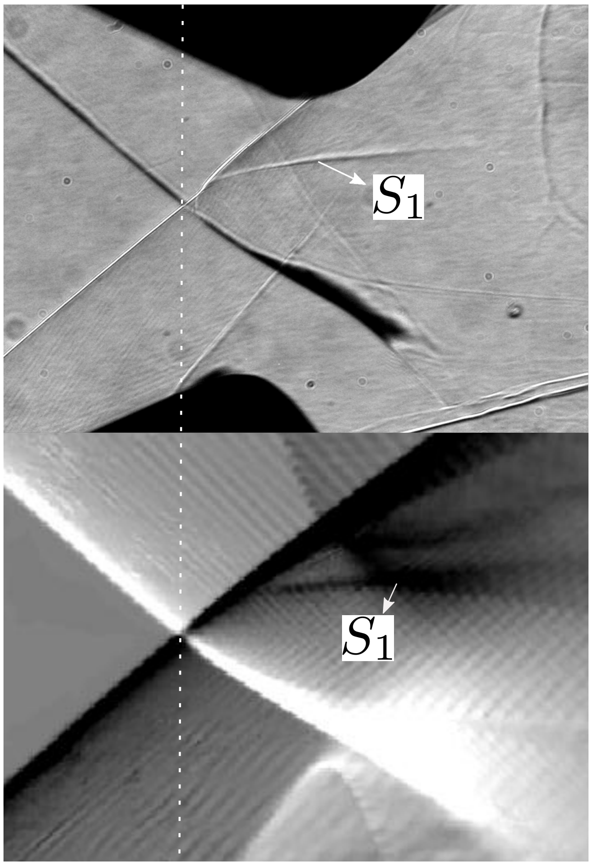

Figure 6.13: Images obtained from experiment and computationally constructed for Model 8 at $M_1 = 3.0$, $\lambda = 15°$, $\phi = 9°$.

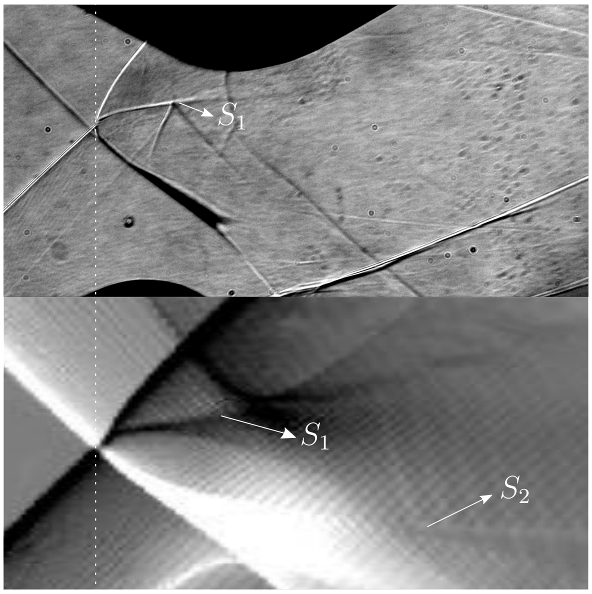

Figure 6.14: Images obtained from experiment and computationally constructed for Model 8 at $M_1 = 3.0$, $\lambda = 30°$, $\phi = 9°$. Shear surfaces labelled as $S_1$ and $S_2$ for near- and far-side features, respectively.

data. However, on side 2 the density gradients along the shear surface are accentuated to the point that it impedes visibility of the triple line and transition point.

In Figure 6.11, in the region between $MS_2$ and the reflected wave there is a dark patch which is easily misinterpreted as the shear surface. This is also seen to various extents in subsequent images with both yaw and roll. The volume-rendering shown in Figure 6.12 was a useful aid in interpreting the images for the location of shear surface $S_2$. The white lines show the approximate locations of the initial portions of the upper ($MS_{2t}$) and lower ($MS_{2b}$) triple lines and thus are the boundaries of the Mach surface on side 2. The lower triple line is visible in the experiment images as well as in some of the constructed ones at higher angles of yaw and thus the shear surface $S_2$ is seen between the upper and lower triple lines. Confirmation was needed of this, as it may be that at very high roll orientations, the shear surface may appear to be below the lower triple line. From the volume-rendering, it can be concluded that the dark patches are due to the confluence of multiple phenomena along the optical path, which gives rise to a large second-order density gradient. These features are the expansion fans and their interaction with the reflected wave surface resulting in image saturation as a result of second-order density gradient field exceeding the range provided by the experimental optics. The same is noted in the constructed images to a more exaggerated extent as this image accounts for first-order density gradients and the final intensity values exceeds the scale range applied. Although an unfortunate consequence of expansion-reflected wave interaction, the fact that the features on side 1 could be favourably be compared with those seen in the experiment image gives confidence that side 2 constructed from the CFD data would match the experimental flow.

The usefulness of higher roll angles is seen when comparing Figure 6.11 to Figure 6.13, the latter obtained with $\phi = 9°$. This is with regards to the shear layer trajectories especially on side 1 of the images. Increasing the yaw angle to $\lambda = 30°$ (figure 6.14) depicts a larger portion of the shear layer trajectory and it is clearer to visualise this on side 1 for the constructed image. However, an important difference between the experimental and constructed images is the extent to which the shear layers are represented. On the near-side, the shear layers are better represented than those on the far-side. The latter is hindered by the superposition of multiple features leading to poorer visibility for the constructed schlierens. The shear layers are only faintly visible on the shadowgraphs on side 2 after zooming. On side 1, the constructed schlierens are free from this confluence effect and hence a larger portion of the shear layer trajectory is able to be inferred from the constructed images than from the experimental ones. This is also aided by the better contrast with which the constructed schlierens depict the shear layers than with the experimental shadowgraphs, which is expected given the order of the density fields that each type of imaging resolves.

A final comment must be made as to the representation of the shock surfaces and spatial locations of interaction points for which excellent agreement between constructed and experimental images is noted. The accuracy of the construction technique to replicate shock profiles can give rise to applications in studies of three-dimensional shock curvature.

### 6.1.6 Conclusions

This section has detailed the development of a method to computationally construct images of integrated density gradients for a three-dimensional flow field viewed with an oblique line-of-sight. It combines ideas used in both ray-tracing and numerical integration of density fields, both of which in past works have been applied to two-dimensional numerical flow solutions, or, when used on three-dimensional flow fields, have assumed the datum configuration of the optical path with $\lambda = 0^\circ$ and $\phi = 0^\circ$ only. The method of image construction was able to show both strong features, such as shocks, as well as those along which density gradients are generally low, such as shear surfaces, on the final constructed images. The methods developed were successfully applied to numerous cases of optical yaw and roll and the combination of both for a numerically-solved fully three-dimensional flow field in order to construct images which were compared with those obtained from experiment for validation purposes.

In the majority of cases, comparisons were easily made using a method of overlaying the constructed images on top of the ones from the experiments, and adjusting opacities to observe spatial correlation between features. In other cases, additional techniques, such as volume-rendering, were required in order to interpret the location of the shear surfaces. Excellent agreement between CFD solutions and experimental image data was demonstrated using the image construction technique, and this was due to the latter being easily given to image scaling and also because of the simple combination of the integrated variables allowing different insights into the nature and appearance of the flow features shown.

## 6.2 Three-dimensional shock interaction in the immediate vicinity of transition

### 6.2.1 Introduction

In practice, the three-dimensional intersection of shock wave surfaces with a symmetry plane produces a flow field topology with a swept incident shock surface such as that shown in Figure 6.15. The test model shown here is of the type used in this study in particular, however, this flow topology and shock surface configuration is typical of all three-dimensional steady flow shock reflections investigated at the time of writing. As noted in [6], the three-dimensional formation and intersection of shock waves leads to an increasing incident wave angle along the sweep of the waves. There comes a point when this results in the reflected shock surface being unable to deflect the flow to be parallel with the symmetry plane and the incident shock surface becomes detached with a Mach surface forming. Although this mechanism of transition is analogous to the detachment criterion for two-dimensional flows, it remains to be investigated whether the von-Neumann and detachment transition criteria are applicable in the analysis plane for a three-dimensional flow. Viewed in three dimensions, transition can be seen at points $T_1$ and $T_2$ in Figure 6.15, and further outwards in a spanwise direction it can be seen that there is the growth of the Mach surface. In this section, first the regular intersection of planar three-dimensional shock surfaces will be examined, after which further analysis regarding the shock systems on either side of the three-dimensional transition point will be undertaken.

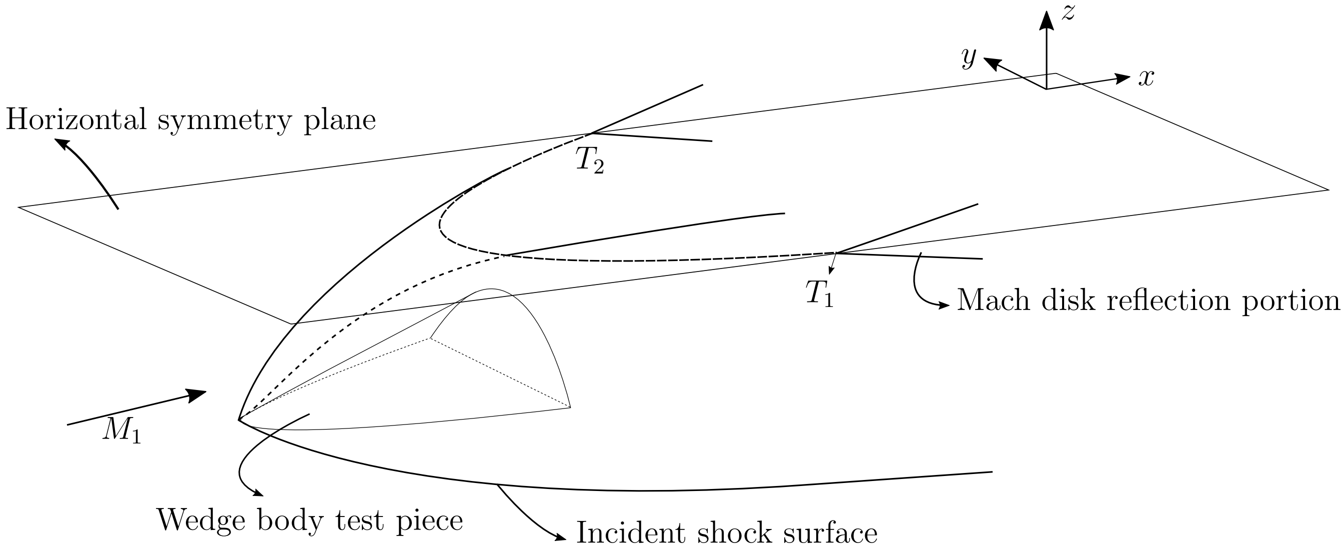

Figure 6.15: Incident shock surface intersection with horizontal symmetry plane.

### 6.2.2 Regular three-dimensional shock interaction

Three dimensional shock interaction is based on the consideration of two opposing shock surface segments the width of which are sufficiently small to approximate them as being plane waves. These represent only a portion of the entire respective shock surfaces, which in general are swept backwards around the object placed in a supersonic steady flow. The standard configuration for this analysis is shown in Figure 6.16. Much of the foundation for the three-dimensional regular interaction of swept shock planes has been laid in the works of Keldysh [34], Emanuel [35], and Migotsky and Morkovin [36]. A recent paper by Domel [37] explores the three-dimensional relations for a single swept shock surface and presents some interesting findings regarding the effects of sweep on the nature of the shock surface and the flow directions downstream of such a surface. The associated complexities of the relations between various parameters was consolidated by Domel into a new relation for the shock geometry and post-shock parameters as a function of sweep, deflection angle and shock angle. This is analogous to the theta-beta-Mach relation for two-dimensional oblique shocks, suitably extended to three-dimensional wave surfaces. In relation to the current work, such a relation is valid for an infinitesimal portion along the continuously swept incident wave surface so that such a portion may be analysed as being planar. The interaction analysis which follows based on Figure 6.16 applies to an infinitesimal portion of a fully-swept wave surface for the interaction of both the incident and reflected waves (such as in Figure 6.15).

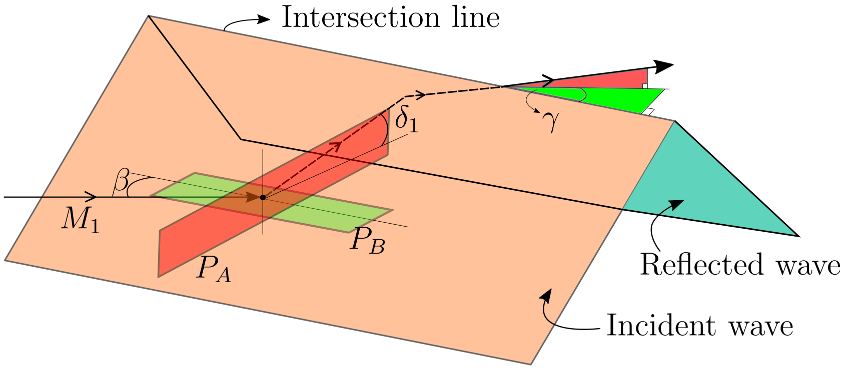

Figure 6.16: Schematic of plane shock wave intersection in space.

In this section, it will be assumed that the free-stream flow is orientated at an angle $\beta$ to the intersection line of the incident and reflected shocks i.e that the shock planes are swept relative to the free-stream. This is the main parameter that differentiates three-dimensional shock interactions from those in two-dimensional flows. Flow vectors are not constrained to within a two-dimensional flow plane, and this is accounted for by the sweep angle $\beta$. It is crucial to note that the definition of the sweep of the shock surfaces used in this work is contrary to that used for the aeronautical definition of sweep. Here, the sweep angle is between the shock surface and the incoming flow vector, as shown in Figure 6.16. The sweep angle is therefore complementary to the way it is defined in, for example, the sweep of a wing.

Upon reaching the incident shock plane, the free-stream is deflected in three directional components, two of which are considered here: one projected onto plane $P_A$ and another onto plane $P_B$, which are perpendicular to one another, shown in red and green respectively in Figure 6.16. Plane $P_A$ lies parallel to a line drawn normal to the intersection line of the shock planes. Plane $P_B$ lies perpendicularly to $P_A$, such that it contains the free-stream vector $M_1$ and is parallel to the reflecting plane at which the incident and reflected shock surfaces intersect. The two component angles of the post-shock streamline are measured relative to a line parallel to and within each plane. Plane $P_A$ is of importance, and will be termed the analysis plane. This is because the two-dimensional oblique relations for shock waves and their interaction apply in Plane $P_A$, as long as all relevant quantities are projected onto this plane. Thus, an ostensibly complex three-dimensional interaction can be suitably reduced to an equivalent two-dimensional one. The corresponding Mach number component in this same plane is $M_1' = M_1 \sin\beta$. It is important to note that in the analysis the effective shock angle is defined as

$$\theta_1' = \sin^{-1}\left(\frac{\sin\theta_1}{\sin\beta}\right) \tag{6.3}$$

where $\theta_1$ is the incident shock angle obtained as seen in an $x-z$ plane slice of the flow field. Note that the prime superscripts refer to effective quantities in the analysis plane. Calculations carried out in the analysis plane are similar to the standard approach used to analyse two-dimensional oblique shocks in which vector components normal to the shock are considered to effect changes across the shock [18, 19].

Once the effective Mach number and either the effective incident shock angle or effective flow deflection angle $\delta_1$ are obtained, one can proceed with a standard two-dimensional consideration of the flow field in the analysis plane. In this study, reflection transition is the primary concern, but first the regular reflection of shocks in the analysis plane is considered (see Figure 6.17).

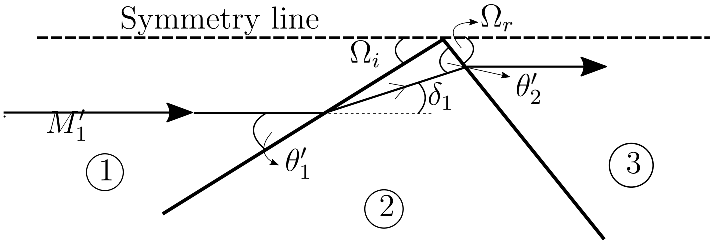

Figure 6.17: Reduction to equivalent two-dimensional reflection configuration in the analysis plane.

Once the flow field and shock wave configurations are viewed from the analysis plane, the two-dimensional two-shock equations can be used for resolving the flow field:

$$\rho_i u'_i \sin(\theta'_i) = \rho_{i+1} u'_{i+1} \sin(\theta'_i - \delta_i) \tag{6.4}$$
$$p_i + \rho_i u'^2_i \sin^2(\theta'_i) = p_{i+1} + \rho_{i+1} u'^2_{i+1} \sin^2(\theta'_i - \delta_i) \tag{6.5}$$
$$\rho_i \tan(\theta'_i) = \rho_{1+1} \tan(\theta'_i - \delta_i) \tag{6.6}$$
$$h_i + \frac{1}{2} u'^2_i \sin^2(\theta'_i) = h_{i+1} + \frac{1}{2} u'^2_{i+1} \sin^2(\theta'_i - \delta_i) \tag{6.7}$$

for $i = 1, 2$ i.e across the incident and reflected shock waves. Note that this the formulation of these equations are identical to those applied to a two-dimensional flow, which means that the underlying assumptions apply here in the analysis plane. Regarding uniformity in each region, it will be seen that this is a significant simplification, as in three-dimensional flows regions of uniform flow properties are reduced in size as compared with two-dimensional flows due to transverse flow components impinging from other parts of the flow field. However, this assumption is considered reasonable when considering a localised region, especially very close to the symmetry plane and to the reflection point of the shock waves, as will be seen later on. Therefore, no account is taken of the effective expansion effects in this analysis as shown in Figure 6.17, although they do exist.

It is important to note that, because of sweep, the analysis-plane component of the free-stream Mach number normal to the incident shock in this same plane (i.e the effective normal Mach number $M'_1 \sin\theta'_1$) is necessarily required to be high enough for the shocks in the analysis plane to exist. This puts limits on the extent of the sweep angle, or on the minimum free-stream Mach number $M_1$, which reduce to

$$\frac{1}{M_1 \sin\beta} \leq \sin\theta'_1 \leq \sin\theta'_{1max} \tag{6.8}$$

where $\theta'_{1max}$ is to be defined as that wave angle beyond which Mach reflection is formed in the analysis plane, and is analogous to the detachment criterion for two-dimensional reflection transition. From the preceding inequality, two things are important: first, the normal Mach number component in the analysis plane is what governs the reflection transition and determines whether or not the shocks in the analysis plane exist or are so weak as to reduce to Mach waves. Secondly, theoretically the same transition criteria (i.e von-Neumann and detachment) apply to the analysis plane as with a purely-two-dimensional interaction. The important difference here is that $\theta'_{1max}$ is additionally dependent on $\beta$ and thus varies all along the intersection line of shock waves in space irrespective of the free-stream Mach number $M_1$ being constant prior to any incident shock surface segment.

The criteria for existence and transition between regular and Mach reflection in the analysis plane are shown in Figure 6.18 for a free-stream Mach number $M_1 = 3.0$. Higher Mach number flows are given to a broader range of effective incident shock angles in which the shock waves both exist and are configured in a regular reflection pattern. The incident wave angles of the von-Neumann and detachment criteria are denoted by $\theta'_{1v-N}$ and $\theta'_{1max}$ respectively. It is apparent that these criteria in the analysis plane are not clearly distinguishable for most of the range of sweep angles from the Mach angle (19.47°) to approximately 50°, at $M_1 = 3.0$. The largest difference in effective shock angle is approximately 2°, occurring near a sweep of $\beta = 90°$. This represents a situation in which the free-stream is perpendicular to the intersection line of the shock planes.

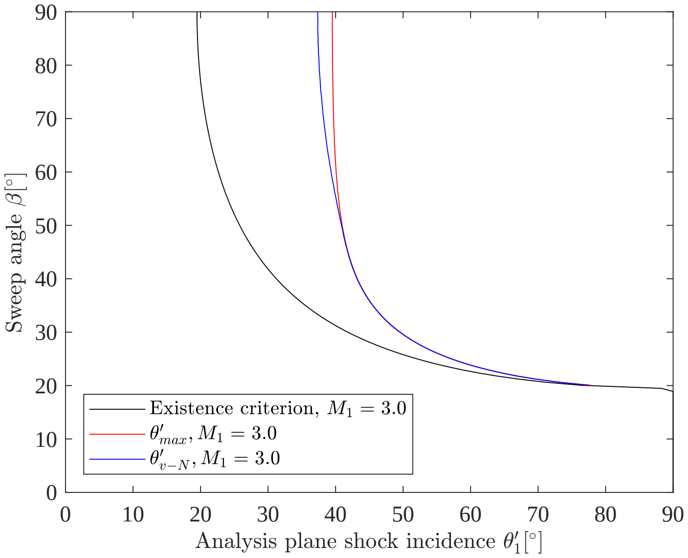

Figure 6.18: Minimum existence criteria and transition criteria for three-dimensional shocks, $M_1 = 3.0$

In order to complete the analysis of spatial phenomena by virtue of three-dimensional shock intersections, attention is given to flow deflections as viewed from a plan elevation view of the top of the intersection. This is shown in Figure 6.19. Although the intersection is viewed from the top, the vectors on this diagram are not the components in the plane of the intersection line and still possess their out-of-plane components where applicable. Again, all quantities with a prime superscript denote the vector component in the analysis plane. The velocity vector emerging from the reflected wave is not parallel to the free-stream vector when viewed in the plan view as in Figure 6.19; however, both vectors are parallel to the symmetry plane (containing the line of intersection) when viewed in the analysis plane or in an $x - z$ plane slice of the flow field. The angular difference between the two vectors is given by $\tau = \beta - \gamma$, where $\gamma$ is the angle between the emergent velocity vector and the line of intersection in the horizontal symmetry plane (i.e., in the plane of the intersection line). From Figure 6.17, the velocity ratio across the entire system of shocks in the analysis plane can be derived based on the fact that the tangential velocity components $w_i$ for $i = 1, 2, 3$ for each region in Figure 6.17 are equal. If the velocity in each region in

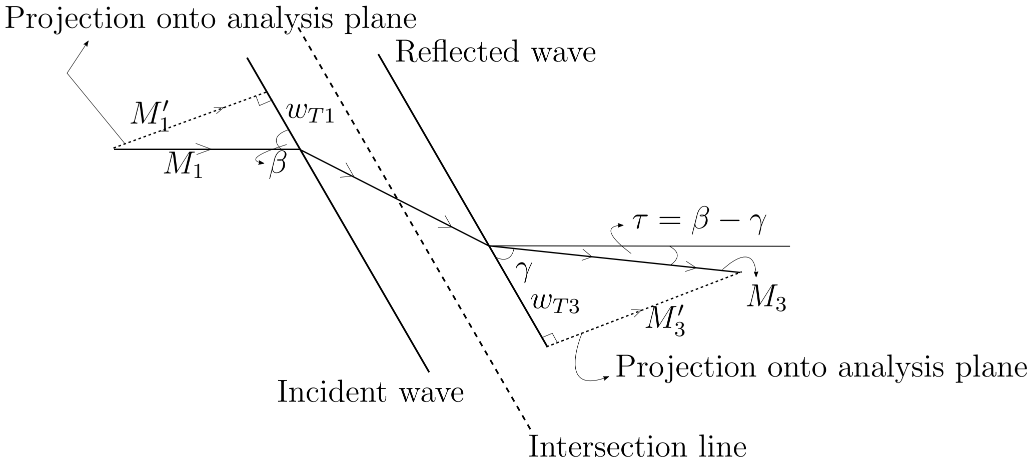

Figure 6.19: Top view of the intersection of the shock planes.

the analysis plane is denoted as $V_i'$ for $i = 1, 2, 3$ then the tangential components are expressed as

$$w_1 = V_1' \cos\theta_1' \tag{6.9}$$
$$w_{21} = V_2' \cos\theta_2' \tag{6.10}$$
$$w_{32} = V_2' \cos(\theta_1' - \delta_1) \tag{6.11}$$
$$w_3 = V_3' \cos(\theta_2' - \delta_1) \tag{6.12}$$

where $w_{21}$ is the tangential velocity component of $V_2'$ relative to the incident wave, and $w_{32}$ is the tangential component of $V_2'$ relative to the reflected wave. Equating Equation 6.9 with 6.10, and Equation 6.11 with 6.12, and solving for $V_2'$ results in

$$V_2' = V_1' \frac{\cos\theta_1'}{\cos(\theta_1' - \delta_1)} \tag{6.13}$$
$$V_2' = V_3' \frac{\cos(\theta_2' - \delta_1)}{\cos\theta_2'} \tag{6.14}$$

Next, equating Equations 6.13 and 6.14 results in the velocity ratio across the entire system of shocks in the analysis plane

$$\frac{V_3'}{V_1'} = \frac{\cos\theta_1'}{\cos(\theta_1' - \delta_1)} \frac{\cos\theta_2'}{\cos(\theta_2' - \delta_1)} \tag{6.15}$$

Denoting the velocity tangent to each of the waves as viewed in Figure 6.19 as $w_{Ti}$, for $i = 1, 2, 3$, we obtain

$$tan\beta = \frac{M_1'}{w_{T1}} \tag{6.16}$$
$$tan\gamma = \frac{M_3'}{w_{T3}} \tag{6.17}$$

Noting that all tangential velocity components are equal across the shock system, it can be seen that

$$\frac{\tan\gamma}{\tan\beta} = \frac{M_3'}{M_1'} \tag{6.18}$$

It is worth mentioning that the two Mach numbers on the right-hand side of Equation 6.18 are in the analysis plane, as are quantities $V_1$ and $V_3$. Therefore, it can be deduced that

$$\frac{M_3'}{M_1'} = \frac{M_3 \sin\gamma}{M_1 \sin\beta} = \frac{V_3'}{V_1'} \tag{6.19}$$

This is an important equation as it related the analysis plane Mach and velocity ratios to the actual Mach numbers in the three-dimensional flow field, which further gives the result

$$\gamma = \tan^{-1}\left(\frac{V_3'}{V_1'}\tan\beta\right) \tag{6.20}$$

Of importance is the fact that the foregoing analysis can be used to relate the flow conditions and flow geometry in the analysis plane to those found in the top view of Figure 6.19. As such we have

$$\tan\beta = \frac{V_1'}{V_3'}\tan\gamma \tag{6.21}$$

$$\implies \tan\beta = \frac{\cos(\theta_1'-\delta_1)}{\cos\theta_1'}\frac{\cos(\theta_2'-\delta_1)}{\cos\theta_2'}\tan\gamma \tag{6.22}$$

which is of clear significance to the understanding of regular reflection in three-dimensional space, while not being limited to any one plane. Thus, the fundamentals of regular reflection have been introduced. This requires extension to consider the flow phenomena in the presence of a transition point, on one side of which there is regular reflection in the analysis plane and on the other, Mach reflection.

### 6.2.3 Model development in the vicinity of transition

The main focus for this section is the flow field in the vicinity of transition, and so attention is given to the regions in the immediate vicinity of the transition points. Observing the shock system from above, the shock intersection in the symmetry plane is as is shown in Figure 6.20. When viewed from above, the shock intersection depicts transition at the point from which a shear layer emanates from the intersection line, shown as the dotted line in Figure 6.20. To one side of the shear layer there is regular reflection and on the other there is Mach reflection. In the immediate surrounds of the shear layer there should theoretically be compatibility between pressure and flow deflections such that

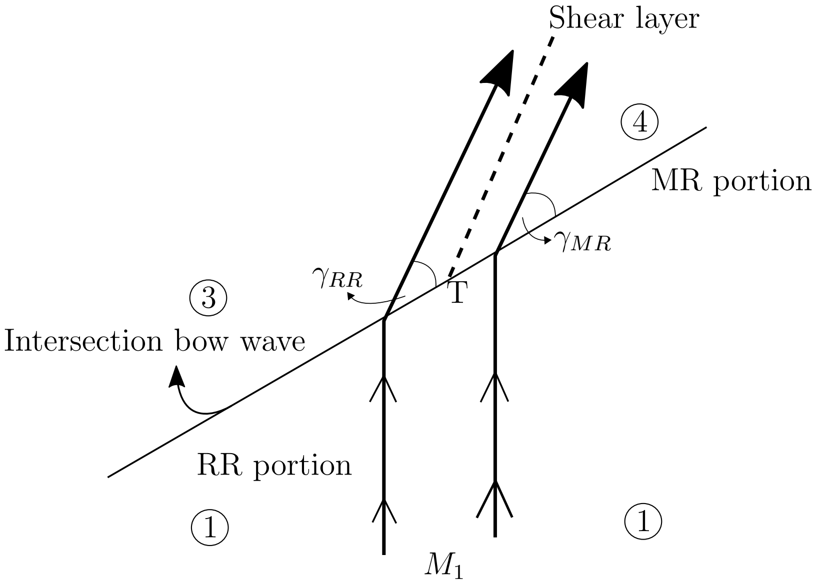

Figure 6.20: Top view of three-dimensional transition at the symmetry plane.

$$\gamma_{RR} = \gamma_{MR} \tag{6.23}$$

$$\implies \tau_{RR} = \tau_{MR} \tag{6.24}$$

$$p_{3RR} = p_{4MR} \tag{6.25}$$

Subscripts RR and MR denote quantities specific to the respective reflection type along the intersection bow wave. It is important to note that Equation 6.24 is obtained due to the fact that the sweep angle $\beta$ for the RR and MR portions on the intersection bow wave are initially assumed identical, and in general, $\gamma = \beta - \tau$. *The assumption of identical sweep angles for the two reflection portions is now examined further in light of the fact that the compatibility relations should hold for the flows behind both the Mach reflection and the regular reflection portions.* This is the main thrust of this work which, as will be discussed later, has important consequences for the shock geometry and physical conditions in the surrounds of the transition points.

The flow fields in the analysis planes for the MR and RR configurations need to be considered in the immediate vicinity of their respective interaction points, and the situations considered are shown in Figures 6.21 and 6.22.

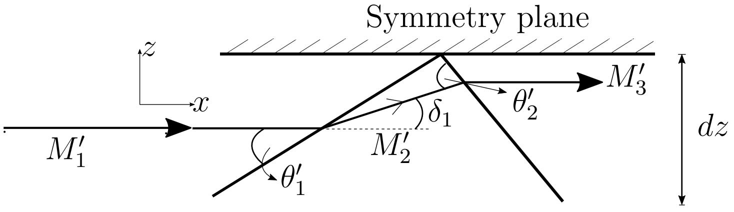

Figure 6.21: Schematic of analysis plane slice of flow field on RR side of transition point.

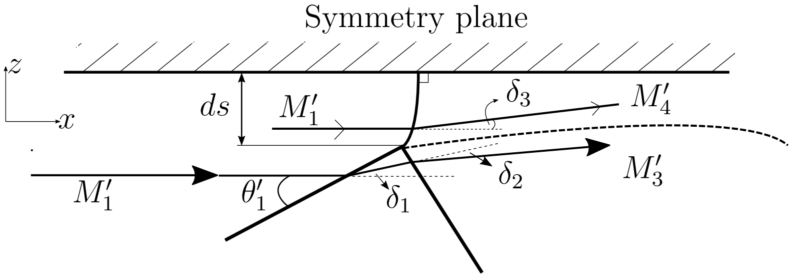

Figure 6.22: Schematic of analysis plane slice of flow field on MR side of transition point.

On the regular reflection side of the transition point $T$, the flow field analysis is constrained to a small vertical distance $\Delta z$ away from the symmetry plane in the limit $\Delta z \to 0$.

Along the entire Mach reflection portion, we consider the finite Mach stem height in the analysis plane to be of arclength $\Delta s$. Note that it is accepted that the Mach stem will have some variation of curvature from where it protrudes at the triple point until where it reaches the symmetry plane at its foot. At this point it is perpendicular to the symmetry plane. Specifically, at the point immediately next to the transition point $T$, the Mach stem height is taken to be infinitesimally small, and so the situation considered at transition is that in the limit $\Delta s \to 0$.

Since the boundary condition of the Mach stem foot being perpendicular to the symmetry plane is still required to hold, it is reasonable to assume that the Mach stem is a normal shock in the analysis plane on the MR side of transition point $T$. The Mach surface just after transition is therefore modelled as an oblique shock relative to the oncoming flow when viewed in three-dimensional space.

The analytical procedures for resolving the flow field in Figures 6.21 and 6.22 and the transition between them are now discussed. For the RR section near transition, two-shock theory is applied in the analysis plane, with the boundary condition that the flow deflection across each of the shocks (incident and reflected) is identical but in an opposite sense in order to satisfy symmetry. The net flow deflection $\tau_{RR}$ across the RR side of the transition point is obtained by manipulation of Equation 6.22 to that of

$$\beta - \tan^{-1}\left(\frac{\cos\theta_1'}{\cos(\theta_1'-\delta_1)}\frac{\cos\theta_2'}{\cos(\theta_2'-\delta_1)}\tan\beta\right) \tag{6.26}$$

The overall pressure ratio relating free-stream pressure to that just after the reflection point is given by

$$\left(\frac{p_3}{p_1}\right)_{RR} = \frac{p_3}{p_2} \times \frac{p_2}{p_1} \tag{6.27}$$

where the pressure ratio terms on the right-hand side can be generally obtained [18] using

$$\frac{p_{i+1}}{p_i} = 1 + \frac{2\chi}{\chi+1}(M_1'^2\sin^2\theta_1' - 1) \tag{6.28}$$

for $i = 1, 2$, where $\chi$ is the specific heats ratio for the fluid used (air in this case). $M_2'$ is obtained from the standard oblique shock theory equations [18], applied within the analysis plane as

$$M_2' = \sqrt{\frac{(\chi-1)M_1'\sin^2\theta_1' + 2}{\sin^2\theta_1'(2\chi M_1'\sin^2\theta_1' + 1 - \chi)}} \tag{6.29}$$

For the MR portion near $T$, only the region at the Mach stem foot is considered and so this portion can be treated as an oblique shock normal to the symmetry plane (or equivalently a normal shock in the analysis plane), which deflects the free-stream flow by

$$\tan\gamma_{MR} = 2\cot\beta\left(\frac{M_1^2\sin^2\beta - 1}{M_1^2(\chi+\cos(2\beta))+2}\right) \tag{6.30}$$

The model used here thus specifies the flow deflection through the Mach stem near the transition point as being a function of only the free-stream Mach number and the sweep angle.

The pressure ratio relating free-stream pressure with post-Mach stem pressure is obtained as

$$\left(\frac{p_4}{p_1}\right)_{MR} = 1 + \frac{2\chi}{\chi+1}(M_1'^2 - 1) \tag{6.31}$$

$$\Longrightarrow \left(\frac{p_4}{p_1}\right)_{MR} = 1 + \frac{2\chi}{\chi+1}(M_1^2\sin^2\beta - 1) \tag{6.32}$$

In order for the compatibility relations about the transition point to hold for the RR and MR portions at the same sweep angle, the following conditions must be satisfied; for the flow deflection condition of Equation 6.24 the following is obtained:

$$\beta - \tan^{-1}\left(\frac{\cos\theta_1'}{\cos(\theta_1'-\delta_1)}\frac{\cos\theta_2'}{\cos(\theta_2'-\delta_1)}\tan\beta\right) = \tan^{-1}\left(2\cot\beta\left(\frac{M_1^2\sin^2\beta - 1}{M_1^2(\chi+\cos(2\beta))+2}\right)\right) \tag{6.33}$$

and for the pressure condition of Equation 6.25

$$\left[1+\frac{2\chi}{\chi+1}(M_2^{2\prime}\sin^2\theta_2'-1)\right]\left[1+\frac{2\chi}{\chi+1}(M_1^{2\prime}\sin^2\theta_1'-1)\right]=1+\frac{2\chi}{\chi+1}(M_1^2\sin^2\beta-1) \qquad (6.34)$$

with $(\frac{p_3}{p_1})_{RR}$ being determined as the left-hand side of Equation 6.34.

Considering sweep and effective shock angles ($\beta$ and $\theta_1'$) at the detachment transition criterion being those used as inputs for Equations 6.33 and 6.34, plots of net flow deflection through the shock system viewed from above (i.e $\tau$) and the post-shock-to-free-stream pressure ratio for each of the RR and MR portions can be investigated for various transition sweep angles. That for net flow deflection is shown in Figure 6.23 whilst that for the pressure ratios is depicted in in Figure 6.24.

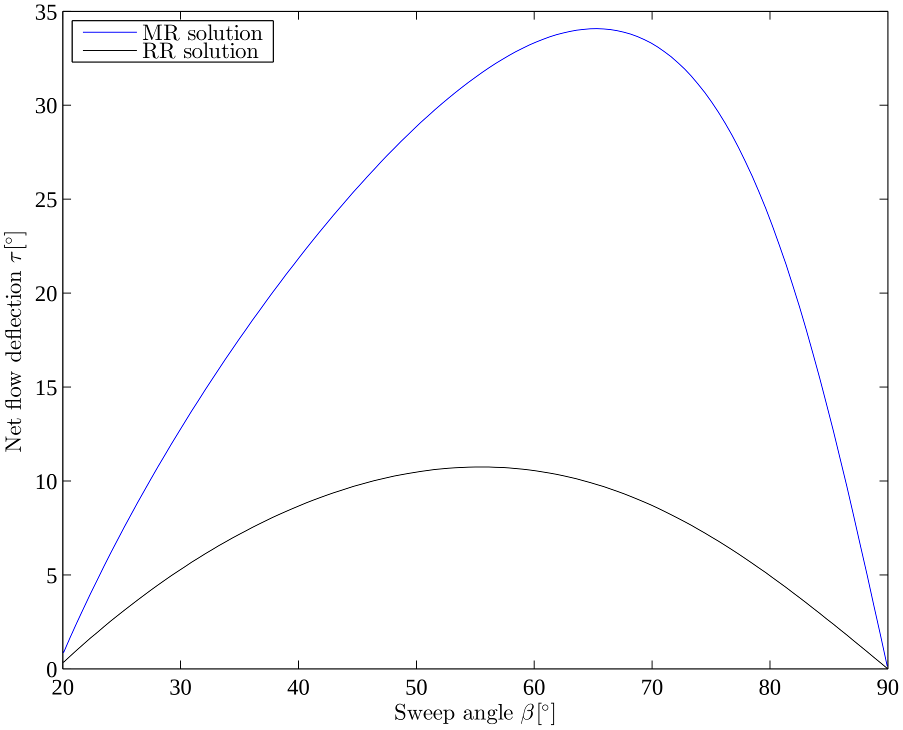

Figure 6.23: Net flow deflection at various sweep angles for RR and MR portions on either side of transition point, $M_1 = 3.0$.

The computations for generating these plots were restricted to a sweep domain above the Mach angle for the free-stream Mach number used, with an upper bound of $\beta = 90°$. It is worth noting that near the Mach angle (which is 19.47° for $M_1 = 3.0$) the flow deflections tend to zero, as is the case in Figure 6.23. This makes sense as regardless of whether one considers the RR or MR portion of the intersection bow wave, as the flow in the symmetry plane effectively passes through a Mach wave - the lower limiting case of strength of an oblique shock. Associated with this is the pressure ratio which is unity at a sweep angle equal to the Mach angle. At the opposite end of the sweep domain at $\beta = 90°$, the net flow deflections are also zero for both RR and MR portions. This also makes physical sense, as in this case the situation is that of a reflection pattern which is fully equivalent to its effective analysis-plane configuration. The corresponding pressure ratios are not equal for $\beta = 90°$, but rather the two values for the RR and MR solutions are those for

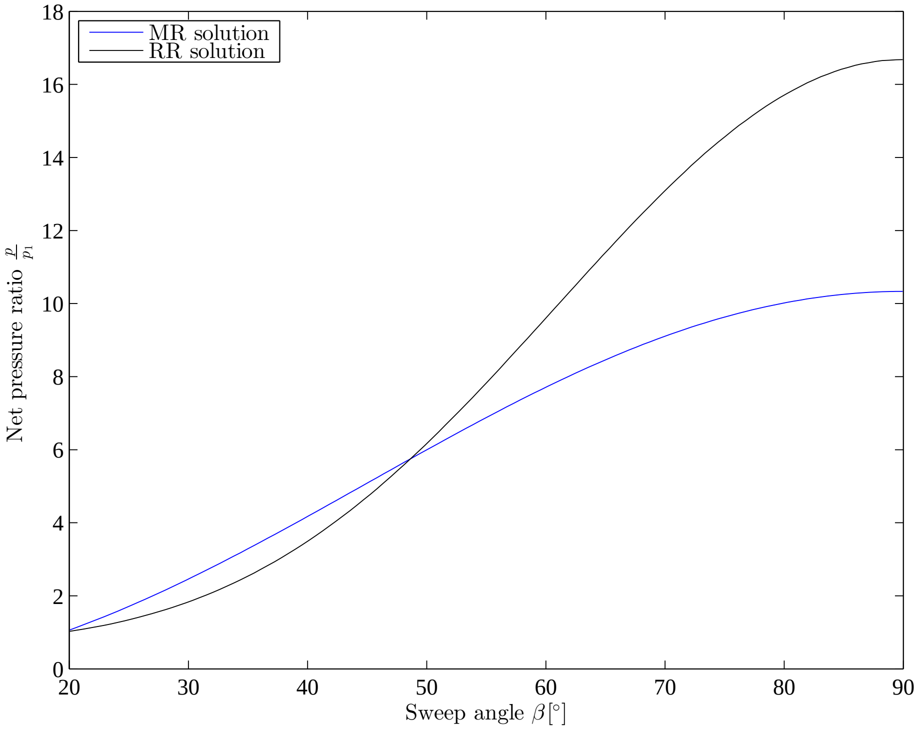

Figure 6.24: Pressure ratio at various sweep angles for RR and MR portions on either side of transition point, $M_1 = 3.0$.

two-dimensional regular reflection and one-dimensional normal shock configurations respectively. The maximum flow deflection for the MR solution is the maximum deflection angle for an oblique shock of the same strength and orientation.

Both of these Figures depict the important result that for the same sweep on the RR and MR portions, the net flow deflections and pressure ratios are both not equivalent on either side of the transition point, and that this is generally the case for all transition sweep angles and all shock configurations conforming to the detachment criterion. This important result means that there must be some physical mechanism by which the compatibility equations can be satisfied. These are fundamental to the existence of the transition point along the intersection line. The solution to this is based on reviewing the fundamental assumption that the sweep angle $\beta$ is common to both the RR and MR portions on either side of the transition point. If the sweep of one portion could be different to the other, there would be some leeway for the compatibility equations to be satisfied across the transition point. A review of the numerical analysis results, two of which are shown in Figures 6.25a and 6.25b, indicate the intersection line to develop a sweep cusp at the transition point. This is more clearly evident from measurements and analysis presented in Figure 6.27 onwards. This means that the sweep angle does not monotonically decrease along the intersection bow wave - at transition the cusp momentarily increases the sweep for the MR portion after which the sweep resumes its monotonic decrease again towards the periphery. Numerical results for all model geometries and for all free-stream Mach numbers ($M_1 = [2.8, 3.0, 3.2, 3.4]$) show the existence of this cusp.

Further inspection of the horizontal symmetry plane streamlines demonstrates the flow deflection compatibility across the transition point, as shown in figure 6.26. Another important point is the sudden change in streamline deflection before and after the transition point, resulting in a compression of the streamlines along the Mach reflection portion. The divergence of the streamlines

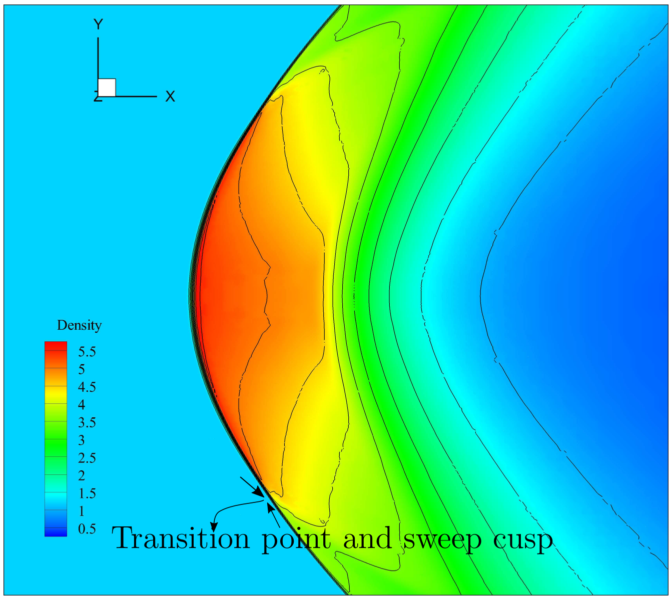

(a) Model 8 with $M_1 = 3.0$.

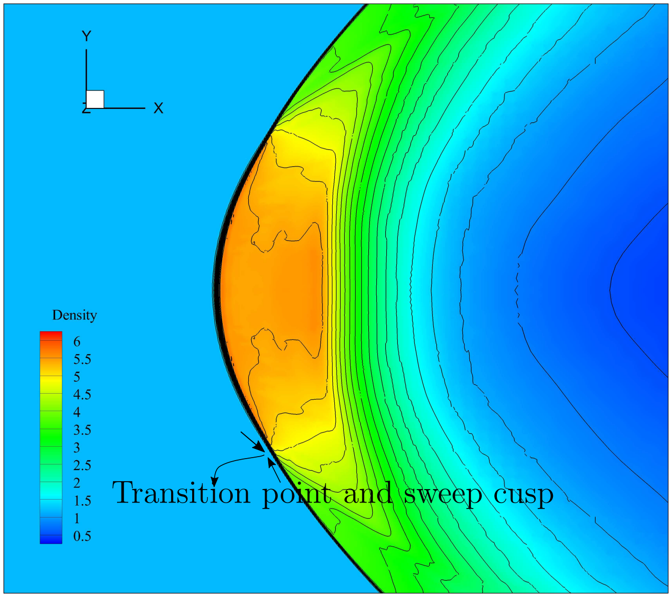

(b) Model 10 with $M_1 = 3.0$.

Figure 6.25: Evidence of sweep cusp in numerical model results. Contour floods and lines depict flow density.

just after transition within the Mach reflection portion is due to the increase in sweep angle of the intersection line, owing to there being a cusp at transition. The oblique shock solution to the Mach reflection portion necessitates highly deflected flow downstream of the cusp and gives rise to divergence from the RR streamlines as seen in figure 6.26. Post-transition compression of the flow in the MR portion is an important consideration for aircraft applications should the transition point location be able to be controlled by model geometry or other means. It is also worth noting that the flow streamlines reduce their deflections along the intersection line towards the periphery, reverting to becoming straight at the wall at the bottom of the Figure. This is as a result of the finite width of the domain which constrains the flow to the space within it and does not permit outflow. This boundary condition was chosen as it accurately represents the reality of the wind tunnel test section. However, real external three-dimensional flows would be unbounded in the peripheral direction, and perhaps the flow streamlines would show an increased net flow deflection all along the intersection line as opposed to the bounded flow shown here. Further evidence of

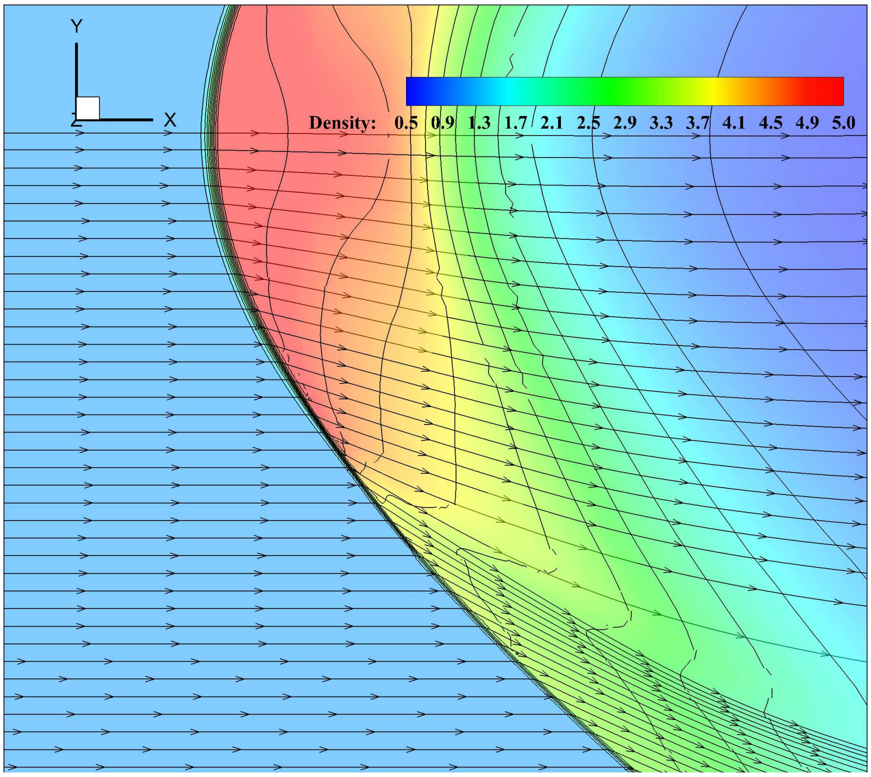

Figure 6.26: Streamlines along symmetry plane showing considerable divergence after the intersection bow wave at transition.

the sweep cusp is now demonstrated by solving the above equations for the inverse problem, this being to obtain the sweep angle for discrete segments along the intersection line given that the net flow deflection $\tau$ and Mach numbers $M_1$ and $M_3$ could be measured from numerical results. The analysis is carried out for a case in which the sweep cusp is not immediately evident from examining the intersection line shape. This was done in order to verify the capability of the analytical three-dimensional transition model developed to resolve gentle sweep cusps. Transition cusps for all test cases were resolved using the analytical model. The solution to this inverse problem is based primarily on Equation 6.20, for which the sweep angle $\beta$ can be solved for as:

$$\beta = \tan^{-1}\left(\frac{M_1'}{M_3'}\tan\gamma\right) \tag{6.35}$$

The analysis plane velocity ratio $\frac{V_1'}{V_3'}$ has been replaced by the equivalent Mach number ratio. The analysis plane Mach number ratio is can be related to the to the actual Mach number ratio with

$$\frac{M_1'}{M_3'} = \frac{M_1 \sin\beta}{M_3 \sin\gamma} \tag{6.36}$$

$$\implies \beta = \tan^{-1}\left(\frac{M_1 \sin\beta}{M_3 \cos\gamma}\right) \tag{6.37}$$

for which, additionally,

$$\gamma = \beta - \tau \tag{6.38}$$

with $\tau$ being the net deflection of the emergent streamline from the streamwise (horizontal) $x-$ axis after it passes through the entire shock system (regardless of whether this system is a Mach surface or regular reflection).

The Mach number of the emergent streamline $M_3$ was directly obtained from the CFD data for the test model in question. The net deflection of the emergent streamline, $\tau$, was readily measured from images similar to Figure 6.26 with streamlines drawn in the vicinity of the transition point. The deflection angles were measured thrice in an image processing software, and an average was taken together with the associated uncertainty. Within the uncertainty of the measurement technique used, the flow deflection on either side of the transition point was found to be quite similar, as should be expected for flow deflection compatibility to hold. Uncertainty ranges were small enough for the subsequent analysis to take consideration only of the nominal values.

This leaves the two equations, 6.37 and 6.38, with two unknown variables, namely $\gamma$ and $\beta$. The system of equations was thus solved iteratively, with initial guess values of $\beta$ ranging from 30° to 90°, as it was clear that the sweep angle did not exceed this range. Equivalently, one may solve for the explicit solution of the sweep angle, obtainable from equations 6.37 and 6.38 as

$$\beta = \tan^{-1}\left(\frac{\frac{M_1}{M_3} - \cos\tau}{\sin\tau}\right) \tag{6.39}$$

The solution for the sweep angle at various span stations on the intersection line for Model 8 are shown in Figure 6.27a for points along the intersection line in space. Figure 6.27b shows the sweep angle variation plotted against a $y-$coordinate that has been non-dimensionalised with the half-span of the intersection line.

This exercise gives important evidence of the intersection bow wave cusp for which the sweep difference is as small as approximately 2.5°. It credits the analytical model developed in the immediate vicinity of transition with the capability of solving the inverse problem of obtaining sweep angles from parameters that are readily measurable from numerical model results. More exaggerated sweep cusps are visually evident for other cases, especially so for higher free-stream Mach numbers and wider geometrical spreads. The physical principles of such differences will be discussed in later sections.

However, upon realising the capability of the analytical model to depict the transition cusp, further numerical models were configured to be further refinements of the initial solutions. The aspect of interest here was the geometrical nature of the sweep cusp to be measured by applying the new model to solving the inverse problem at stations closer to the transition point. Furthermore, corresponding viscous simulations were undertaken in order to assess the effect of viscosity on the cusp measurements. A selection of results are shown in Figure 6.28 for measurements taken from inviscid and viscous cases.

The decision to investigate the cusp at a higher resolution showed some important geometrical aspects related to transition. It is interesting that the cases shown here depict the regular and Mach reflection curves tending to merge towards each other. It is also notable that the viscous cases contain transition points that are consistently stationed further outwards along the span of the intersection line compared to inviscid cases. However, this difference is at most approximately 2 mm. These figures also show the transition points consistently occurring at higher sweep angles for viscous cases than for the corresponding inviscid ones with a maximum 8° difference. This, together with the transition points being located further outwards along the intersection line span leads to the conclusion that the viscous cases contain intersection lines that are slightly more spread out in the transverse direction than the corresponding inviscid cases, albeit by a small margin. Overall, there is good correlation between the viscous and inviscid cases to the point that the viscous measurements look as if they are offset from the inviscid ones in most cases of

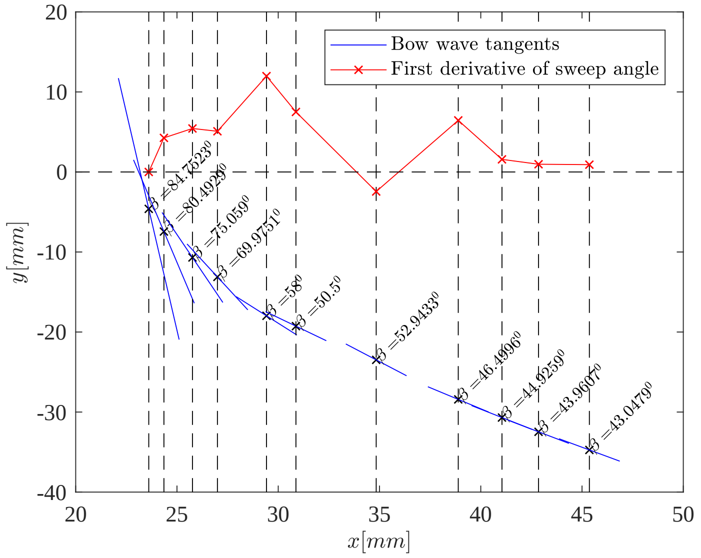

(a) Points along intersection bow wave shock front with sweep tangents.

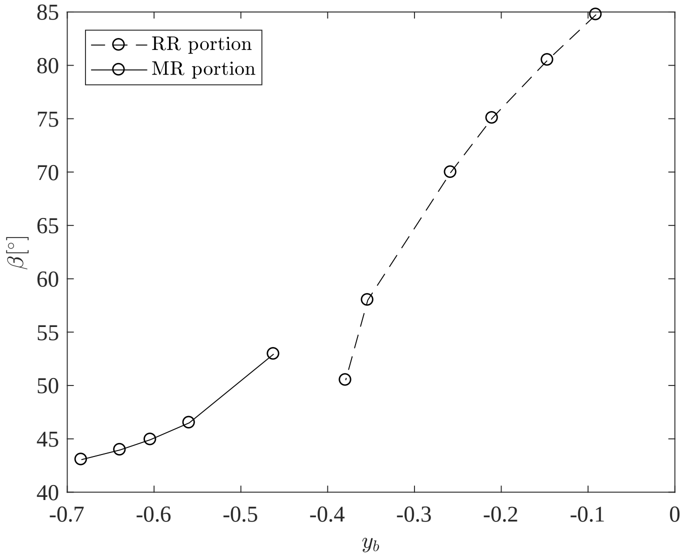

(b) Sweep at non-dimensionalised locations along the half-span of the intersection bow wave.

Figure 6.27: Evidence of sweep cusp using measured data from numerical models.

Figure 6.28. Perhaps the most important fact of these additional cases is that the addition of fluid viscosity reduces the extent of the sweep discontinuity. This points to the fact that the inclusion of viscosity in these numerical models leads to a more gentle sweep discontinuity as evidenced by the smaller jump between the regular and Mach reflection curves of Figure 6.28 compared to the inviscid cases.

### 6.2.4 Experimental evidence of sweep cusps

Oblique shadow photography techniques employed to visualise the above flow fields experimentally were found to show important information regarding the swept shock configurations. In specific relation to the sweep cusps, evidence of a slight perturbation along the intersection line was noted. This is seen in Figure 6.29 for optical orientations in both yaw and roll.

Figure 6.29a shows a highly yawed point of view and the optical path passes through the Mach reflection portion on the near side of the tunnel so that it seems that there is Mach reflection at

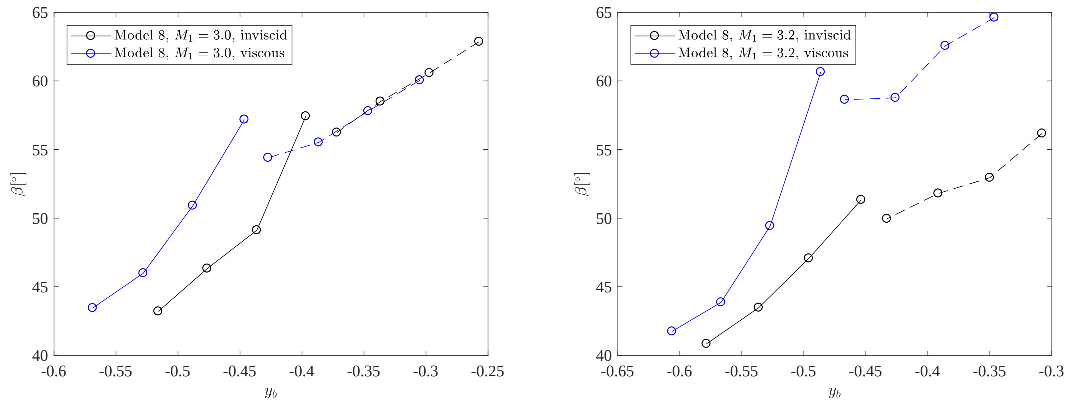

(a) Model 8, $M_1 = 3.0$

(b) Model 8, $M_1 = 3.2$

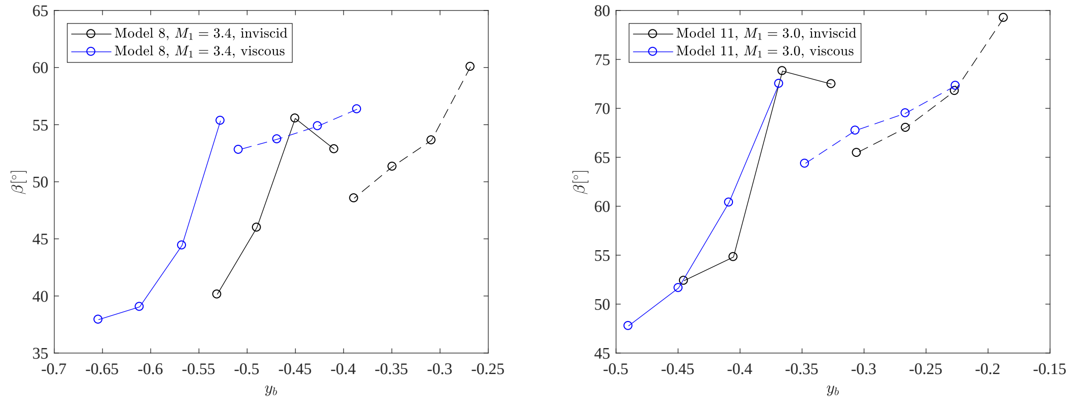

(c) Model 8, $M_1 = 3.4$

(d) Model 11, $M_1 = 3.0$

Figure 6.28: Sweep angle at non-dimensionalised spanwise locations for a selection of viscous and inviscid results.

the interaction point on the image centreline. In fact, the Mach stem surface is viewed almost head-on along its trajectory around the intersection line. As the Mach surface is swept around the near-side portion of the flow field towards the apex of the intersection line, it decreases in height towards the downward-pointing arrow seen in the image. It is important to note that the image is foreshortened due to optical yaw which, in this context, means that certain features are depicted over a shorter spatial distance than in reality. The height decrease of the Mach surface therefore takes place over a much larger distance than this image depicts. The Mach surface then transitions to a regular reflection line towards the right, and this line continues further backwards along its sweep until it too transitions once more to the Mach reflection portion on the far-side at the point indicated by the arrow towards the right-hand side of the image. A better view of the near- and far-side transition points is shown in the zoomed-up and enhanced images of Figure 6.30 which correspond to the optical orientation of Figure 6.29a.

It is in the vicinity of the near-side transition from Mach reflection to regular reflection (see left-hand side of Figure 6.29a) that a small bulge is seen as also shown in Figure 6.30a. This indicates some sort of disturbance in that region, and is attributed to the sweep cusp. Further evidence is seen in Figure 6.29b which is at a lower yaw angle but with the optics system rolled by 5° in order to slightly elevate the point-of-view. Here, the intersection line is seen as the white line just above the reflected wave (labelled as RR line in the sketch below it). As it is swept round towards the transition point on the near-side (indicated by the arrow) there appears to be a slight disturbance resembling the cusp. The fact that such a feature is located at the point from which the shear surface edge emanates is further justification of experimental evidence of the sweep cusp.

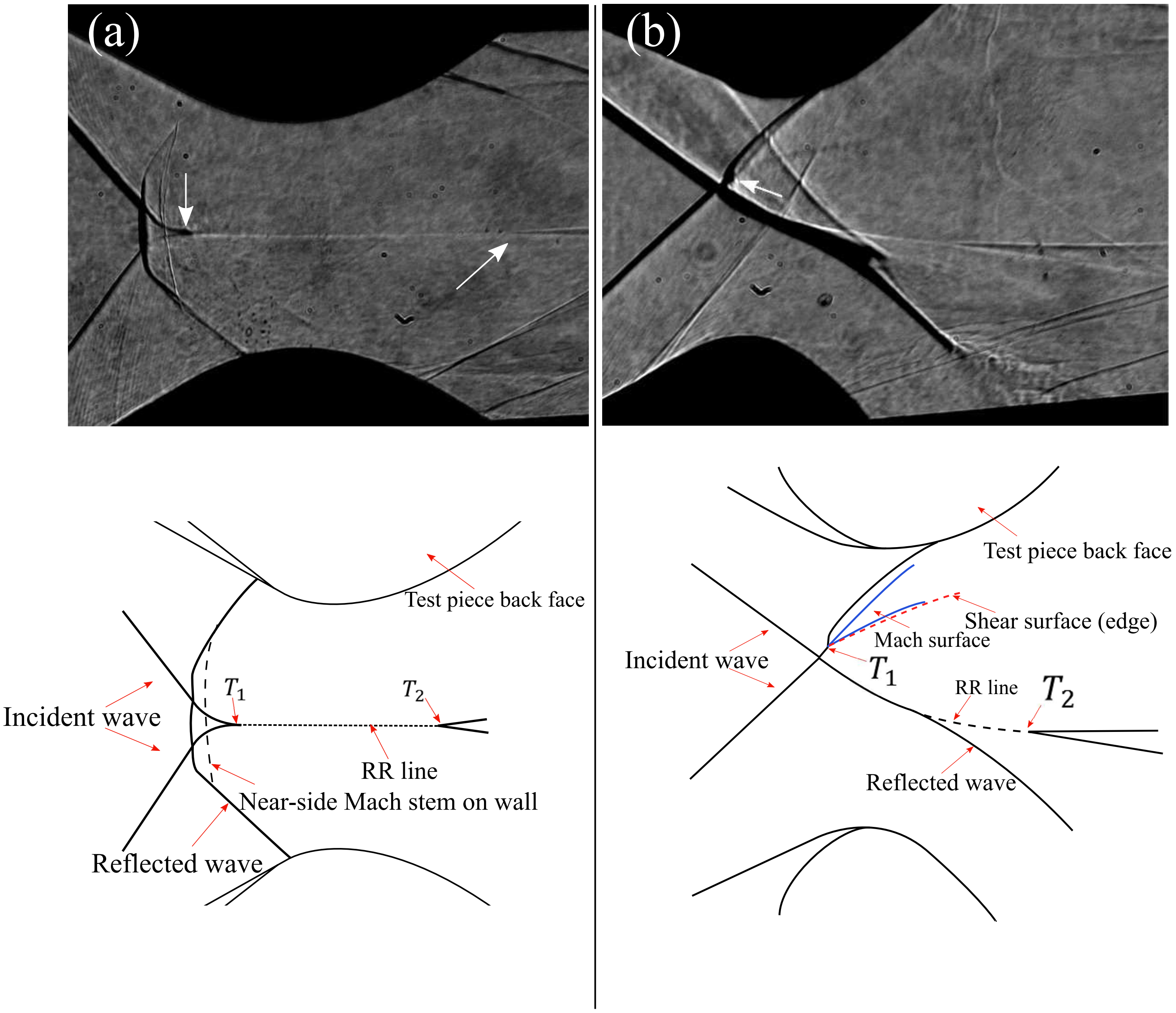

Figure 6.29: Evidence of sweep cusp from oblique shadowgraphs (sketches included at the bottom) with yaw ($\lambda$) and roll ($\phi$) for $M_1 = 3.4$. (a) $\lambda = 40°$, $\phi = 0°$; (b) $\lambda = 25°$, $\phi = 5°$. The white arrows on each image indicate the observed transition points.

The intersection line visualised as a numerical shadowgraph is isolated from the rest of the CFD solution data and is shown in Figure 6.31 at the same optical orientation as Figure 6.29b.
The slight distortion on the intersection line can thus be seen in the numerical shadowgraph (circled). However, there is no clear evidence of the cusp on the far-side transition point $T_2$ in the experimental images for example, at the right-hand arrow on Figure 6.29a. This may be due to interference from the shear surfaces being superimposed onto the image and thus obscuring the field of view. It would be an interesting exercise to rotate the test model configuration by 90° about the longitudinal axis of the tunnel and view the intersection line with the optical system in the datum configuration ($\lambda = 0°, \phi = 0°$). This may provide clearer evidence of the sweep cusp. It should be noted that the cusp feature was not clear to see in the orthogonal shadowgraphs of double-wedge experiments taken by Skews in [8], for which edge effects were intentionally allowed to envelope the the three-dimensional transition points as well as the central core regions of the flow field. However, the bulge at the near-side transition point was very clearly depicted as shown

in Figure 6.32 [16] which provides tentative evidence of the cusp in this type of double-wedge flow field with edge effects.

### 6.2.5 Conclusions

The three-dimensional transition point has been investigated from an analytical, numerical and experimental standpoint. In particular, the analytical flow model has shown that the same sweep angle for the regular and Mach reflection portions on either side of transition is not a physically tenable situation. This results in a sweep cusp in order for the flow compatibility conditions to be satisfied across the transition point. This has been further examined by solving the inverse problem using the model developed - that is, to obtain the sweep along the intersection line based

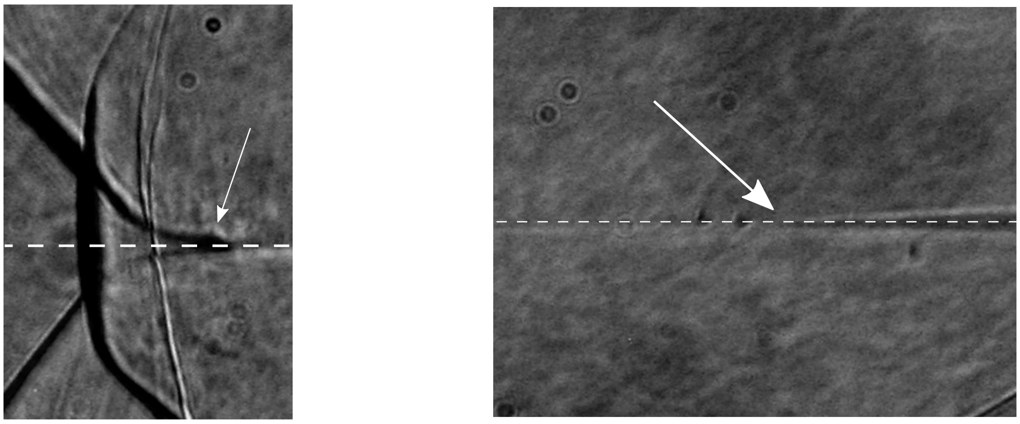

(a) Zoomed view of near-side transition point with bulge indicated with an arrow.

(b) Zoomed view of far-side with transition point indicated with an arrow.

Figure 6.30: Zoomed views of transition points for Model 8, $M_1 = 3.4$, $\lambda = 40°$, $\phi = 0°$. White dotted lines indicate the intersection line on both images.

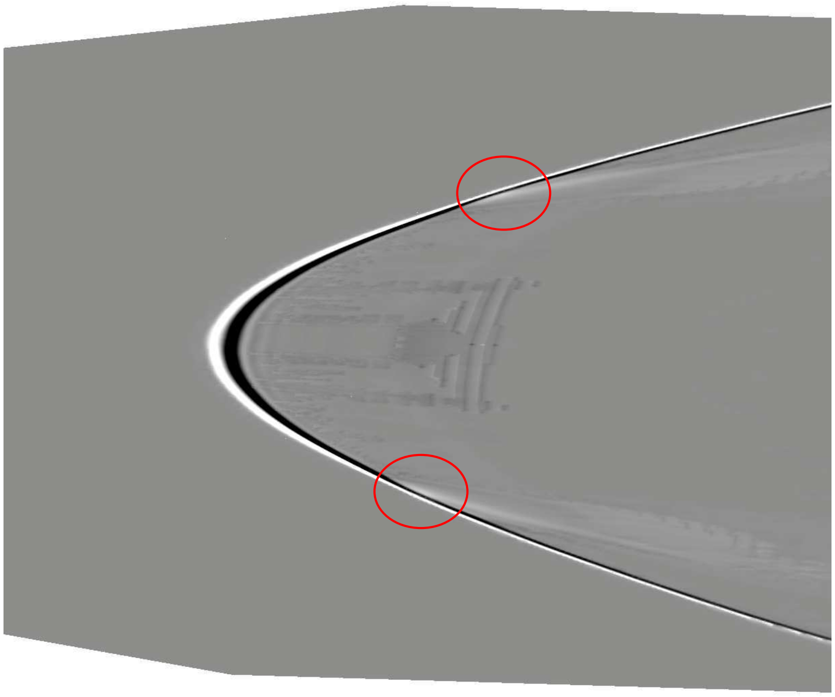

Figure 6.31: Numerical shadowgraph of intersection bow wave viewed at $\lambda = 25°$, $\phi = 5°$.

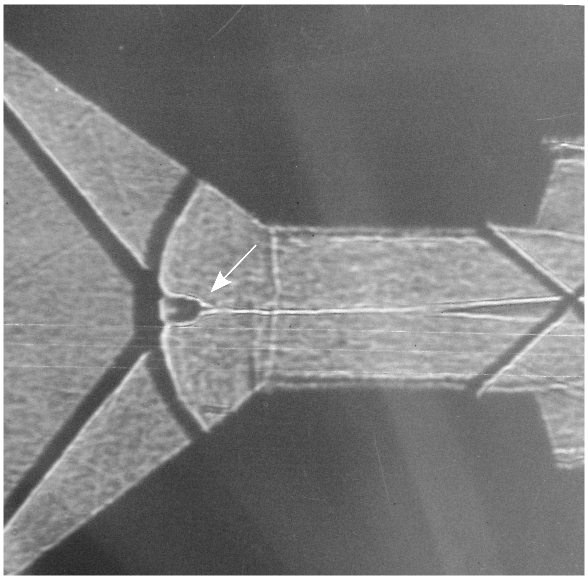

Figure 6.32: Oblique shadowgraph (with $M_1 = 3.1$ and optical yaw $\lambda \approx 45°$ inferred from the work of Skews in [8], $\phi = 0°$) for a finite aspect ratio double wedge configuration with transition points enveloped by edge Mach cones depicting the bulge (indicated with an arrow) at transition more dramatically than for the current results. Image provided by B.W. Skews [16].

on measured net streamline deflections and post-interaction Mach numbers on the horizontal symmetry plane. This has been carried out for all test cases and verified the capability of the model to solve for the sweep cusp. Further evidence of the cusp was given from the experimental images in the form of an optical disturbance at the transition point as well as a bulge for highly-yawed views of the flow field. The latter observation was also noted for finite aspect ratio double wedge setups and points to tentative evidence of a cusp in the presence of edge effects to a greater extent than in flows without them.

# 6.3 The nature of the transition points and intersection line profiles

## 6.3.1 Introduction

This section is dedicated to the analysis of a number of aspects of the three-dimensional flow fields investigated. Consideration is given to the shapes of the intersection lines, the points of transition along them, and the manner in which these vary in shape and location, respectively, for different test model geometries and free-stream Mach numbers. Discussion around the sweep cusp is furthered here as well with a view to understanding its effects on the transverse flow deflections in the vicinity of the transition point downstream of the intersection line. It is the intention of this section to also investigate certain geometrical aspects of the shock system, these being primarily focused on the spread and sweep of the intersection line.

The intersection line is formed by the reflection of the incident bow wave surfaces with the horizontal symmetry plane, as shown in Figure 6.33. The intersection lines considered here are also formed by the intersection of the Mach surfaces with the horizontal symmetry plane, as shown. The reflected waves are omitted here for clarity.

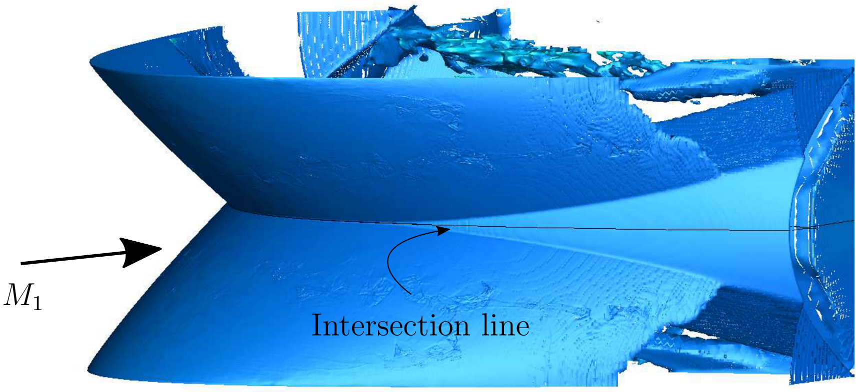

(a) Density isosurface with intersection line shown, Model 8, $M_1 = 3.0$

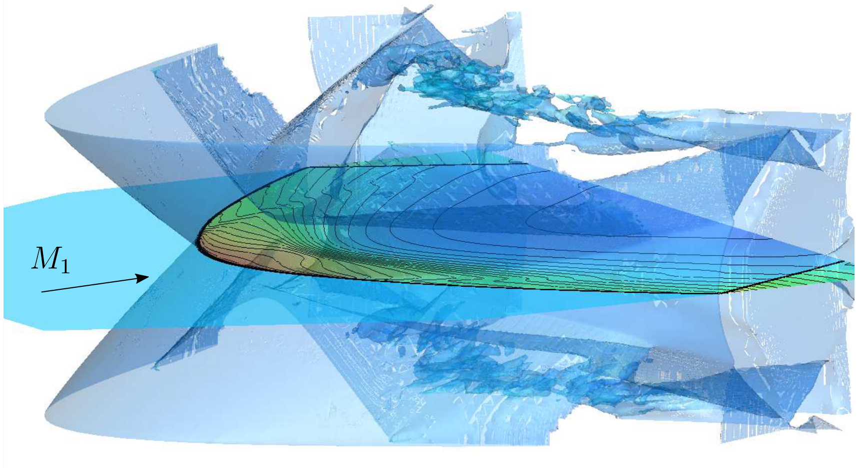

(b) Translucent isosurface with full extent of intersection line shown, Model 8, $M_1 = 3.0$.

Figure 6.33: Illustration of intersection line as formed by reflection of incident bow wave surfaces.

There are two main reasons for paying special attention to the intersection line. Firstly, the point at which the reflection configuration undergoes transition is located on this line at the horizontal symmetry plane. It is therefore instructive to obtain the flow properties and investigate the flow physics surrounding this region. This idea was used as the basis for demonstrating the existence of the sweep cusp in Section 6.2, and can be further used to understand other physical aspects of transition based on the fact that it is an idealised surface free of viscous effects and is perfectly smooth, rigid and adiabatic. Secondly, the intersection line provides an indication as to the geometrical nature of the incident shock configurations as a whole as the intersection line sweep and overall form is similar to the rest of the incident bow wave. Having established the usefulness of considering the intersection line, its overall shape and the points of transition along it is next investigated.

### 6.3.2 Effect of free-stream Mach number on intersection line geometry

Figure 6.34a shows the extracted intersection lines for Model 8 at four different Mach numbers in the range $M_1 = 2.8$ to $M_1 = 3.4$. Below this in Figure 6.34b is a zoomed-in region of Figure 6.34a for clear illustration of the difference in transition point locations and intersection line shapes for the different free-stream Mach numbers.

It is seen that higher free-stream Mach numbers shape the incident bow waves such that they sweep downstream to a greater extent than for lower Mach numbers. To understand the physical nature of this, consider Figure 6.35 taken from the CFD data for the cases shown in Figure 6.34. Half of the domain is shown here, with the quarter model having been reflected about the horizontal symmetry plane for each case. The intersection line is shown by the black line density contours on the horizontal symmetry plane. A few $x$-plane slices of the dataset volume are also shown with a reduced opacity for clarity to view the slices further downstream. The location of all slices in space is the same for all datasets shown.

The fact that a the intersection lines are swept further downstream at higher Mach numbers is relevant in that it is not exclusively the shock angles in the vertical $x-z$ planes (termed "actual" shock angles here) that reduce, as will be discussed in Section 6.4, but so do the sweep angles $\beta$. The result is that the weaker nature of the shock surfaces (incident and reflected) for higher Mach numbers gives rise to higher compression of the flow, as evidenced in Figure 6.35 by the higher post-reflection densities for increasing free-stream Mach numbers.

In addition, the net streamline deflection through the intersection line is shown to increase with a decrease in Mach number as per Figure 6.36, which was formulated using the data for streamlines drawn on the horizontal symmetry plane along the regular reflection portion prior to transition. The fractional half-span coordinate $y_f$ is zero at the apex of the intersection line (at the vertical symmetry plane) and unity at the transverse periphery of the domain (the tunnel windows in this case).

The measured data shown in this figure was terminated at the transition point at the left-most point on each curve, after which deflections corresponding to oblique shock theory are relevant for the Mach reflection portion following transition. There is a significant difference in the net deflection for each case, suggesting that the net deflection of the streamlines through a three-dimensional regular shock interaction is highly Mach number-dependent: the extent of the transverse component ($y$-component) of this post-interaction flow is markedly larger for lower free-stream Mach numbers. It can be seen that there is a considerable increase in the deflection angle for the

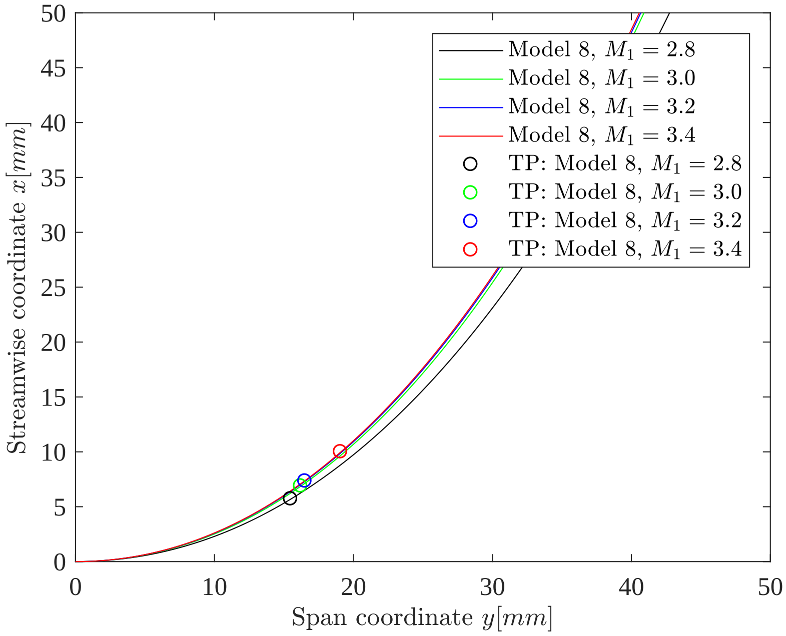

(a) Intersection line shape comparison for free-stream Mach number variation for Model 8. Approximate transition points (TP) indicated with unfilled circles.

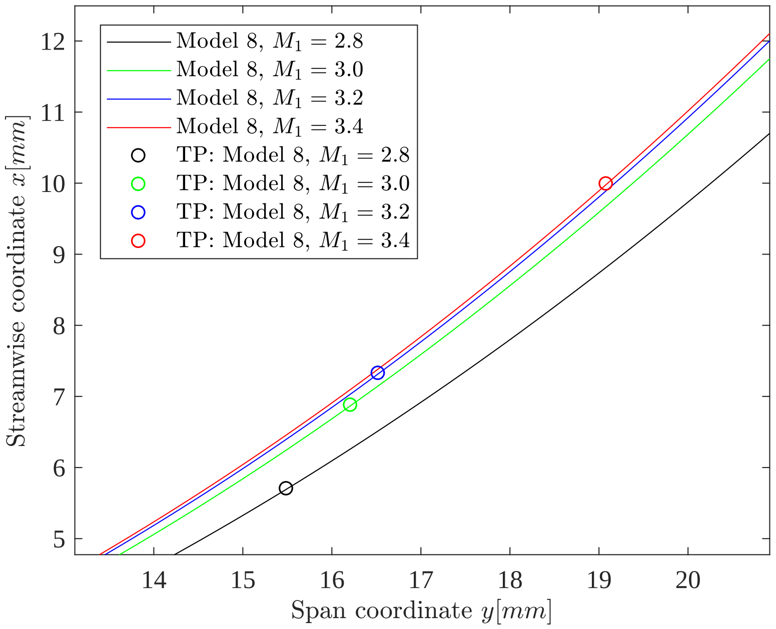

(b) Zoomed-in image of Figure 6.34a showing difference in transition point (TP) locations.

Figure 6.34: Shape of intersection line and transition point locations for different Mach numbers tested on Model 8.

streamlines approaching the transition point from the regular reflection side, as much as a 15° change in net deflection leading up to the transition points. The actual shock angles measured for the same regions along the incident shock surface (shown in the next Section) show that there is not as dramatic a change in such measurements as the transition points are approached as there is for streamline net deflections. This suggests that the net deflection parameter is largely dependent on the sweep of the shock surface, and additionally on the free-stream Mach number, both of which seem to influence the transverse flow components to a greater extent than the shock angles.

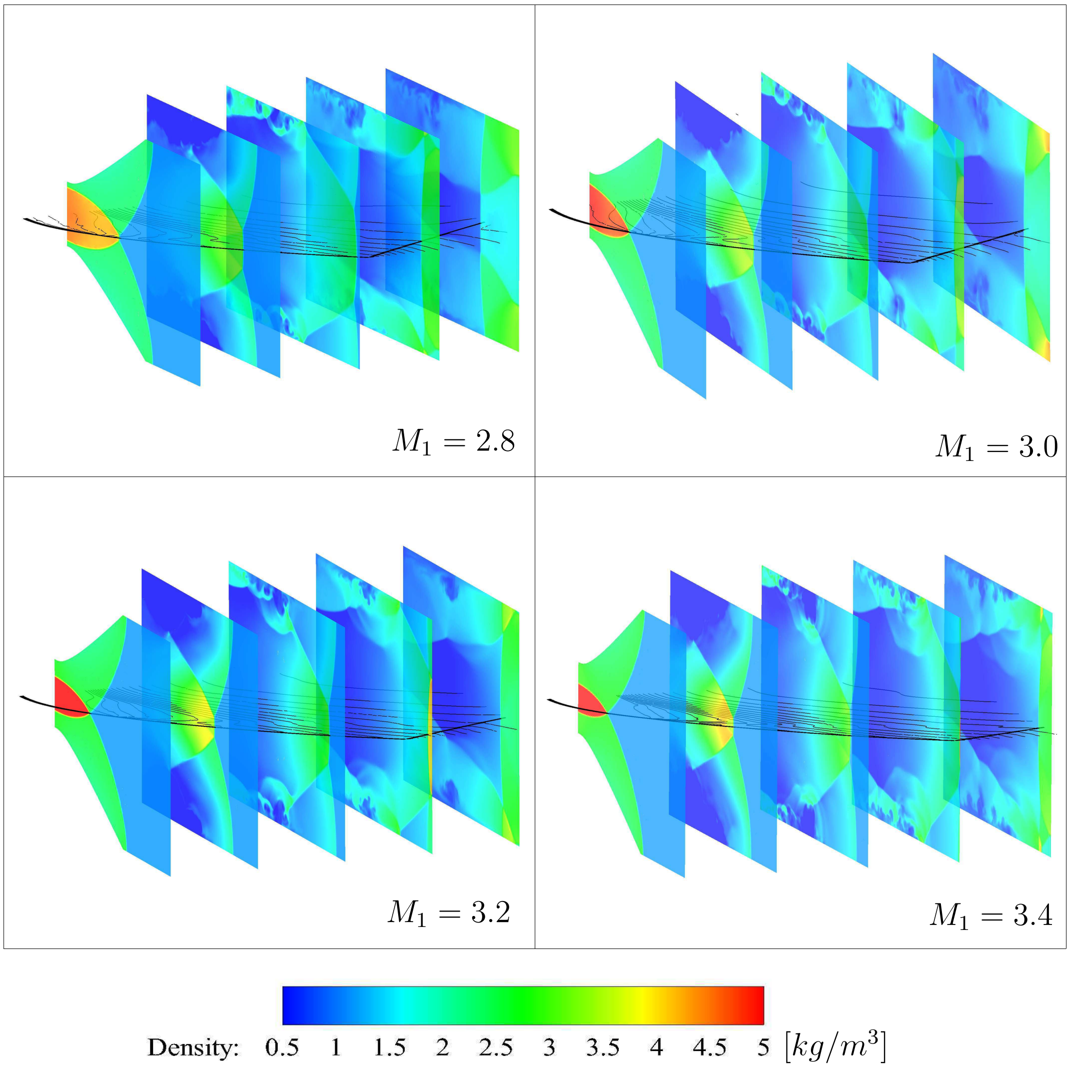

Figure 6.35: Mechanism of weakening of intersection line for higher free-stream Mach numbers. Flooded density contours for $x-$plane slices along the streamwise direction, line density contours on the horizontal symmetry plane depicting the intersection line.

Thus the flow deflections on the regular reflection side have been considered for a variation in Mach number. The deflections on the Mach reflection side following transition are now considered. This is most clearly illustrated by considering the $y$-components of velocity in the plane of the intersection line, as shown in Figure 6.37.

These images are taken for half of the intersection line, with negative velocity components indicating flow in the downwards direction as these images are viewed, meaning transverse defection towards the periphery. The central regions (in the vicinity of $\beta \approx 90°$) are relatively unaffected by sweep and present negligible transverse flow components. Moving outwards along the intersection line, the transverse components gradually increase as the sweep of the intersection line is encountered by the free-stream flow. This continues until transition is reached, at which point interesting effects are noted. There is clearly a large and abrupt increase in the transverse velocity component, starting at the transition points and propagating downstream within a certain bounded region. This region is extended both in downstream length and in span for higher Mach numbers, and is also shown to contain flow with a larger transverse flow component. This sudden

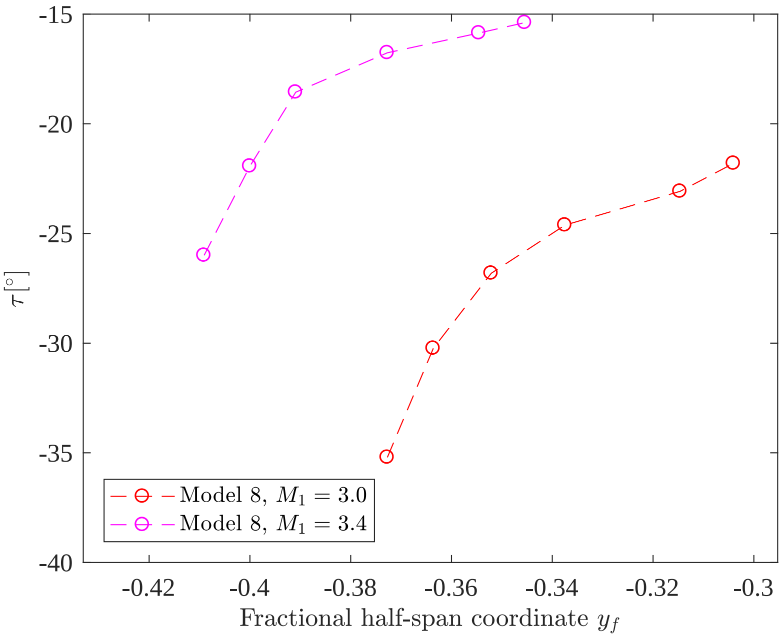

Figure 6.36: Streamline deflection on the horizontal symmetry plane with variation in free-stream Mach number for Model 8. Curves progress from right to left in going from the central regions towards being terminated at transition at the left-most point.

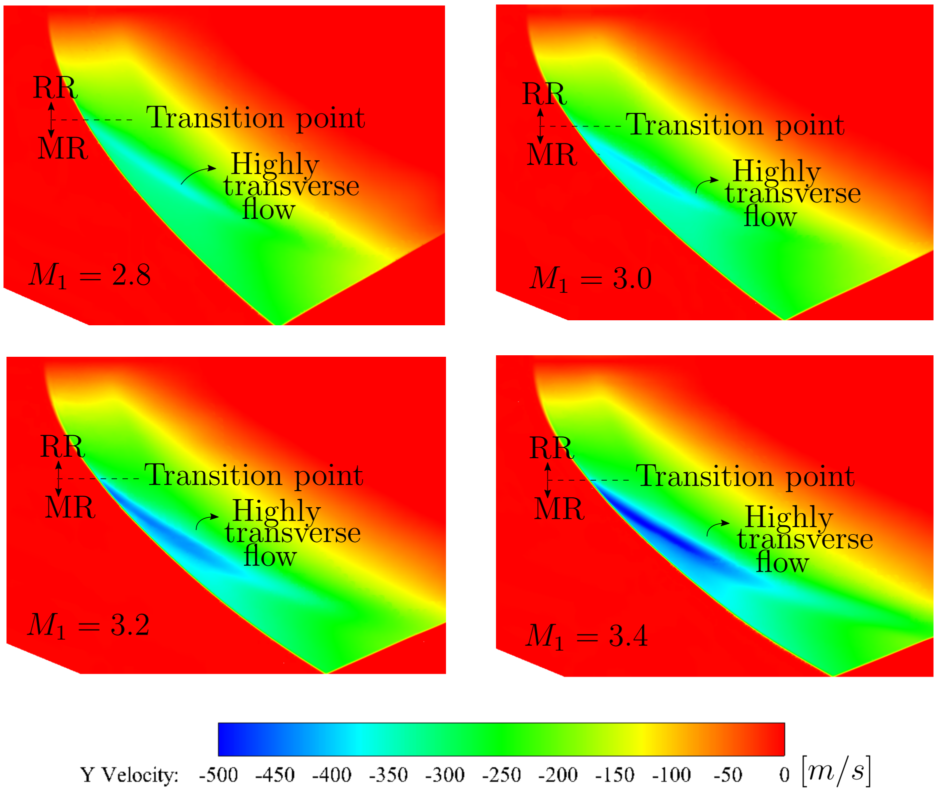

Figure 6.37: Horizontal symmetry plane with flood contours of $y$-component of velocity across the Mach number range for Model 8. Regular and Mach reflection portions are labelled on either side of the transition points, with transverse flow regions as indicated.

change in behaviour corresponds with the change in the nature of the reflection configuration and demonstrates the relevance of the reflection configuration to the nature of the post-reflection flow further downstream. It was shown in Section 6.2 that, for the same sweep angle, the Mach reflection oblique solution and that for the regular reflection portion resulted in significantly different net deflections. This was accounted for by the sweep cusp, existing so as to correct the net deflection on the Mach reflection side to match with that on the regular reflection portion. The extent to which this occurs is seen here in Figure 6.37. At the lowest Mach number of $M_1 = 2.8$, the deflection adjustment is localised to be in the near vicinity of the cusp and transition point, as evidenced by the elongated blue region emanating from the intersection line. This is compared with the case shown for $M_1 = 3.4$ where there is a more severe spike in the transverse velocity component as transition is reached, and this is propagated downstream for a markedly larger distance.

There are two further aspects to consider here. The first is to do with the manner in which the transverse component of velocity increases at transition, and that the extent to which it does demonstrates dependence of the transverse components on free-stream Mach number for the cases shown here. This has a lot to do with the transition cusp, the cusp itself being an adjustment mechanism to the transition in reflection. This aspect will be discussed in a later section dealing with the Mach number and intersection line geometry influences on the nature of the cusp (see Section 6.5). The second aspect, considered here, is the way in which the transverse components vary just after transition and along the Mach reflection region. It is clear that there are greater transverse deflections for higher free-stream Mach numbers behind the Mach reflection portion. This seems to be in contradiction with the aforementioned model of the Mach reflection portion as an oblique shock because the associated lower sweep angles along the intersection line should theoretically give a lower transverse flow deflection behind the intersection line for higher Mach numbers. The physics of this is gleaned from the images shown in Figure 6.37 which shows a sudden increase in the transverse deflection component at transition, which is exacerbated for higher Mach numbers. However, what is important is the recovery rate of the net deflection along the span of the intersection line within the Mach reflection portion, as seen in Figure 6.37. It is clear that this recovery rate is retarded for the higher Mach number cases, as evidenced by the extended blue portion behind the intersection line for the $M_1 = 3.4$ image, whilst for the $M_1 = 2.8$ case, the recovery seems to be almost as sudden as the increase in net deflection at the cusp. It should be emphasised that this is not to say that the net deflection does not coincide with oblique shock theory for the Mach reflection portion, as there is certainly agreement with oblique shock deflections just behind the Mach surface. However, the contours shown in Figure 6.37 do not clearly show this small region in which the initial transverse components immediately behind the Mach surface decrease in going from $M_1 = 2.8$ to $M_1 = 3.4$ in agreement with oblique shock theory. However, when examining a plot of the streamlines in these regions (such as Figure 6.26 in Section 6.2) it was noted that the net deflection along the Mach reflection portion would continue to increase downstream of the intersection line, especially for the higher Mach numbers, thus conforming to what is plotted for the contours of Figure 6.37.

The physical basis for the increased net deflection with an increase in free-stream Mach number is traced back to the deflection adjustment occurring at the transition point. As seen in Figure 6.38 for the same sweep angles on both the regular and Mach reflection sides, the necessary adjustment increases with Mach number, with the sweep cusp becoming a lot more visible for these cases. It is important to state that although the cusp is of greater visibility, and the sweep adjustment increases with Mach number, the intersection line is swept downstream to a greater extent with increases in Mach number nonetheless. The plots of Figure 6.34a show this peripheral sweep variation with Mach number to a high level of accuracy and the curves narrow with Mach number as expected. The flow emanating from the transition point is highly biased towards the periphery of the domain in Figure 6.37, and whilst the flow passing through the oblique portions of the Mach surface undergo a net deflection predicted by oblique shock theory, the highly deflected flow from closer to the transition point acts to deflect this flow more than it already is, so as to cause a region of elevated post-interaction transverse flow deflection. These regions are labelled and indicated in Figure 6.37. That such regions are larger in size and exist along a more extended portion of the intersection line for higher Mach numbers results from the sweep cusp increasing the deflection at transition in these cases. This means that the divergence of the flow at the transition point is greater, which in turn compresses the flow passing through the more peripheral portions of the Mach surface to a greater extent, thus leading to higher deflections further along the intersection line for higher Mach numbers. It is interesting that the weakening of the incident shock surface does not fully counteract the compression effect occurring behind the intersection line. This is an illustration of the post-reflection physical conditions that can occur when there is no clear boundary condition that constrains the flow on the horizontal symmetry plane, thus leading to the transverse components being so strong in the vicinity of transition. It would be interesting to see just how the transition points would be affected should there be a geometrical boundary condition that is directly linked with the generation of an intersection line as discussed here, and along which there is a transition of reflection. This could be a vertical plane surface located closer to the apex of the intersection line than the tunnel walls are in the current setup. It may be that there are other adjustment mechanisms which may be seen in such configurations.

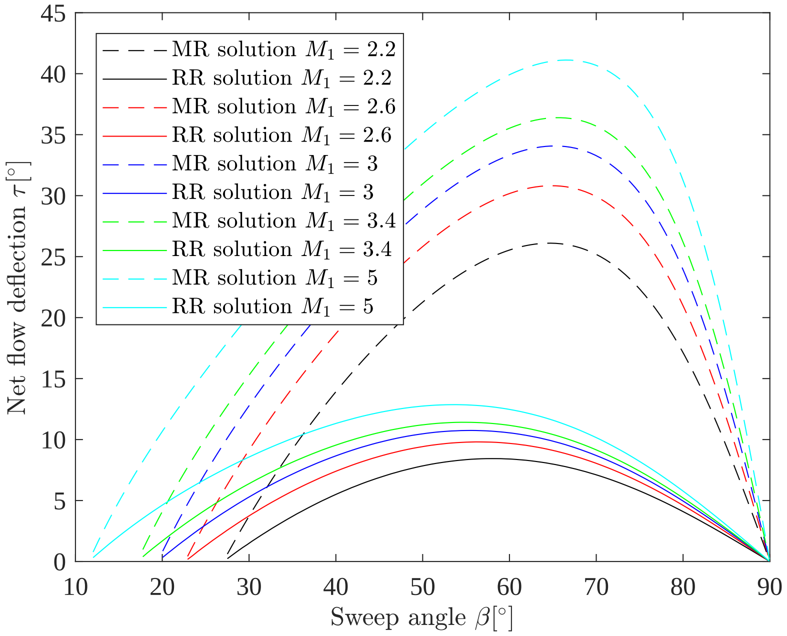

Figure 6.38: Effect of Mach number on net deflection discrepancy for regular and Mach reflection portions with the same sweep angle, illustrating the requirement for a greater sweep adjustment with an increase in Mach number.

### 6.3.3 Mach number effect on transition point location

An important point to take from the previous discussion is that the three-dimensional nature of the flow field allows for an extra degree-of-freedom by which the flow topology may be altered compared to two-dimensional situations. It is seen that the increase in free-stream Mach number results in not only a reduction of shock angles in a streamwise direction, but also in the transverse direction by virtue of the intersection lines being swept further downstream in such cases. These effects shall comprise what will be termed the weakening of the three-dimensional shock system, in the same way as an attached oblique shock on a wedge is weakened by virtue of it being angled closer to the wedge surface for higher free-stream Mach numbers with a constant wedge angle.

This dual-nature of weakening of the shock system is relevant to the locations of the transition points along the intersection lines of each case indicated in Figure 6.34a. This shows the transition points themselves are swept further downstream in accordance with an increase in Mach number. The explanation for this is obtained from Figure 6.39, which shows the various relationships among the shock angles (actual and effective) and the sweep of the intersection line. These are helpful in interpreting the relationships between the three-dimensional shock geometrical parameters.

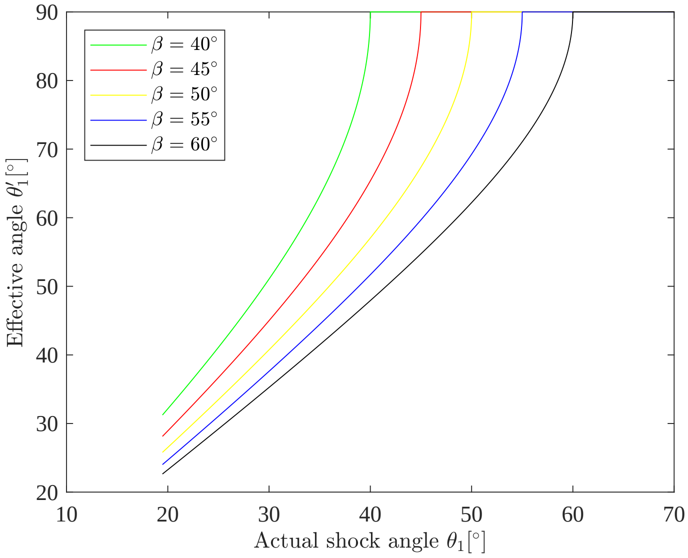

(a) Effect of sweep angle on shock angles (actual and effective).

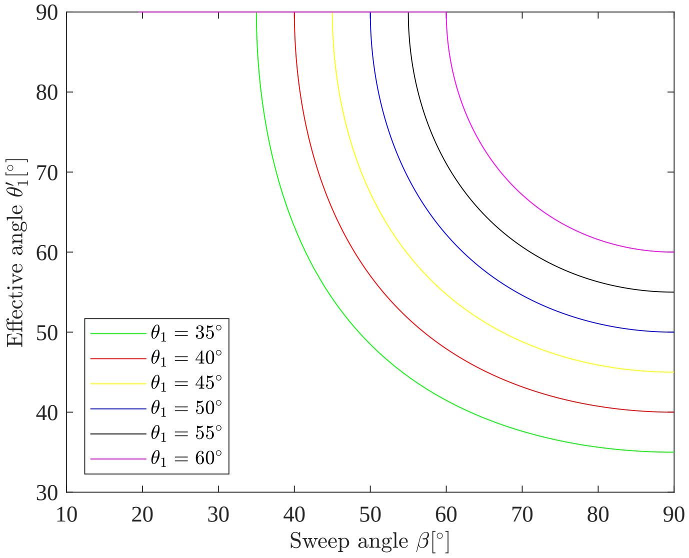

(b) Effect of actual shock angle in vertical planes on sweep and effective angle.

Figure 6.39: Inter-dependencies of actual shock angle, effective shock angle,and sweep.

The weakening of the shock system results in both a lower actual shock angle and a lower sweep angle. It makes understanding the effect of Mach number on the transition point locations more convenient if each mode of weakening of the shock system is considered separately and in succession. As seen in Figure 6.39, the effect of a lower shock angle for a given constant sweep angle, is to obtain a reduction in the effective shock angle. If there is next a decrease in the sweep angle, this counters the previous shock angle effect and acts to increase the effective angle. As previously shown, it is the increase in effective angle that brings about transition. The effect of an increase in Mach number is to reduce the actual shock angle, but the fact that transition is seen to occur at lower sweeps (Figure 6.34a) then this must mean that the sweep is reduced to the extent that it is able to trip the reflection condition and cause transition. This illustrates the dominance of the sweep angle parameter over the shock angle in creating physical conditions that favour transition, and the variation in free-stream Mach number readily shows this.

It is therefore very relevant to investigate the way in which the intersection line sweep angle may be altered in order to address the effects that it may have on the flow field. This was achieved to a limited extent by varying the free-stream Mach number. Larger sweep variations were made possible by testing different models each with a successively wider geometrical spread, which therefore altered the sweep profile of the incident bow wave and the intersection line. The effect of model geometry is discussed next.

### 6.3.4 Effects of model geometry spread

As shown in Section 4.4.4, the back face NURBS formulation for the test pieces gave a measure of spread to the frontal surfaces. The idea behind this was to have the central vertical plane of the model deflect the central flow at the same angle that would theoretically produce Mach reflection in a two-dimensional wedge-type flow field. Therefore, the vertical plane flow deflection angle was set at 24.2° which is well beyond the dual-solution domain for a two-dimensional setup. It was initially expected that the flow over the models with a lower spread would produce a greater relieving effect, such as the flow field over a cone as opposed to a wedge set at the the same half-angle as the cone [18]. It was thought that this relief effect would hinder transition to Mach reflection in the centre-most portions and result in regular reflection for test pieces producing a high degree of relief for the flow between it and the incident shock surface. Hence, the idea of testing models with a wider spread in order to reduce the relief effect in an effort to obtain Mach reflection in the vertical mid-plane.

The dimensions of the test section put an upper limit on the extent to which the models could be spread out in the transverse direction, as a higher spread increased the back face area of the test pieces. This contributed significantly to the blockage effect of both the test pieces and the sting assembly to which the models were attached in the test section. The test pieces used were Models 8, 10, and 11 in order of increasing spread. Two further models were intended to undergo testing and were close but within the area limits for preventing blockage. Unfortunately, blockage effects were encountered with these models due to real flow effects, such as the slight boundary layer growth on the tunnel walls that decreased the effective test section area and thus promoted blockage. Nevertheless, the models that were able to be tested in the wind tunnel gave a good indication of the effects of an increase in geometrical spread. Furthermore, the back face spread increase led to a lower face that was also spread outwards. This meant that the geometrical boundary condition on the incident bow wave surface was altered in a controlled manner. This section gives some indication as to how the intersection line was thus affected as well as the resulting reflection configurations.

The general profiles of the intersection lines for the different models are shown in Figures 6.40a and 6.40b for $M_1 = 3.0$ and $M_1 = 3.4$ respectively. The coordinate axes are transposed to be fixed to the leading (apex) portion of the intersection line.

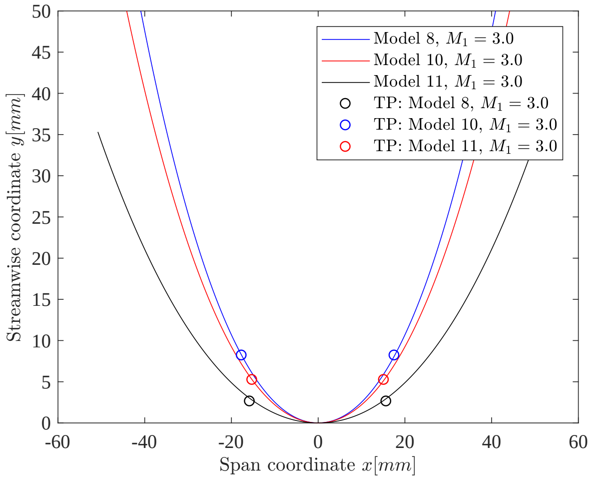

(a) Intersection line profiles, $M_1 = 3.0$

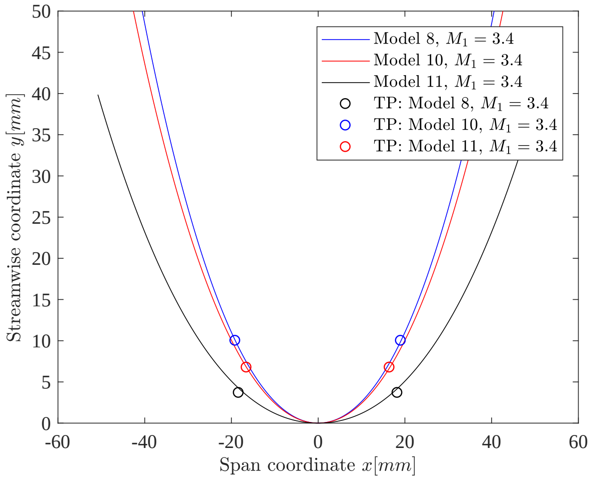

(b) Intersection line profiles, $M_1 = 3.4$

Figure 6.40: Intersection line profiles for various model geometries at $M_1 = 3.0$ and $M_1 = 3.4$. Approximate transition points (TP) indicated with unfilled circles.

It is clear that the effect of a greater spread is to widen the intersection line, this effect being independent of the Mach numbers shown here. This means that the effect of increasing the spread of the lower face of the test pieces increases the spread of the incident bow wave to the extent that the spread of the intersection line is affected in the same way. This illustrates the effect of the change in geometrical boundary condition for the flow field at the lower face of the model. This is expected in the same way that a two-dimensional oblique shock angle is expected to increase upon encountering an object that imparts a greater flow turning effect to the free-stream. The details concerning the implications of this are now examined from a physical standpoint using Figure 6.41 which shows coloured contours of the transverse velocity component (in the $y$-direction) along the incident shock surface for various cases. A very clear trend is that there is an overall increase in the transverse flow components when models with a higher spread are used. There is also a change in the region containing a transverse component close to zero (i.e. the central flow region), which increases with model spread as seen by the red central region in each figure. This shows that the idea to reduce central flow divergence by introducing a spread for the test models was successfully realised from these results. What is even more notable is the encroaching of a highly divergent region from the peripheral sections of the incident wave surface (i.e sections

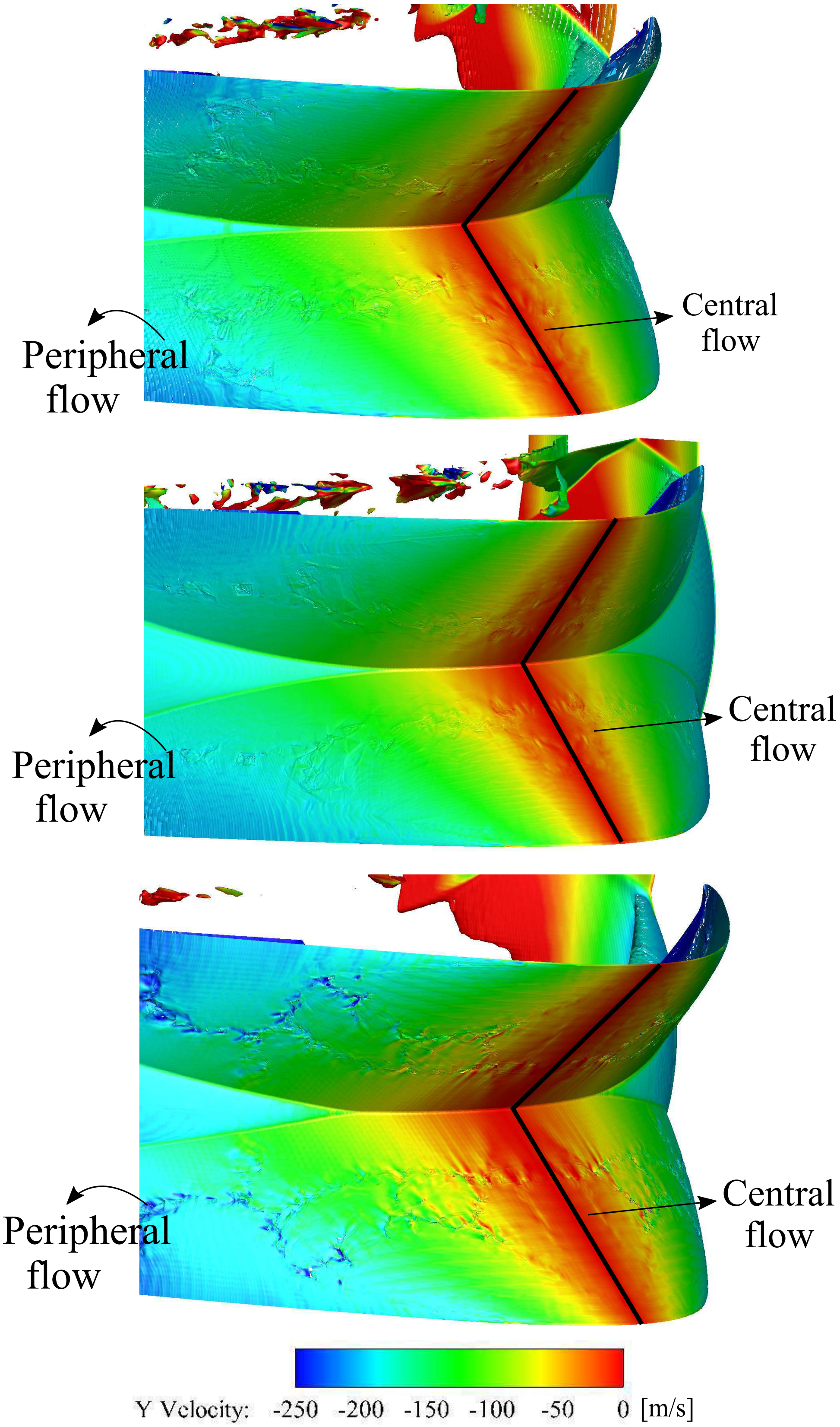

Figure 6.41: Transverse flow components at $M_1 = 3.0$ on shock iso-surfaces for Models 8, 10, and 11 (top, middle, and bottom respectively). Negative values of velocity depict flow moving away from the vertical symmetry plane towards the periphery. Shock intersection at vertical symmetry plane shown with solid black lines on incident wave surfaces. Central and peripheral flow regions are as indicated.

on the incident wave below the Mach surface portions) for the images of Figure 6.41. These are labelled as peripheral regions. Their encroachment is a consequence of the overall flattening effect of the incident wave relative to the free-stream with increased spread. The reasons for the encroachment of regions of highly diverted flow towards the central portions are attained by examining Figure 6.42. It is first important to note that the regions in which the flow experiences

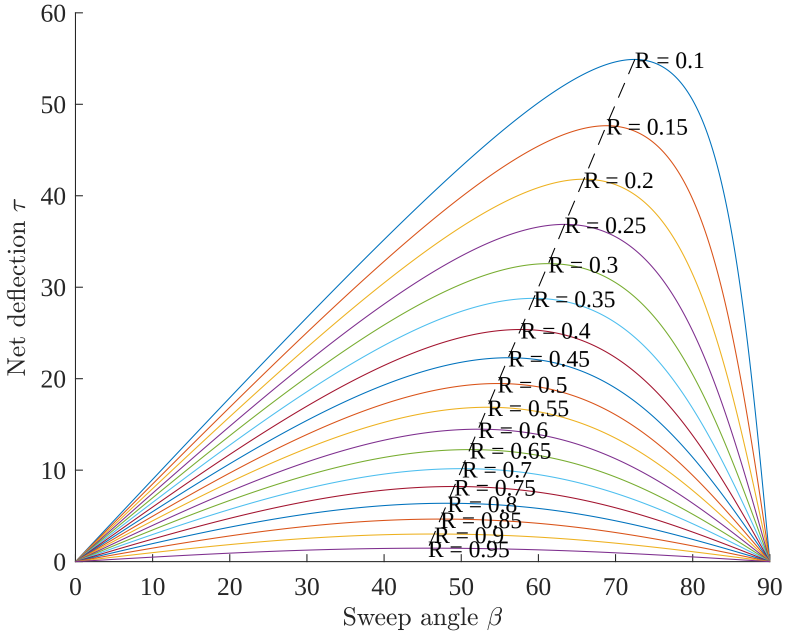

Figure 6.42: Relationship between sweep angle and net flow deflection angle with variation in velocity ratio across the incident and reflected wave surfaces.

higher transverse components are located towards the periphery, which are regions in which the sweep angle change is relatively small. Another important point to mention is that the peripheral regions possess significantly higher actual shock angles than those regions in the centre and more so for models with a larger spread. This, together with the lower influence (and variation) of the sweep angle in these regions, results in a higher effective shock angle in such regions for models with a larger spread. The analysis can thus be reduced to an effective two-dimensional one by considering only effective quantities. A higher effective shock angle would result in a reduction in the post-interaction Mach number $M_3'$, as per two-shock and three-shock theory. This means that the effective Mach number ratio $\dfrac{M_3'}{M_1'}$ is reduced accordingly, and from Section 6.2 it was shown that this results in a reduction in the effective velocity ratio $\dfrac{V_3'}{V_1'} = R$. From Figure 6.42, it can be seen that a reduction in $R$ returns an increase in net flow deflection $\tau$ independent of sweep angle. Figure 6.42 was formulated without regard for transition from a regular shock intersection to that of a Mach interaction, and the relationships among the various parameters in that Figure may be taken to hold (albeit only qualitatively) even for the Mach reflection portion where only the incident and reflected wave surfaces are concerned (and not the Mach surface nor the shear surface).

The converse of the above line of reasoning can be used to understand the mechanisms behind the transition points being located towards the apex of the intersection line for increased model spreads (Figure 6.40). Figure 6.43 shows the streamline deflections for Models 8 and 10 at two different Mach numbers ($M_1 = 3.0$ and $M_1 = 3.4$).

As mentioned in relation to Figure 6.36, it is also evident here that there is quite a large net deflection variation as the transition points are approached, this being more accentuated for Model

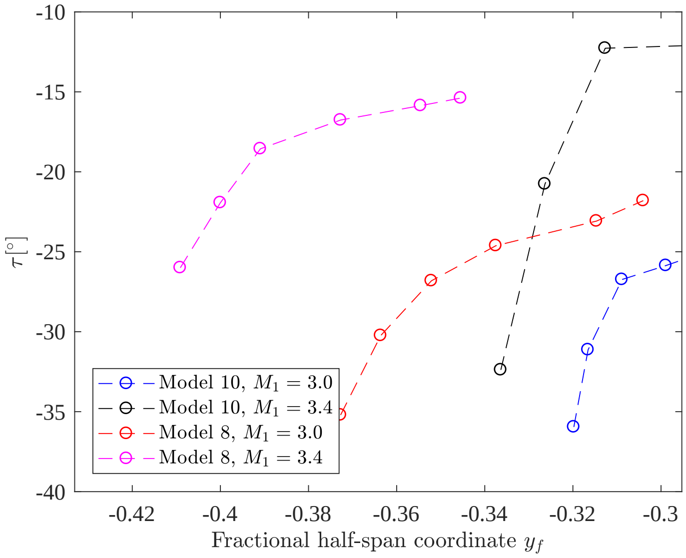

Figure 6.43: Streamline net flow deflections along regular reflection portion prior to transition on the intersection line (same data as Figure 6.36 with Model 10 data added). Curves progress from right to left in going from the central regions towards being terminated at transition at the left-most point.

10 than for Model 8. Additional information about Figure 6.43 is obtained from that provided by Figure 6.44, which shows the spanwise sweep derivative for each of the cases in Figure 6.43.

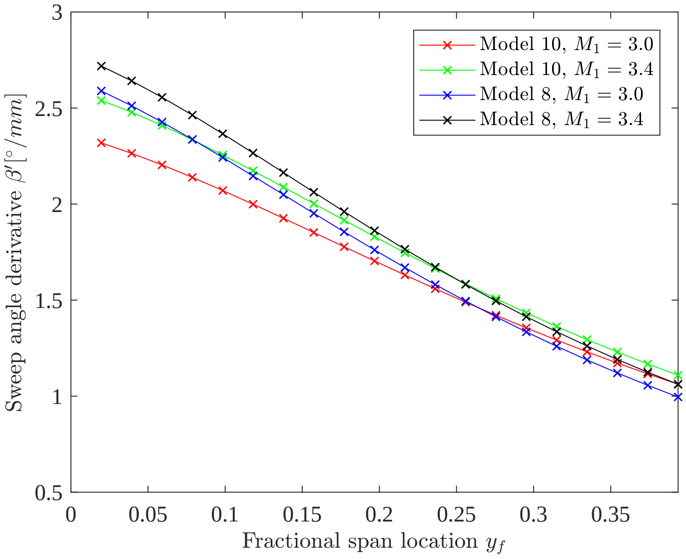

Figure 6.44: Absolute spanwise sweep derivative for Models 8 and 10 at $M_1 = 3.0$ and $M_1 = 3.4$. Curves progress from left to right showing sweep derivative from the central to the peripheral regions.

The fact that the intersection line is swept further downstream for cases with a higher free-stream Mach number is shown clearly in Figure 6.44, where such cases for $M_1 = 3.4$ have a higher rate of change of sweep in the spanwise direction than those cases at $M_1 = 3.0$. Specifically related to transition, however, is the observation that the sweep derivative for the low-spread cases (Model 8) reduces leading up to the transition points and is slightly lower than that in the corresponding regions for the high-spread cases (Model 10). This means that the high-spread cases have a reducing sweep angle that is monotonically decreasing at a higher rate near transition than the low-spread cases. Referring to Figure 6.42, this higher sweep reduction is what causes an increase in the net deflection of the streamlines, with this happening for high-spread cases as seen in Figure 6.43.

Now that the deflection increase for high-spread cases has been identified, its relevance to transition can be explained. The effect of an increase in net flow deflection through the regular intersection of shock surfaces is a decrease in the effective velocity ratio $R$. As pointed out previously, this results in the decrease of the analysis-plane Mach number ratio and since an effective two-shock theory analysis is valid within this plane, this would mean an increase in the effective shock angle. This happens at an accelerated rate for high-spread cases and since the effective angle governs transition, transition is thus hastened for the high-spread cases. This explains the fact that the transition points for each case of increasing spread is located closer towards the intersection line apex as seen in Figure 6.40.

The consideration of the Mach reflection regions in the context of changes in model spreads is very similar to that for free-stream Mach number variations. The net effect on the Mach reflection regions of an increase in spread is the same as that for a reduction in Mach number, which was discussed previously. This illustrates similarity in the effects of the two methods of control (geometrical spread and Mach number changes) over the kinds of three-dimensional flows discussed in this study.

### 6.3.5 Conclusions

Aspects related to the geometry and physical nature of transition have thus been investigated, and it was seen that their underlying phenomena are responsible for an increase in the effective shock angle to the extent that conditions in favour of transition are suitably created. The effect of increasing the free-stream Mach number was shown to elucidate two modes of weakening of the shock system related to the decrease in sweep angle and shock angle. An important finding was the dominance of the sweep angle parameter over the shock angle in determining transition phenomena related to the locations of the transition points and the central flow deflections. Effects of geometry spread were analysed in order to better understand the impact of controlled variation of the test piece geometrical boundary condition. It was seen that the intersection line varied in a similar way to this, with it having a wider spread in accordance with an increase in geometrical spread. It was found that the transition points were located closer towards the intersection line apex for higher spread cases, in addition to an increase in the transverse components of the post-interaction flow with increasing intersection line spread. The results for this section show consistency with the effects of free-stream Mach number on the intersection bow waves and transition points. A clear extrapolation from the observed tendency for the transition points to be located further inwards along the intersection line with an increase in model spread leads to the idea that there is possibly a full Mach reflection pattern that could be brought about with an even greater spread. This is to be discussed in a later section.

In the following section, the increase in effective angle is studied more closely, and in particular its correspondence with two dimensional transition criteria.

## 6.4 Three-dimensional transition and shock geometry

### 6.4.1 Introduction

The primary purpose of this section is to examine the geometry of the shock system at transition, particularly in terms of sweep angle $\beta$ and shock angle $\theta_1$. These parameters are combined to give an effective shock angle $\theta_1'$. With this effective parameter, the visualisation of the three-dimensional shock system is reduced to that within a two-dimensional analysis plane normal to the line of intersection, as described in [6, 34, 37]. Initially, however, the incident shock surface geometry is studied based on the way in which the actual shock angles $\theta_1$ vary along the swept surface profile. Next to be considered is the variation of effective shock angle with sweep. Effects of model geometry spread as well as free-stream Mach number are considered throughout the analyses. Finally, the degree of correspondence of the three-dimensional transition points, to two-dimensional transition criteria is considered with particularly interesting discrepancies found.

### 6.4.2 Incident shock surface angles

Angular orientation is an important aspect of the shock surfaces studied in this work as the angles of the incident shock surface are closely related to the physical mechanisms involved with transition. It is known that the incident shock surface exhibits an increasing angle of incidence in the vertical streamwise planes as it sweeps backwards and downstream. This plays an important role in the transition of the reflection configuration. It is instructive to find out the extent of this angular increase and to assess the effect of model geometry and free-stream Mach number on the configuration of the incident wave. The processing procedures used for the CFD solution data is next described, after which the extracted data is discussed.

Vertical slices were extracted from the CFD data obtained for each of the three models used. These were Models 8, 10 and 11 (in order of increasing spread, respectively). Typical slices extracted are shown in Figure 6.45. Next, a MATLAB Canny edge-detection script was implemented in order to extract the shock waves as white pixels, with the rest of the image shown with black pixels. Edge detection is well-suited to shock geometry extraction as such methods are designed to mask regions of an image for which there is a significant change in image intensity. For the slices obtained from the CFD, these intensity changes coincided with the various shock fronts. The resulting binary image is of the same dimensions and size as the original, but with the regions of large intensity changes marked with white pixels (with a value of 1), and the rest of the image blacked out (with zero-value pixels). Examples of the binary images after edge detection are also shown in Figure 6.45 in the right-hand column corresponding to the slices with filled density contours in the left-hand column.

The incident shock surface appears to weaken for slices further outwards along its span. In these regions the density jump across the incident wave is not as great as that for the central slices. As will be seen later, this is attributed to the reduced peripheral sweep angle, leading to a lower effective incident Mach number which reduces the effective shock strength. Nevertheless, the incident wave shape in this region is readily detected in the binary image which was critical to obtaining important insight into the extent to which the incident wave may have its shock angle increased - far beyond that which would be realisable for weak two-dimensional attached shocks in double wedge experiments.

Tecplot macro scripts were used to extract up to 50 slices per CFD model in order to give approximately one slice per millimetre along the half-span of the flow domain. Each slice was imported

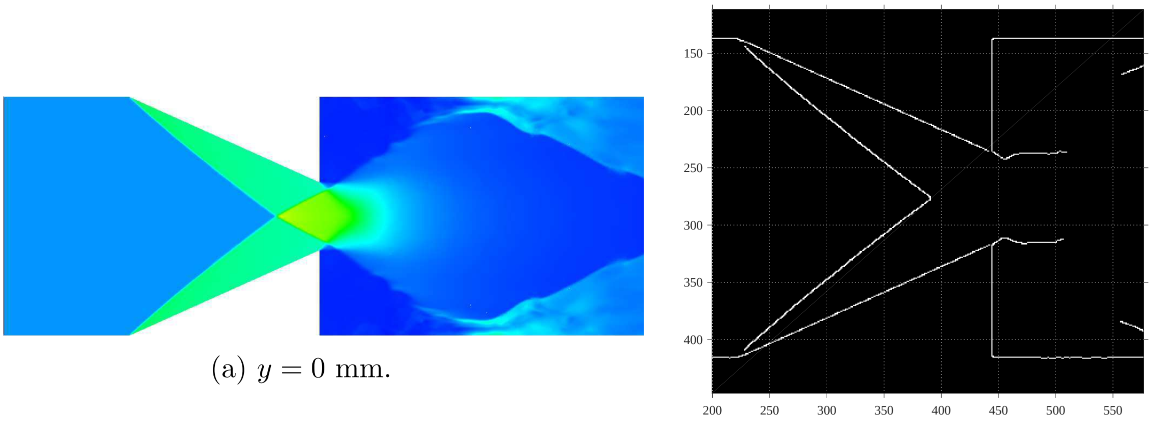

(a) $y = 0$ mm.

(b) Binary image $y = 0$ mm.

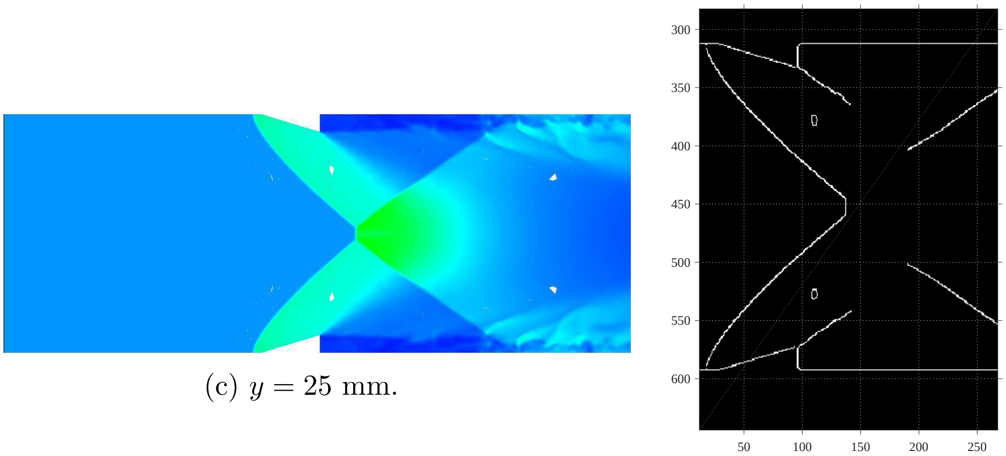

(c) $y = 25$ mm.

(d) Binary image $y = 25$ mm.

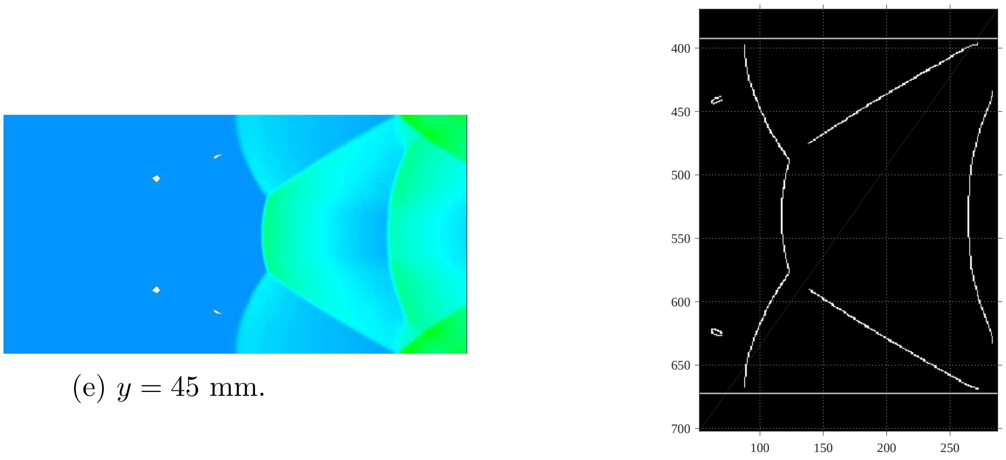

(e) $y = 45$ mm.

(f) Binary image $y = 45$ mm.

Figure 6.45: Left-hand column - typical examples of vertical slices for shock extraction from dataset for Model 8. Right-hand column - images after Canny edge detection.

into MATLAB and the Canny edge detection algorithm applied to each. The software was written so that the edge detection threshold could be adapted for each slice in order that the relevant flow features would be visible in the binary image. This was especially important for the weaker features seen in the peripheral slices. Following this, the start and end pixels of the shock front were obtained and used as inputs for an edge-following algorithm which traced out the shock front. This was loosely based on the Moore boundary tracing algorithm, which incorporates additional statements to point out when the start point is reached for a second time, thus indicating that a closed boundary has been traced. This is not necessary for tracing a shock wave, and so the algorithm was modified based on the knowledge that only right-running waves were considered and the start and end pixels along the shock were known. Once the shock front was extracted, a power-law curve was fitted and differentiated in order to obtain the angle near the interaction point of the shock front on each specific slice. The results are shown in Figure 6.46 for three cases with $M_1 = 3.0$, plotted for fractional locations of the domain half-span $0.5w$.

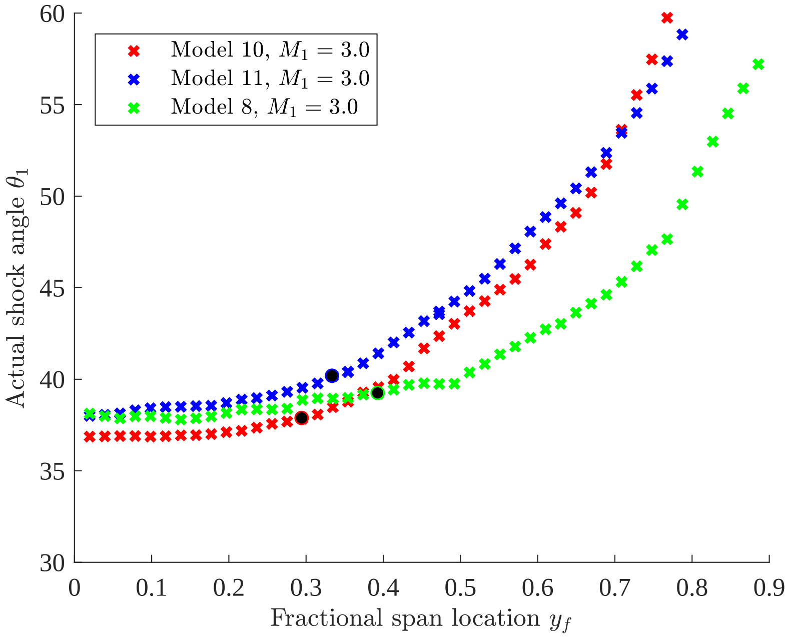

Figure 6.46: Actual shock angles for three different models with a free-stream Mach number $M_1 = 3.0$ measured along the domain half-span. Points of transition marked in black.

It is immediately apparent from these Figures that there is a steep increase in the shock incident angle along the Mach reflection regions. In fact, the incident angles for the regular reflection portion show only a slight increase from that near to the central plane at $y_f = 0$. There is some limiting criteria on the increase in shock incidence angle before transition occurs and, for the cases presented here, this is reached only after a small increase after which Mach reflection ensues. The models with a greater spread show a more pronounced shock incidence angle increase in the regions following transition than those with lower spreads. A consequence of the increased spread of Model 10 relative to 8 and 11 relative to 10 is that the entire incident shock surface is spread out to a greater extent in the transverse direction compared to models with a lower spread (as discussed previously). This in turn increases the transverse flow deflections for larger spreads and, as such, a large quantity of the flow near the central portions is turned towards the periphery. The increasing transverse deflection brought about by the bow waves of the models with a higher spread is counteracted by the steeper angle increase of the shock orientations at the interaction locations. This acts to deflect the oncoming flow to a greater extent in the $z-$ direction for increasing incident shock angles and into the regions in which there is a build-up of flow having been deflected transversely from the central regions.

One final point to mention regarding the shock angle measurements along the incident bow wave is the effect of Mach number. This is shown in Figure 6.47. It is evident that a higher free-stream Mach number results in a lower measured shock angle independent of span location. This phenomenon is analogous to that occurring with two-dimensional oblique shocks but it is interesting to find that the same phenomenon holds in a fully-three-dimensional situation. As noted above, the actual shock angles alone are not enough to fully understand the physical aspects of the three-dimensional flows investigated here. This is further justified by the inconsistencies seen when considering transition angles and their correlation with two-dimensional reflection theory, the former as shown in Figures 6.46 and 6.47. As an example, at $M_1 = 3.0$ the two-dimensional detachment criterion is 39.5° whilst transition at the von-Neumann condition is 37.4°. Therefore, the bow shock sweep angle must necessarily be coupled to the analysis of transition when considering shock angles. It is because of the variation in intersection line profiles of the various cases that the sweep angle needs to be accounted for. This is the foundation for the use of the effective angle, as defined in Chapter 2, Section 6.2.2, Equation 6.3, which reduces the three-dimensional situation into an effective two-dimensional one with sweep and actual shock angles taken into consideration. This is considered in the next subsection.

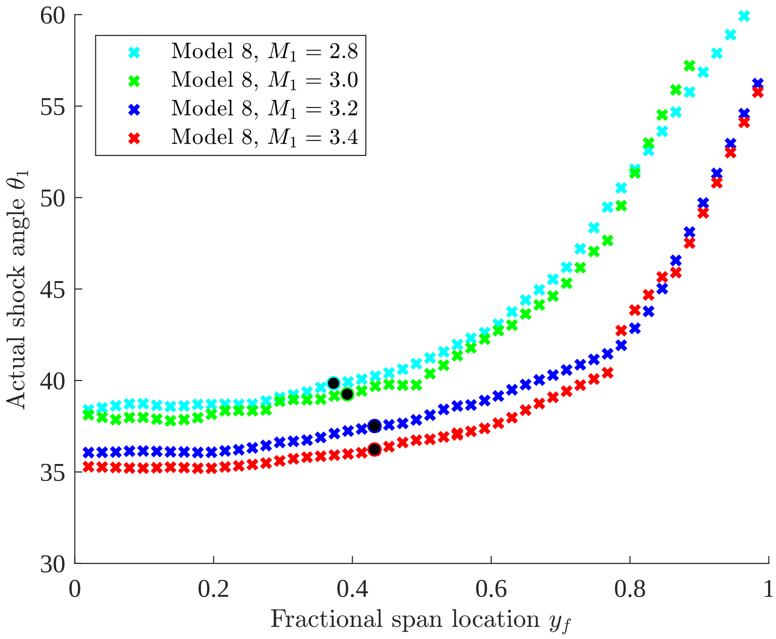

Figure 6.47: Actual shock angles as measured along the domain half-span for Model 8 at different free-stream Mach numbers. Points of transition marked in black.

### 6.4.3 Effective analysis of three-dimensional transition

The measured actual shock angles from the vertical plane slices are transformed to effective shock angles using Equation 6.3. Here, the sweep angle for the intersection line of each model was obtained using the same edge-detection and shock front curve-fitting method used on the vertical slices. These methods were applied to the horizontal symmetry plane. Although each of the cases processed showed evidence of the sweep cusp, this did not alter the bow wave shape severely enough to render the curve fits beyond use for extracting sweep angles along it.

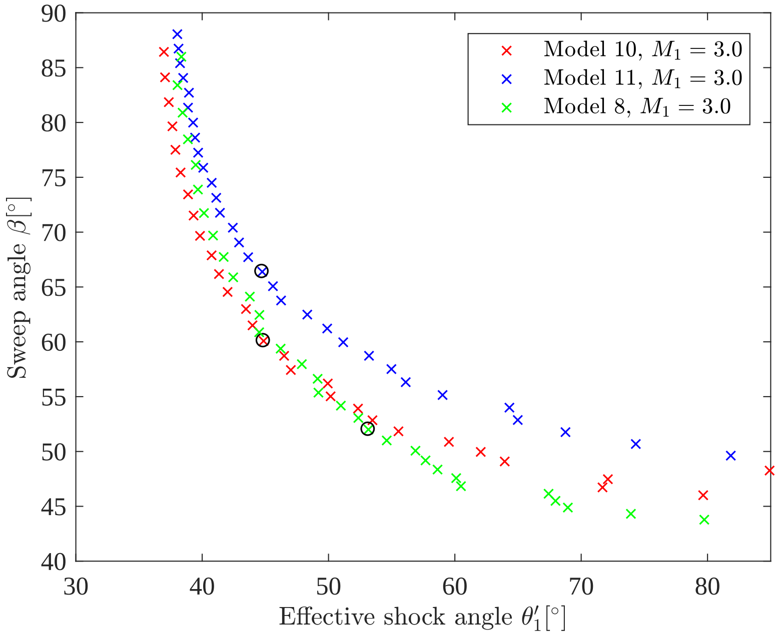

Figure 6.48: Effective shock angles at various sweep locations along intersection line for Models 8, 10, and 11 at $M_1 = 3.0$. Open circles show the points at which reflection transition occurs.

For each set of points shown on Figure 6.48, which includes open circles at the points of transition, it is clear that the effective shock angle increases with a decreasing sweep angle. This was seen for all models at all Mach numbers. Noting that the sweep angle is defined as the angle between the intersection line and the free-stream flow vector, the decreasing sweep along the bow wave acts together with the increasing actual shock angle to result in the increased effective angle. Plots such as these consider the incident bow wave with the central portions located to the top, near a sweep of 90°, decreasing along the sweepback with a corresponding increasing effective shock angle.

What is pertinent here is the effect that model geometry has on the effective angles and the manner in which these angles vary along the sweep of the bow waves. A higher spread of model is seen to increase the rate at which the effective angle increases with sweep along the bow wave. This gives a set of points that form shallow locus for high-spread cases (such as Model 11) in comparison with low-spread cases (such as Model 8). A higher geometrical spread creates a bow wave that is shallow, and increases its sweep angle compared to lower-spread models, for corresponding transverse locations. Importantly, this demonstrates that the sweep angle has more of an influence than the shock angle in determining the effective angle for large sweep angles near the central portions of the flow fields. This has also been indicated previously, where the spatial rate of change of the sweep angle affected the shock interaction to the extent that the transition points were shifted in space when comparing models of different spread. In the peripheral portions where the sweep angle is fairly unchanging, it must be the actual shock angle that comes to the fore in determining the effective shock angle.

It is suggested that the change in the degree to which one parameter has the majority of influence on the effective shock angle occurs at the transition points. These points are circled on Figure 6.48 and for each case there is evidence of the reduced dependence on sweep of the effective shock angle following transition, seen by the way in which the points flatten towards the right of the Figure. This suggestion is also based on the fact that the sweep of the intersection line does not change considerably along its latter peripheral portions, whilst the effective angle does. The fact that the sweep angle along the Mach reflection portions does not exhibit a large variation was shown by the way in which the sweep derivative decreased in a spanwise direction (Figure 6.44, Section 6.3). However, whether the change in influence occurs exactly at the transition point is unfortunately not clearly discernible in Figure 6.48, but does seem to be well-founded considering the points raised in Section 6.3.

A further comparison is shown for Model 8 at different Mach numbers ranging from $M_1 = 2.8$ to $M_1 = 3.4$ in Figure 6.49. Here, unlike for a variation of geometrical spread, the rate of effective shock angle increase with bow wave sweep is approximately constant across the range of Mach numbers shown - all curves are similar to one another. However, corresponding points for each dataset are located at an increasingly lower sweep and lower effective shock angle. The fact that, on the whole, a lower sweep angle is realised for an increase in free-stream Mach number is in keeping with what was discussed previously regarding the greater extent to which the intersection line is swept downstream for high Mach number cases. It is worthwhile to understand the reasons behind the reduced effective angle that an increase in Mach number produces given that this delays transition to occur further along the intersection line when comparing between the various cases of Figure 6.49. This is fundamentally due to the weakening of the incident bow wave surface as a whole. It is primarily the steep initial sweep reduction occurring for the central regions, more accentuated with Mach number increase, that results in an effective angle offset for the loci of points for each case in Figure 6.49. This is in accordance with what is expected for a two-dimensional oblique reflection study with an increase in free-stream Mach number: the incident shock angle would be expected to decrease in a similar manner to the way in which the effective angle is shown to be offset and reduced as higher free-stream Mach numbers are used in Figure 6.49.

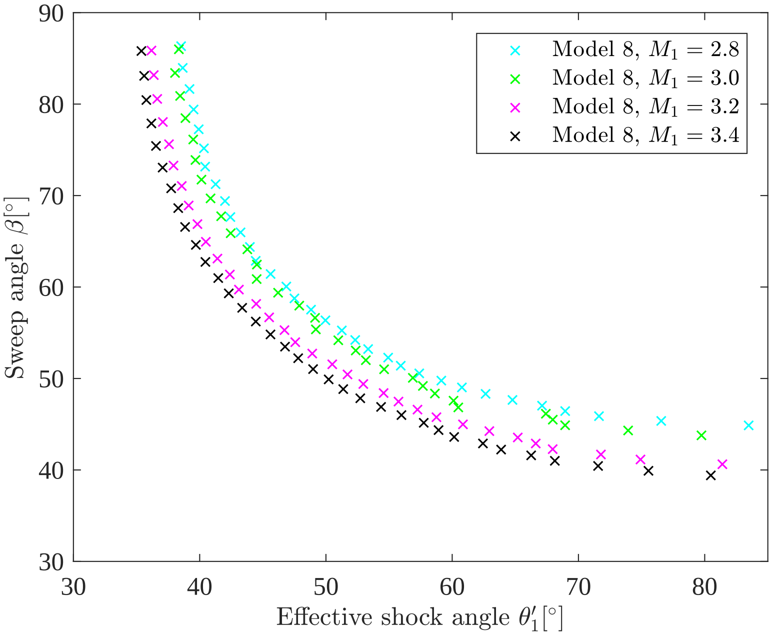

Figure 6.49: Effective shock angles at various sweep locations along intersection line for Models 8 for a range of free-stream Mach numbers.

A further important observation from Figure 6.48 is that the transition points do not match up with the criteria suggested by the theory for planar wave surfaces. This is not particular to these set of results, and was noted for all cases with varying extents of discrepancy. In order to display the following results more economically, the two-dimensional transition criteria were transposed onto the $(M'_1, \theta'_1)$ plane. The effective quantities at transition were calculated from the measured shock and sweep angle data at the transition points for all cases of geometry and free-stream Mach number. The transition points on these data sets were marked as those points just before Mach reflection was first noticed in the image stacks of vertical slices for each case. The transition points given in effective quantities, as well as the corresponding two-dimensional transition criteria are shown in Figure 6.50. The original model point is based on the initial low-spread geometry trial described previously in Section 4.4.4 dealing with model geometry creation.

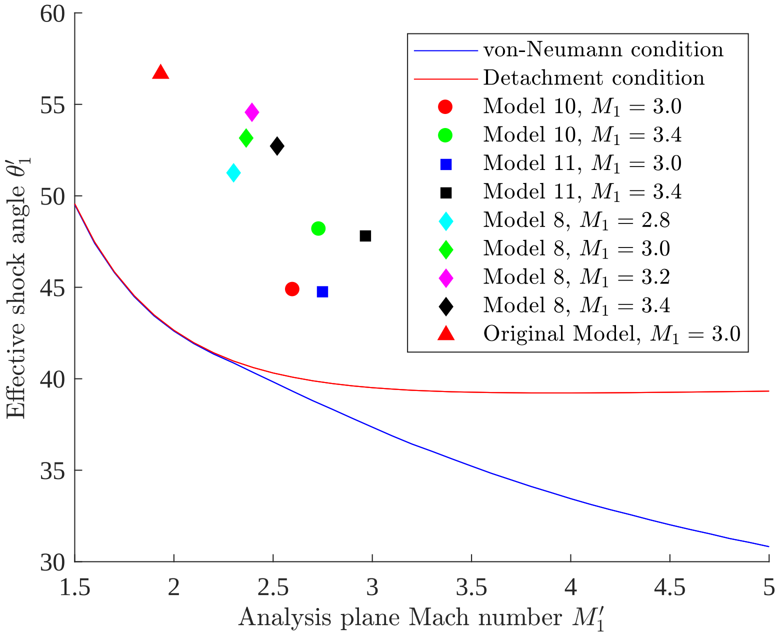

Figure 6.50: Comparison of transition points within an $(M'_1, \theta'_1)$ map with two-dimensional transition criteria shown. Results from the original model concept (see Section 4.4.4) are included.

It is clear that the three-dimensional transition points, although mapped onto effective quantities, exceed the range of the two-dimensional dual-solution domain at the corresponding effective Mach numbers at which transition occurs. This is an important phenomenon as it shows that regular reflection persists even beyond effective detachment, and the effective shock angle increases to the point where transition conditions are favourable, although delayed to various degrees depending on Model geometry and free-stream Mach number. The latter dependency is examined first.

The effect of an increase in free-stream Mach number seen in Figure 6.50 is twofold. The first is the increase in the analysis plane Mach number. The fact this occurs shows that the increase in Mach number for the range tested here is unable to alter the sweep profile of the incident bow wave to the extent that the effective Mach number at transition is affected to a large extent.

It is the effective shock angle at transition that undergoes a larger change with Mach number that is more pronounced for high-spread cases. This clarifies the reason behind the downstream spatial shift in transition point locations when comparing between the various cases discussed in Section 6.3 in relation to increases in free-stream Mach number. The parameter relations examined in Figure 6.39 in the previous section showed that it required a relatively small change in actual shock angle to effect a significant change in the effective angle for a given sweep orientation, or in regions where sweep variation was not significant. The changes in Mach number for the cases presented here did little to alter the pre-transition sweep profile for each case (i.e., within the regular reflection portion). Sweep angle changes could be considered not to play a major role in shifting the transition points for Mach number variation tests, and therefore transition conditions are brought about by the rate at which the actual shock angle increases along the incident bow wave. The rate of increase of the shock angle with distance from the central regions of the flow field is a lot slower for the higher Mach number cases. This is due to the weakening of the incident bow wave and the location of its surface closer to the test models themselves, in the same way as a two-dimensional oblique shock is weakened in the presence of a high-Mach number free-stream. Therefore, the incident actual shock angle has to increase over a larger span distance in order for there to be conditions conducive to transition to be realised. This is the reason for the downstream shift of the transition points with increase in Mach number. This is also the reason for the higher effective shock angle at transition for the cases of increased Mach number in Figure 6.50.

Th effects of geometry are clear to distinguish in Figure 6.50, which show well-defined clusters of points for each Model. Note that the results for the original low-spread concept model are included for comparison purposes. The increase in spread seems to return an increase in the effective Mach number at transition and a reduction in the effective shock angle. There are clearly significant differences regarding the effective angle and Mach number for each case of spread, with Models 10 and 11 located relatively close together due to the change in back face spread for these models being less drastic compared to that for Models 8 and 10. As shown previously, the change in geometrical boundary condition affects the incident bow wave profile to a large extent, to the point where the intersection line was seen to also differ significantly for the various cases of spread assessed. Therefore the sweep parameter is most directly affected by the geometry changes undertaken for the models used in this work.

The effect of an increase in geometrical spread (and thereby sweep angle) is a reduction in the effective transition angle, as seen in Figure 6.50, such that higher spread cases seem to have their effective transition points tend towards the two-dimensional detachment line shown. An important aspect of shock reflection is thus demonstrated through the controlled spread increase methodology used in this work. It is thus suggested that, in the absence of edge effects influencing the reflection plane, and with the opening up of the incident bow wave surface to tend towards planarity with increased geometrical spread, the shock system analysed permits transition to occur in the immediate vicinity of detachment. It will be discussed in a later section that, if the incident bow wave is spread to the extent that the spatial rate of incident wave sweep change is low enough along the transverse direction, transition can be made to occur in the vertical mid-plane at the centre of the flow field such that Mach reflection is obtained for all portions along the horizontal symmetry plane.

For now, however, attention must be given to the physics behind the fact that the effective transition angles for the three-dimensional cases significantly exceed those governed by two-dimensional analyses (i.e., the von-Neumann and detachment criteria). This was also noted for the three-dimensional studies in [8] in which the wedge angle (and thus effective shock angle at the vertical mid-plane) was required to be increased to 5° above the detachment condition in order to effect transition to Mach reflection in the central region. The situation encountered here is slightly different in that transition occurs such that it is coupled to the sweep of the incident wave surface, which itself terminates at the reflection plane with an increasing actual shock angle as transition is approached from the regular reflection portion.

The fact that the two-dimensional criteria are exceeded by the conditions in existence at the three-dimensional transition points requires a closer look at the ways in which the effective angle could be increased and yet permit the incident shock to remain physically attached to the reflection plane beyond those angles predicted by two-dimensional theories. This is brought about by a transverse relieving effect. This has to do with the way in which the flow in the central regions is deflected transversely upon encountering the incident swept shock. The deflected flow from the center is then able to compress the flow passing through more peripheral regions of the incident shock surface. The result is a relief effect due to an increase in the transverse deflection of the streamlines passing through the incident wave surface. Note that these considerations are not in reference to what is happening at the horizontal symmetry plane, but rather at horizontal planes away from the symmetry plane and closer to the test model geometry. The result is the weakening of the incident shock surface such that the actual shock incident angle (especially near the horizontal symmetry plane) is reduced compared to what it would be in the absence of these relieving effects. Since the lower face geometrical boundary condition dictates the sweep profile of the incident bow wave to a large extent, the sweep angle is continually decreasing leading up to transition. This, coupled with the relatively small increment of the actual shock angle at successive transverse locations along the incident bow wave from the centre outwards, means that the effective angle increases well beyond that predicted by two-dimensional analyses. The discrepancy with two-dimensional theories is even more pronounced for bow wave surfaces that are further closed, as opposed to being flatter and open for high-spread and low Mach number cases. This is what accounts for the transition conditions for Model 11 at $M_1 = 3.0$ to tend towards being in agreement with the detachment condition.

### 6.4.4 Conclusions

Three-dimensional shock geometry has undergone further consideration in this section with particular emphasis on shock orientations along the incident shock surface. Effects of Mach number and geometrical spread were considered, both of which provide important free-stream and boundary conditions on the resulting shock configurations respectively, as well as those realised in the analysis planes. Further to this, it was important to investigate the extent to which the three-dimensional transition points differed in effective shock orientation and effective Mach number to those predicted by standard two-dimensional theories (using the von-Neumann and detachment criteria). An important realisation was that the cases tested in this work tended to return transition points which approached the detachment condition when there was an increase in geometrical spread and a decrease in Mach number. This was identified to be caused by a transverse relieving effect occurring behind the incident shock surface.

## 6.5 Flow structures in the surrounds of the transition points

### 6.5.1 Introduction

Shear surfaces are physical phenomena that result from a difference in thermodynamic states of a fluid in the regions on either side of such a surface. In the more common two-dimensional situation, a shear layer or slipline is seen to form in the Mach reflection configuration (Figure 6.51). This is due to the state of the emergent gas processed by the incident and reflected shocks being different to that processed by the Mach stem alone. As shown in Figure 6.52, the three-dimensional case is also seen to give rise to two shear surfaces on either side of the symmetry plane and the region of Mach reflection extends over a significant portion of the intersection line. The triple point, as it is named for two-dimensional cases, is therefore termed a triple line in three-dimensions and it is along this line that each shear surface is generated. For reflection configurations that incorporate both regular and Mach reflections, the initial edge of the shear surface (see Figure 6.52) is propagated from the confluence of two different reflection types on the intersection line. The point at which the edge of the shear surface starts corresponds to the transition point $T$ as previously defined. From previous sections it is known that there is a sweep difference across this point, leading to the existence of the sweep cusp. After this point Mach reflection ensues along the intersection line, and the shear surface forms with it being attached to the triple lines all along the Mach reflection portion. From its inception at the triple line, the shear surface may have a variation of curvature along it, depending on the the physical conditions of the fluid on either side

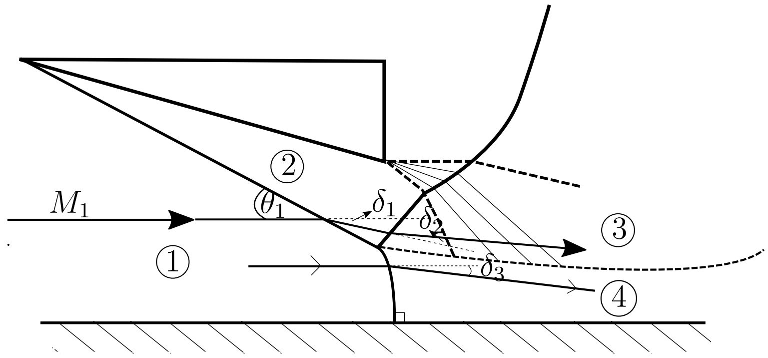

Figure 6.51: Two-dimensional Mach reflection configuration with shear layer emanating from the triple point (shown as a dotted line).

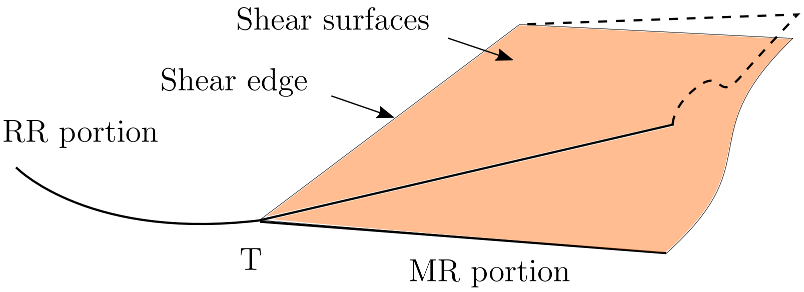

Figure 6.52: Schematic representation of shear surfaces with edge emanating from transition point $T$. Lower shear surface is coloured orange and the outlines of the upper surface are dotted as shown. The shear surface edge is as indicated.

of it. In this subsection, the nature of the edge of the shear surface will be explored, after which attention will be turned to the nature of the shear surface as a whole in conjunction with the Mach surfaces in the next subsection.

### 6.5.2 Shear surface edge trajectory

The edge of the shear surface gives an idea of the conditions on either side of the transition point, that is, for the different reflection configurations in the vicinity of transition. This is the portion of the shear surface that is simultaneously located at the horizontal symmetry plane as well as on the border of the Mach reflection region. This edge therefore gives a good idea as to the variation of streamline deflection and other physical conditions on the horizontal symmetry plane in the vicinity of transition in the absence of edge influences. The shear layer edges were extracted from the CFD solution data using the streamline that followed this edge most closely. Positional data for the shear layers for various cases are shown in Figure 6.53, grouped based on free-stream Mach number and geometry spreads. These figures do not necessarily depict the direct influence of free-stream Mach number and geometry on the shear layer edge trajectory. Rather, the effect of the intersection line profile and the sweep differential around the transition cusp is what is relevant to the nature of the shear surface edges.

The first aspect to consider is the effect of free-stream Mach number on the intersection line and the resulting shear layer edge, as shown in Figure 6.53a for Model 8. It is clear that there is a considerable divergence (in the transverse direction) of the shear layer edge from the central vertical plane. This is seen for all cases in Figure 6.53, and was also noted for double wedge experiments with pitched optics showing a top view of the intersection line in [8]. Some results from oblique shadowgraphs taken during experiments conducted for this work are shown in Figure 6.54 which also show the edge of the shear surfaces having a strong tranverse component on their respective trajectories.

There are two important aspects linked with the compatibility conditions on either side of the shear layer that influence the shape and trajectory of the shear layer edge, and these give insight as to the reasons for the divergence of the shear layer from being straight and to the varying extents to which its trajectory diverges for various cases. The first aspect is the natural tendency for the flow passing through the intersection line on the regular reflection side, and that passing through the oblique Mach surface to deflect transversely due to the sweep of the wave system and in accordance with the model outlined in Section 6.2. In this regard, the shear layer is required to possess a transverse divergence in order to sustain equivalent thermodynamic states across the transition point $T$. This would clearly be impossible should the shear surface edge be straight, for example, due to the unsustainable pressure difference across this shear edge. This brings up the next aspect to consider - that of static pressure equivalence on either side of the shear surface edge. The pressure increase associated with three-dimensional regular reflection is shown in Figure 6.55 for a number of free-stream Mach numbers and for a range of sweep angles. Also shown in this figure is the Mach reflection solution for various sweep angles on the other side of the transition point $T$. The central region containing regular reflection is seen to result in a considerable pressure increase, given that this region has a large sweep angle. For regular reflection configurations at high sweep angles towards the right of Figure 6.55 there is no point on the Mach reflection curve that can result in the same post-reflection pressure for the same sweep. From the foregoing discussions, it is concluded that at such sweep angles equal to that on the regular reflection side transition is not permissible. Only when the post-reflection pressure resulting from regular reflection is able to be matched by an equivalent increase on the Mach reflection curve is

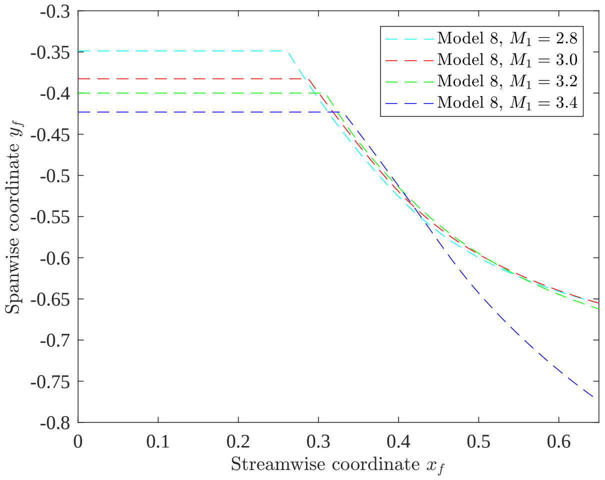

(a) Edge trajectories for Model 8 over the free-stream Mach number test range.

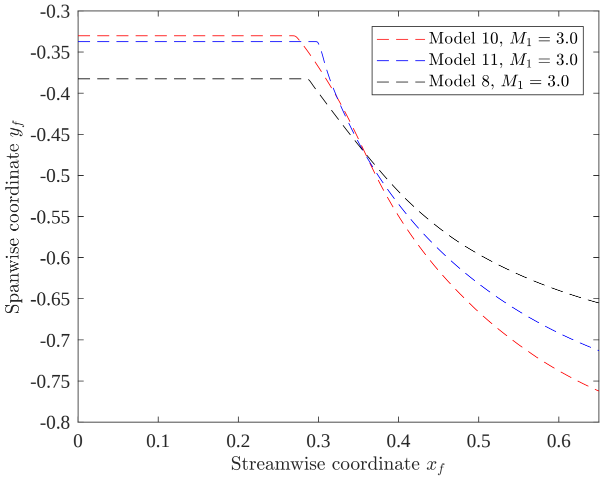

(b) Edge trajectories for various intersection line geometries at $M_1 = 3.0$.

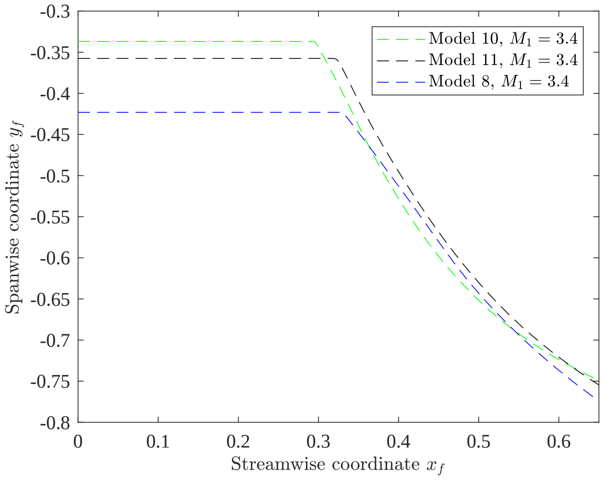

(c) Edge trajectories for various intersection line geometries at $M_1 = 3.4$.

Figure 6.53: Shear surface edge trajectories for various free-stream Mach numbers and test models plotted for a short distance behind the respective transition points on the intersection lines. These plots are shown with the horizontal symmetry plane being observed from a top view. $x_f$ is the $x-$coordinate normalised with the length of the domain (110 mm for all cases) and is zero at the start of the domain 20 mm upstream of the model leading edge. $y_f$ is the $y-$ coordinate normalised with the half-span of the domain (50.8 mm for all cases) and is zero at the vertical symmetry plane.

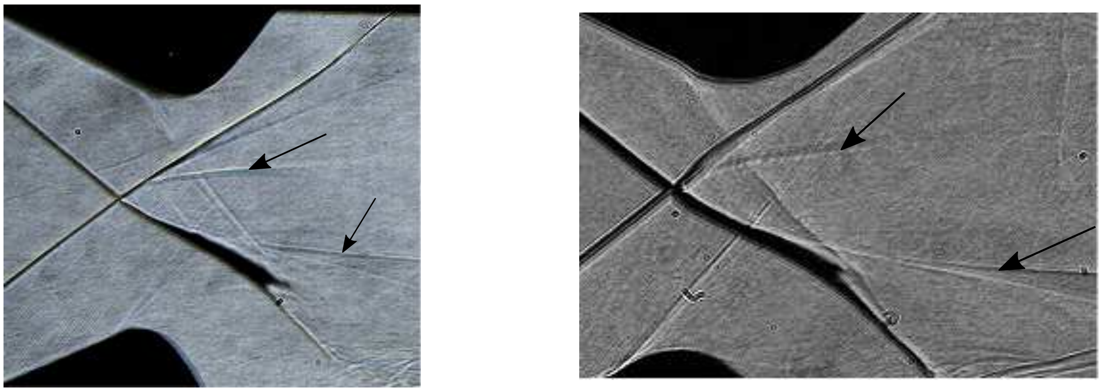

(a) Oblique shadowgraph taken at $\lambda = 15°$, $\phi = 5°$ for Model 8 at $M_1 = 3.2$.

(b) Oblique shadowgraph taken at $\lambda = 15°$, $\phi = 5°$ for Model 8 at $M_1 = 3.4$.

Figure 6.54: Strong transverse components of shear surface edge (indicated with arrows) noted in experiments.

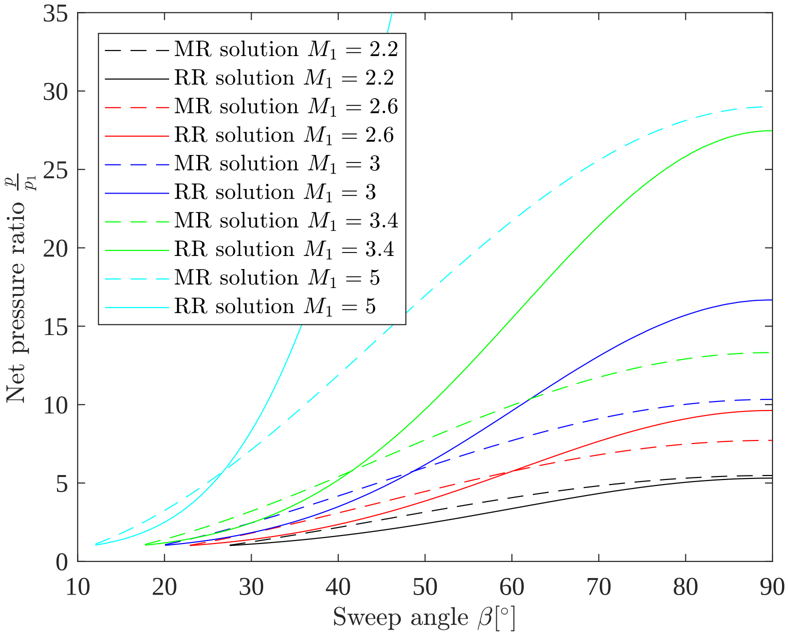

Figure 6.55: Pressure ratio for regular and Mach reflection portions on a three-dimensional swept wave system.

three-dimensional transition permitted. It is clear from Figure 6.55 that matching of pressures on either side of a transition point is not possible without a sweep cusp so that the sweep angle on the regular reflection side is different (and importantly, lower) than that on the Mach reflection side.

Particularly relevant to the shear layer edge trajectories is the situation following the sweep cusp on the Mach reflection side. Here, the sweep angle is again monotonically decreasing, and as per Figure 6.55, so is the post-Mach surface pressure. This therefore demonstrates that the reasons for the transverse shear surface edge trajectory are twofold: first, the pressure increase resulting from three-dimensional regular shock reflection which is coupled with the transverse deflection of the flow due to sweep; and secondly, the pressure drop in the flow on the Mach reflection side away from the sweep cusp which results in additional bias downstream along the shear edge towards the periphery.

An important detail that all plots of Figure 6.53 show is the varying extents to which the different shear surface edges are deflected transversely just after passing through the intersection line. This is an indication of the degree to which the shock systems on either side of the transition point differ in the conditions they create for the post-reflection flow. As seen from Figure 6.55, an increase in free-stream Mach number results in an increased pressure along the regular reflection portion. The implication for the shear surface edge is that it is highly deflected as seen in Figure 6.53a. Furthermore, the higher the central region pressure build-up is, the greater the sweep difference would be between the regular and Mach reflection portions which results in a more exaggerated sweep cusp. The implications of the large sweep difference and the associated deflection of the edge of the shear surface is straightforward to understand when the Mach reflection side is considered. The Mach surface is an oblique shock at the horizontal symmetry plane, and an increase in sweep angle $\beta$ is accompanied by in increase in deflection of the streamlines through this wave. This holds right up until just next to the transition point, and in the limit as the transition point is approached from the Mach reflection side, the deflection through the Mach surface and the edge of the shear surface would be identical for deflection compatibility to hold. Therefore, because a large sweep difference implies a high sweep angle for the initial portion of the Mach surface, this ensures a large divergence in the shear surface edge trajectory. Higher sweep differentials are required at high free-stream Mach numbers, and hence the large divergence of the shear layer edge (especially for $M_1 = 3.4$) seen in Figure 6.53a.

An interesting situation was found for results obtained using Model 11 (see Figure 6.56) for which the required sweep difference was large enough for there to be subsonic flow behind the transition point. For the case of placing Model 11 in a free-stream flow at $M_1 = 3.4$, the flow in the subsonic patches behind the sweep cusp reached Mach numbers as low as 0.90.

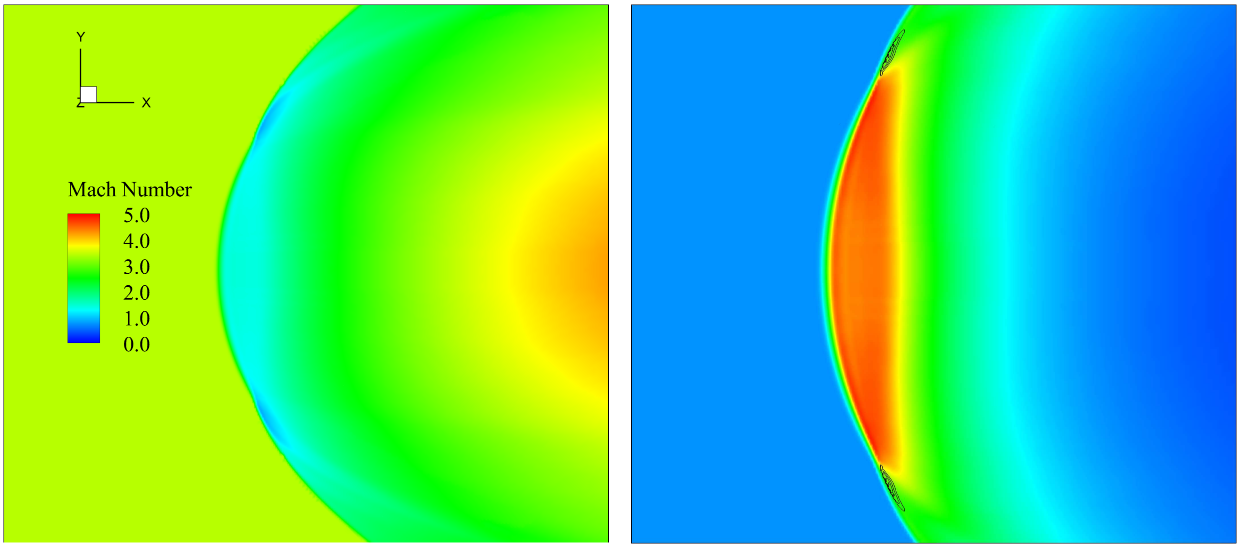

(a) Flooded Mach number contours for horizontal symmetry plane.

(b) Flooded density contours with contour lines for $M < 1$ located just after transition.

Figure 6.56: Phenomenon occurring when the required sweep difference at transition is large enough to render the post-interaction flow subsonic, as shown for Model 11, $M_1 = 3.4$.

The significance of this is that the required sweep difference between the regular and Mach reflection portions across the transition point is large enough to cause the sweep of the Mach surface just after transition to be a strong oblique shock, after which the flow is subsonic. Another important aspect is that the flow deflection on either side of such a transition point, as well as the shear surface edge itself, has a reduced transverse deflection as seen in Figure 6.53c as expected for a strong oblique shock. The strong shock solution persists along the sweep of the intersection line for a short distance before switching back to a weak shock solution with supersonic post-interaction flow.

Figures 6.53b and 6.53c show the effect of intersection line spread on shear surface edge trajectories. Due to the fact that the cases with test models of lower geometrical spread have an intersection line that is swept back further downstream than those of higher geometric spreads, there is not as great an increase of regular reflection portion pressure for low-spread intersection lines (as seen in Figure 6.55 for lower sweep angles). This gives rise to the shear edges for these cases having a shallow trajectory. From these figures, it can also be deduced that these cases have lower sweep differences across their transition points, and that the deflection through the initial portion of the Mach surface following transition is lower for Model 8 compared to Model 10. Model 11 presents a special case in terms of there being a strong shock solution for the Mach surface, and therefore it is seen that the shear edge trajectories for these cases are not as shallow as for Model 8 and not as divergent as for Model 10 at the same free-stream conditions.

### 6.5.3 Nature of the shear and Mach surfaces

The relation between the shear and Mach surface is clear: the geometry of the triple lines which bound the Mach surface is determined by the extent of the the Mach surface height, with the shear surface emanating from the triple lines. In this subsection, focus will be shifted to those regions further towards the periphery of the flow field and within the Mach reflection portion of the shock interaction domain. It is clear from the physical relation between Mach surface and shear surface that the conditions behind the Mach surface would be predicative of the nature of the shear surface. The converse seems to also hold merit by virtue of the fact that the conditions below the shear surface for the flow passing through the incident and reflected waves would have a bearing on the shear surface itself. The geometry of the shear surface therefore influences the nature of the flow behind the Mach surface because of compatibility of flow direction and pressure across the shear surface.

It is important to mention at the outset that the Mach surface was observed to be oriented convex relative to the free-stream flow as shown in Figure 6.57. This is of importance when considering the orientation of the shear surface along the triple lines (discussed later on in this section), but this also gives an overview of the type of surface geometry of the Mach reflection portion on which the following discussion is based.

For two-dimensional flows, the geometry of the slipline is what determines the location of a sonic throat [5], which in turn limits the subsonic patch behind the Mach stem and the region in which transverse influences may affect the Mach stem [8, 11]. The same cannot be said for three-dimensional flows (where there is central regular and peripheral Mach reflection) in terms of the shear surface being responsible for the location of a sonic throat because the flow behind the oblique Mach surface is supersonic.

Plots for the extents of the various Mach surfaces is shown in Figure 6.58 for a number of different cases as projected to be viewed along the span of the intersection line.

The main point about these figures is to show the trajectory of the triple lines which bound the Mach surfaces at the top and bottom, and from which the shear surfaces originate. From Figure 6.58a, it is clear that the higher free-stream Mach numbers resulted in a more gentle (i.e. shallower and flatter) trajectory of the triple lines towards the periphery and consequently a reduced area

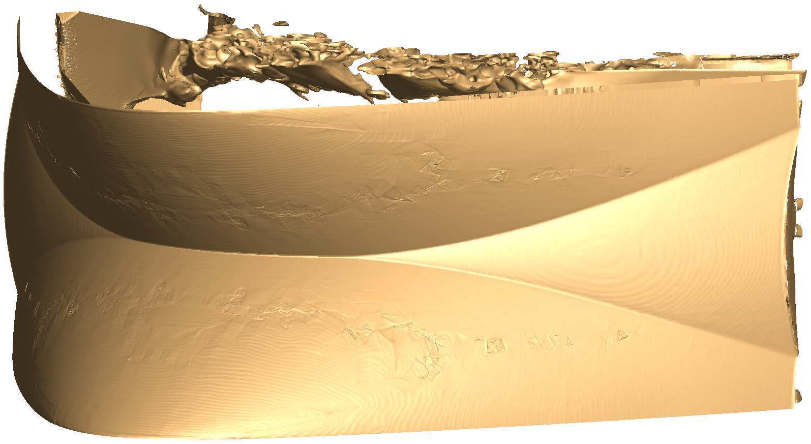

Figure 6.57: Overview of shock surfaces showing the convex curvature of the Mach surface, particularly noticeable to the left of the figure.

of the Mach surface as a whole. This is due to the weakening of the shock system as discussed previously, which in relation to the Mach surface manifests as a reduction in height of this surface compared to cases with lower free-stream Mach numbers.

However, the increase in Mach number does not do as much to alter the nature of the Mach surface compared to the geometry changes of the intersection line, which results from using different model spreads. There is a considerable difference in the triple line trajectory for Model 10 compared to Model 8 in Figures 6.58b and 6.58c. In both cases the intersection line for Model 10 was further spread out than that for Model 8. The difference in Mach surface height shows the extent to which Mach reflection is established on the intersection line. For Model 8 this region is delayed in being established and is so only further outwards and downstream of the apex of the intersection line than for Model 10. The growth rate of the Mach surfaces in the spanwise directions also corresponds with the strength of the peripheral shock system as a whole, with that for Model 8 being notably lower than for Model 10, regardless of free-stream Mach number. In fact, further towards the outermost regions of the domain, the triple lines appear to have a non-linear increasing trajectory which is more exaggerated for intersection lines with a wider spread. This is a consequence of the flatter nature of the incident bow wave. The higher effective Mach number for a larger sweep angle obtained from a wider spread of the intersection line thus leads to a more established Mach surface which accommodates for the increase in divergent flow from the central regions by deflecting more of the oncoming peripheral flow through it.

An interesting aspect to point out from Figure 6.58 is the manner in which the Mach surfaces for Model 11 do not follow the expected trend of an increased height associated with a wider spread of the intersection line. These results indicate that the Mach surface, whilst taller and the triple lines more divergent than those for Model 8, are less so when compared with Model 10. The reason for this is linked to what was observed to happen at the transition points for Model 11 related to the high sweep difference on either side of the transition point such that part of the Mach surface close to this point forms a strong oblique shock. Following this, the Mach surface transitions to a weak oblique shock along the horizontal symmetry plane. The extent to which the peripheral regions are required to accommodate the transverse flow from the central regions is therefore reduced because of the subsonic patch around the transition point which relieves some of the compression experienced by the peripheral flow due to central flow divergence. Therefore, there is not as great a need for a tall Mach surface and therefore the Mach surface heights are

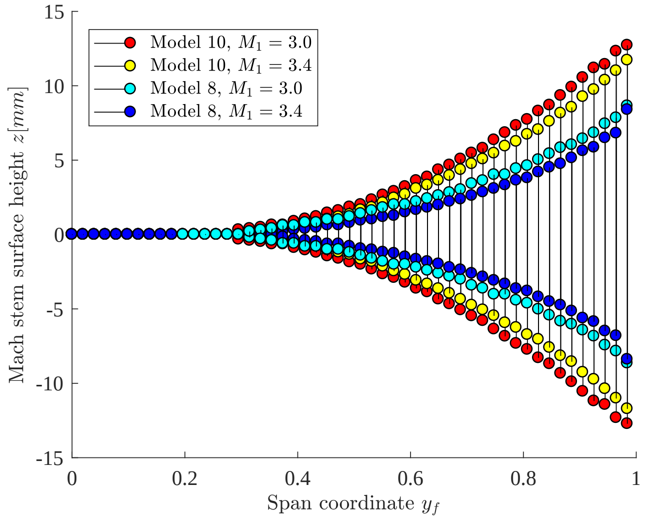

(a) Mach surface height comparison for $M_1 = 3.0$ and $M_1 = 3.4$.

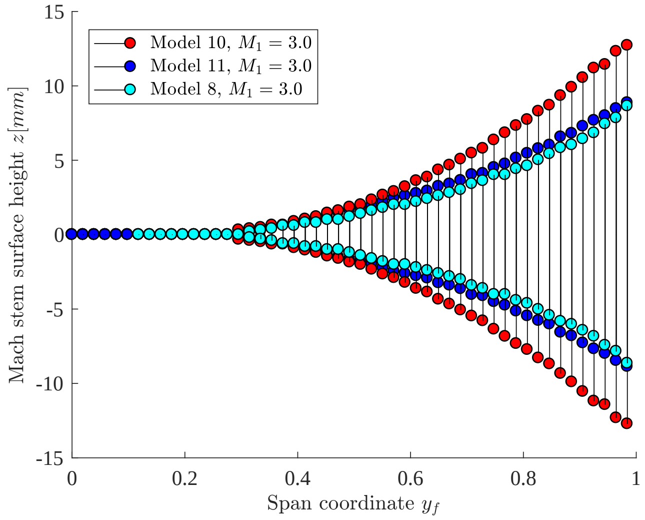

(b) Mach surface height comparison for different models at $M_1 = 3.0$.

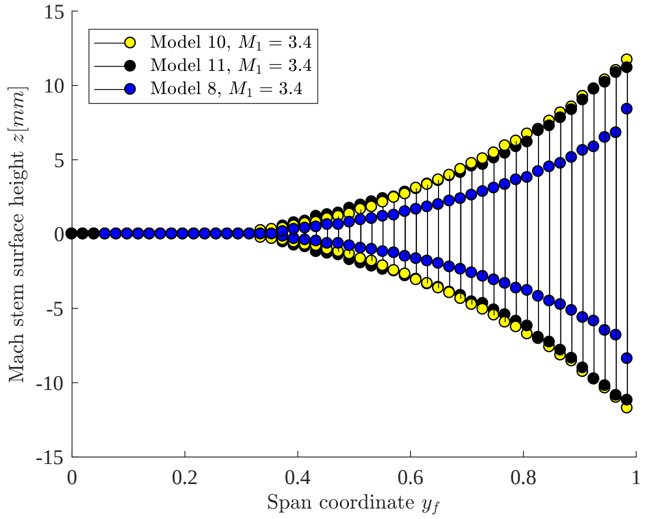

(c) Mach surface height comparison for different models at $M_1 = 3.4$.

Figure 6.58: Mach surface height comparisons along the respective bow waves for various cases.

reduced for the Model 11 cases.

Having examined the Mach surfaces and the various trajectories of the triple lines, it is the next logical step to turn attention to the orientations of the shear surfaces which originate along the triple lines. Again, such surfaces are visualised by extracting the streamlines which travel through points along the triple lines. Their three-dimensional visualisation is made possible by displaying the streamtraces as volume lines (streamtubes) along which $z$-velocity contours are plotted. This is shown in Figure 6.59 for the cases as labelled at the top of each image.

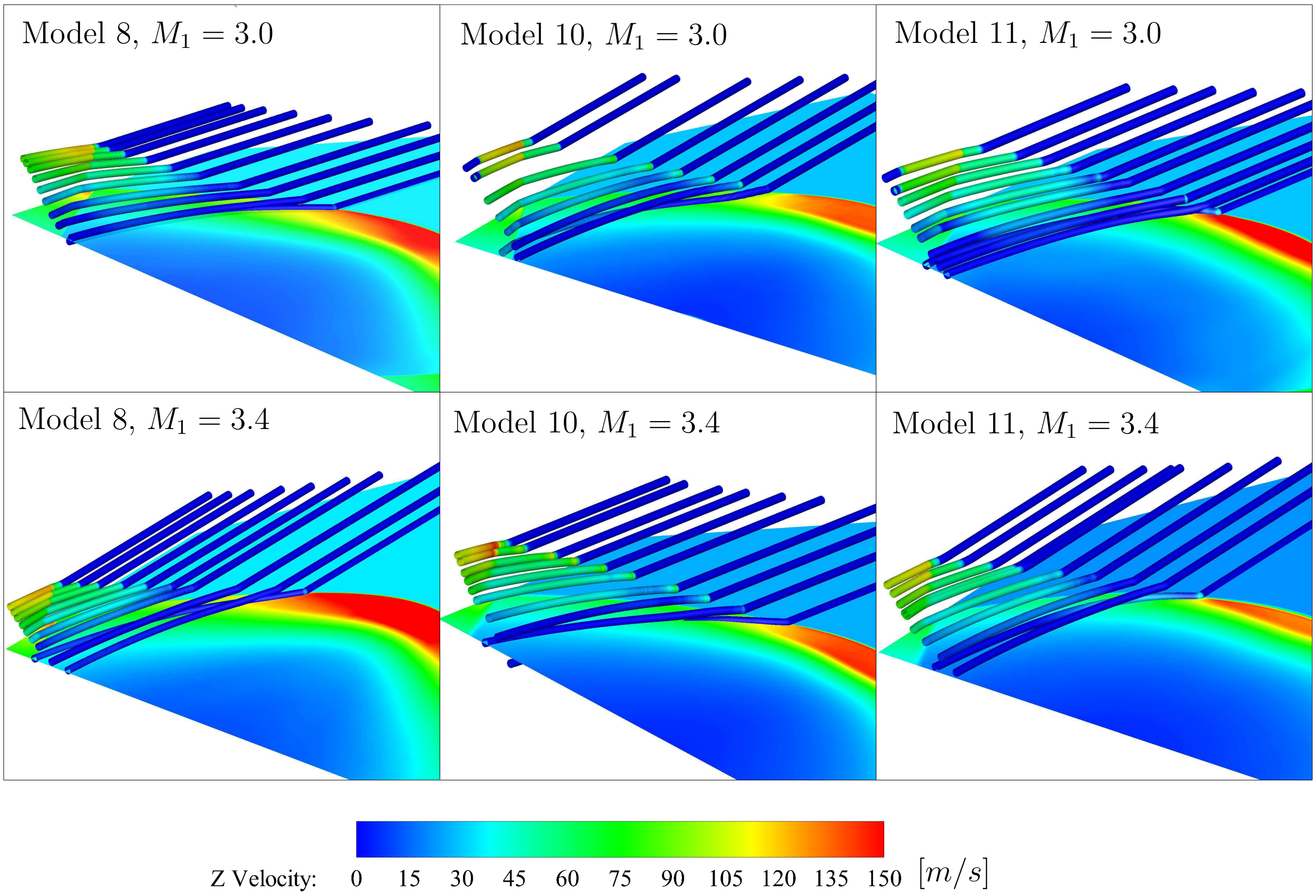
Model 8, $M_1 = 3.0$

Model 10, $M_1 = 3.0$

Model 11, $M_1 = 3.0$

Model 8, $M_1 = 3.4$

Model 10, $M_1 = 3.4$

Model 11, $M_1 = 3.4$

Figure 6.59: Qualitative nature of the shear surface as approximated with $z$-velocity-contoured streamtubes travelling through the triple lines. Horizontal symmetry plane shown with filled density contours. Free-stream flow is from the top right of each image.

The streamtubes are shown for their entire trajectory until they reach the end of the flow domain, that is, the streamwise extent of the domain which is three test model chord lengths downstream of the trailing edge of the model. For each of the streamtubes located towards the central regions and which are unaffected by the peripheral reflected shock, it is clear that the $z$-velocity component increases along them. Upon reaching approximately 50% of the distance between the apex of the intersection line and the end of the domain, this velocity component is then decreased accompanied by a flattening of the streamtube in the streamwise direction. This is due to the expansion effects which cause a streamwise drop in pressure along the streamtubes, as in [5] for two-dimensional flows. This results in a curvature of the opposite sense that causes the flattening of their trajectory.

It is clear that conditions on the horizontal symmetry plane permit the streamtube of the shear surface edge to sustain its initial deflection over a prolonged distance, to the point that it is seen to propagate underneath those originating at points higher up along the triple line. It is important to emphasise that the shear surface edge starts to attenuate and diffuse by mixing into the flow regions on either side of it, quite a short distance downstream of its inception at the transition point, more so than for any other streamtube along the shear surface. This was also noted from the experimental images for the shear surface edge. Therefore, the fact that this streamtube undergoes a sustained deflection (i.e. a prolonged extent of transverse deflection) for so large a distance after the transition point may demonstrate roll-up of the shear surface beginning from this edge.

The contours of the $z$-component of velocity plotted along the streamtubes demonstrates initial curvature of the shear surface about the $y$-axis such that the flow behind the Mach surfaces is initially deflected away from the horizontal symmetry plane. This is an interesting feature that is not typical of direct Mach reflection (DMR) configurations for which, in steady flows, the shear layer has an initial deflection towards the symmetry plane as shown in Figure 6.60a for two-dimensional situations. It has been thought that in steady flows only direct Mach reflection with a concave Mach stem was permissible. The case for which there is a convex Mach stem is termed a triple configuration (TC) of the first type i.e. TC-1 [47]. The experimental evidence of the TC-1 pattern in three-dimensional steady flow was made known by the work of Skews [8] which served to confirm earlier numerical results by Ivanov [48]. Important differences between TC-1 and DMR configurations comprise the orientation of the Mach stem, as well as the trajectory of the slipline originating from the respective triple points for each configuration. These aspects are well-known for the DMR case, and there are interesting implications of the convex Mach stem and divergent shear layer for the TC-1 configuration. In the latter case, the Mach stem is also a strong shock everywhere along it, just as with DMR, with it possessing a curvature that results in it being perpendicular to the symmetry line at its foot. However, its left-running orientation means that streamlines closest to the triple point deflect away from the symmetry plane as seen in Figure 6.60b. In order for deflection compatibility across the shear layer to be satisfied, the net deflection through the incident and reflected waves must also be orientated in the same manner.

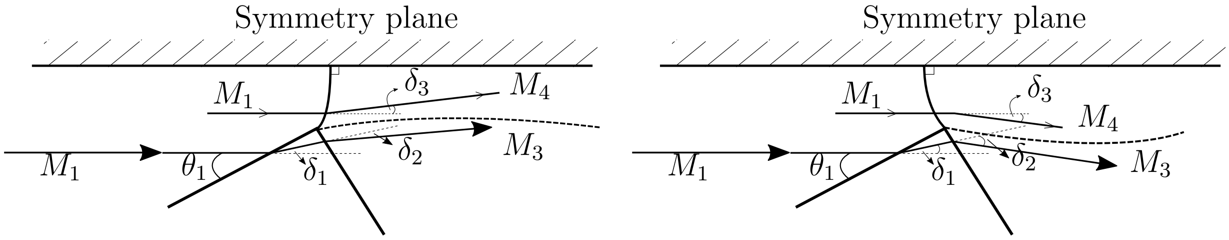

(a) Direct Mach reflection (DMR).

(b) Triple configuration of the first type (TC-1).

Figure 6.60: Schematics illustrating the differences in shock configurations for DMR and TC-1 reflection patterns.

The same type of deflection is noted in Figure 6.59 in which the streamtubes plotted diverge upwards and away from the horizontal symmetry plane. Based on the the TC-1 configuration discussed and the fact that it is known to exist in three-dimensional flows, this is expected. However, it is important to note that the $z$-velocity component of the streamtubes, just after passing through the respective points on the triple line, increases from the central regions towards the periphery. A large $z$-velocity component is not only indicative of a high curvature of the Mach surface near the triple point, but because this happens symmetrically on either side of the Mach surface, this alludes to an increase in curvature of the entire Mach surface in the transverse direction. The increasing $z$-velocity component for stations further out at the periphery also shows that the Mach surface curvature increases for all cases investigated here. This means that the Mach surface has a low curvature near the transition point $T$ which increases towards the periphery.

With regards to drawing comparisons between the different cases of Figure 6.59, this is restricted to that of a qualitative nature based on the extent to which high $z$-velocity initial deflections of the streamtubes are realised when passing through the triple lines. It can be seen that stronger vertical deflections of the shear surface away from the horizontal symmetry plane are achieved with an increase in Mach number and an increase in spread of the intersection line, the latter observed to happen for Models 8 and 10. This is due to an accommodation of the deflected flow from the central portions by virtue of vertical deflections at the periphery. These effects for Model 11 are less pronounced perhaps owing to the fact that the relieving effect of the post-interaction flow due to the presence of the sweep cusp does not make it necessary for there to be large vertical deflections of the flow behind the Mach surface. For Model 11 cases, any larger vertical deflections due to a higher Mach surface curvature could drop the pressure on the horizontal symmetry plane to the point where the transition cusp itself could exhibit instability. This demonstrates the effect that transverse influences could have on three-dimensional transition points after which there are subsonic patches. Therefore the vertical deflections for Model 11 are somewhat limited as shown in Figure 6.59.

### 6.5.4 Conclusions

This section has elaborated on the trajectory of the shear surface edge and the geometry of the Mach and shear surfaces. It was seen that the shape and orientations of the shear surfaces are dependent on the flow conditions created by the incident and reflected shock systems, as well as the sweep orientation of the intersection lines. The edge of the shear surface was found to be closely associated with the nature of the transition sweep cusp. An interesting phenomenon was observed to exist for the flow system created by Model 11 in that the required sweep difference on either side of the transition point was large enough to cause a strong oblique portion close to transition along the Mach surface with subsonic flow behind it. The influence of such a situation was also found to be far-reaching in that the Mach surface for this case diverted from trends seen for Models 8 and 10. All cases were found to have convex Mach surfaces with a type 1 triple configuration (TC-1), which, although noted in the works of previous researchers, is an important result for three-dimensional steady flows free of edge effects. A notable conclusion is that the existence of a TC-1 configuration is not dependent on the presence of edge effects as such a pattern was found to exist for all cases presented here. An examination of the shear surfaces was undertaken which was in agreement with expected orientations for a TC-1 reflection, and which was able to qualitatively demonstrate curvature of the convex Mach surface which increased in the transverse direction to a greater extent for wider spreads of the intersection lines and higher free-stream Mach numbers.

## 6.6 Full reflection transition and special cases

### 6.6.1 Introduction

This section revolves around situations in which there is transition to full Mach reflection all along the intersection line. First, a set of experimental results for Model 11 is discussed in which full transition to Mach reflection was observed, which does not agree with results from the numerical simulations. Reasons for this shall be elaborated which provides good insight as to the flow conditions for this case. Secondly, full transition to Mach reflection was obtained for numerical calculations for a highly spread model concept which was beyond the size of the wind tunnel test section used at the Flow Research Unit. Nevertheless, some interesting flow physics was noted and is discussed further here. Finally, attempts at obtaining a complex reflection configuration are demonstrated. Such configurations consist of central Mach reflection transitioning to regular reflection at the sides further outwards with a further transition to Mach reflection at the periphery.

### 6.6.2 Full transition: experimental results

Experimental test results for Model 11 at $M_1 = 3.0$ and $M_1 = 3.4$ are given in Figure 6.61. These showed that Mach reflection was obtained all throughout the reflection plane. The type of reflection obtained in the vertical mid-plane is shown by way of a standard shadowgraph taken with a datum configuration of the optical system (i.e $\lambda = 0°$ and $\phi = 0°$). Downstream of the Mach stem in these images, it is interesting to note the trajectories of the shear surfaces, which appear to have a high curvature at the triple line resulting in them approaching the horizontal symmetry plane at $S_{conv}$ as shown. This is unlike with two-dimensional flows, and for the current results there is no clear divergence of the shear surfaces and distinct formation of a nozzle-like geometry as they project downstream. Mixing effects seem to have a greater influence on their structure further downstream and eventually the central portions of these surfaces mix with each other. Indications of the swept Mach surface along the interaction line can be observed as the dark line just below the upper reflected wave (labelled as the line between points $AB$ in Figure 6.61a). A more complete idea of the flow field is gained by observing images taken at higher yaw and roll angles as shown in Figures 6.61c to 6.61f.

The shear surfaces are clearly depicted in these images and it is important to note their initial converging nozzle-like configuration, after which divergence occurs for the peripheral sections of the shear surfaces as for a two-dimensional situation. This shows that mixing is quite dominant in the central portions and the central shear surfaces converge so close together that the mixing effects cause confluence. Further outwards, the top and bottom shear surfaces are further apart, and therefore their divergence can be visualised for images of higher optical yaw and roll. There seem to be subsequent undulations of the shear surfaces, which are especially evident in Figure 6.61f and were noted to a lesser degree for the $M_1 = 3.0$ cases at corresponding optical orientations. Whether this is Mach number-dependent or is typical of instability along the shear surfaces due to mixing requires further investigation.

The shape of the intersection line for the full Mach reflection cases appears to be quite different to those discussed previously with regular reflection transitioning to Mach reflection further out along the span. Figure 6.62 shows an image taken with zero optical yaw and with the optics set at the highest roll configuration of 9°. This enabled an oblique view of the intersection line, which is aided by the shear surfaces seen as the two lines above the reflected wave at the bottom of Figure 6.62 (as labelled), and rather faintly as the two below the reflected wave at the upper part of the image. It can be seen that there is a sudden increase in the extent to which the Mach surfaces are swept backwards. This is attributed to the largely flat central portion of reflection configuration (labelled in Figure 6.62) which is typical of full Mach reflection configurations, as will be discussed further in the next subsection with the numerical model results for a case of full Mach reflection. These experimental results show that, because of a relatively narrow model geometry with full Mach reflection, the flatter central portion can only be sustained to a certain extent, after which an abrupt decrease in sweep angle $\beta$ ensues for the more peripheral reflection portions further downstream. The dark line just underneath the upper reflected wave is the triple line (edge of the Mach surface) and is only faintly visible in Figure 6.62. It is seen to grow monotonically to its full height at the tunnel walls. This is also seen in Figure 6.61 and is depicted clearer in those images. Comparisons with the numerical models reveal that these are not in agreement with the experimental results. These are shown in Figure 6.63. The numerical results show central

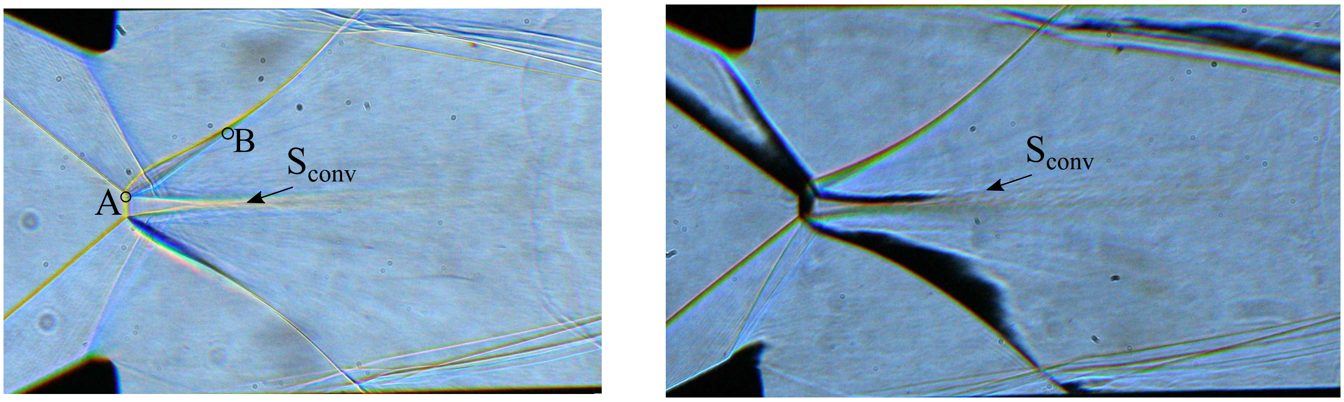

(a) Datum configuration shadowgraph, $\lambda = 0°$, $\phi = 0°$ at $M_1 = 3.0$.

(b) Datum configuration shadowgraph, $\lambda = 0°$, $\phi = 0°$ at $M_1 = 3.4$.

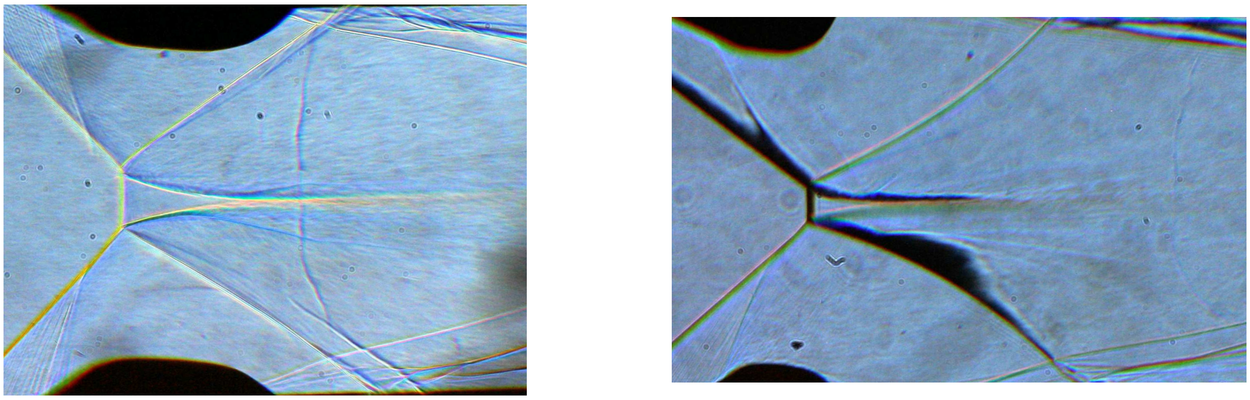

(c) $M_1 = 3.0$, $\lambda = 20°$ and $\phi = 0°$.

(d) $M_1 = 3.4$, $\lambda = 10°$ and $\phi = 0°$.

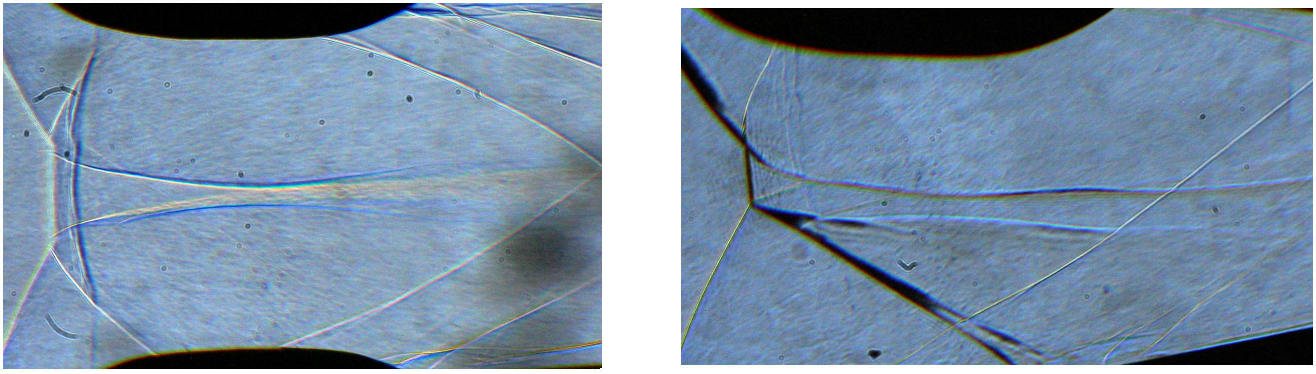

(e) $M_1 = 3.0$, $\lambda = 40°$ and $\phi = 0°$.

(f) $M_1 = 3.4$, $\lambda = 40°$ and $\phi = 5°$.

Figure 6.61: Some experimental results for Model 11 at $M_1 = 3.0$ and $M_1 = 3.4$.

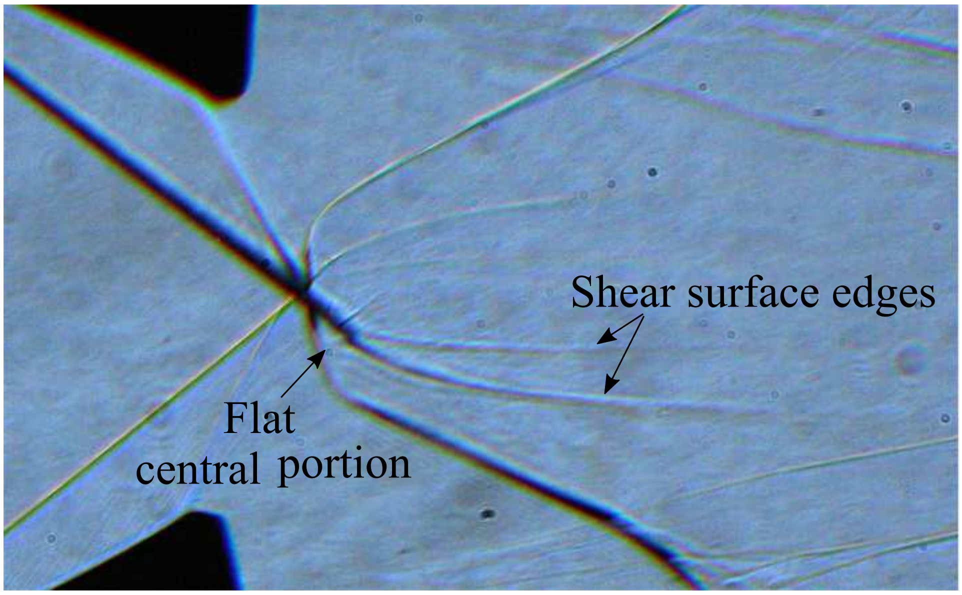

Figure 6.62: Model 11, $M_1 = 3.0$, $\lambda = 0°$, and $\phi = 9°$.

regular reflection transitioning to Mach reflection. The quantity of experiments done using Model 11 and the consistency of the flow features visualised over the range of optical configurations used shows that the shock system was indeed at steady state when all the images were captured. The difference in results is thus attributed to tunnel free-stream noise, for which turbulent eddies are responsible. Although the effect of these is reduced by baffle cones and screens in the settling chamber, numerical results by Mouton as well as observations made during experiments [20] indicate that tripping of transition from regular to Mach reflection is indeed plausible in this case. The mechanism of such a transition should comprise an inward motion of the transition points, and the transient nature of these situations would be interesting to investigate. The lower-spread models (8 and 10) also had central regular reflection but the experimental results were in good agreement with the numerical models. Since this is not the case for Model 11, it is suggested that the subsonic patches (shown in Figures 6.63c and 6.63d) may have an influence on the inwards transverse propagation of the effect of disturbances in the free-stream to the point that full transition occurs.

In order to gain more insight into cases with a full Mach reflection, very highly spread numerical model geometry was processed until this was obtained. This is the subject of the following subsection.

### 6.6.3 Full transition: numerical results

In order to achieve full transition to Mach reflection all along the intersection line, increasingly wider model spreads were used for the numerical calculations. In the end, after several geometries were tested and at different Mach numbers, full transition was achieved for Model 15 at $M_1 = 3.0$ shown in Figure 6.64.

The Mach surface height is shown to increase monotonically in height from the centre outwards, which was not seen for the full Mach reflection configuration obtained by Ivanov [12, 13], in which the decrease in Mach surface height coincided with the influence of the edge Mach cones on the reflection plane. This is an important realisation of the implications of the absence of edge effects on the final geometry of the Mach surface all along the intersection line.

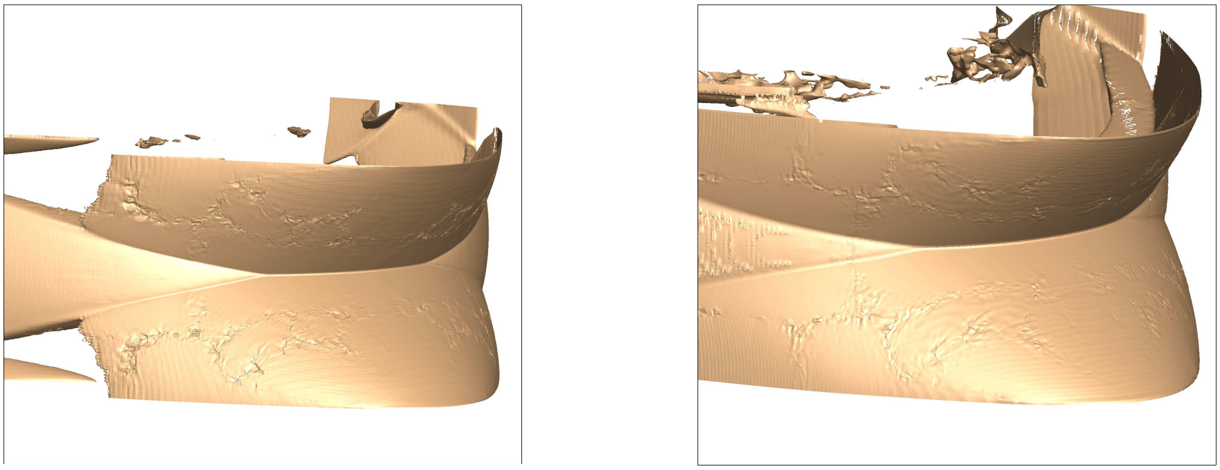

(a) Incident shock front surface, $M_1 = 3.0$. (b) Incident shock front surface, $M_1 = 3.4$.

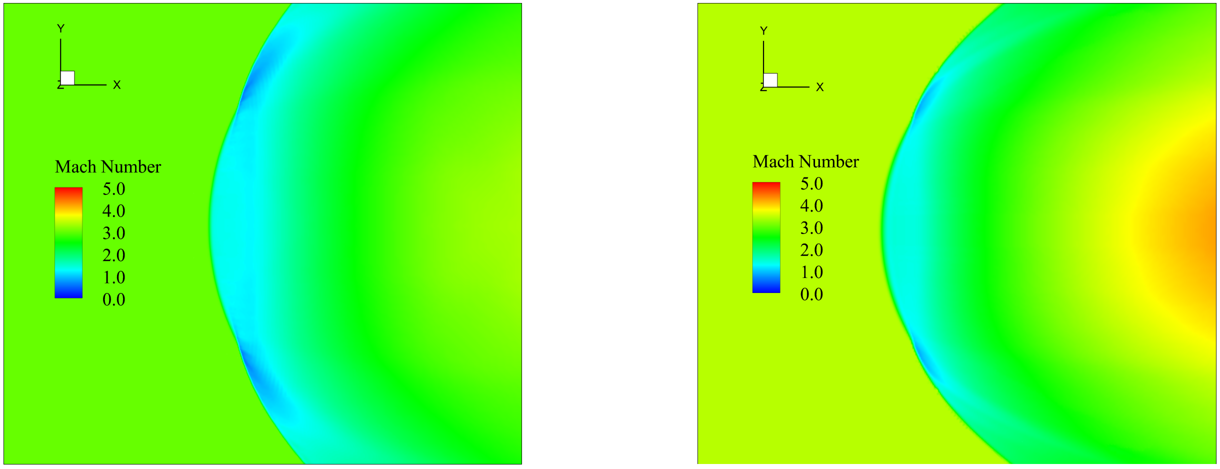

(c) Horizontal symmetry plane, Mach contours for $M_1 = 3.0$.

(d) Horizontal symmetry plane, Mach contours for $M_1 = 3.4$.

Figure 6.63: Numerical results for Model 11 for $M_1 = 3.0$ and $M_1 = 3.4$.

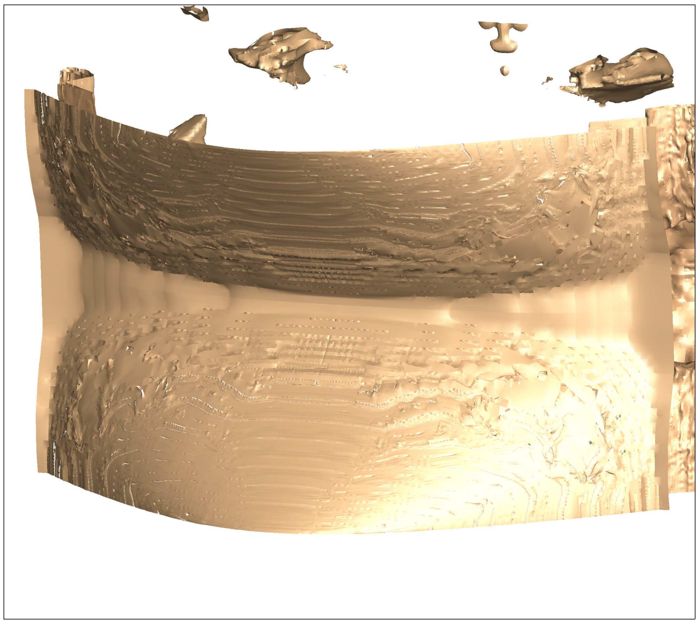

Figure 6.64: Shock surface for full Mach reflection, $M_1 = 3.0$.

The horizontal symmetry plane shown in Figure 6.65 shows some interesting details. First, the wide and spread-out shape of the intersection line is noted, which is a consequence of the highly spread model geometry which affects the incident bow shock and intersection line likewise. The next is the subsonic flow behind the Mach surface all along the reflection regions. This is expected for the central regions in which the sweep angle is 90°, but further outwards this is indicative of strong shock solutions all along the Mach surface. The sonic line coincides with the central regions of highly compressed flow (with high density), and extends the subsonic regions up until the point that the expansion effects from the test pieces trailing edges begin to drop the pressure and re-accelerate the flow to supersonic conditions. Looking at the vertical slices taken along the span of the domain (Figure 6.66) reveals that the Mach surface is straight and not convex in shape as was noted for the cases with regular reflection in the middle transitioning to Mach reflection further outwards. Finally, one last point is that concerning the Mach reflection region at the spanwise edges of the domain. This is due to the designation of the side walls of the domain, which themselves act as a reflecting surface. Due to the high incidence angle with which the peripheral Mach surface encounters the side walls, the Mach surface itself being an oblique shock surface, it gives rise to it detaching from the side wall thus producing the secondary Mach reflection seen in Figures 6.64 and 6.65. It is interesting that this reflection is continued further towards the bottom of the incident shock surface, which points to the fact that this surface is very close to being fully planar in this region. This is compared with the previously discussed cases where the peripheral regions exhibit a highly double-curved geometry which acts to cause the side wall interaction to be regular. This is also consistent with the fact that high spreads of the incident shock surface is one of the pre-requisites for the shock system being more likely to produce Mach reflection at the central regions, as shown for the case of Model 15, because the curvature component arising from sweep is reduced in the centre.

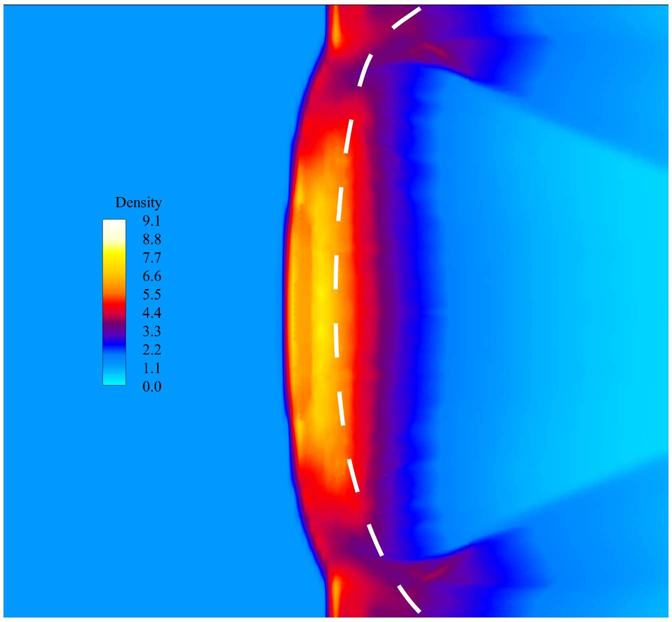

Figure 6.65: Horizontal symmetry plane for full Mach reflection with dotted sonic line (white).

Having obtained Mach reflection for Model 15, the next step was to attempt at obtaining the complex reflection configuration shown by Ivanov [12, 13] with a central Mach reflection portion which transitions to regular reflection further out and again to peripheral Mach reflection. Several

(a) Vertical slice $y_f = 0.0$.

(b) Vertical slice $y_f = 0.5$.

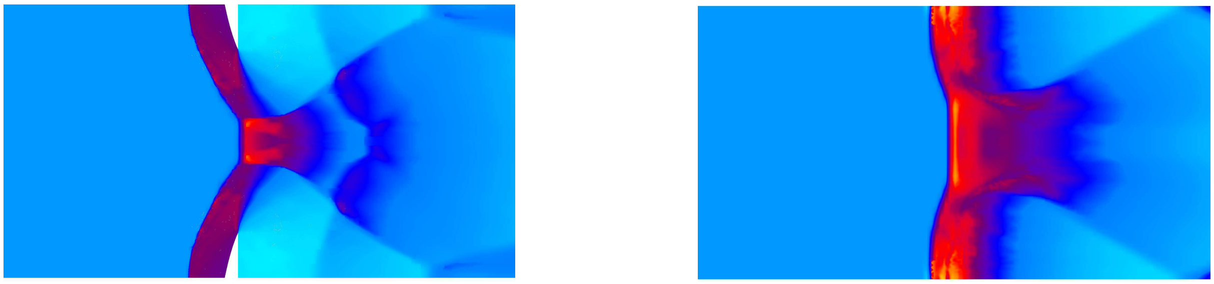

(c) Vertical slice $y_f = 0.75$.

(d) Vertical slice $y_f = 1.0$.

Figure 6.66: Vertical slices along domain half-span for Model 15 showing Mach surface shape.

attempts were made at obtaining such a configuration in the absence of edge effects for the types of models used throughout this work. These are elaborated briefly in the following subsection.

### 6.6.4 Complex reflection attempts

Several attempts were made at obtaining complex reflection with central Mach reflection transitioning to regular reflection outwards along the spanwise direction, and again transitioning to Mach reflection at the periphery. Table 6.1 shows details of the different geometry types used for the back faces of the test models. The lower face was always formed using three control vertices, and the chord length of the lower face is given in Table 6.1 as $x_L$. The height of the back face is denoted $z_H$, and $h_1$ and $h_3$ are the distances from the outer model edge to the inner control vertices as shown in Figure 4.18 in Chapter 4, Section 4.4.4. Following the methods of Ivanov [12, 13], it was decided to aim to obtain full Mach reflection after which either the free-stream Mach number or geometry could be altered in ways to achieve complex reflection. However, having found that the full Mach reflection result did not produce a non-monotonically varying Mach surface height along the span, it was concluded that Mach number variation would do little but to alter the entire reflection configuration to the standard central regular and peripheral Mach reflection patterns, as seen previously, or else to increase the Mach surface height. It was thus decided to test further geometries with spread-out wave-like back faces to control the degree to which the flow was constrained or relieved in order to produce conditions favourable to each type of reflection. Models 17 and 18 had slightly different geometrical parameters than the previous ones. That for Model 17 is shown in Figure 6.67. The red control vertices have the same designation as in Table 6.1, and the central control vertex is located halfway along the back-face span. The idea behind using a double wave-like geometry for the back-face of Model 17 was to limit the transverse flow components with the two crests acting to confine the central flow to an extent that a central Mach surface was forced to form. Then, it was anticipated that peripheral relieving effects would induce regular reflection after which the swept nature of the intersection line would be cause for peripheral Mach reflection to exist. The fact that this complex reflection did not occur was most probably due to the relieving effect provided by the central trough of the model,

Table 6.1: Test model geometric parameters. All lengths in mm, angles in degrees. Initial test models 8 - 11 included for comparison.

| Model no. | $z_H$ | $x_L$ | $h_1$ | $h_3$ | Span | Vertical symmetry angle | LE spacing |
|---|---|---|---|---|---|---|---|
| 8 | 13.6 | 30.3 | 30 | 24 | 60.0 | 24.20 | 38 |
| 10 | 13.6 | 30.3 | 20 | 14 | 50.0 | 24.20 | 38 |
| 11 | 11.0 | 24.5 | 20 | 8 | 50.0 | 24.20 | 38 |
| 12 | 11.0 | 24.5 | 15 | 4 | 50.0 | 24.20 | 38 |
| 13 | 11.0 | 24.5 | 10 | 4 | 50.0 | 24.20 | 38 |
| 14 | 13.6 | 29.3 | 5 | 2 | 80.0 | 24.8 | 38 |
| 15 | 16.5 | 30.3 | 5 | 2 | 80.0 | 28.57 | 58 |
| 16 | 16.5 | 30.3 | 5 | 2 | 60.0 | 28.57 | 58 |
| 17 | 15.2 | 30.3 | 13.9 | 2 | 100 | 26.64 | 58 |

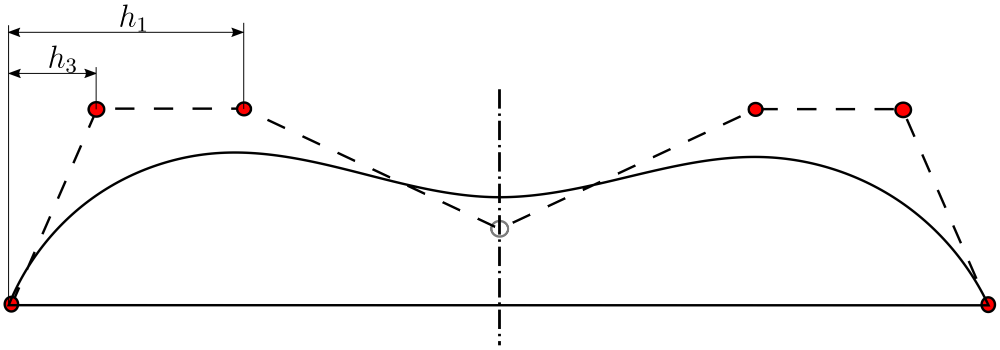

Figure 6.67: Model 17 back-face configuration with NURBS control polygon shown with dotted lines. Red control vertices are corresponding points referenced in Table 6.1, as shown.

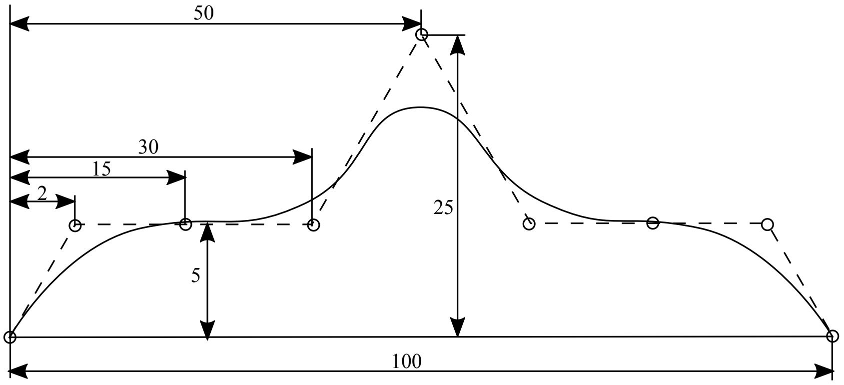

Figure 6.68: Model 18 back-face configuration with model length $x_L = 30.3$ mm and dimensions as indicated. Leading edge spacing is 68 mm.

which did not in fact constrain the central flow as much as it did reduce the incident shock angle below that required for Mach reflection to occur. This led to the development of the geometry of Model 18 shown in Figure 6.68. Here, the back-face geometry can be thought of as the spatial inverse or “negative” of Model 17. The central crest of the wave-like profile had an increased height so that the central vertical symmetry plane angle was 29.27°, significantly higher than any previous test cases. This was done to help induce a central Mach reflection given that this was achieved for Model 15. The reduced height of the outer plateaus were in an attempt to introduce relief effects such that regular reflection would arise just prior to the sweep of the intersection line causing a second transition to a peripheral Mach reflection. Unfortunately, complex reflection was not realised for this case due to relief effects from the side plateaus inducing central regular reflection. For the results obtained by Ivanov [12, 13], a reduction in the Mach surface height coincided with the influence of edge Mach cones impinging on the reflection plane. It was due to this height reduction that there could be a small further adjustment in wedge geometry that was able to further reduce the Mach surface height to the point that regular reflection could be obtained next to the central Mach reflection region after which the swept nature of the intersection line caused a second transition to Mach reflection and hence the complex reflection. The problem thus remains to obtain such a configuration where edge effects are eliminated from influencing the reflection plane.

### 6.6.5 Conclusions

This section has explored full Mach reflection cases under a number of circumstances from both an experimental and numerical viewpoint. Certain experimental results showed there to be full Mach reflection for Model 11 which contradicted the numerical results. This was attributed to noise in the flow field that was shown to be capable of tripping the reflection configuration from one of central regular and peripheral Mach reflection by way of disturbances propagating via subsonic patches in the flow field. Further numerical investigation of full Mach reflection was carried out numerically by varying the test model geometry without regard for wind tunnel test section dimensional constraints. This resulted in a highly-spread model geometry being conceived which resulted in a full Mach reflection configuration. It was shown that the strong shock solution existed all along the span of the intersection line with secondary Mach reflections occurring at the periphery of the domain. It is also important that Mach surface undulations were not present in this case unlike for double-wedge setups in which edge effects are present. The Mach surface for full Mach reflection showed a monotonic height increase in the transverse direction. Further model geometry test cases were numerically trialled with the intention of realising complex reflection. This was not obtained with the cases tested here, even with more convoluted back-face geometries with greater transverse spreads than for previous cases discussed. This was primarily because the Mach surface for full Mach reflection could not be made to reduce in height to the point that it closed up on itself producing regular reflection in between central and peripheral Mach reflections. It thus remains to be seen whether complex reflection is indeed possible in the absence of edge effects.

# Chapter 7

# Conclusions and Recommendations

An experimental and numerical investigation into multiple physical aspects of three-dimensional shock reflection transition was completed. This involved the development of lofted NURBS surface geometry of varying lateral spreads which allowed the study of reflection transition that was free of edge effects influencing the reflection plane. These models also established a known geometrical boundary condition that allowed controlled variation of the shape of the intersection line. As a result, a number of aspects of three-dimensional reflection could be systematically studied based on effects of intersection line geometry and free-stream Mach number on the resulting configurations. Three models (8, 10, and 11) of increasing spread were tested in the supersonic wind tunnel and the Flow Research Unit at the University of the Witwatersrand. The tunnel test section size placed an upper limit on the spread of the models that could be used. Oblique shadow photography was used extensively to visualise the three-dimensional flow fields. Precise orientation of the optics was made possible with the use of an inertial measurement unit (IMU), the implementation of which combined and integrated output from the three-axis accelerometers and gyroscopes to give absolute angular orientation of the optics gantry.

Conclusions from the various Sections of Chapter 6 are given here, with each section exploring a separate aspect of three-dimensional shock reflection transition. Thereafter, a few recommendations will be given.

## 7.1 Conclusions

**Section 6.1 - Numerical schlieren/shadowgraph reconstruction and validation:** Obtaining an accurate and precisely known optical orientation with the IMU for the optical system used during experiments was a crucial step towards developing a novel validation method for comparing the CFD solution data with the experimental images. This method consisted of numerically reconstructing the oblique shadowgraphs by integrating the CFD datasets along any line-of-sight used. It was shown that this methodology is applicable to any optical configuration in yaw, roll and pitch. The variety of combinations of the integrated density spatial derivatives that this method permits was instrumental in proper visualisation of flow features because different combinations selectively enhanced certain features over others when applying the reconstruction technique. As such, it was found that all of the flow features seen in the experimental images were successfully able to be visualised with the numerical data. By overlaying the constructed image over the experimental one and adjusting opacities to confirm spatial correspondence between various flow features across numerous optical configurations, it was concluded that the numerical models were successfully validated by the experimental results. As such, the numerical results were able to be used extensively in conjunction with the experimental images to derive further interpretations of the flow physics.

**Section 6.2 - Three-dimensional shock interaction in the immediate vicinity of transition:** Both experimental and numerical results revealed the existence of the two distinct reflection portions (regular and Mach reflection) along the intersection line at the horizontal symmetry plane. These reflection configurations exist next to each other with a three-dimensional transition point in between them. By considering an infinitesimal section of the flow field on either side of the transition point, an analytical model was developed that gives insight into the flow physics of the coexistence of both reflection types in a three-dimensional flow field. An important find was the that the compatibility conditions would not be simultaneously satisfied for both reflection portions on either side of transition having the same sweep angle. This gave rise to the existence of a sweep cusp, which is a physical mechanism that equilibrates the pressure and flow deflections on either side of the transition point so that the coexistence of regular and Mach reflection types is physically tenable. This was confirmed by the numerical results and to a certain extent by the experimental results by virtue of a region of optical disturbance at the point of transition along the intersection line. This has important implications for the study of three-dimensional transition.

**Section 6.3 - The nature of the transition points and intersection line profiles:** This section involved taking a closer look at certain aspects related to transition, namely the geometrical variation of the intersection line, the associated implications for transition point locations and proportion of reflection configurations realised, as well as the streamline deflections at the horizontal symmetry plane on either side of the transition point for each reflection type. It was found that higher free-stream Mach numbers and lower geometrical spreads gave rise to intersection lines that were narrow and swept to a greater extent than those for lower free-stream Mach numbers and higher spreads. It was also suggested that a dual mode of weakening of the shock system is present for certain flow free-stream conditions and geometrical boundary conditions. This is by way of a decreasing shock angle in the vertical streamwise planes and a lower sweep angle $\beta$ for flows with a high Mach number and low geometrical spread. This illustrates the idea of an additional degree of freedom by which three-dimensional shock waves may alter the the flow passing through them. This led to the idea of the dominance of certain parameters, such as the sweep angle over the shock angle, in determining the transition point locations. Transverse flow deflections were found to increase for the same modes of weakening of the shock system, with interesting compression effects on the horizontal symmetry plane, particularly in the vicinity of transition. The transition cusp was found to play an important role associated with transverse deflections. This section provided important insights into the physical mechanisms, particularly at the horizontal symmetry plane, underlying transition.

**Section 6.4 - Three-dimensional transition and shock geometry:** In this section, attention was paid to the variation of shock geometry along the incident shock surface. This variation, when coupled with the sweep angle along the intersection line, provided useful insights into the conditions and shock geometry existing in the analysis plane normal to the line of intersection. Reflection in the analysis plane was characterised by the normal Mach number component and the effective shock angle. The physical mechanisms were elucidated which necessitated the increase of the effective angle prior to transition. Examination of the correspondence of three-dimensional transition, as viewed in the analysis plane, with two-dimensional criteria for transition revealed interesting discrepancies. It was found that the transition points approached the two-dimensional detachment condition with a reduction in free-stream Mach number and an increase in geometrical spread.

**Section 6.5 - Flow structures in the surrounds of the transition points:** In this section, consideration was given to the nature of the shear and Mach surfaces. Initially, attention was focused on the edge of the shear surface. This feature is significant as it is the singular point for which the shear surface meets the horizontal symmetry plane. Its form was found to be dependent on the nature of the transition point from which it originated. In certain cases, such as for Model 11, the sweep differential across the transition point was large enough for there to a be a strong shock solution along the initial parts of the Mach reflection portions just after transition, causing there to be post-reflection subsonic flow in this region. This was shown to have important implications for the trajectory of the shear surface edge which deviated from trends observed for Models 8 and 10. The Mach surface heights were found to be influenced by both intersection line spread and Mach number, but perhaps the most interesting aspect of the Mach surfaces is their convex nature noted for configurations with central regular reflection and Mach reflection further outwards. It is an important result that this was found to occur in a flow field with no edge effects influencing the reflection plane, as it was for flows with edge influences by previous researchers. This gave rise to a triple configuration of the first type (TC-1) which seems to have a large domain of existence for three-dimensional flows with dual reflection types (i.e both regular and Mach reflection) given that they have been noted to be readily realisable for such flows. The shear surfaces were found to be influenced to a large extent by the convex nature of the Mach surfaces, with the shear surfaces diverging away from the horizontal symmetry plane and flattening out further downstream due to trailing edge expansion effects. Data from the shear surfaces were found to demonstrate an increasing convex curvature of the Mach surface from transition towards the periphery, and even more so for higher intersection line spreads and free-stream Mach numbers.

**Section 6.6 - Full reflection transition and special cases:** The final section contained three aspects regarding special cases of reflection configurations. The first was the discrepancy between experimental and numerical results, the former of which showed Mach reflection for Model 11 cases all throughout the horizontal symmetry plane. The numerical results did not show this, the reflection configuration appearing as a central regular and peripheral Mach reflection type. As was demonstrated by previous researchers, this was attributed to tunnel noise which tripped transition to full Mach reflection. This tripping mechanism is also credited by the fact that subsonic patches may exist for a short time in the experimental flow field as the transition points are propagating inwards along the intersection line, and the disturbances caused by turbulent eddies are very likely to trip the reflection configuration to full Mach reflection. Further attempts to obtain full Mach reflection for the numerical calculations resulted in a highly-spread conceptual model being developed. It was interesting that the central portions of the reflection were extremely flat and did not exhibit extensive curvature due to sweep nor convexity of the Mach surface. A secondary Mach reflection was found to exist at the side-walls of the domain, and which extended further down the incident shock pointing to the very low curvature of these surfaces necessary to produce such a reflection pattern. Finally, numerous attempts were made at obtaining complex reflection consisting of central Mach reflection, transitioning to regular reflection at the sides and further out transitioning to Mach reflection at the periphery. Unfortunately, this was not able to be obtained, and it remains to investigate this possibility given that the required closure of the central Mach surface was found, by previous works, to coincide with the influence of edge effects on the horizontal symmetry plane.

## 7.2 Recommendations

A number of recommendations are briefly outlined which would facilitate further study on three-dimensional shock wave reflection transition based on the work carried out here.

1. The sweep cusp was an important finding in this work, and was shown to account for interesting physical phenomena regarding transition. It would be an important step to obtain more conclusive experimental evidence of the sweep cusp. In addition, it would be worthwhile to investigate the existence of the sweep cusp in the presence of edge effects, which would enable determination of the extent to which edge effects influence three-dimensional transition depending on whether or not the sweep cusp was found to exist in such flows as well. Three-dimensional numerical simulations like the ones used in this work would be required for this latter aspect.

2. An interesting find of Section 6.4 was the discrepancy of three-dimensional transition points with two-dimensional transition criteria. It was found that this discrepancy was able to be significantly reduced. However, it remains to be found specifically at which criterion/criteria transition occurs for flows which do not comprise of edge effects influencing the reflection plane. It may be necessary to obtain a free-stream at a higher Mach number so that the difference between the von-Neumann and detachment criteria are large enough to preclude measurement uncertainty of the effective angles and Mach numbers at transition. It would also be interesting to investigate if any hysteresis effects exist for such flows and the transient nature of transition occurring due to inwards propagation of the three-dimensional transition points.

3. The convex Mach surfaces shown in this work are particularly interesting, as well as the associated shear surface geometry. Whist the existence of the convex Mach surface in a configuration with transition points was explained, it is important to understand the reasons for the flat Mach surface obtained for full Mach reflections.

4. The complex reflection configuration was not able to be obtained for the cases and geometry tested in this work. The problem remains to obtain central Mach reflection, transitioning outwards to regular reflection, and again to Mach reflection at the periphery in a flow field that precludes edge influences on the horizontal symmetry plane of reflection. This could be extended to furthering a deeper understanding the physical mechanisms that permit or inhibit this reflection configuration.

5. The experimental tests consisted of images obtained from single-shot photography. It is recommended to observe the flow field for transient phenomena, particularly during the establishment of the steady shock configurations which may be preceded by changes in position of the transition points. This would be useful for understanding the mechanisms behind obtaining full Mach reflection for Model 11 cases due to free-stream disturbances. Perhaps these results are a consequence of the existence of a three-dimensional dual-solution domain, and further work on this is recommended.
6. Finally, some interesting reflection configurations may be obtained with asymmetrical test piece configurations which do not permit edge influences to affect reflection. It may be that complex reflection is realised in these arrangements.

# References

[1] W.F. Hinson, "Transonic and supersonic ejection release characteristics of six dynamically scaled external-store shapes from an 0.086-scale model of a current fighter airplane," NASA Langley Research Center, Hampton, VA, Tech. Memo. X-128 (Declassified), Dec. 1959.

[2] W.J. Monta, "Effect of conventional and square stores on the longitudinal aerodynamic characteristics of a fighter aircraft model at supersonic speeds," NASA Langley Research Center, Hampton, VA, Tech. Memo. TM 81791, Jun. 1980.

[3] P. Mardsen and A.B. Haines, "Aerodynamic loads on external stores: a review of experimental data and method of prediction," Aero. Res. Counc., London, Rep. Memo. No. 3503, Nov. 1962.

[4] H.G. Hornung, H. Oertel and R.J. Sandeman, "Transition to Mach reflection of shock waves in steady and pseudosteady flow with and without relaxation.," *J. Fluid Mech.*, vol. 90, pp. 541–559, 1979.

[5] H.G. Hornung and M.L. Robinson, "Transition from regular to Mach reflection of shock waves, Part 2. The steady-flow criterion," *J. Fluid Mech.*, vol. 123, pp. 155-164, 1982.

[6] F. Marconi, "Shock reflection transition in three-dimensional steady flow about interfering bodies," *AIAA J.*, vol. 21, no. 5, pp. 707-713, May 1983.

[7] B.W. Skews, "Aspect ratio effects in wind tunnel studies of shock wave reflection transition," *Shock Waves*, vol. 7, pp. 373–383, 1997.

[8] B.W. Skews, "Three-dimensional effects in wind tunnel studies of shock wave reflection," *J. Fluid Mech.*, vol. 407, pp. 85–104, 2000.

[9] D.M. Scott, B.W. Skews, "Shock wave reflection in steady flow," *Aero. Merid.*, vol. 12, issue 36, 1996.

[10] V.M. Fomin, M.S. Ivanov, A.M. Kharitonov G.P. Klemenkov, A. N., Kudryavtsev, & H. G. Hornung, "The study of transition between regular and Mach reflection in different wind tunnels", in *12th Intl. Mach Reflection Symp.* (ed. B.W. Skews), pp. 138–151.

[11] M.S. Ivanov, D.V. Khotyanovsky, A.N. Kudryavtsev, G.N. Markelov, S.B. Nikiforov, "Experimental study of 3D shock wave configurations during RR/MR transition," in *Proc. of* $23^{rd}$ *International Symposium on Shock Waves*, Fort Worth, TX, 2001, Paper 1771

[12] M.S. Ivanov, "Trasition between regular and Mach reflection of shock waves: new numerical and experimental results," presented at the *European Congress on Computational Methods in Applied Sciences and Engineering*, Barcelona, Spain, 2000.

[13] M.S. Ivanov, A.M. Kharitonov, D.V. Khotyanovsky, A.N. Kudrayavtsev, S.B. Nikiforov and A.A. Pavlov, "Three-dimensional steady shock wave interactions. Numerical simulations and experimental validation," presented at the *European Congress on Computational Methods in Applied Sciences and Engineering*, Jyväskylä, Finland, 2004.

[14] B.W. Skews and J.A. Mohan, "Three-dimensional shock wave reflection transition," presented at the *15th International Symposium on Flow Visualization*, Minsk, Belarus, 2012.

[15] N. Menon and B.W. Skews, "Lasr vapour screen visualisation of three-dimensional compressible flow fields," *R & D Journal*, vol. 21, pp. 10–18, 2005.

[16] B. W. Skews, private communication, Oct. 2017.

[17] S. S. Lewin, "Transition from Regular to Mach Reflection in Steady Supersonic Flow," unpublished.

[18] J. D. Anderson, *Fundamentals of Aerodynamics*, $3^{rd}$ ed. New York City, NY: McGraw-Hill, 2001.

[19] J. D. Anderson, *Modern Compressible Flow with Historical Perspective*, New York, NY: McGraw-Hill, Inc., 1982.

[20] C. A. Mouton and H. G. Hornung, "Experiments on the mechanism of inducing transition between regular and Mach reflection," *Phys. Fluids*, vol. 20, Dec. 2008.

[21] C. A. Mouton and H. G. Hornung, "Mach Stem Height and Growth Rate Predictions," *AIAA J.*, vol. 45, no. 8, pp. 1977-1987, Aug. 2007.

[22] A. Chpoun, D. Passerel, H. Li and G. Ben-Dor, "Reconsideration of oblique shock wave reflections in steady flows, Part 1. Experimental Investigation," *J. Fluid Mech.*, vol. 301, pp. 19–35, 1995.

[23] J. Vuillon, D. Zeitoun and G. Ben-Dor, "Reconsideration of oblique shock wave reflections in steady flows, Part 2. Numerical Investigation," *J. Fluid Mech.*, vol. 301, pp. 37–50, 1995.

[24] B. W. Skews, "Study of three-dimensional shock wave reflection transition using oblique shadowgraphs," presented at the $22^{nd}$ International Symposium on Shock Waves, London, UK, 1999.

[25] American Society of Mechanical Engineers, "Procedure for Estimation and Reporting of Uncertainty Due to Discretization in CFD Applications," *J. Fluids Eng.*, vol. 130, 2008.

[26] P.J. Roache, "Quantification of uncertainty in computational fluid dynamics," *Annu. Rev. Fluid. Mech.*, no. 29, pp. 123–160, 1997.

[27] G. Ben-Dor, *Shock Wave Reflection Phenomena*, $2^{nd}$ ed. New York, NY: Springer-Verlag, 2007.

[28] L.H. Tan, Y.X. Ren and Z.N. Wu, "The Analytical and numerical study of the near flow field and shape of the Mach stem in steady flows," *J. Fluid Mech.*, vol. 546, pp. 341–362, 2006.

[29] B. Gao and Z.N. Wu, "A study of the flow structure for Mach reflection in steady supersonic flow," *J. Fluid Mech.*, vol. 656, pp. 29–50, 2010.

[30] C.Y. Bai and Z.N. Wu, “Size and shape of shock waves and slipline for Mach refection in steady flow,” *J. Fluid Mech.*, vol. 818, pp. 116–140, 2010.

[31] D. J. Azevedo and C. S. Liu, “Engineering approach to the prediction of shock patterns in bounded high-speed flows,” *AIAA J.*, vol. 31, no. 1, pp. 83-90, Jan. 1993.

[32] N. Curle and H. J. Davies, *Modern Fluid Dynamics Vol. II*, 1st ed. London: Van Nostrand Reinhold Company, 1971.

[33] B-Spline Curves, lecture notes (supplemental) for Fundamentals of Computer Aided Engineering and Design, School of Aero. Eng., Georgia Institute of Technology, Atlanta, GA, spring 2004.

[34] V.V. Keldysh, “Intersection of two plane shock waves in space,” *PMM.*, vol. 30, no. 1, pp. 189-193, Jan. 1966.

[35] G. Emanuel, *Analytical Fluid Dynamics*, 2nd ed. Boca Raton, FL: CRC Press, 2000.

[36] E. Migotsky and M.V. Morkovin, “Three-dimensional shock wave reflections,” *J. Aero. Sci.*, vol. 18, no. 7, pp. 484-489, Jul. 1951.

[37] N.D. Domel, “General three-dimensional relation for oblique shocks on swept ramps”, *AIAA J.*, vol. 54, no. 1, pp. 310–319, Jan. 2016.

[38] Y. Tamura and K. Fujii, “Visualization for computational fluid mechanics and the comparison with experiments”, AIAA Paper 90-3031, Aug. 1990.

[39] L.A. Yates, “Images constructed from computed flowfields”, AIAA Paper 92-4030, Jul. 1992.

[40] M. Sun, “Computer modeling of shadowgraph optical setup,” presented at the 27th International Congress on High-Speed Photography and Photonics, Xi’an, China, 2007.

[41] A. Dauptain, B. Cuenot, and L. Y. M. Gicquel “Large Eddy Simulation of Stable Supersonic Jet Impinging on Flat Plate,”, *AIAA J.*, vol. 48, no. 10, pp. 2325–2338, Oct. 2010.

[42] G.S. Settles, M.J. Hargather, “A review of recent developments in schlieren and shadowgraph techniques”, *Meas. Sci. Technol.*, vol. 28, Paper 042001, Feb. 2017.

[43] R. Faletič, A.F.P. Houwing, R.R. Boyce, “Tomographic reconstruction of shock layer flows,” *Shock Waves*, vol. 17, pp. 153–170, 2007.

[44] J.J. Quirk, “A contribution to the great Riemann solver debate,”, *Int. J. Num. Methods Fluids*, vol. 18, pp. 555–574, 1994.

[45] A. Hadjadj and A. Kudryavtsev, “Computation and flow visualization in high-speed aerodynamics,”, *J. Turbulence.*, vol. 6, no. 16, 2005.

[46] Z. Wang, A. Bovic, H. Sheikh and E. Simoncelli, “Image quality assessment: from error visibility to structural similarity,”, *IEEE Trans. Image Proc.*, vol. 13, no. 4, pp.600–612, 1997.

[47] M. V. Silnikov, M. V. Chernyshov, and L. G. Gvozdeva, “Analytic description of the domain of existence of triple configurations with a negative slope of reflected shock”, *Tech. Phys.*, vol. 61, No. 11, pp. 1633–1637, 2016.

[48] M. Ivanov, G.P. Klemenkov, A. N., Kudryavtsev, S. B. Nikiforov, A. A. Pavlov, V.M. Fomin, A.M. Kharitonov, D.V. Khotyanovsky, & H. G. Hornung, "Experimental and numerical study of the transition between regular and Mach reflections of shock waves in steady flows", in *Proc. 21st Intl Symp. on Shock Waves* (ed. A. F. P. Houwing & A. Paull), pp. 819–824, Panther Publishing.

# Appendices

# Appendix A

## .1 Manufacturing drawings

The following pages contain the manufacturing drawings of the test models and the model support rods for the sting assembly in that order. The G-code files generated for the CNC machine operator are included in the digital appendices.

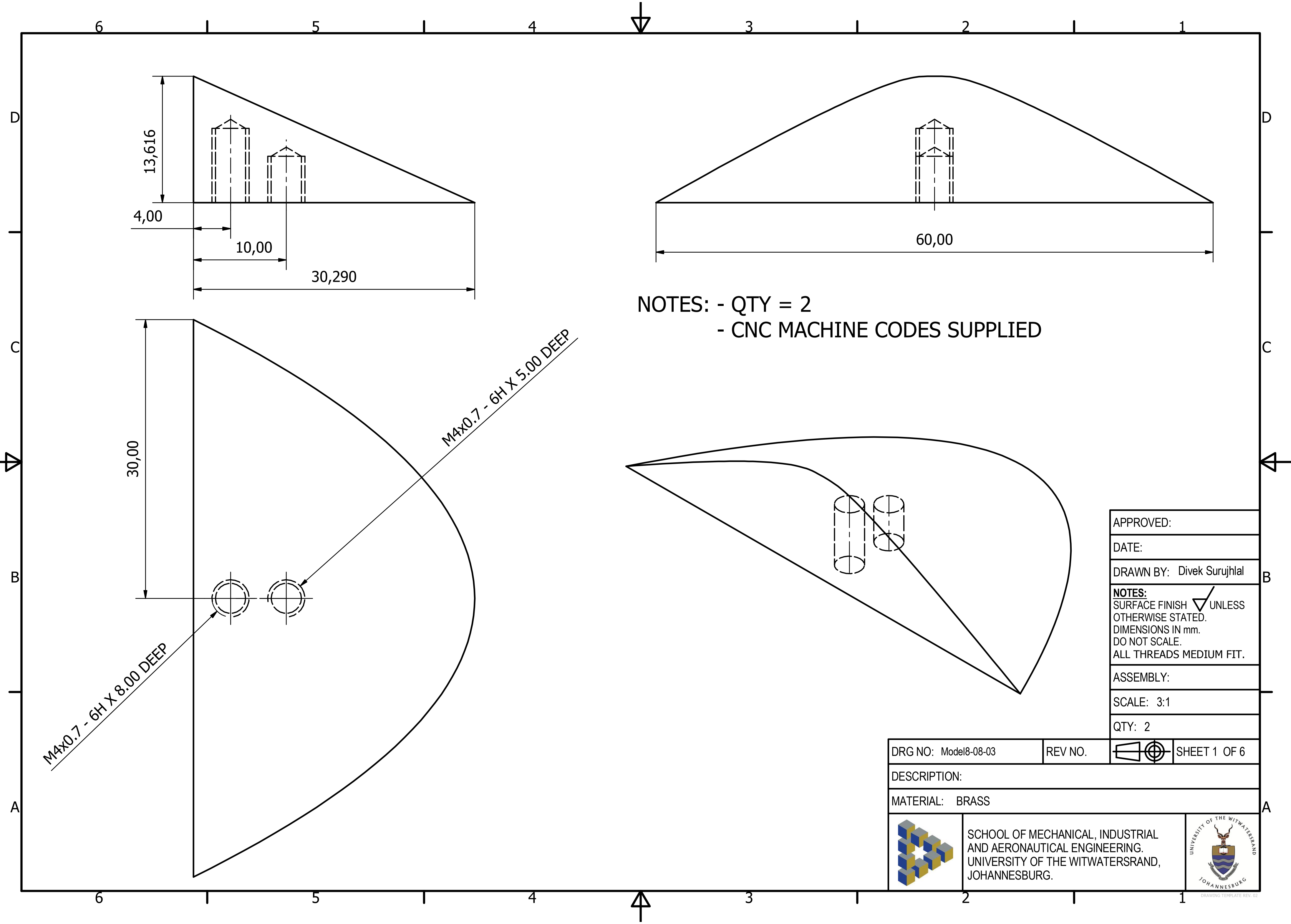

NOTES: - QTY = 2
- CNC MACHINE CODES SUPPLIED

| | |
|---|---|
| APPROVED: | |
| DATE: | |
| DRAWN BY: | Divek Surujhlal |
| **NOTES:**<br>SURFACE FINISH ∇ UNLESS OTHERWISE STATED.<br>DIMENSIONS IN mm.<br>DO NOT SCALE.<br>ALL THREADS MEDIUM FIT. | |
| ASSEMBLY: | |
| SCALE: | 3:1 |
| QTY: | 2 |

| | | | |
|---|---|---|---|
| DRG NO: Model8-08-03 | REV NO. | | SHEET 1 OF 6 |
| DESCRIPTION: | | | |
| MATERIAL: BRASS | | | |
| SCHOOL OF MECHANICAL, INDUSTRIAL<br>AND AERONAUTICAL ENGINEERING.<br>UNIVERSITY OF THE WITWATERSRAND,<br>JOHANNESBURG. | | | |

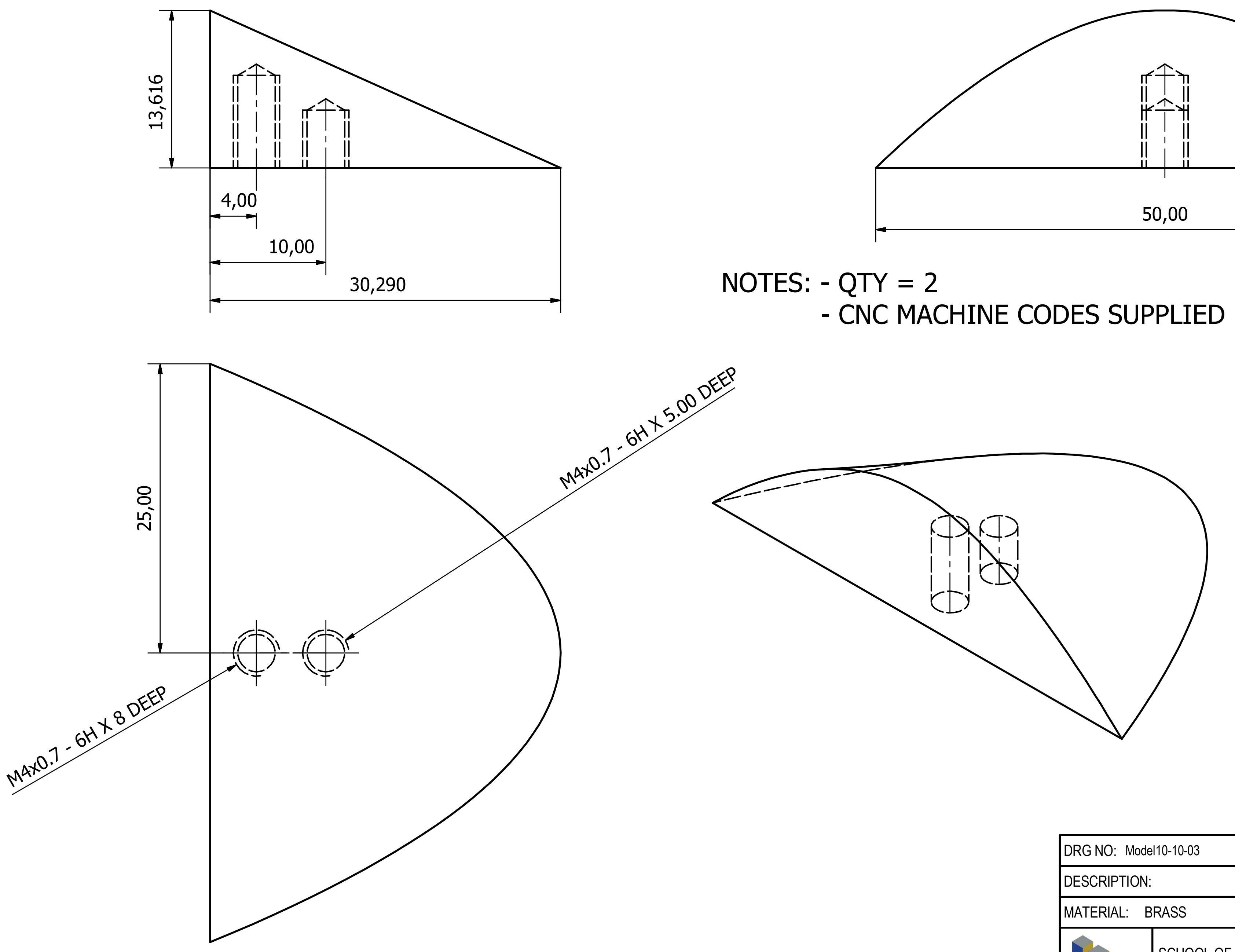

NOTES: - QTY = 2
- CNC MACHINE CODES SUPPLIED

APPROVED:
DATE:
DRAWN BY: Divek Surujhlal

**NOTES:**
SURFACE FINISH ∇ UNLESS
OTHERWISE STATED.
DIMENSIONS IN mm.
DO NOT SCALE.
ALL THREADS MEDIUM FIT.

ASSEMBLY:
SCALE: 3:1
QTY: 2

DRG NO: Model10-10-03
REV NO.
SHEET 2 OF 6
DESCRIPTION:
MATERIAL: BRASS

SCHOOL OF MECHANICAL, INDUSTRIAL
AND AERONAUTICAL ENGINEERING.
UNIVERSITY OF THE WITWATERSRAND,
JOHANNESBURG.

DRAWING TEMPLATE REV. 02

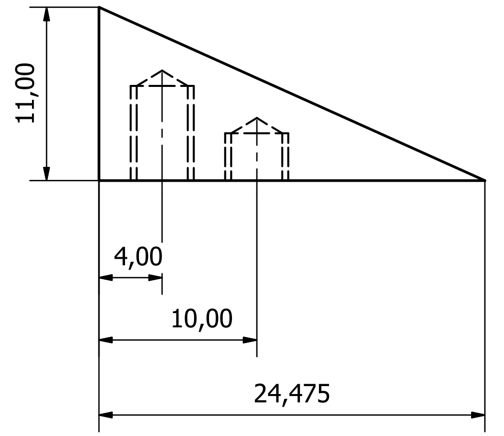

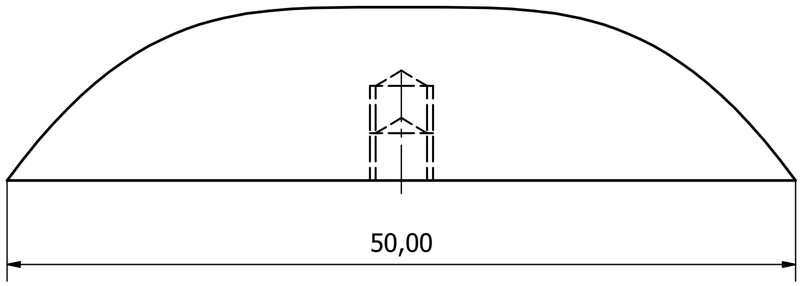

NOTES: - QTY = 2
- CNC MACHINE CODES SUPPLIED

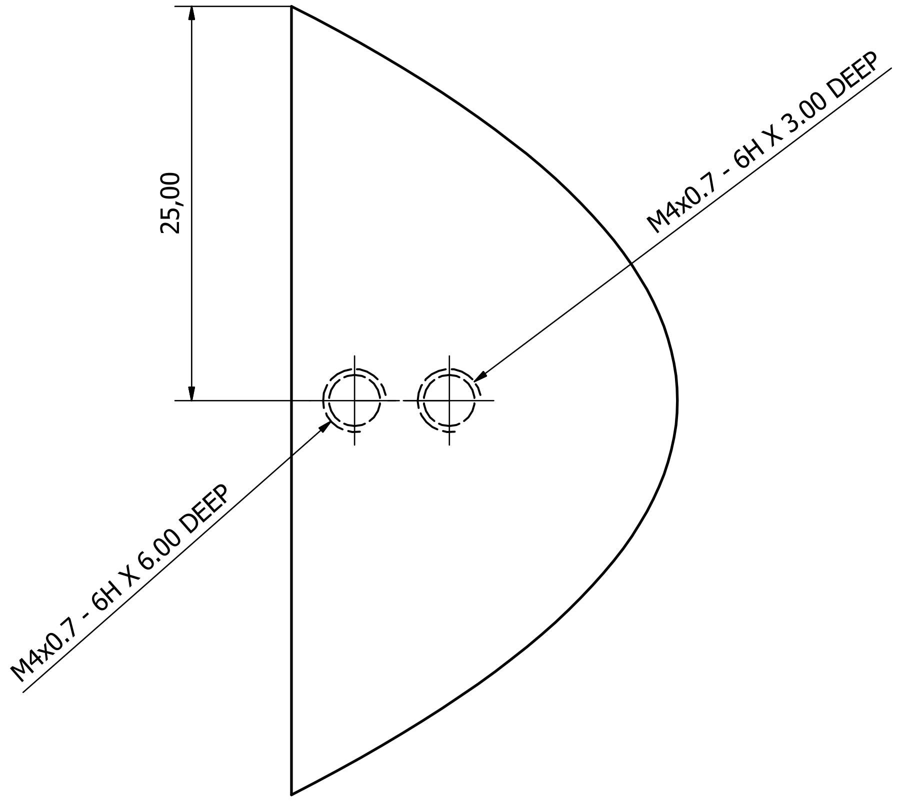

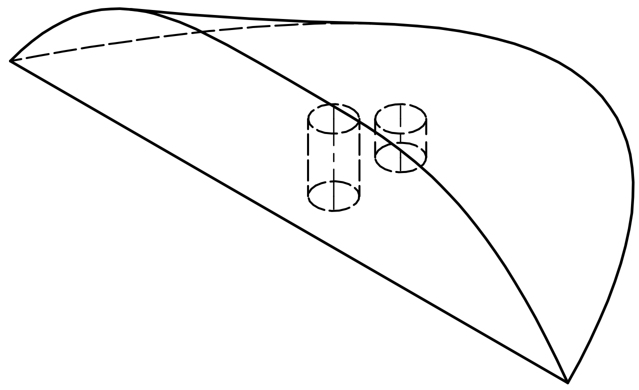

| | | |
|---|---|---|
| APPROVED: | | |
| DATE: | | |
| DRAWN BY: Divek Surujhlal | | |
| **NOTES:**<br>SURFACE FINISH ▽ UNLESS<br>OTHERWISE STATED.<br>DIMENSIONS IN mm.<br>DO NOT SCALE.<br>ALL THREADS MEDIUM FIT. | | |
| ASSEMBLY: | | |
| SCALE: 3:1 | | |
| QTY: 2 | | |
| DRG NO: Model11-10-03 | REV NO. | SHEET 3 OF 6 |
| DESCRIPTION: | | |
| MATERIAL: BRASS | | |

SCHOOL OF MECHANICAL, INDUSTRIAL
AND AERONAUTICAL ENGINEERING.
UNIVERSITY OF THE WITWATERSRAND,
JOHANNESBURG.

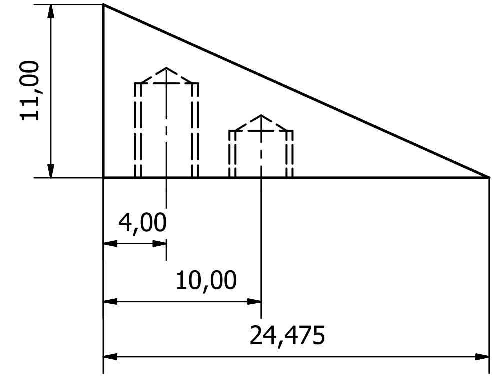

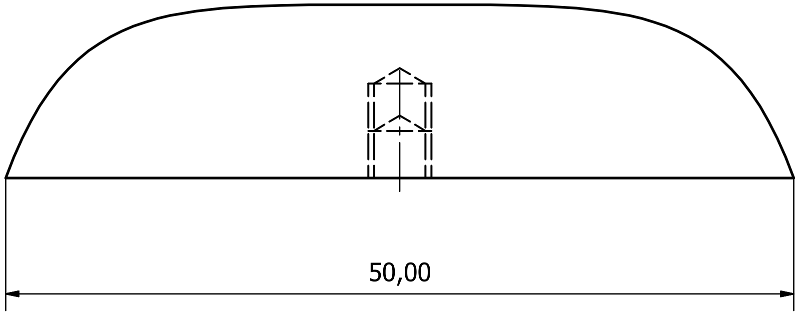

NOTES: - QTY = 2
- CNC MACHINE CODES SUPPLIED

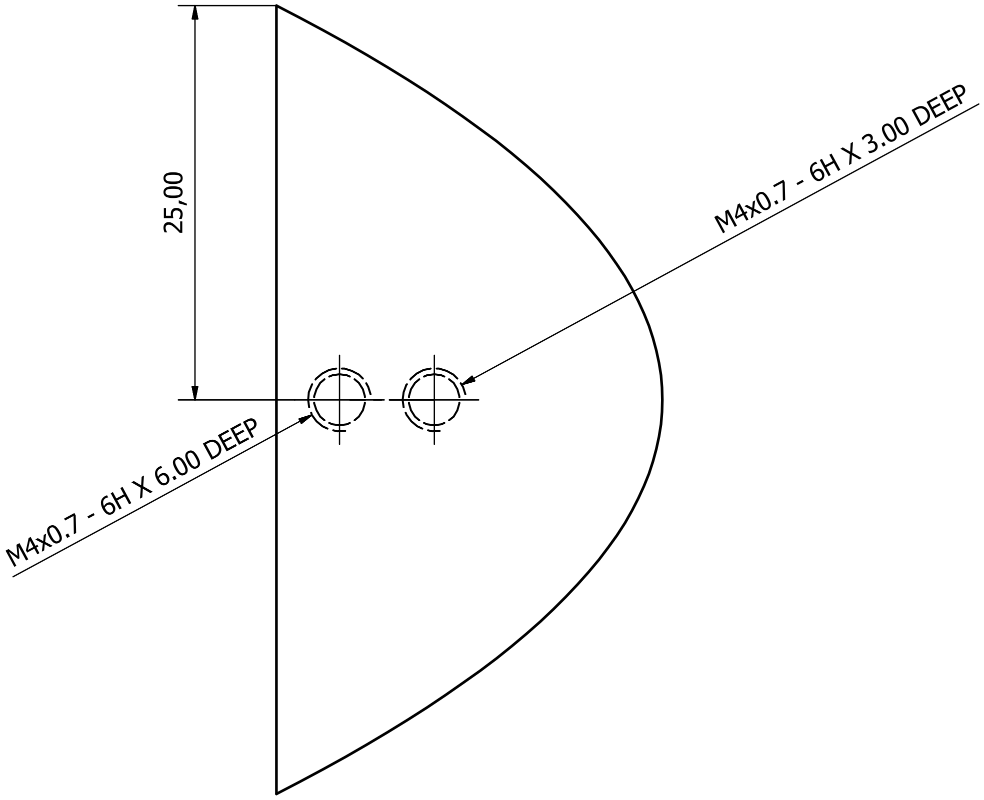

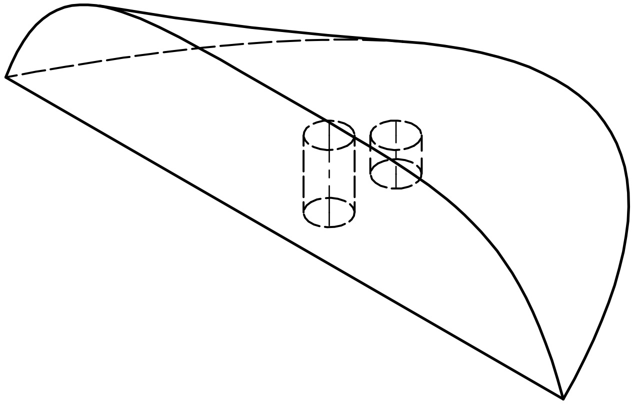

APPROVED:
DATE:
DRAWN BY: Divek Surujhlal

**NOTES:**
SURFACE FINISH ▽ UNLESS
OTHERWISE STATED.
DIMENSIONS IN mm.
DO NOT SCALE.
ALL THREADS MEDIUM FIT.

ASSEMBLY:
SCALE: 3:1
QTY: 2

| | | | |
|---|---|---|---|
| DRG NO: Model12-10-03 | REV NO. | | SHEET 4 OF 6 |
| DESCRIPTION: | | | |
| MATERIAL: BRASS | | | |

SCHOOL OF MECHANICAL, INDUSTRIAL
AND AERONAUTICAL ENGINEERING.
UNIVERSITY OF THE WITWATERSRAND,
JOHANNESBURG.

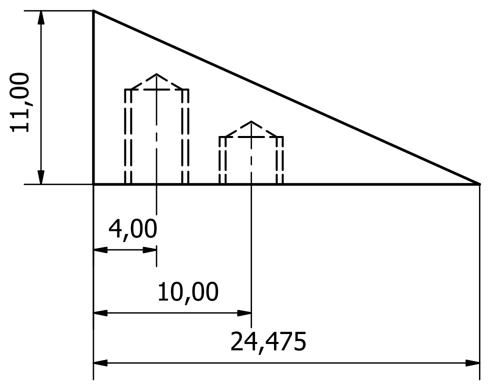

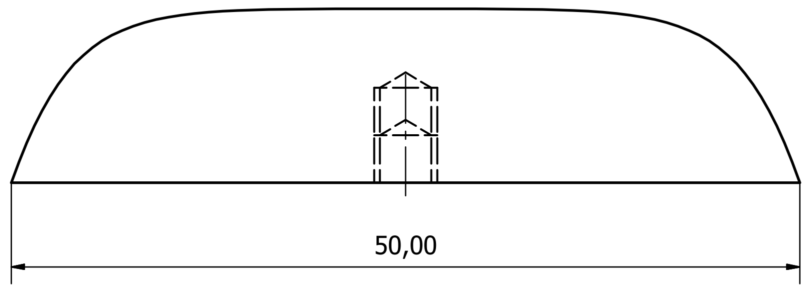

NOTES: - QTY = 2
- CNC MACHINE CODES SUPPLIED

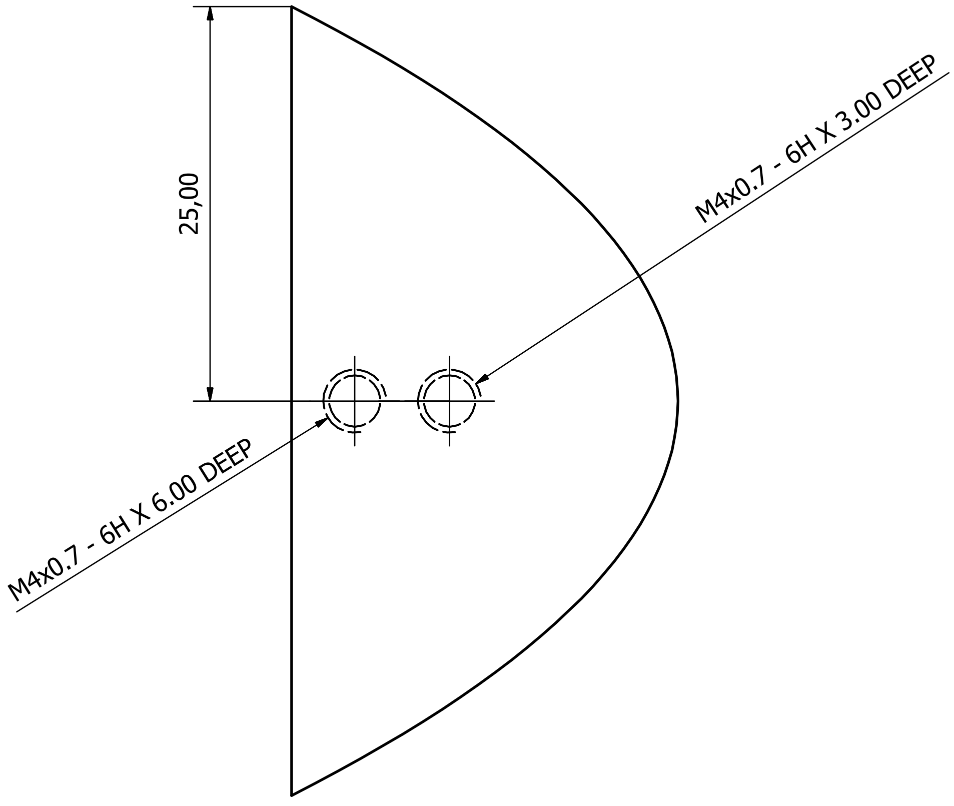

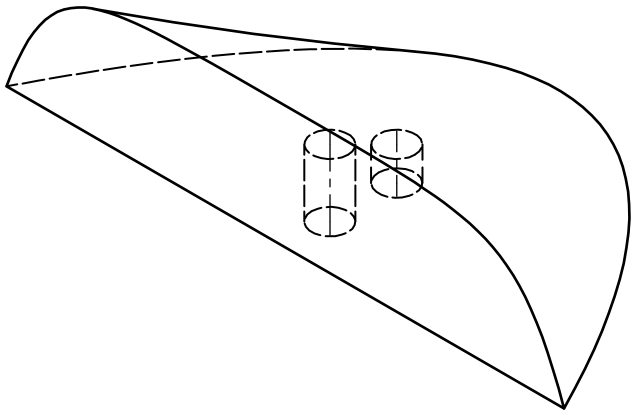

APPROVED:

DATE:

DRAWN BY: Divek Surujhlal

**NOTES:**
SURFACE FINISH ▽ UNLESS
OTHERWISE STATED.
DIMENSIONS IN mm.
DO NOT SCALE.
ALL THREADS MEDIUM FIT.

ASSEMBLY:

SCALE: 3:1

QTY: 2

| | | | |
|---|---|---|---|
| DRG NO: Model13-11-03 | REV NO. | | SHEET 5 OF 6 |

DESCRIPTION:

MATERIAL: BRASS

SCHOOL OF MECHANICAL, INDUSTRIAL
AND AERONAUTICAL ENGINEERING.
UNIVERSITY OF THE WITWATERSRAND,
JOHANNESBURG.

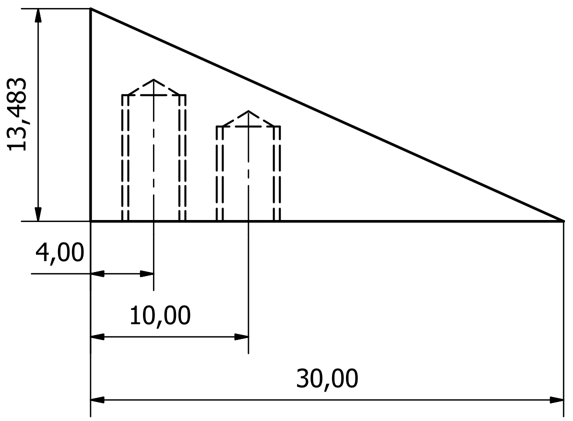

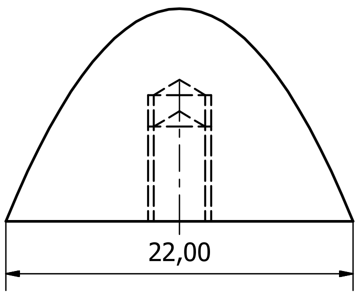

NOTES: - QTY = 2
- CNC MACHINE CODES SUPPLIED

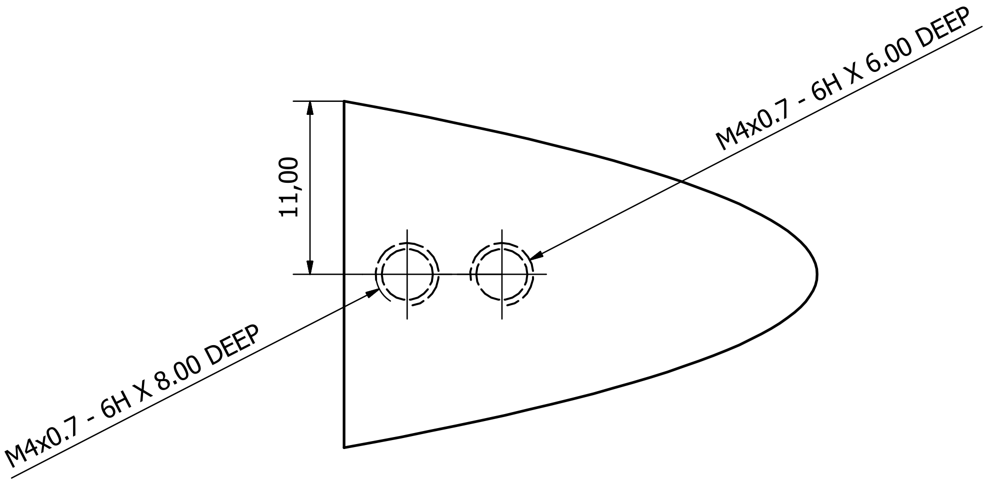

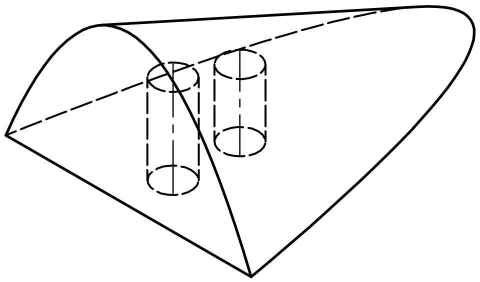

APPROVED:
DATE:
DRAWN BY: Divek Surujhlal

**NOTES:**
SURFACE FINISH ▽ UNLESS
OTHERWISE STATED.
DIMENSIONS IN mm.
DO NOT SCALE.
ALL THREADS MEDIUM FIT.

ASSEMBLY:
SCALE: 3:1
QTY: 2
DRG NO: ModelOriginal-19-03
REV NO.
SHEET 6 OF 6
DESCRIPTION:
MATERIAL: BRASS

SCHOOL OF MECHANICAL, INDUSTRIAL
AND AERONAUTICAL ENGINEERING.
UNIVERSITY OF THE WITWATERSRAND,
JOHANNESBURG.

DRAWING TEMPLATE REV. 02

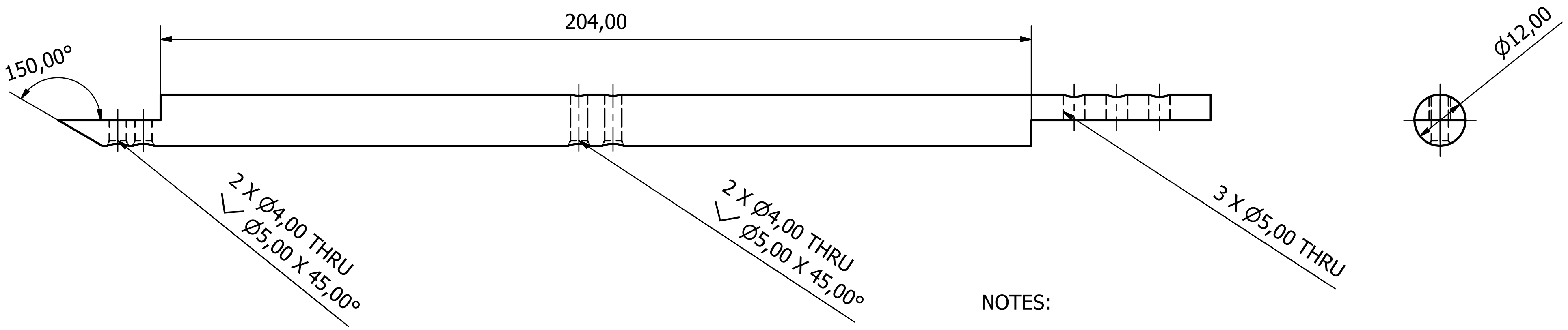

NOTES:

- 4 X ⌵ Ø4 HOLES SPACED AS SHOWN

-START COUNTERSINK FROM ARROW SIDE

- 3 X Ø5 HOLES SPACED AS SHOWN

- PART QTY = 2

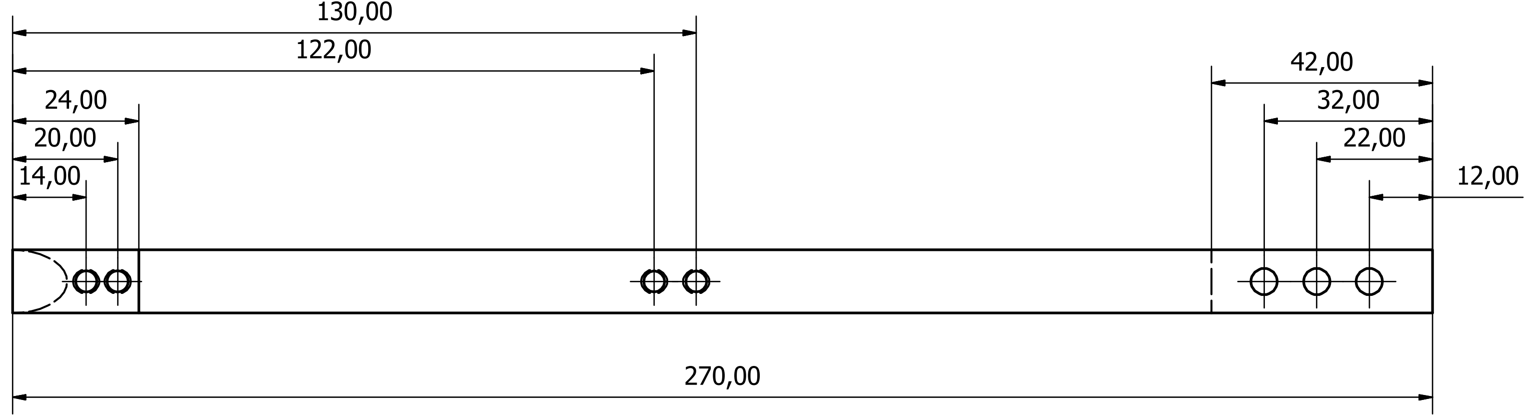

APPROVED:
DATE:
DRAWN BY: Divek Surujhlal

**NOTES:**
SURFACE FINISH ✓ UNLESS
OTHERWISE STATED.
DIMENSIONS IN mm.
DO NOT SCALE.
ALL THREADS MEDIUM FIT.

ASSEMBLY: STING ASSEMBLY
SCALE: 1:1
QTY: 2

DRG NO: SUPPORT RODS
REV NO.
SHEET 1 OF 1
DESCRIPTION: SUPPORT RODS
MATERIAL: SILVER STEEL

SCHOOL OF MECHANICAL, INDUSTRIAL
AND AERONAUTICAL ENGINEERING.
UNIVERSITY OF THE WITWATERSRAND,
JOHANNESBURG.

## .2 Wind tunnel facility specifications

Specifications of the various equipment and instruments used in this research are tabulated in this section (Tables 1 to 7). A schematic of the layout of the various facilities interfaced with the wind tunnel and necessary for its operation was given in Figures 4.1, 4.2 and 4.4.

Table 1: Compressor specifications.

| | |
|---|---|
| Company | Reavell |
| Model | CompAir |
| Type | CSA GE |
| Machine no. | 226092 |
| Speed | 1000 rpm |
| Pressure | 450 psi |
| Oil | Shell Turbo Oil T 78 |

Table 2: Induction motor specifications.

| | |
|---|---|
| Company | English Electric Benoni Works |
| Serial no. | PC5927/18 |
| Size | C286 |
| Power | 25 hp |
| Speed | 1455 rpm |
| Voltage | 380 V |
| Connection | 3-phase delta |
| Current | 36.3 A, 50 Hz |
| Standard | 2613 |
| Bearings | DE: SKF 6310<br>NDE: SKF 6308 |
| Insulation class | E |
| Lubricant | Shell Alvania no. 2 (Li-base grease) |
| Overhaul co. | L.H Marthinusen (ref: 92.6680) |

Table 3: Programmable time delay unit specifications.

| | |
|---|---|
| Company | ElectroDi |
| Trigger | 3.0 V |
| Exposure time | 3300 $\mu$s |

Table 4: Settling chamber pressure transducer specifications.

| | |
|---|---|
| Company | Kyowa Electronic Instruments Co. Ltd. |
| Type | PG - 10KU |
| Capacity | 10 kg.f/cm$^2$ |
| Serial no. | YB9330137 |

Table 5: Test section pressure transducer specifications.

| | |
|---|---|
| Company | Kyowa Electronic Instruments Co. Ltd. |
| Type | PG - 2KU |
| Capacity | 2 kg.f/cm$^2$ |
| Serial no. | YP9468 |

Table 6: Supply pressure vessel specifications.

| | |
|---|---|
| Year of manufacture | 1968 |
| Code | BS 1515, 1965 |
| Design temp. | 122 °F |
| Capacity | 319 cuft |
| Radiography | Spot |
| Test pressure | 146 psi |
| Vessel no. | 53/1 |
| Company | Kies & Travers Ltd. |

Table 7: Air drier specifications.

| | |
|---|---|
| Company | Arlec Engineering Works CC |
| Makers no. | J38996 |
| Working pressure | 2136 kPa |
| Test pressure | 2777 kPa |
| Working temp. | 100 °C |
| Design temp. | 100 °C |
| Cubic capacity | 0.036 |
| Code | ACIF8101A02 |

# Digital Appendices

Th digital appendices are contained on a USB drive the contents of which is detailed in Table 8. For the naming conventions, place holders have been used in place of numbers specific to the version number or creation date of the files. Hence, “X” is used in place of a version or model number and “DD” or “MM” is used for day or month of creation. MATLAB scripts were used throughout and the relevant .m file names are given.

Table 8: Contents of digital appendix.

| Folder | Contents/main application | File naming convention |
|---|---|---|
| CFD data | CFD case and data files as used for post-processing | ModelX-DD-MM-MESHX_M($M_1 \times 10$).cas or .dat |
| CFD STEP files | STEP geometry input files required for ANSYS Design Modeler | ModelX-DD-MM-Domain.stp |
| CFD Mesh files | Fluent input .msh files | ModelX-DD-MM-MESHX.msh |
| Mach surfaces | Plots processed Mach surface data (image processing: MS_processing.m; plotting and formatting: MS_surfaces.m) | Processed data: Mach_stem_CFD_ModelX_M($M_1 \times 10$).xlsx |
| Shear edges | Plots shear edge trajectory (Shear_layer_edge.m) | Input data from TecPlot: ModelX_M($M_1 \times 10$).xlsx |
| Streamline deflection | Computes streamline deflection angles from extracted CFD data (Processing and plotting: Defl_processing.m) | Extracted CFD data stored in: ModelX_M($M_1 \times 10$)_defl.mat) |
| Validation image construction | Constructs shadowgraph and schlieren images from CFD data (Main application: Shadow_plot_no_zero.m; input data: Slice_data_wkspace.mat) | Final images: Integrated_Shlieren_[Model no.]-$\lambda$-$\phi$-$M_1$.jpg |
| Effective analysis | Performs operations on effective data in analysis planes (Effecive_Analysis.m) | Input data: ModelX_M($M_1 \times 10$)_Analysis.mat; 3D effective theoretical transition data: TransitionCriteria_workspace.mat |
| Transition-pt-int-line | Plots transition points on intersection lines. (Main files: Transition_Location_Comparison_VaryM_Model8.m and Transition_Location_Comparison_Geom_M30/M34.m) | - |